

Structural and biochemical analysis of selected nucleic acid-protein complexes

Dissertation

zur Erlangung des Doktorgrades der Naturwissenschaften (*Dr. rer. nat.*)

an der Fakultät für Mathematik, Informatik und Naturwissenschaften

der Universität Hamburg

Fachbereich Chemie

vorgelegt von

Christina Schmidt

Hamburg, 2019

Die vorliegende Arbeit wurde im Zeitraum von Juli 2015 bis Januar 2019 in der Arbeitsgruppe von Prof. Christian Betzel im Laboratorium für Strukturbiologie von Infektion und Entzündung am Institut für Biochemie und Molekularbiologie des Fachbereichs Chemie angefertigt.

1. Gutachter: Prof. Ch. Betzel
2. Gutachter: Prof. A. Torda

Datum der Druckfreigabe: 27.09.2019

Publications

- Schmidt Christina**, Markus Perbandt, Sven Klußmann, and Christian Betzel. 2019. “Molecular Characterization of a Ghrelin L-Aptamer Complex.” *Journal of Molecular Structure*. **(Submitted)**
- Botha, Sabine, Daniela Baitan, Katharina. E.J. Jungnickel, Dominik Oberthür, **Christina Schmidt**, Stephan Stern, Max. O. Wiedorn, Markus Perbandt, Henry N. Chapman, and Christian Betzel. 2018. “*De Novo* Protein Structure Determination by Heavy-Atom Soaking in Lipidic Cubic Phase and SIRAS Phasing Using Serial Synchrotron Crystallography.” *IUCrJ* 5: 524–30.
doi:10.1107/S2052252518009223.
- Martirosyan, Arayik, Lawrence J. DeLucas, **Christina Schmidt**, Markus Perbandt, Deborah McCombs, Martin Cox, Christopher Radka, and Christian Betzel. 2019. “Effect of Macromolecular Mass Transport in Microgravity Protein Crystallization.” *Gravitational and Space Research*. **(Accepted)**

Table of contents

Publications	I
Table of contents	I
List of Abbreviations	VII
1. Zusammenfassung	1
1. Abstract	5
2. Introduction	7
2.1. Nucleic acid-protein complexes	7
2.2. <i>Mycobacterium avium</i> ssp. <i>paratuberculosis</i> Ferric uptake regulator A (MAP FurA)	7
2.2.1. <i>Mycobacterium avium</i> ssp. <i>paratuberculosis</i> (MAP)	7
2.2.2. Paratuberculosis	7
2.2.3. Metal ion homeostasis in MAP	9
2.2.4. Ferric uptake family (Fur)	9
2.2.5. Oxidative stress in bacteria and Iron-containing enzymes	11
2.2.6. MAP FurA	12
2.3. Aptamer selection and their drug potential	14
2.3.1. Mirror image L-RNA Aptamers (Spiegelmers)	16
2.3.2. Ghrelin-NOX-B11	17
2.3.2.1. Physiological role of Ghrelin	17
2.3.2.2. Structural Information	20
2.3.2.3. Ghrelin-NOX-B11	21
2.4. Crystallization of nucleic acid-protein complexes	22
2.4.1. Difficulty of protein-nucleic acid complex crystallization and structure determination	22
2.4.2. The phase problem	23
2.4.2.1. Multi- and Single-wavelength anomalous diffraction (MAD/SAD)	24
2.4.2.2. Native SAD	27
2.5. Aims of the thesis	29
3. Materials and Methods	30
3.1. Materials	30
3.1.1. Chemicals	30
3.1.2. Consumables	30
3.1.3. Equipment	31
3.1.4. Buffer, Media and Solutions	34
3.1.4.1. Growth media and antibiotics used for cultivation of recombinant <i>Escherichia coli</i> strains	34
3.1.4.2. Generally used buffers and solutions	36

3.1.4.3. Buffers for Ghrelin•NOX-B11 complex formation and purification.....	38
3.1.4.4. Buffer for <i>Mycobacterium avium</i> ssp. <i>paratuberculosis</i> FurA purification.....	38
3.1.4.5. Buffers for <i>Mycobacterium avium</i> ssp. <i>paratuberculosis</i> (MAP) FurA solubility screening	39
3.1.4.6. Stock solutions for buffer preparation or soaking to generate derivative crystals .	40
3.1.5. Molecular-weight size markers.....	41
3.1.6. Commercial kits.....	41
3.1.7. Bacterial strains.....	42
3.2. Molecular biology and biochemical Methods.....	42
3.2.1. Agarose-gel electrophoresis.....	42
3.2.2. DNA cleanup	43
3.2.3. Determination of nucleic acid concentration	43
3.2.4. Preparation of chemically competent <i>E. coli</i> cells.....	44
3.2.5. Transformation of competent <i>E. coli</i> cells with pFurA	44
3.2.6. Preparation of bacterial plasmid DNA.....	45
3.2.7. DNA sequencing.....	45
3.2.8. Recombinant gene expression of <i>Mycobacterium avium</i> ssp. <i>paratuberculosis</i> (MAP) <i>furA</i>	46
3.2.9. Preparation of cleared <i>E. coli</i> lysates	46
3.2.10. Anion exchange chromatography	47
3.2.11. Buffer exchange and sample desalting.....	47
3.2.11.1. Desalting with a spin filter.....	47
3.2.11.2. Dialysis	48
3.2.12. SDS polyacrylamide gel electrophoresis (SDS-PAGE).....	48
3.2.13. Native PAGE	50
3.2.14. Protein quantification.....	51
3.2.15. Sample concentration.....	51
3.2.16. Size exclusion chromatography (SEC)	51
3.2.17. Dynamic light scattering.....	52
3.2.18. Circular dichroism (CD) spectroscopy	53
3.2.19. Observation of protein oxidation with Fast Protein Liquid Chromatography (FPLC)	54
3.2.20. MAP FurA DNA binding site analysis with Electrophoretic Mobility Shift Assay (EMSA).....	54
3.2.21. MALDI mass spectrometry.....	55
3.2.22. Small angle X-ray scattering (SAXS).....	57
3.2.23. Thermal shift assay	58
3.2.24. Solubility Screening.....	59
3.2.25. Complex formation	59

3.2.26. Complex formation evaluation with Electrophoretic Mobility Shift Assay (EMSA)	60
3.2.27. Screening for crystallization conditions	60
3.2.28. Crystallization conditions optimization	61
3.2.29. <i>In situ</i> DLS	62
3.2.30. Streak-Seeding	63
3.2.31. Fluorescent labeling of nucleic acids crystals	63
3.2.32. Cryo protection and soaking procedure for derivative crystal production	63
3.2.33. Data collection	65
3.2.34. Data evaluation	66
3.2.34.1. Indexing	66
3.2.34.2. Data reduction	66
3.2.34.3. Data analysis and multi crystal merging	67
3.2.35. Experimental Phasing	67
3.2.35.1. Substructure determination	67
3.2.35.2. Substructure refinement and Phasing	68
3.2.36. Molecular replacement	68
3.2.36.1. Search model generation by comparing experimental SAXS profiles and <i>in silico</i> generated 3D models	68
3.2.36.2. Molecular replacement using secondary structural fragments according to Robertson and Scott (2008)	69
4. Results	71
4.1. Structural and biochemical analysis of <i>Mycobacterium avium</i> ssp. <i>paratuberculosis</i> (MAP) Ferric Uptake Regulator A (FurA)	71
4.1.1. Expression of MAP FurA	71
4.1.2. Purification of MAP FurA	72
4.1.3. Crystallization trials	75
4.1.4. Bioinformatical information	77
4.1.5. SAXS	79
4.1.6. Secondary structure information	82
4.1.7. Analysis of the MAP FurA dimer dissociation rate	84
4.1.8. Influence of different metal ions and metal chelators on MAP FurA stability	85
4.1.9. Metal binding analysis	86
4.1.10. Influence of reducing agents on MAP FurA	87
4.2. Structural insights into the Ghrelin•NOX-B11 complex	89
4.2.1 Complex verification	89
4.2.2. Complex stability	89
4.2.3. SAXS	91
4.2.4. Crystallization and data collection	95

Table of contents

4.2.5. <i>De novo</i> phase determination approaches.....	98
4.2.5.1. Native P-SAD with intrinsic phosphates as anomalous scatterers.....	98
4.2.5.2. Ca-MAD for substructure determination.....	104
4.2.5.3. Derivative production for phase retrieval (Co-MAD/Co-SAD).....	106
4.2.5.4. Substructure determination and phasing.....	110
4.2.5.5. Racemic crystals for easier structure determination.....	112
4.2.6. Molecular replacement phase retrieval approaches.....	114
4.2.6.1. Molecular replacement with the use of helical L-RNA fragments.....	114
4.2.6.2. Molecular replacement with generated 3D models.....	117
5. Discussion.....	119
5.1. Structural and biochemical analysis of MAP FurA.....	119
5.2. Structural insights into Spiegelmer-Peptide complexes.....	123
5.2.1. Ghrelin•NOX-B11 characterization and crystallization.....	123
5.2.2. Ghrelin•NOX-B11 phasing approaches.....	124
6. Conclusion and Outlook.....	135
6.1. Biochemical analysis of MAP FurA.....	135
6.2. Ghrelin•NOX11 phasing and structure solution.....	136
References.....	138
Appendix.....	167
A1. Chemicals and Hazards.....	167
A1.1. Chemicals.....	167
A1.2. Crystallization Screens.....	171
A1.3. GHS and Risk Symbols.....	172
A1.4. Hazard Statements.....	173
A1.5. Precautionary Statements.....	174
A2. List of Figures.....	176
A3. List of Tables.....	178
Acknowledgements.....	179
Eidesstattliche Versicherung.....	181

List of Abbreviations

(GHSR)1a	Growth Hormone Secretagogue Receptor 1a
¹ H NMR	Proton Nuclear Magnetic Resonance
Å	Ångström
AgRP	Agouti-related Peptide
<i>ahp</i>	Alkyl Hydroperoxide Reductase CF encoding gene
AIEX	Anion Exchange Chromatography
AMD	Age Related Macular Degeneration
approx.	Approximately
APS	Ammonium Peroxydisulfate
<i>B. subtilis</i>	<i>Bacillus subtilis</i>
Bicine	2-(Bis(2-hydroxyethyl)amino)acetic acid
BLAST	Basic Local Alignment Search Tool
bp	Base Pair
C	Celsius
CCD	Charge-Coupled Device
CCL2	CC-chemokine ligand 2
CD	Circular Dichroism
CNS	Central Nervous System
Ca-MAD/SAD	Multi-/Single-wavelength anomalous diffraction with calcium as anomalous scatterer
Co-MAD/SAD	Multi-/Single-wavelength anomalous diffraction with cobalt as anomalous scatterer
cP	Centipoise
cv	Column Volume
CXCL12	Chemokine (C-X-C motif) ligand 12
Da	Dalton
ddH ₂ O	Double-distilled water
DESY	Deutsches Elektronen Synchrotron
DLS	Dynamic Light Scattering
D _{max}	Maximum Particle Diameter
DNA	Desoxyribonucleic Acid
DTT	(2S,3S)-1,4-Disulfanyl-2,3-butanediol
<i>E. coli</i>	<i>Escherichia coli</i>
EDTA	2,2',2'',2'''-(1,2-Ethanediyldinitrilo)tetraacetic acid
EGTA	3,12-Bis(carboxymethyl)-6,9-dioxa-3,12-diazatetradecane-1,14-dioic acid
EMBL	European Molecular Biology Laboratory
et al.	et <i>alii</i> /et <i>aliae</i>
FDA	U.S. Food and Drug Administration
FEL	Free Electron Laser
FOM	Figure of Merit
FPLC	Fast Protein Liquid Chromatography
FUR	Ferric Uptake Regulator
g	Gram
ger.	German
GH	Growth Hormone

List of Abbreviations

GHS	Globally Harmonised System
GOAT	Ghrelin-O-Acyl-Transferase
h	Hours
HEPES	4-(2-hydroxyethyl)-1-piperazineethanesulfonic acid
HREM	High Remote Energy Dataset for MAD phasing Dataset collected at absorption inflection point for MAD
Infl	Phasing
IPTG	Isopropyl-1-thio- β -D-galactopyranosid
K	Kelvin
k	Kilo
KatA	Catalase A
Kd	Dissociation constant
kDa	Dalton $\cdot 10^3$
L	Liter
LB	Luria Bertani
LonA	ATP-dependent Serine Protease from <i>Bacillus subtilis</i>
m	Meter
M	Molar
<i>M. tuberculosis</i>	<i>Mycobacterium tuberculosis</i>
MAD	Multi-wavelength Anomalous Diffraction
MAP	<i>Mycobacterium avium</i> ssp. <i>paratuberculosis</i>
MAPK	mitogen-activated protein kinase
max.	Maximum
MCO	Metal-catalyzed Oxidation
MES	2-(N-morpholino)ethanesulfonic acid
min	Minutes
MIR	Multiple Isomorphous Replacement
MIRAS	Multiple Isomorphous Replacement using Anomalous Scattering
MR	Molecular Replacement
ms	Millisecond
MS	Mass Spectrometry
Mur	Manganese Uptake Regulator
MW	Molecular Weight
MWCO	Molecular Weight Cut-off
NaCl	Sodium chloride
Ni-NTA	Nitrilotriacetic acid
nm	Nanometer
NMR	Nuclear Magnetic Resonance
NPY	Neuropeptide Y
NTS	<i>Nucleus Tractus Solitarius</i>
Nur	Nickel Uptake Regulator
OD _{600nm}	Optical Density at 600 nm
OxyR	Hydrogen Peroxide-inducible Genes Activator from <i>Escherichia coli</i>
P/D1	Cells producing ghrelin and line the fundus of the human stomach
P-SAD	Single-wavelength anomalous diffraction with phosphorous as anomalous scatterer

PAGE	Polyacrylamide Gel Electrophoresis
PBS	Phosphate Buffered Saline
PCR	Polymerase Chain Reaction
PDB	Protein Data Bank
Peak	Dataset collected at Absorption Peak for MAD Phasing
PEG	Polyethylene Glycol
PerR _{BS}	Peroxide Response Protein from <i>Bacillus Subtilis</i>
PETRA	Positron Elektron Tandem Ring Analyse
pH	<i>potentia hydrogenii</i>
PMSF	Phenylmethanesulfonyl fluoride
qPCR	quantitative Polymerase Chain Reaction
R _g	Radius of Gyration
R _h	Hydrodynamic Radius
RMS	Root Mean Square
RNA	Ribonucleic Acid
ROS	Reactive Oxygen Species
rpm	Rounds per Minute
RT	Room Temperature
s	Seconds
S-SAD	Single-wavelength anomalous diffraction with sulfur as anomalous scatterer
SAD	Single-wavelength Anomalous Diffraction
SAXS	Small Angle X-ray Scattering
SDS	Sodium dodecyl sulfate
SEC	Size Exclusion Chromatography
SELEX	Systematic Evolution of Ligands by EXponential enrichment
SIR	Single Isomorphous Replacement
SIRAS	Single Isomorphous Replacement with Anomalous Scattering
SNP	Single Nucleotide Polymorphism
SONICC	Second Order Nonlinear Imaging of Chiral Crystals
SoxRS	Superoxide Response protein from <i>Escherichia coli</i>
SPR	Surface Plasmon Resonance
ssp	Subspecies
TAE buffer	Tris-acetate-EDTA buffer
TEMED	Tetramethylethylenediamine
TFE	Tetrafluoroethylene
TFZ	Translation Function Z-Score
T _m	Melting temperature
TRIS	Tris-(hydroxymethyl)-aminomethane
UV	Ultraviolet
V	Volt
v/v	Volume per volume
VIS	visible
W	Watt
w/v	Weight per volume
XANES	X-ray Absorption Near-edge Structure Spectroscopy
XFEL	X-ray Free Electron Laser

List of Abbreviations

Zur	Zinc Uptake Regulator
α	Alpha
β	Beta
γ	Gamma
μ	Micro
σ	Sigma
χ	Chi

One letter Code	Three letter Code	Amino Acid
A	Ala	Alanine
C	Cys	Cysteine
D	Asp	Aspartate
E	Glu	Glutamate
F	Phe	Phenylalanine
G	Gly	Glycine
H	His	Histidine
I	Ile	Isoleucine
K	Lys	Lysine
L	Leu	Leucine
M	Met	Methionine
N	Asn	Asparagine
P	Pro	Proline
Q	Gln	Glutamine
R	Arg	Arginine
S	Ser	Serine
T	Thr	Threonine
V	Val	Valine
W	Trp	Tryptophan
Y	Tyr	Tyrosine

Abbreviation	Base
A	Adenine
C	Cytosine
G	Guanine
U	Uracil
T	Thymine

1. Zusammenfassung

Nukleinsäure-Protein-Komplexe sind essentiell für die Genregulation, Transkription und Translation sowie die Zellhomöostase. Das Verständnis der strukturellen Wechselwirkungen zwischen Nukleinsäuren und Proteinen ist wichtig für die Grundlagenforschung und Arzneimittelentwicklung. Im Rahmen dieser Arbeit wurden strukturelle und biochemische Informationen über einen Transkriptionsfaktor aus dem pathogenen Bakterium *Mycobacterium avium* ssp. *paratuberculosis* (MAP) und einem L-RNA-Aptamer, in Komplex mit dem wichtigen Appetit anregenden Peptid Ghrelin, gewonnen.

Der erste Teil dieser Arbeit umfasst die Untersuchung des Peroxids empfindlichen Transkriptionsfaktors (MAP Ferric Uptake Regulator, FurA) aus *Mycobacterium avium* ssp. *paratuberculosis* (MAP), der Erreger der Paratuberkulose bei Wiederkäuern, insbesondere bei Nutztieren. Diese Krankheit ist oft tödlich und verursacht enorme wirtschaftliche Verluste für die Milchindustrie weltweit. In dieser Arbeit werden erste strukturelle Informationen zu MAP FurA vorgestellt. Zum ersten Mal wurde die offene und die geschlossene Konformation von MAP FurA beobachtet, während die offene Form vermutlich DNA binden kann, um die Genexpression zu regulieren. Die offene Form hat Metallionen gebunden und ist nicht oxidiert. Es konnte gezeigt werden, dass MAP FurA neben Zink auch Mangan und Eisen binden kann. Dies könnte darauf hindeuten, dass bei der Bindung verschiedener Metallionen ein Feinabstimmungsmechanismus der Regulation in Abhängigkeit von der aktuellen cytosolischen Zusammensetzung möglich ist. Das Apo-Protein und die oxidierte Form liegen in geschlossener Form vor, was in einem Verlust der DNA-Bindung resultieren könnte. Wenn oxidativer Stress auftritt, wird Eisen oxidiert und vom Protein dissoziiert, woraufhin eine Konformationsänderung stattfindet. Kristallisationsversuche wurden durchgeführt und erste Mikrokristalle wurden erhalten. Weitere Optimierungen sind erforderlich, um strukturelle Informationen über die Metallbindung und die DNA-Wechselwirkung zu erhalten.

Der zweite Teil der Arbeit umfasst strukturelle Analysen des Ghrelin•NOX-B11-Komplexes und stellt verschiedene Methoden vor, die für die experimentelle Bestimmung der Phaseninformation von Nukleinsäure-haltigen Kristallen verwendet werden können. In den 1990er Jahren führte die Entwicklung von SELEX (*Systematic Evolution of*

Ligands by Exponential enrichment; dt: systematische Evolution von Liganden durch exponentielle Anreicherung) zur Entwicklung von Aptameren, eine neue Gruppe von DNA- oder RNA-Molekülen, die über ihre 3D-Struktur mit hoher Affinität an ihre Zielmoleküle binden.

Spiegelmer wurden von der NOXXON Pharma AG entwickelt und sind eine spezielle Klasse von Aptameren, die aus den stereochemischen Spiegelbildern der natürlich vorkommenden Nukleotiden (L-Nukleotide) bestehen, und daher gegenüber Endo- und Exonukleasen nicht anfällig sind. NOX-B11 ist ein Spiegelmer, der das aktive Octanoyl-Ghrelin mit hoher Affinität bindet und dessen Wirksamkeit *in vitro* und *in vivo* nachgewiesen wurde. Ghrelin ist ein Appetit anregendes Peptid, das mit verschiedenen physiologischen Prozessen in Verbindung gebracht wird, hauptsächlich bei der Regulation des Lebensmittelstoffwechsels und des Hungers. Es ist daher ein wichtiges Molekül für die Entwicklung von Arzneimitteln. Die aktive Form von Ghrelin, das seinen Rezeptor (*growth hormone secretagogue receptor* (GHSR) 1a) bindet, hat eine posttranslationale und für Säugetiere einzigartige Modifizierung, eine am Ser3 gebundene Fettsäuren-Seitenkette. Im Rahmen dieser Arbeit wurden erste Strukturinformationen über die Komplexbildung gewonnen. Es wurde gezeigt, dass die L-RNA und der Komplex hochstabil sind. *In-situ*-DLS-Studien zeigten eine Konformationsänderung des Spiegelmers nach Ghrelin-Zugabe. Die Stabilität der L-RNA und des Komplexes wurde über einen Zeitraum von 40 Tagen überwacht. Weiterhin konnten SAXS Messungen die Konformationsänderung bestätigen. NOX-B11 ist elongiert, wohingegen NOX-B11 im Komplex mit Ghrelin eine kompaktere Konformation einnimmt. Umfangreiche Kristallisationsversuche wurden durchgeführt und es war möglich, für Röntgenbeugungsexperimente geeignete Kristalle zu erhalten. Röntgenbeugungsdaten wurden von einem Einkristall mit einer Auflösung von 2.65 Å gesammelt, in der Raumgruppe C2. Da weder strukturelle Informationen über das Spiegelmer noch über Ghrelin bekannt waren, wurden verschiedene Methoden zur Phasenbestimmung angewendet. Das Phasenproblem der Kristallographie ist nach wie vor der größte limitierende Faktor bei der Strukturbestimmung, da nur die Amplituden einer Reflexion, und nicht die Phasen, gemessen werden können. Natives SAD ist ein vergleichsweise neuer Ansatz zur Phasenrückgewinnung, bei dem die intrinsischen Atome (z.B. Schwefel für Proteine, Phosphor für Nukleinsäuren) als anomale Streuer verwendet werden. Die Daten müssen hochredundant sein und ein möglichst geringes Signal-Rausch-Verhältnis aufweisen. Um die relativ schwachen anomalen Signale zu verstärken, wurden

Diffractionsdaten bei langen Wellenlängen an speziell dafür konzipierten Beamlines gemessen (EMBL Beamline P13 und I23 an der Diamond Light Source). Es wurden mehrere Datensätze gesammelt und eine Mehrkristallanalyse durchgeführt. Nach der Analyse wurden statistisch ähnliche Kristalle kombiniert, wodurch das Signal-Rausch-Verhältnis, sowie das anomale Signal erhöht werden konnten. Da die Substrukturlösung nicht erfolgreich war, wurden Schweratomderivate erzeugt. Kobalt-Derivatdaten wurden gesammelt mit einer Auflösung von bis zu 2.3 Å. Da die Phasenwiederherstellung fehlschlug, wurde mehrere helikale Fragmente als Suchmodelle für molekularen Ersatz verwendet, was jedoch ebenfalls erfolglos blieb. 3D-RNA-Modelle wurden unter Einbeziehung der durch SAXS-gewonnenen experimentellen Daten generiert. Das Modell, das am besten zu den experimentellen SAXS-Daten passte, wurde als Suchmodell für den molekularen Ersatz verwendet, aber auch eine Strukturlösung war nicht möglich. Die Phasenrückgewinnung war leider bei allen Ansätzen nicht erfolgreich, was die Schwierigkeiten aufzeigt, die bei der Kristallisation von RNA- und Peptidkomplexen auftreten können, wenn keine Phaseninformationen bekannt sind.



1. Abstract

Nucleic-acid-protein complexes are essential for gene regulation, transcription, translation and cell homeostasis. The study of these interactions and the understanding of structural interactions between nucleic acids and proteins is important for general research and drug development. In the course of this work, structural and biochemical information about a transcription factor from the pathogenic *Mycobacterium avium* ssp. *paratuberculosis* and of an L-RNA aptamer, in complex with the orexigenic peptide ghrelin, was obtained.

In the first part of the thesis the peroxide sensitive, transcription factor Ferric Uptake Regulator (FurA) from *Mycobacterium avium* ssp. *paratuberculosis* (MAP), the causative agent for paratuberculosis in ruminants and especially in livestock, was studied. This disease is often fatal and responsible for huge economic losses for the livestock industry worldwide. Here, first structural information about MAP FurA is presented. For the first time, the open and the closed confirmation of MAP FurA were observed, where the open form is putatively able to bind DNA to regulate gene expression. The open form is the metalized, unoxidized MAP FurA. It was shown, that MAP FurA is able to bind manganese and iron, as well as zinc. This might indicate, that upon binding of different metal ions, a fine-tuning mechanism of regulation is possible, depending on the current cytosolic composition. The apo-protein and the oxidized form are in the closed form, indicating that these forms are not able to bind DNA. When peroxide stress is occurring, the iron gets oxidized and dissociated from the protein resulting in a conformational change. Crystallization trials were performed and first initial microcrystals were obtained. Further optimization is needed to obtain structural information about the metal binding and DNA interaction.

The second part of this thesis provides structural insights into the Ghrelin•NOX-B11 complex and presents several methods that can be used for phase retrieval for nucleic acid containing crystals. In the 1990s the development of SELEX (Systematic Evolution of Ligands by Exponential enrichment) led to the development of aptamers, a novel group of DNA or RNA molecules that bind to their cognate targets with high affinity via their 3D structure. Spiegelmers were developed by the NOXXON Pharma AG and are a special class of aptamers that consist of unnatural L-nucleotides and are hence not susceptible to endo- and exo-nucleases. NOX-B11 is a Spiegelmer that binds the active octanoyl-ghrelin

with high affinity and effectiveness has been demonstrated *in vitro* and *in vivo*. Ghrelin is an orexigenic peptide that is associated with various physiological processes, mostly in the regulation of food metabolism and hunger. It is therefore an important drug target. The active form of ghrelin, which binds its receptor (growth hormone secretagogue receptor (GHSR)1a), has a posttranslational, and for mammals unique, modification, namely a fatty acid side chain bound at Ser3. Here, first structural information about complex formation was obtained. It was shown, that the L-RNA and the complex are highly stable. *In situ* DLS studies revealed a conformational change of the Spiegelmer upon ghrelin addition and stability of the L-RNA and the complex was monitored over 40 days. Furthermore, SAXS measurements demonstrated the conformational change as well, as the L-RNA transitions from an elongated molecule to a more compact complex with ghrelin. Extensive crystallization trials were performed and it was possible to obtain X-ray diffraction suitable crystals. X-ray diffraction data were collected from a single crystal to a resolution of 2.65 Å and the space group was determined to be C2. Since no structural information about the Spiegelmer, nor ghrelin, was known, several phase retrieval methods were applied. The phase problem of crystallography is still the main bottleneck of structure determination, as only the amplitudes of a reflection can be measured and the phases are not observed. Native SAD is a comparatively new approach for phase retrieval, using the intrinsic atoms (sulfur for proteins, phosphorous for nucleic acids) as anomalous scattering atoms. Data needs to be highly redundant and with as low signal/noise ratios as possible. To enhance the small anomalous signals data were measured at long wavelengths at designated beamlines at EMBL Beamline P13 and I23 at the Diamond Light source. Multiple datasets were collected and multi crystal analysis was performed. After cluster analysis, the I/σ and $\Delta F/\sigma(\Delta F)$ was enhanced and data were subjected to substructure solution. As substructure solution was not successful, heavy atom derivatives were generated. Cobalt-derivative data were collected and crystals diffracted up to 2.3 Å. Since phase retrieval failed, molecular replacement with fragments was applied, but was also unsuccessful. SAXS data information were used as restraints for 3D RNA modelling. The best model that fit to the SAXS experimental data was used as a search model, but structure solution was again not successful. Phase retrieval was unsuccessful for all approaches, highlighting the difficulties that can arise during the structural analysis of RNA and peptide complexes, when phase information is not available.

2. Introduction

2.1. Nucleic acid-protein complexes

Nucleic acid-protein interactions are common in biology and are essential for survival and cell homeostasis. They range from genetic information to proteins, DNA replication, repair and recombination, posttranscriptional modifications, expression regulation, RNA processing and much more. Beside the molecular mechanisms that have been known for a long time, new interactions are complementing our understanding for gene regulation and homeostasis, e.g. small regulatory RNAs. Furthermore, aptamers, which are synthesized DNA or RNA fragments with specificity for a particular target molecule, were discovered. This opens up a new perspective for various applications.

2.2. *Mycobacterium avium* ssp. *paratuberculosis* Ferric uptake regulator A (MAP FurA)

In general terms, transcription factors are proteins that bind directly to the promoter regions of genes. Upon DNA binding, the expression profiles of the genes can be modulated to enable the cells to react to environmental changes and to restore homeostasis, which is required for the survival of the organism. MAP FurA is a transcription factor from the pathogenic *Mycobacterium avium* ssp. *paratuberculosis*, which is involved in several physiological regulatory pathways.

2.2.1. *Mycobacterium avium* ssp. *paratuberculosis* (MAP)

Mycobacterium avium ssp. *paratuberculosis* (MAP) is a slow growing, rod-shaped gram-positive member of the genus *Mycobacterium* of the family *Mycobacteriaceae* (Eckelt 2014; Ventura et al. 2007). MAP is the causative pathogen of Johne's disease (paratuberculosis), a chronic transmural inflammation of the small intestine in ruminants (Twort and Ingram 1912).

2.2.2. Paratuberculosis

Johne's disease, or paratuberculosis in cattle, was first described in Germany by Johne and Frontingham in 1895 (Johne and Frothingham 1895). The causative agent was termed

2. Introduction

Mycobacterium M. pseudotuberculosis, because of its dissimilarity to *Mycobacterium tuberculosis*. The disease is spread worldwide and causes huge economical losses for the livestock industry (Losinger 2005).

The pathogen is located in macrophages in the small intestinal *lamina propria* and surrounding lymph nodes, resulting in a host granulomatous inflammation and an enteropathy, which is often fatal (Whittington et al. 2017).

The disease gets transmitted unnoticed, as the chronic disease is not easy to diagnose and incubation periods can vary between 1-14 years (Salem et al. 2013). Infection mostly occurs in young calves, due to an immature immune system. (Cocito et al. 1994; Valentin-Weigand and Goethe 1999). The pathogen is ingested by contaminated milk, water or food (Sweeney 2011). MAP reaches the gastric tract and starts to express genes coding for surface proteins (e.g. fibronectin attachment protein) (Valentin-Weigand and Moriarty 1992), which enables it to cover the surface for opsonization and to bind to the fibronectin receptors of the host cells (Secott, Lin, and Wu 2004). Host macrophages take up the pathogen in which the MAP cells are able to multiply in the phagosomes (Kuehnelt et al. 2001). This is enabled due to the fact that MAP adapts to the host's metabolism and is able to persevere the host's defense mechanisms, although the exact mechanisms involved are not yet fully understood (Eckelt et al. 2015; Weigoldt et al. 2011, 2013; Trivedi et al. 2012).

Despite being a common pathogen for livestock, MAP is not host specific and also infects wild animals, such as rabbits, domesticated animals, such as cats, and even humans (Clarke 1997; Greig et al. 1999).

There is a need for paratuberculosis control and treatment, as a link between MAP and Crohn's disease in humans has been reported. MAP could therefore become a public health issue, since the pathogen gets distributed through the food chain and water supply (Eltholth et al. 2009; Salgado et al. 2013). A further involvement in the development of other immunological disorders, such as diabetes type I, autoimmune thyroiditis and multiple sclerosis has been described as well (Paccagnini et al. 2009; Naser et al. 2013; Cossu et al. 2011; Sisto et al. 2010).

There is no vaccine for humans available at this time. So far, the illness in humans is managed by suppressing the inflammatory response (Davis, Kuenstner, and Singh 2017).

A vaccine would be important to prevent MAP in livestock and ergo from the water supply and food stream. In human patients with Crohn's disease, antibiotics against tuberculosis (except for ethambutol) are futile, whereas a combination of clarithromycin, rifabutin and clofazimine showed some effect, as well as ciprofloxacin and metronidazole (Chamberlin, Borody, and Campbell 2011). On the downside, 80-90% of patients will eventually relapse while undergoing therapy or thereafter (Chamberlin, Borody, and Campbell 2011).

2.2.3. Metal ion homeostasis in MAP

One mechanism of the host's non-specific immune response is the sequestration of iron, as iron is an essential trace element in bacteria. It often serves as a cofactor in proteins, even though high levels are toxic (Nelson 1999; Blencowe and Morby 2003). Upon cytoplasmic iron shortage, bacteria respond with an elevated expression of metal uptake proteins. On the transcriptional level, the expression of metal dependent regulator proteins (metalloregulators) is used for metal homeostasis (Nelson 1999; Agranoff and Krishna 2004; Braun 2001). Iron homeostasis in bacteria is regulated by the metalloregulators of the Fur (Ferric Uptake Regulator) family (Hantke 2001), amongst others. In *Mycobacteria*, two Fur-like proteins (FurA and FurB) are present, but recent studies suggest that iron homeostasis is not entirely regulated by Fur family members. The DtxR family proteins are also associated with this regulation (Hantke 2001; Andrews, Robinson, and Rodríguez-Quñones 2003; Louvel et al. 2009; Zhu et al. 2013).

2.2.4. Ferric uptake family (Fur)

The conserved Fur proteins are present in over 4000 bacterial species (Fillat 2014). Aside from iron-dependent Fur proteins, there are also other Fur-like proteins that are involved in manganese uptake (Mur), nickel uptake (Nur), zinc uptake (Zur) and peroxide stress response (PerR) (Diaz-Mireles et al. 2004; Ahn et al. 2006; Patzer and Hantke 1998). Fur from *Escherichia coli* is the best studied representative of Fur-like proteins. It is iron-dependent and regulates approx. 100 genes associated with iron homeostasis and general metabolism (Fillat 2014; Hantke 1981). Fur proteins are also associated with pathogenesis and the expression regulation of virulence factors, rendering them important for drug development (Sevilla et al. 2008; Allard, Viswanathan, and Cianciotto 2006; Kim et al. 2013; Ochsner, Vasil, and Vasil 1995).

Fur levels are autoregulated by repression via binding of Fur proteins to their cognate promoters. Furthermore, upon metal binding, the proteins undergo a conformational change that enables them to bind the promoter sequences of the regulated genes. Most bacterial species contain more than one Fur protein, that albeit having similar sequences and overall structure, have different regulatory functions (Hantke 2001; Botello-Morte et al. 2013; Fuangthong and Helmann 2003; Fillat 2014). Fur proteins are mostly repressing gene expression, but can also be activators (Butcher et al. 2012; Eckelt et al. 2015; Bagg and Neilands 1987; Carpenter et al. 2013; Grifantini et al. 2003). Regulation can also be indirect, via iron repressed binding to small regulatory RNAs (Massé and Gottesman 2002).

In general, two Fur-like proteins form a homodimer and contain a DNA binding domain and several metal-binding sites. The proteins have a histidine-rich motif at the beginning of their dimerization domain. They contain either two or three metal binding sites, where one is a structural binding site, and one or two are regulatory binding sites (Fillat 2014). A less conserved CXXC motif close to the carboxyl moiety binds zinc, which is tightly bound and is required for dimerization and stability (Althaus et al. 1999; Zheleznova, Crosa, and Brennan 2000; D'Autréaux et al. 2007). A second metal binding site is located between the dimerization and DNA-binding domains. Amino acid residues from both domains are involved in metal binding, enabling a conformational change of the protein. The affinity for different metals varies, and therefore a fine-tuned regulation of genes is possible (Fillat 2014). Some Fur proteins have a third metal binding site at the core of the dimerization domain. The site is proposed to have additional structural function and occurs in a diverse group of proteins that serve different functions in the cell (Butcher et al. 2012; Dian et al. 2011; Shin et al. 2011; Lucarelli et al. 2007; Ma, Gabriel, and Helmann 2011). It is worth noting that some Fur proteins also bind DNA in their apo-form, where only the structural zinc or no zinc is present (Dian et al. 2011).

The DNA-binding domain is comprised of a winged helix at the N-terminus. The proteins bind to palindromic A/T-rich sequences (Fillat 2014). For *E. coli* Fur, a 19 bp consensus sequence was determined, with a minimum of three repeats of the hexameric motif GATAAT, necessary for binding (Escolar, Pérez-Martín, and de Lorenzo 1998). The sequence identity of Fur boxes range from 50-80% throughout all bacterial species (Baichoo et al. 2002; Thompson et al. 2002; Sebastian et al. 2002; Fillat 2014).

2.2.5. Oxidative stress in bacteria and Iron-containing enzymes

Another mechanism involved in the host's innate immune cell's fight against pathogens is the use of reactive oxygen species (ROS) and reactive nitrogen species to induce, for the most part fatal, oxidative stress in the pathogen's cells (Fang 2004). This leads to an oxidative inactivation of iron containing enzymes, as H_2O_2 reacts with Fe^{2+} -ions, forming highly reactive hydroxyl radicals that can damage DNA and proteins (Imlay 2013). In *E. coli*, superoxide dismutase is catalyzing the reaction from superoxide to hydrogen peroxide. H_2O_2 is directly removed by catalases and alkylhydroperoxide reductase (Imlay 2013; Seaver and Imlay 2001). Furthermore, OxyR and SoxRS control pathways to combat ROS (Imlay 2013). OxyR acts as a redox sensor, by sensing hydrogen peroxide through disulfide formation (Pinochet-Barros and Helmann 2017). In many gram-positive bacterial species intracellular hydrogen peroxide levels are sensed by the metal-catalyzed oxidation (MCO) of regulator proteins, e.g. in *Bacillus subtilis* PerR (PerR_{BS}). PerR_{BS} is a paralog of *E. coli* Fur and its mode of action has been well studied (J.-W. Lee and Helmann 2006; Bsat et al. 1998). PerR_{BS} has the highest structural identity to MAP FurA of all the known Fur homologues with known crystal structures. PerR_{BS} is a metal-containing DNA-binding transcription factor, which represses genes that are directly involved in the detoxification of hydrogen peroxide (*katA*, a vegetative catalase and *ahpCF*, a alkylhydroperoxide reductase) and iron homeostasis upon oxidative stress (Bsat et al. 1998; Chen, Keramati, and Helmann 1995; Faulkner and Helmann 2011; Imlay 2013).

The other group of enzymes, that are controlled by PerR_{BS}, are the heme biosynthesis operons (*hemAXCDBL*) (Faulkner et al. 2012). Furthermore, proteins involved in iron sequestration and iron efflux are regulated directly or indirectly by PerR_{BS} (Chen and Helmann 1995; Chiancone and Ceci 2010; Guan et al. 2015). PerR_{BS} moreover regulates its own expression and the expression of another Fur paralog, Fur_{BS}, which regulates genes for iron sequestration and iron uptake (Ollinger et al. 2006; Gaballa et al. 2008; Smaldone et al. 2012).

PerR_{BS} is a homodimer with a structural zinc binding site and a second metal binding site, that binds iron with high and manganese with lower affinity (Traoré et al. 2006). The structural zinc is bound tightly in a cysteine pocket (Cys4:Zn) even when high peroxide levels are present *in vitro* (Traoré et al. 2006). PerR_{BS} is a transcription factor, which binds

to the operator regions of its controlled genes, when metal is bound. Upon a metal induced conformational change the protein adopts a more compact DNA-binding shape (Jacquamet et al. 2009; Traoré et al. 2006). This is facilitated by the fact that H37 and H91, both involved in metal binding, are located in different protein domains and get closer to together through metal binding (Ahn and Baker 2016).

When iron is bound, the protein is highly sensitive to hydrogen peroxide, resulting in oxidative stress related genes such as *mrgA*, *katA*, *pfeT*, *ahpC* and *hemA* being induced (Helmann et al. 2003; Fuangthong et al. 2002), whereas the expression of *perR_{BS}* and *fur_{BS}* is weakly repressed (Fuangthong et al. 2002).

Redox sensing is enabled through several redox-active cysteines and two mechanisms have been proposed: the first proposed mechanism is that H₂O₂ binds the bound iron of Per_{BS} and a localized hydroxyl radical is formed. This results in a modification of H37 and H91 to 2-oxo-histidine (Schöneich 2000; Lee and Helmann 2006; Traoré et al. 2008). The other mechanism postulates a heterolytic H₂O₂ cleavage, where the released water results in an Fe(IV)-oxo intermediate (Sethu et al. 2016). After this the iron is released from the oxidized protein and Per_{BS} is degraded by the LonA protease (Ahn and Baker 2016).

2.2.6. MAP FurA

In *Mycobacteria* two Fur homologues are present, FurA and FurB. The function and structure of FurB, a zinc homeostasis regulating protein from *Mycobacterium tuberculosis*, is well studied, whereas the function of FurA is less well understood (Maciag et al. 2007; Canneva et al. 2005; Fillat 2014). The genes encoding the respective proteins share a sequence identity of only 25% and seem to have completely dissimilar roles in *mycobacteria*.

FurA is located upstream of *katG* in all sequenced mycobacterial strains. *KatG* encodes a catalase-peroxidase and is involved in the oxidative stress response and a major virulence factor in *M. tuberculosis* (Pym et al. 2001). The genes are co-expressed and autoregulated by FurA via binding to its own promoter region as a repressor, as shown in *M. tuberculosis* (Sala et al. 2003).

This hints at FurA being involved in oxidative stress defense, similarly to Per_{BS} (Lucarelli et al. 2008; Zahrt et al. 2001; Pym et al. 2001). In MAP, 13 genes have higher expression levels, whereas 35 genes are lower expressed in $\Delta furA$ deletion mutants.

Surprisingly, the expression of genes that are known to be involved in iron homeostasis were unaffected by this deletion (Eckelt et al. 2015).

These results suggest that MAP FurA acts as a repressor and an inducer and that its function may differ from that of known homologues. As a repressor, MAP FurA might bind to the operator region of genes that are involved in oxidative stress response and redox processes (Eckelt et al. 2015). The downregulated gene cluster *map1589c-1587c* codes for the alkyl hydroperoxide reductases (*ahp*), which are known to be involved in resistance against oxidative stress and drug resistance in *M. tuberculosis* (Master et al. 2002; Sherman et al. 1999).

Deletion of *furA* results in the downregulation of 35 genes that are mainly involved in metabolism, stress response, two putative transporters and 13 genes of unknown function (Eckelt et al. 2015). Furthermore, 11 virulence associated genes were reported to be downregulated in the absence of FurA (Eckelt et al. 2015). FurA also seems to autoregulate itself, as has been reported in *M. tuberculosis* (Eckelt et al. 2015; Sala et al. 2003). Interestingly, only four genes have a putative *fur* box in their 5' upstream region (*furA*, *ahpC*, *map0847* and *map3421c*) (Eckelt et al. 2015). In contrast to other homologues, iron starvation has only little impact on the expression of *furA*, whereas it was heavily induced by H₂O₂ (Eckelt et al. 2015). Surprisingly, the expression of *ahpC* and *ahpD* was induced by both iron starvation and oxidative stress. Other genes that are either regulated directly or indirectly by FurA show no change in their expression profiles under any of the stresses. These results suggest, that FurA acts as a repressor under oxygen stress and iron starvation, whereas it induces expression of other virulence associated genes in its apo form (Figure 1) (Eckelt et al. 2015). The data also suggests a more restricted role for FurA regulation, as opposed to other members of the family where they act as global regulators.

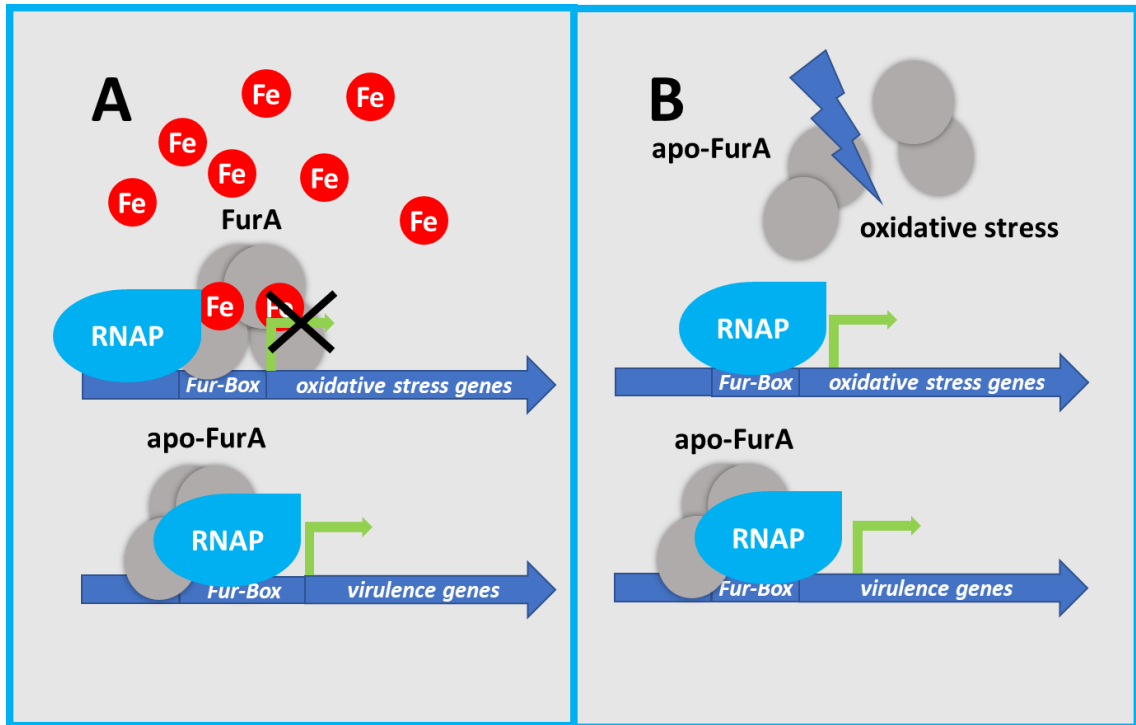


Figure 1: Putative regulatory mechanisms of FurA in MAP (Eckelt et al. 2015) (with modifications). A: Iron ions present: MAP FurA homodimers bind iron ions, repressing the expression of oxidative stress genes. MAP FurA homodimers also induce the expression of virulence genes independently from iron ion binding. B: Iron starvation or oxidative stress: homodimers are detached from the promoter regions and the expression of oxidative stress genes is derepressed, while the expression of virulence genes is still induced.

Preliminary experiments with *M. tuberculosis* FurA suggest that one single zinc atom is bound tightly per monomer, and another metal site can be filled with either iron or zinc (Lucarelli 2006). Further structural information or a more in depth understanding of MAP FurA metal binding and gene regulation, as well as biochemical information on the protein level, are still lacking and would give more insights into the response to oxidative stress in *mycobacteria*.

2.3. Aptamer selection and their drug potential

Aptamers are chemically synthesized, highly soluble DNA or RNA fragments that bind to their targets with very high affinities, comparable to the binding affinities of antibodies. They hold several advantages over antibodies, as they can be chemically synthesized, and therefore modified, are supposedly non-toxic and highly specific. They can be selected against single atoms, proteins, peptides, amino acids and even cells (Hofmann et al. 2019; Biesecker et al. 2019; Guo et al. 2006). Aptamers can be used as therapeutics, either as antagonists that block e.g. protein-protein interactions or receptor-ligand binding, or as

agonists for receptor activation. Another approach is to use the aptamers as carriers for the delivery of other therapeutic agents to distinct cells or target molecules.

For screening, a large library of oligonucleotides (DNA or RNA) is exposed to the target molecule. This technique is called SELEX (Systematic Evolution of Ligands by EXponential enrichment) (Robertson and Joyce 1990; Tuerk and Gold 1990; Ellington and Szostak 1990). SELEX is used to iteratively identify and isolate suitable aptamers for a particular target, that can then be amplified, sequenced and their binding affinities characterized. The secondary structure of the chosen candidate is then predicted and the minimal binding motif is examined experimentally. The aptamer should be as short as possible to save manufacturing costs that increase with every nucleotide (Bouchard, Hutabarat, and Thompson 2010). DNA-aptamers and RNA-aptamers share similar functionalities, but whereas DNA-aptamers are more stable and production costs are lower, RNA-aptamers can inherit more diverse three-dimensional conformations with strong RNA-RNA intra-strand interactions. This makes them more specific and more affine to their targets (Shu et al. 2014).

As aptamer lengths vary between 30 and 50 nucleotides, their *in vivo* potency as therapeutics is limited by renal filtration, instability in body fluids, translocation from the plasma to the liver or spleen and non-specific immune activation. Consequently, several chemical modifications were developed to counteract these problems (Kuwahara and Sugimoto 2010). For example, 2'-fluoro, 2'-amino and 2'-O-methyl modifications enhance stability against endo- and exonucleases, which are abundant in plasma (Keefe, Pai, and Ellington 2010). On the downside, those modifications often lead to affinity loss. An alternative to those modifications are Spiegelmers (NOXXON Pharma AG; *Spiegel* (ger.)=mirror), a special group of RNA-aptamers, that are synthesized with unnatural L-nucleotides and are therefore biostable against nucleases (Klußmann et al. 1996; Vater and Klussmann 2015). To antagonize renal filtration, a 40 kDa PEG moiety is routinely conjugated via a site specific linker, so several positions can be tested to prevail activity loss (Keefe, Pai, and Ellington 2010).

Till now, only one aptamer is FDA approved as a drug against age-related macular degeneration (AMD) (Macugen®, Pfizer) (FDA 2004). Ten other aptamers, agonists against diseases involving macular degeneration, coagulation, and inflammation, as well as oncological applications, are currently undergoing clinical trials. (Zhou and Rossi 2017). Even though aptamers hold several advantages over the market leader, antibodies,

clinical application still seems to be delayed and repressed, as thorough information about toxicity in humans is still lacking (Choi et al. 2011; Steffensmeier et al. 2007).

2.3.1. Mirror image L-RNA Aptamers (Spiegelmers)

As stated above, one of the main complications of aptamers as therapeutics is their instability in bodily fluids. The degradation through nucleases can be circumvented with the use of L-nucleotides, that do not occur naturally and are therefore not recognized by the stereoselective nucleases (Ashley 1992). The only chirality center is the (desoxy)ribose sugar of each nucleotide. By inversion of this chirality center, exact mirrors of the D-nucleotides are produced (Vallazza et al. 2004). The NOXXON Pharma AG produces Spiegelmers, a novel class of aptamer therapeutics. The selection process is similar to the conventional SELEX process, apart from the lack of available molecular biology tools for L-nucleotides. Hence the selection process is performed with a standard D-RNA fragment library, but the target protein or target binding domain is inverted to its mirror D-amino acid form. With chemical synthesis, 100-150 long D-amino acid chains can be routinely produced to date (Vater and Klussmann 2015). After selection, the determined D-RNA sequence is chemically synthesized out of L-nucleotides. The affinity of the Spiegelmer to its natural target is comparable to the affinity of the D-RNA aptamer to its mirrored target (Klußmann et al. 1996). The Spiegelmers are highly specific to their cognate targets, which is important for clinical trials, as they might not bind to the same animal homologous target proteins as during the pre-clinical, *in vivo* animal studies (Vater and Klussmann 2015; Eulberg et al. 2008).

In 2019, two Spiegelmer candidates are undergoing clinical studies. NOX-A12 (olaptased pegol) binds two key sites of the Chemokine (C-X-C motif) ligand 12 (CXCL12) (Sayyed et al. 2009; Hoellenriegel et al. 2014). This signaling protein bridges the communication between tumor cells and their environment and is responsible for tumor proliferation and reduces tumor apoptosis (Guo et al. 2016). The second Spiegelmer, NOX-E36 (emapticap pegol), targets the human chemokine CCL2, a key chemokine for migration and infiltration of monocytes/macrophages regulation (Eulberg et al. 2008; Maasch et al. 2008).

2.3.2 Ghrelin-NOX-B11

A further Spiegelmer, NOX-B11, binds the bioactive form of ghrelin with nanomolar affinity (K_d of 35 nM) (Helmling et al. 2004). Ghrelin is one of the key players in energy metabolism and is involved in many other physiologically important functions in humans. It is therefore a highly promising target for therapeutics development.

2.3.2.1 Physiological role of Ghrelin

Ghrelin is the endogenous ligand for the growth hormone secretagogue receptor (GHSR)1a, which mediates growth hormone (GH) release from the pituitary gland (Kojima et al. 1999). The discovery of ghrelin sparked a huge research interest, as the peptide was found to be involved in the regulation of food intake, body weight, adiposity and glucose metabolism (Tschöp et al. 2001). In humans, the *GHRL* gene that encodes ghrelin is located on the short arm of chromosome 3 and comprises five exons for the precursor proghrelin. From this, the first two code for a signal-peptide and the mature 28-amino acid peptide (Sato et al. 2012; Higgins, Gueorguiev, and Korbonits 2007). The *GHRL* gene is polymorphic, with approx. 300 single nucleotide polymorphisms (SNPs), of which four SNPs rendered pathogenic (Koutouratsas et al. 2019).

Ghrelin has a large variety of physiological functions. Beside acting directly in pituitary somatotrophs (GH release) (Kojima and Kangawa 2005; Davenport et al. 2005; Sanger and Furness 2016), it also acts on appetite stimulation. Here it affects the vagal afferent neurons in the stomach, which leads to signal transduction to the *nucleus tractus solitarius* (NTS) of the brainstem. This region of the central nervous system (CNS) connects to the hypothalamic feeding centers (Andresen and Kunze 1994; Wren et al. 2001; Sanger et al. 2016). Furthermore, it acts on the arcuate nucleus cells of the hypothalamus, causing an upregulation of the orexigenic neuropeptide Y (NPY) and agouti-related peptide (AgRP) (Kojima and Kangawa 2005; Morton and Schwartz 2001; Briggs and Andrews 2011).

Moreover, ghrelin is also associated with gut motility stimulation and gastric acid secretion (Masuda et al. 2000; Asakawa et al. 2001), sleeping (Tolle et al. 2002; Weikel et al. 2003; Szentirmai et al. 2006), reward seeking and taste sensation (Cai et al. 2013; Druce et al. 2005; Overduin et al. 2012; Skibicka et al. 2012; Tong et al. 2011). It also acts in the regulation of glucose metabolism (Date et al. 2002; Reed et al. 2008; Wortley et al. 2005; Zhao et al. 2010), regulation of stress and anxiety (Lutter et al. 2008; Spencer

et al. 2012; Chuang et al. 2011) and many more (Filigheddu et al. 2007; Rizzo et al. 2013; Okumura et al. 2002; Sato et al. 2012; Tack et al. 2006).

Ghrelin is a structurally unique peptide and circulates in the plasma in two forms. The gene is highly conserved (Gutierrez et al. 2008) and ghrelin is produced in most human tissues, most abundantly in P/D1 oxyntic cells in the fundus of the stomach, the small and large intestinal cells, pancreatic cells and in the kidney glomeruli (Veldhuis and Bowers 2010; Inui et al. 2004; Gnanapavan et al. 2002; Sato et al. 2012; Kojima and Kangawa 2005; Date et al. 2002).

The active form carries a scarce post-transcriptional modification at its Ser3, where a fatty acid chain (mostly C8 or C10) is added. This octanoylation is catalyzed by ghrelin O-acyl-transferase (GOAT) (Gutierrez et al. 2008; Jing Yang et al. 2008; Sato et al. 2012; Veldhuis and Bowers 2010). For thioesterification with Coenzyme A, GOAT needs des-acyl ghrelin and short- to mid-chain fatty acids as substrates. Both the peptide and the enzyme are expressed in similar tissues, with the highest expression in humans occurring in the pancreas and the stomach, and in the stomach and intestines for mice (Gutierrez et al. 2008; Sakata et al. 2009; Lim et al. 2011). The lipids for octanoylation are partly recruited directly from the pool of ingested lipids (Kirchner et al. 2009; Nishi et al. 2005).

The length of the added fatty acid chain is linked to metabolic function, as receptor activation and affinity differs with varying lengths *in vitro* (Bednarek et al. 2000). There was also an effect on food intake and adiposity *in vivo*, suggesting a fine-tuning mechanism with different naturally occurring ghrelin isoforms (Heppner et al. 2012). The length might act as a concise signal to the brain that caloric food is available and so the regulation of nutrient distribution and growth signals can be sent and regulated precisely (Kirchner et al. 2009; Nishi et al. 2005).

The second form, desacylated ghrelin, is most abundant in the plasma, albeit not being able to activate (GHSR)1a. Nevertheless, some physiological effects on the anti-apoptotic and hypotensive actions on the cardiovascular system have been proposed (Sato et al. 2012; Veldhuis and Bowers 2010; Baldanzi et al. 2002).

The octanoylation of ghrelin is essential for receptor binding and GH release. Ghrelin's receptor, (GHSR)1a, is a rhodopsin-like G-protein coupled receptor with seven membrane spanning segments (Yin, Li, and Zhang 2014; Davenport et al. 2005). The

receptor is located in the hypothalamic neurons that are involved in food uptake and satiety (Guan et al. 1997; Dickson and Luckman 1997; Willesen, Kristensen, and Rømer 1999; Bowers et al. 1980). The minimal binding motif for receptor binding is Gly1, Ser3 and Phe4, whereas Ser2, Leu5, Ser6 and Pro7 seem to be less important for receptor binding (Yang et al. 2008).

Besides ghrelin, motilin, which has got a 36% homology to ghrelin, is another ligand for the (GHSR)1a receptor. Upon binding, several downstream cascades such as MAPK are induced, making it a functional agonist to ghrelin-(GHSR)1a signaling (Sato et al. 2012; Veldhuis and Bowers 2010; Sanger and Furness 2016; Yin, Li, and Zhang 2014).

Ghrelin secretion is induced by positive regulators, such as fasting, muscarinic stimulation by the vagus nerve, beta-adrenergic stimulation, estrogen, cholecystokinin, glucagon and deep sleep, amongst others. The secretion is inhibited by alpha-adrenergic stimulation, insulin, glucose, leptin, long chain fatty acids and somatostatin (Veldhuis and Bowers 2010; Sanger and Furness 2016).

Reflected by these secretion regulators, ghrelin was found to have an orexigenic effect. Total plasma levels are the highest before meal ingestion and the lowest within an hour after food intake (Veldhuis and Bowers 2010; Inui et al. 2004). After endogenous ghrelin intake, the sensation of hunger is induced and food uptake is increased in humans of all weight classes and sizes (Wren et al. 2001). In mice, fasting induces enhanced ghrelin levels, whereas the des-acyl ghrelin levels are higher than acyl-ghrelin levels, which might be linked to a lack of dietary lipids. This is also reflected in decreasing GOAT transcripts (Kirchner et al. 2009). Mutational studies revealed that GOAT knock out mice had enhanced ghrelin levels (only des-acyl ghrelin) and a lower body weight and fat mass (Kirchner et al. 2009; Gutierrez et al. 2008). On the contrary, GOAT and ghrelin overexpressing mice showed a higher body weight and fat mass, highlighting the role of ghrelin for energy balance and adiposity (Kirchner et al. 2009).

The peptide was termed 'hunger hormone' after its discovery, but recent research proposes a more complex role in the regulation of food intake and adiposity. Ghrelin might be relevant for weight gain, but its complex role needs yet to be clarified. Mice lacking ghrelin have normal meal intervals, thus it is not required for sustainment and meal initiation (Callahan et al. 2004). Furthermore, obese patients and obese binge eaters have low ghrelin levels (Shiyya et al. 2002; Geliebter, Gluck, and Hashim 2005),

suggesting ghrelin levels as rather a consequence than the reason for overeating (Müller et al. 2015). Patients with cachexia, *anorexia nervosa* and *bulimia nervosa*, on the contrary, have very high ghrelin levels (Atalayer et al. 2013; Kamiji and Inui 2008; Müller et al. 2010). Furthermore, patients with Prader-Willi-Syndrome are often obese because of their lack of satiety, and also have highly increased levels of ghrelin (Cummings et al. 2002; DelParigi et al. 2002). One explanation could be that ghrelin acts as a priming agent for signaling the brain that food is ingested, to ensure an efficient metabolism and storage (Kirchner et al. 2009).

2.3.2.2. Structural Information

Despite its impressive function in a large variety of physiological pathways, ghrelin is also unique structurally, as it is known to be lipid modified. The length of the added fatty acid allows a fine-tuning mechanism to the receptor binding and the lipid containing short N-terminal segment (Gly1 to Phe4) is enough for (GHSR)1a binding. This however doesn't displace acyl-ghrelin from the receptor, nor does it lead to GH release *in vivo*, suggesting that the rest of the peptide is also involved in receptor binding (Bednarek et al. 2000; Torsello et al. 2002). ¹H NMR studies and CD data suggest that ghrelin is extremely flexible in solution with no distinct structure, independent from Ser3 octanoylation (Silva Elipe, Bednarek, and Gao 2001). In membrane mimicking solutions with SDS and TFE, an α -helix formation could be observed (Staes et al. 2010). Molecular dynamics simulations suggest that this helix spans from Pro7 to Gln13 (Beevers and Kukol 2006). This was validated by chemical shift data from ¹H NMR experiments in a water/hexafluoroacetone mixture, where a stable α -helical core between Pro7 and Glu14 was proposed (De Ricco et al. 2013). Furthermore, chemical shift data from ¹H NMR data in PBS and in live cells indicated a putative α -helix between Glu8 and Lys20 (Martín-Pastor et al. 2010). ssNMR studies indicate that acyl-ghrelin binds to the membrane via its fatty acid chain and Ser3 and Phe4 and is highly flexible (Vortmeier et al. 2015). Because of this, no conclusive NMR model of acyl-ghrelin could be produced. Upon membrane binding, there may be a polyproline II helix between amino acids 21-23 and 26-27 at the C-terminus. The flexibility of ghrelin might enable the peptide to adopt amphiphatic conformations, with the basic residues interacting with the polar headgroups. Polyproline II helices have different biological functions, as they linked to amyloid formation, nucleic acid binding and muscle tissue formation (Blanch et al. 2000; Eker,

Griebenow, and Schweitzer-Stenner 2004; Hicks and Hsu 2004; Ma, Kan, and Wang 2001). Ghrelin is also the first known membrane associated peptide containing a PII helix (Vortmeier et al. 2015). Recent saturation transfer difference NMR data and modelling approaches suggest that acyl-ghrelin is binding the receptor with an extended binding surface. Aside from the known binding motif, His9 in the core helix is also involved and further interacts with the central cavity of the receptor. It has also been proposed that the C-terminal residues 18 to 27 are highly flexible and most likely not involved in receptor binding (Bednarek et al. 2000; Bender et al. 2019).

2.3.2.3. Ghrelin-NOX-B11

The molecular pathways that mediate the production and release of ghrelin are not yet fully understood. Even though ghrelin is evidently not the only reason for weight gain and adiposity, it is nonetheless an interesting drug target with huge potential.

The Spiegelmer NOX-B11 binds the bioactive form of ghrelin with nanomolar affinity (K_d of 35 nM) (Helmling et al. 2004). It is a 47 bp L-aptamer that neutralizes circulating acyl-ghrelin. Mutational studies revealed that the negatively charged NOX-B11 does not bind to the hydrophilic positively charged C-terminus, but to the more hydrophobic N-terminus that carries the fatty acid chain (Helmling et al. 2004).

Furthermore, it interferes with acyl-ghrelin-(GHSR)1a binding and is effective as GH suppressor in rats and blocked imminent induced food uptake after ghrelin ingestion (Helmling et al. 2004; Kobelt et al. 2006). As it selectively binds only the bioactive form, the aptamer can also be used for assays studying ghrelin levels *in vitro/in vivo*. It has, for example, been used for a study in Siberian hamsters to study food hoarding and foraging (Teubner and Bartness 2013).

This example of a peptide-Spiegelmer complex demonstrates the feasibility of the Spiegelmer SELEX procedure against small peptides. Structural information about the peptide-Spiegelmer complex would give insights into the structure of a non-natural RNA, as well as a unique structural peptide.

2.4. Crystallization of nucleic acid-protein complexes

As stated above, the scientific importance of nucleic acid-protein complexes is obvious. To understand the mechanisms and basis of the complex formation and function, X-ray crystallography is most suitable.

2.4.1. Difficulty of protein-nucleic acid complex crystallization and structure determination

For crystallization, pure macromolecules need to be available in relative high quantities. This is one of the major bottlenecks of structure determination. Chemically synthesized DNA and RNA molecules are commercially available for short sequences, but costs increase with length and modifications of certain nucleotides at the 5' end can be costly as well. Bacteriophage T7 DNA-dependent RNA polymerase facilitated *in vitro* transcription is an alternative for longer, natural RNA strains (Ferre-D'Amare and Doudna 1996). In this case, homogeneity and premature strand termination can be problematic and several purification steps make it cumbersome and can lead to sample loss (Groebe et al. 1987; Schürer et al. 2002; Walker, Avis, and Conn 2003). Also, the complex needs to be stable over a longer time period, so extensive screening for additives, often divalent cations, needs often to be performed, as well as the incubation time, annealing and temperature needs to be evaluated.

The second bottleneck is the crystallization of nucleic acids and their complexes. In general, RNA molecules adapt into several secondary structures, hindering complex formation or reducing the homogeneity of the sample (Turner, Sugimoto, and Freier 1988). Furthermore, the phosphates that form the regular backbone of nucleic acids can be detrimental for crystal contact formation. This can result in heterogeneous crystals of low quality (McPherson 1991).

In general, screening for crystallization conditions is similar to standard protein crystallization and sparse matrix screens can be used for high throughput screening (Doudna et al. 1993; Jancarik and Kim 1991; Scott et al. 1995). Hydrophilic polyethers, lithium salts, alcohols and buffers with physiological buffering ranges (e.g. HEPES, Tris) are often used successful crystallization cocktails (Doudna et al. 1993; Carter and Carter 1979; Scott et al. 1995; Jancarik and Kim 1991; Jurica et al. 2002). To counteract the polyanionic nucleic acids divalent cations such as magnesium or Spermidine are added

occasionally as additives (Jurica et al. 2002; Ferré-D'Amaré and Doudna 2000). The suitable pH range is narrower (approx. between 5 and 8) in comparison to proteins, as hydrolysis and complex instability is common at very high or low pHs.

2.4.2. The phase problem

To obtain structural information about molecules that are discretely ordered into a crystal, wavelengths in the X-ray range need to be used. As there are no lenses for hard X-rays, direct imaging is impossible. This leads to the so-called phase problem of crystallography, as only the intensities of a reflection can be measured, but not its phase. Each Bragg reflection is characterized by its scattering intensities (Miller indices h, k, l), and its structure factor, consisting of the respective amplitude $|F(h,k,l)|$ and phase $\varphi(h,k,l)$. This phase information is essential to calculate the electron density in real space.

Phase retrieval by other means is therefore necessary. Molecular replacement is the most commonly used method for phase determination today (Rossmann 1990). In this method, the phases from a homologous structure with a similar fold are used to substitute the missing phase information, while combining them with the measured intensities. The obtained model and calculated structure factors are then iteratively refined against real space constraints and the measured structure factor amplitudes, respectively. This method however only works if a similar model with relative high sequence identity is available, and sometimes not even then. For novel structures, such as Spiegelmers or proteins with novel folds, where no homolog is available, the phases need to be determined from the experimental data.

This can be done with the following two approaches, which can also be combined. For single isomorphous and multiple isomorphous replacement (SIR/MIR), one or more different derivative crystals are produced (e.g. soaking the crystal in a heavy atom solution) and the scattering differences introduced by the heavy atoms relative to the native protein are used for phase retrieval. Single wavelength anomalous diffraction and multiple wavelength diffraction (SAD/MAD) directly uses the anomalous scattering contribution from the heavy atoms for phase calculation. The combination of SAD/MAD and SIR/ MIR is termed SIRAS/MIRAS.

All of these methods rely on first solving the so-called heavy atom substructure by direct methods or Patterson methods, which are adapted from the structure determination methods used for small molecules (Karle and Hauptman 1950, 1956).

2.4.2.1. Multi- and Single-wavelength anomalous diffraction (MAD/SAD)

Multiwavelength anomalous diffraction (MAD) is a phase retrieval method where one or more crystals are measured at different X-ray wavelengths. This was catalyzed by the broader accessibility of synchrotron radiation, as tunable X-ray sources are needed, making SAD/MAD phasing the most common techniques for experimental phase determination today (Rosenbaum, Holmes, and Witz 1971; Phillips et al. 1978).

The first structure that was solved with a four wavelength MAD experiment was the iron containing lamprey hemoglobin in 1985 by Hendrickson *et al.*, who also established the term MAD (Hendrickson 1985; Hendrickson et al. 1988). The first published MAD solved structure was parvalbumin from the toadfish *Opsanus tau*, using data from three different wavelengths (Kahn et al. 1985). The first novel structure followed in 1988 (cucumber basic blue protein), after other structure determination methods failed (Guss et al. 1988). Another noteworthy MAD experiment was the solution of Streptavidin in complex with Selenobiotin, as the structure could only be solved with one Se-atom present in the entire molecule, which sparked the idea of using seleno incorporation in proteins (Hendrickson et al. 1989; Hendrickson, Horton, and LeMaster 1990). This convenient invention is also responsible for the success of MAD and SAD today.

Diffraction data from one crystal, if radiation damage is limited, at different wavelengths eliminates the difficulties that arise with non-isomorphism between crystals in SIR/MIR experiments. Most of the time, diffraction data collection at three different wavelengths is sufficient to solve the trigonometric phase ambiguity. One dataset is measured at the absorption peak of the heavy atom scatterer (f'') (λ_1), and another at the inflection point of the absorption curve (λ_2), (where f' has its minimum, as it is the derivative of the f'' curve). A third or fourth dataset can be collected at remote wavelengths (λ_3 , λ_4) in order to maximize the dispersive differences relative to λ_2 (Figure 2). The differences in structure factor amplitudes between Friedel pairs caused by the anomalous scatterers are very small and therefore need to be measured very accurately. Noisy data is detrimental

for phase retrieval with MAD. A fluorescence scan at the beamline is helpful to determine the exact absorption and dispersion curves for a crystal, as the chemical environment around the scatterer can influence the absorbance. Furthermore, highly redundant, as well as high completeness data should be collected, without having unfavorable effects of radiation damage, introducing noise into the data.

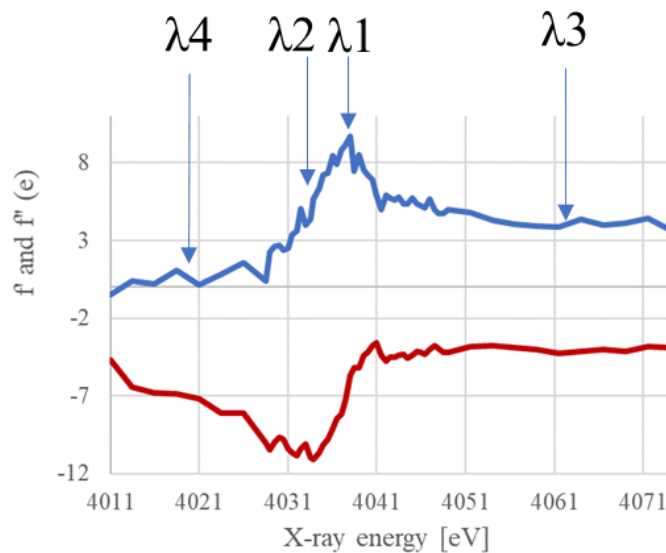


Figure 2: Experimental absorption spectra for a calcium containing macromolecular crystal around the theoretical K-absorption edge of calcium. λ_1 represents the wavelength at the absorption peak, λ_2 is the wavelength at the respective inflection point and λ_3 and λ_4 depicting remote wavelengths, where data for a MAD experiment can be collected to maximize dispersive differences relative to λ_2 .

For a SAD experiment, data are only collected at one wavelength (Wang 1985). The feasibility of this method was first shown for Crambin (Hendrickson and Teeter 1981) and then 18 years later with the 129 residue long lysozyme (Dauter and Dauter 1999). This method is now applied routinely, as computational tools became much more powerful.

SAD experiments provide only the measured Bijvoet differences $\Delta F^\pm = |F_{PH}(+)| - |F_{PH}(-)|$, which can be used as estimates of heavy atom contributions to the scattering. X-rays are anomalously scattered when hitting electrons at the absorption edge of a heavy atom scatterer. The anomalous scattering fraction has a phase shift of 90° (Figure 3). This manifests itself in measurable differences between the two reflections of a Bijvoet pair.

The overall structure factor F_{PH} (protein and heavy atom contribution), is the sum of the contribution from F_P (structure factor fraction from the protein) and F_H (structure factor

fraction from the heavy atom) and F_H'' , the anomalous fraction of the structure factor. From the anomalous differences between Friedel pairs, the positions of the heavy atoms in the crystal can be determined by applying Patterson or direct methods, known as substructure solution.

For the correct substructure, the calculated amplitudes and phases can now be drawn in an Argand diagram (F_H) for a unique pair of Friedel reflections, known as a Harker diagram. Since we know the anomalous contribution to the structure factors introduced by the heavy atoms, and also the magnitude of the structure factors of the protein derivative crystal (phase shifted by 90°) we can geometrically assign for two possible phase angles for each reflection hkl . This solution is known as the phase ambiguity, due to the two possible solutions for the phase angle for one structure factor, where values are symmetrically located around the absorption contribution (f'') to the anomalous scattering. This phase ambiguity can be broken with density modification techniques (Chen et al. 1991), provided the collected data are of very good quality.

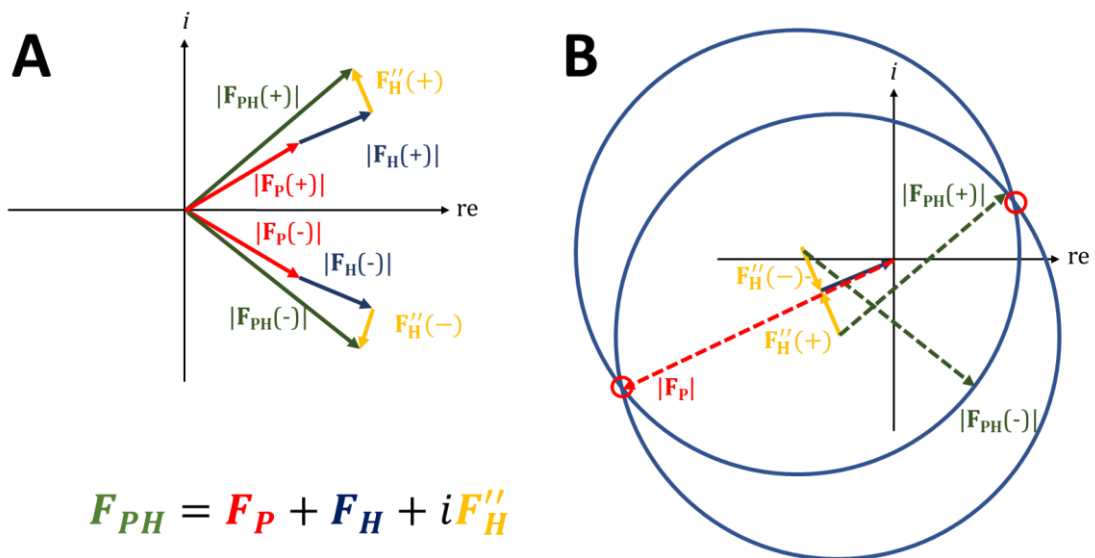


Figure 3: Structure factor relationship for the anomalous scattering contribution and Harker diagram for single wavelength anomalous diffraction. A: Vector relationship of the anomalous scattering contribution with $F_{PH} = F_P + F_H + iF_H''$ for the two reflections making up a Friedel pair. B: Harker Diagram for single wavelength anomalous diffraction for a unique reflection hkl . F_{PH} : protein and heavy atom distribution; F_P : structure factor fraction from the protein; F_H : structure factor fraction from the heavy atom; F_H'' : anomalous fraction of the structure factor.

2.4.2.2. Native SAD

For native SAD, the anomalous signal comes from the naturally present anomalous scatterers ($Z \leq 20$) in macromolecules (e.g. sulfurs ($Z=16$) for proteins, phosphates ($Z=15$) for nucleic acids). The advantages are evident, as there is no need for heavy atom derivatives, that are sometimes hard to obtain or produce non-isomorph crystals, or selenomethionine substitution. Furthermore, the number of anomalous scatterers is known from the sequence, therefore substructure solution can be in principle easier compared to an uncertain number of heavy atom scatterers. But since the native anomalous scatterers have less electrons than commonly used heavy atoms, the anomalous contribution to the scattering is even lower making the anomalous signal even smaller in comparison to the overall diffraction signal. In general, background noise is a big problem that even gets worse with lower signals. Therefore, several data collection strategies have been developed for native SAD, with the aim of increasing the signal to noise ratio. Small wedges correlated by Friedel symmetry are collected consecutively, to assure similar radiation damage affects between Friedel Pairs, for accurately determining the anomalous contribution to these differences. Furthermore, the crystals can be measured at longer wavelengths, where the f'' values of the lighter atoms increase (Figure 4A). On the downside, with lower energies the absorption increases, and diffuse scattering might be a problem, as well as larger Bragg angles, limiting the resolution limits (Figure 4B). A possible solution is to collect diffraction data in vacuum or in a helium atmosphere and the use of shaped detectors (geodesic dome or cylindrical) for recording higher scattering angles. It is also important to reduce the amount of solvent around the crystal to reduce absorption effects.

Long wavelength beamlines have been implemented recently in Japan (Photon Factory), the United Kingdom (Diamond Light Source) and at P13 at PETRAIII at DESY where a helium cone can be installed for long wavelength experiments down to 4.5 keV. At Diamond, an in-vacuum short-gap undulator and optimized optics to stabilize the X-ray microbeam is established and specialized equipment, such as a helium filled chamber, special beam port, multi-axis goniometer and a semi cylindrical Pilatus M12 detector are set up. Wavelength ranges between 12.4 keV and 2.1 keV can be used and recently, *de novo* phasing of thaumatin was performed at approx. 2.5 keV, only approx. 30 eV below the sulfur K-edge (Aurelius et al. 2016).

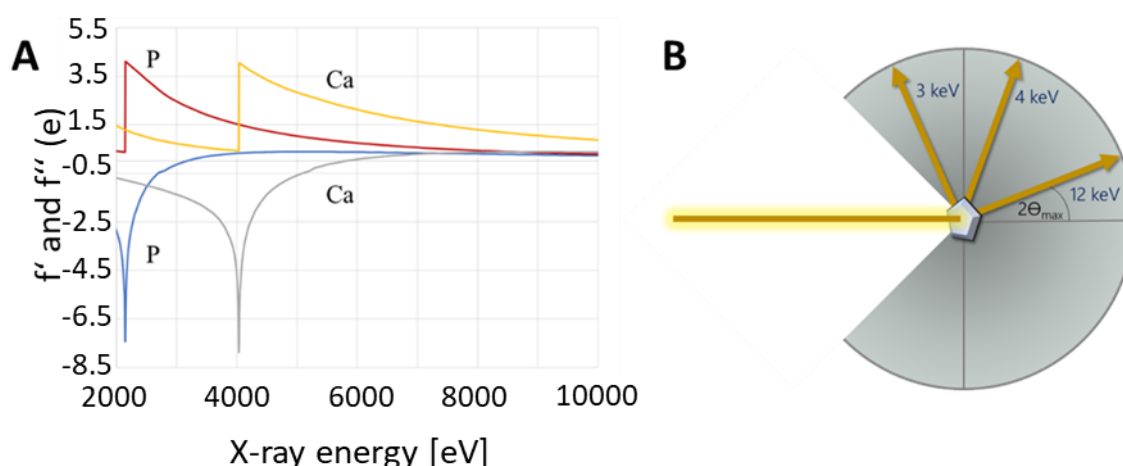


Figure 4: Properties of long wavelength experiments.

A: Absorption spectra of phosphorous and calcium. The plot was generated on the following website: http://skuld.bmsc.washington.edu/scatter/AS_form.html. B: Maximum Bragg angles at different X-ray energies (Liu, Liu, and Hendrickson 2013) (modified).

To further enhance the anomalous signal, highly redundant and complete data should be collected. This is either obtained collecting multiple datasets from one crystal at one or multiple orientations, or if radiation damage occurs, multiple crystals can be merged, if non-isomorphism is not a problem. With the multi-crystal merging approach, several structures could be phased *de novo* and it was shown, that some structures could be only solved upon merging several crystals, highlighting the necessity of high data multiplicity (Rose, Wang, and Weiss 2015; Liu, Zhang, and Hendrickson 2011; Olieric et al. 2016).

In the first successful phosphorus SAD approach (Dauter and Adamiak 2001), multiplicity was also the determining factor for substructure solution and phasing. It also proposed phosphorous phasing as a promising tool for phase retrieval of nucleic acid diffraction data. Since then, however, it was only possible to solve one other nucleic acid structures utilizing only the phosphates as anomalous scatterers (Raiber et al., 2015). Every nucleotide has a phosphorous atom, so substructures can become quite large, making substructure determination by direct or Patterson methods quite difficult, even if the resolution and the signal to noise ratio are high.

Despite its advantages, native SAD is till now not yet fully established, which is reflected in the number of deposited structures solved with native SAD in the Protein Data Bank (PDB), which is less than 200.

2.5. Aims of the thesis

FurA from *Mycobacterium avium* ssp. *paratuberculosis* (MAP), which is the causative agent for paratuberculosis, is a redox-sensing transcription factor, that is important for cell homeostasis in response to host-defense mechanisms, as described before. At present, no structural information about MAP FurA is available. Hence, a protocol for efficient recombinant expression of *furA* and the purification of pure, soluble and stable protein in large amounts shall be established. Furthermore, low resolution structures of different MAP FurA conformations shall be obtained, that mimic the active form, as well as the conformations that occur during oxidative stress and metal starvation. Biochemical assays shall be conducted to study the protein functions, especially after peroxide treatment.

Ghrelin is an orexigenic peptide that sparked a huge research interest due to its involvement in metabolism and hunger. NOX-B11 is a Spiegelmer, that binds bioactive ghrelin and was found to be effective *in vitro* and *in vivo* and can reduce food uptake in rats (Helmling et al. 2004; Kobelt et al. 2006). In this thesis, the Ghrelin•NOX-B11 complex shall be structurally characterized, as no conclusive ghrelin structure is available to date, due to its high flexibility. First, the complex formation shall be monitored and the stability evaluated. After that, first structural information about the complex shall be obtained with the aid of SAXS measurements. Furthermore, crystallization trials shall be performed in order to obtain crystals with sufficient quality for diffraction data collection for a high-resolution structure of the Ghrelin•NOX-B11 complex.

In terms of the research activities, several approaches to phase nucleic acid-protein complex data, including native P-SAD, calcium MAD, derivative production and conventional MAD experiments should be applied and established, further racemic crystallization and molecular replacement approaches should be applied.

3. Materials and Methods

3.1. Materials

3.1.1 Chemicals

All chemicals were purchased in analytical grade from the companies AppliChem GmbH (Germany), Honywell Fluka (USA), Merck KGaA (Germany), Thermo Scientific Inc. (USA), Carl Roth GmbH + Co. KG (Germany), Serva Electrophoresis GmbH (Germany), Bachem Holding AG (Switzerland), ProSpec-Tany TechnoGene Ltd. (Israel), Molecular Dimensions Limited (USA) or Sigma-Aldrich Corp. (USA).

3.1.2. Consumables

Reaction tubes, Falcon tubes, serological pipettes and pipette tips used were purchased from Sarstedt AG und Co. KG (Germany). Further consumables are listed below (Table 1).

Table 1: Consumables used.

Description	Manufacturer/Supplier
96-well Vapor Batch Diffusion Plates	Douglas Instruments Limited, UK
96-well SWISSCI MRC2 plates	Hampton Research Corp., USA
48-well SWISSCI MRC plates	Hampton Research Corp., USA
24-well Linbro Plates	Jena Bioscience GmbH, Germany
Amicon® Ultra 4, Ultra 15, Ultra 0.5, MWCO 3 kDa, 10 kDa	Merck Millipore (Merck KGaA), Germany
Cellulose acetate membrane filter 0.2 µM	VWR International LLC, USA
Chelex® 100 resin	Bio-Rad Laboratories, Inc., USA
Cover slips	VWR International LLC, USA
DEAE Sephadex A-50 matrix	GE Healthcare, USA

Description	Manufacturer/Supplier
Highly Viscous Vacuum Grease	GE Bayer Silicones
Ni-NTA Agarose matrix	Macherey-Nagel GmbH & Co. KG, Germany
Syringes 1 mL, 2 mL, 5 mL, 10 mL, 20 mL, 50 mL	VWR International LLC, USA
Syringe filter 0.22 µm, 0.45 µm	VWR International LLC, USA
ZipTip®C18 Pipette Tips	Merck Millipore (Merck KGaA), Germany

3.1.3. Equipment

The following table lists the laboratory equipment used (Table 2).

Table 2: List of equipment used.

Device	Instrument	Manufacturer/Supplier
Agarose gel electrophoresis chamber	BlueMarine 100	Serva Electrophoresis GmbH, Germany
	PerfectBlue Gelsystem Mini M	PEQLAB Biotechnologie GmbH, Germany
BeamLines	P11	DESY, PETRA III, DESY, Hamburg, Germany
	P12	EMBL, PETRA III, DESY, Hamburg, Germany
	P13	EMBL, PETRA III, DESY, Hamburg, Germany
	P14	EMBL, PETRA III, DESY, Hamburg, Germany

Device	Instrument	Manufacturer/Supplier
Beamlines	I23	Diamond Light Source, Didcot, United Kingdom
Blue Light Scanner	Bio-1000F	Microtek International Inc., Taiwan
CD spectrometer	J-815 CD	Jasco Inc., USA
Centrifuges	5415R/ 5415C/ 5804R/ 5810R MinispinPlus	Eppendorf AG, Germany
	Multifuge X3R	Thermo Fisher Scientific Inc., USA
Crystallization Robots	Honeybee 961	Genomic Solutions Inc., USA
	Oryx 4	Douglas Instruments Limited, UK
Crystal plate incubator 4 °C and 20 °C	RUMED 3001 incubator	<i>Rubarth</i> Apparate GmbH, Germany
DLS Device	SpectroLight 300	Xtal Concepts GmbH, Germany
	SpectroLight 600	Xtal Concepts GmbH, Germany
FPLC	ÄKTA Purifier P-901	GE Healthcare, USA
	ÄKTA Prime	
Freezer -20°C	Liebherr premium	Liebherr International S.A., Switzerland
Freezer -80°C	B35-85	FRYKA-Kältetechnik GmbH, Germany

Device	Instrument	Manufacturer/Supplier
Imaging	CLSM Zeiss	Carl Zeiss AG, Germany
	CrystalScore	Diversified Scientific Inc., USA
	Leica TCS SP8 Confocal Platform	Leica Microsystems GmbH, Germany
	Microscope SZX12 with camera DP10	Olympus K.K., Japan
Incubator 37°C	BD 56	BINDER GmbH, Germany
Incubation shaker	Innova 4330	New Brunswick Scientific Co., Inc. (Eppendorf AG), Germany
	KS 3000 i control	IKA Werke GmbH & Co. KG, Germany
Magnetic Stirrer	VMS-A	VWR International LLC, USA
Microbalance	Sartorius TE3102S CP2245- OCE	Sartorius AG, Germany
pH Meter	SevenEasy	Mettler-Toledo Inc., USA
Photospectrometer	Nanodrop 2000c	Thermo Fisher Scientific Inc., USA
	NanoDrop Lite	
Pipettes	Eppendorf Research, 2 µL, 10 µL, 200 µL, 1000 µL	Eppendorf AG, Germany
Pipetting robots	Lissy	Zinsser Analytic GmbH, Germany
Real Time PCR cyclers	Mini8 Plus	Coyote Bioscience co., LTD., USA

Device	Instrument	Manufacturer/Supplier
SDS-PAGE	Four Gel Caster (SE275)	Hoefer Inc., USA
	SE260 Mighty Small II Deluxe Mini electrophoresis unit	Hoefer Inc., USA
SDS-PAGE	EV 231 (Power supply)	PEQLAB Biotechnologie GmbH, Germany
Thermomixer	Comfort	Eppendorf AG, Germany
UV-light source	CrystalLIGHT 100	Nabitec GmbH, Germany
Vortex Mixer	VF2	IKA Werke GmbH & Co. KG, Germany
X-ray source	I μ S	Incoatec GmbH, Germany
Imaging Plate X-ray Detection System		marresearch GmbH, Germany

3.1.4. Buffer, Media and Solutions

The buffers, media and solutions were prepared, if not stated otherwise, with bi-distilled water (ddH₂O). The pH was adjusted with HCl or NaOH.

3.1.4.1. Growth media and antibiotics used for cultivation of recombinant *Escherichia coli* strains

Table 3: Growth media for bacterial cultures.

Buffer, media or solution	pH	Components	Concentration
LB-Agar	7	Tryptone	10 g/L
		Yeast extract	5 g/L
		NaCl	10 g/L
		Agar agar	15 g/L

Buffer, media or solution	pH	Components	Concentration
LB broth (Lennox)	7	NaCl	5.0 g/L
		Tryptone	10 g/L
		Yeast extract	5.0 g/L
TB broth	7.2	Casein	12 g/L
		Yeast extract	24 g/L
		K ₂ HPO ₄	12.5 g/L
		KH ₂ PO ₄	2.3 g/L
		Glycerol	0.4% (v/v)
2YT	7	Tryptone	16 g/L
		Yeast extract	10 g/L
		NaCl	5 g/L

Table 4: Antibiotics used for *E. coli* mutant strain selection.

Antibiotics	Solvent	Working concentration
Ampicillin	50% Ethanol	100 µg/mL
Chloramphenicol	100% Ethanol	34 µg/mL
Tetracyclin	100% Ethanol	10 µg/mL
Kanamycin	ddH ₂ O	25 µg/mL

3.1.4.2. Generally used buffers and solutions

Table 5: Generally used buffers and solutions.

Name of buffer/solution	Composition	Concentration
Buffer for competent cell production	CaCl ₂	100 mM
	Glycerol	10% (v/v)
Isopropyl-β-D-thiogalactopyranosid (IPTG)	IPTG	1 M
Phenylmethylsulfonylfluoride (PMSF)	PMSF	100 mM (dissolved in 100% isopropanol)
Coomassie Staining Solution	Isopropanol	25% (v/v)
	Acetic Acid	10% (v/v)
	Coomassie Brilliant Blue R-250	0.1% (w/v)
Coomassie Destaining Solution	Acetic Acid	20% (v/v)
2 x sample buffer SDS PAGE	Tris-HCl, pH 6.8	20 mM
	SDS	4% (w/v)
	Glycerol	20% (v/v)
	DTT	50 mM
	Bromophenol blue	0.04% (w/v)
Ethidium bromide staining solution	Ethidium bromide	0.5 µg/mL

Name of buffer/solution	Composition	Concentration
5 x native sample buffer native PAGE	Tris-HCl, pH 6.8	50 mM
	Glycerol	50% (v/v)
	Bromophenol blue	0.1% (w/v)
Separating Gel Buffer	Tris-HCl, pH 8.8	1.5 M
	SDS	0.4% (w/v)
Stacking Gel Buffer	Tris-HCl, pH 6.8	0.5 M
	SDS	0.4% (w/v)
50x Tris-Acetate-EDTA (TAE) buffer	Tris base	2.5 M
	Acetic acid	1 M
	EDTA	50 mM
10x electrode buffer	Glycine	1.920 M
	Tris-HCl	250 mM
	SDS	1% (w/v)
1x Native PAGE electrode buffer	Glycine	192 mM
	Tris-HCl	25 mM
DNA Loading Dye (5x)	Bromophenol blue	0.05% (w/v)
	Xylene cyanol	0.35% (w/v)
	EDTA	1 mM
	Glycerol	60% (w/v)

3.1.4.3. Buffers for Ghrelin•NOX-B11 complex formation and purification

Table 6: Buffers used for Ghrelin•NOX-B11 complex formation and purification.

Name of buffer/solution	Composition	Concentration
Binding Buffer	HEPES, pH 7.4	20 mM
	NaCl	100 mM
	MgCl ₂	1 mM
	CaCl ₂	1 mM
	KCl	5 mM
Peptide Buffer	HEPES, pH 7.4	20 mM
	NaCl	100 mM
Complex SEC Buffer	HEPES, pH 7.4	20 mM
	NaCl	150 mM
	MgCl ₂	10 mM
	CaCl ₂	1 mM
	KCl	5 mM

3.1.4.4. Buffer for *Mycobacterium avium* ssp. *paratuberculosis* FurA purification

Table 7: Lysis and purification buffers for cell lysis and FurA purification.

Name of buffer/solution	Composition	Concentration
FurA Lysis Buffer	Bicine, pH 8.5	20 mM
	NaCl	150 mM
	DTT	2 mM
FurA Wash Buffer	Bicine, pH 8.5	20 mM
	NaCl	150 mM
	DTT	2 mM

Name of buffer/solution	Composition	Concentration
FurA Low Salt Buffer	Bicine, pH 8.5	20 mM
	DTT	2 mM
FurA High Salt Buffer	Bicine, pH 8.5	20 mM
	DTT	1000 mM
	NaCl	2 mM
FurA SEC Buffer	Bicine, pH 8.5	20 mM
	NaCl	150 mM
	DTT	2 mM

3.1.4.5. Buffers for *Mycobacterium avium* ssp. *paratuberculosis* (MAP)

FurA solubility screening

Table 8: Buffers used for solubility screening (Benvenuti and Mangani 2007).

Buffer	pH	Concentration
Ammonium acetate	7.3	500 mM
Bicine	8.5	500 mM
	9.0	
Bis-Tris propane	6.5	500 mM
HEPES	7.0	500 mM
	7.5	
	8.0	
MES	5.8	500 mM
	6.2	
	6.5	
Potassium/sodium phosphate	5.0	500 mM
	6.0	
	7.0	

Buffer	pH	Concentration
Sodium acetate	4.5	500 mM
	5.0	
Sodium citrate	4.7	500 mM
	5.5	
Tris	7.5	500 mM
	8.0	
	8.5	

3.1.4.6. Stock solutions for buffer preparation or soaking to generate derivative crystals

Table 9: Stock solutions for buffer preparation or soaking to generate derivative crystals.

Stock solution	Concentration
[Co(NH ₃) ₆]Cl ₃	20 mM
C ₂₀ H ₂₃ ClN ₅ O ₄ Tb (Polyvalan Crystallophopre N° 1	100 mM
CaCl ₂	100 mM
CdBr ₂	1 M
CdI ₂	100 mM
CdSO ₄	100 mM
CH ₄ N ₂ Se	1 M
Fe(III)Cl ₃	100 mM
HgBr ₂	100 mM
IrCl ₃	100 mM

Stock solution	Concentration
K ₂ (HgI ₄)	100 mM
MgCl ₂	100 mM
MnCl ₂	100 mM
NaBr	1 M
NaI	1 M
NiSO ₄	100 mM
OsCl ₃	100 mM
Sm(CH ₃ CO ₂) ₃	1 M
ZnCl ₂	100 mM

3.1.5. Molecular-weight size markers

Table 10: Molecular-weight size markers and their size ranges.

	Name	Size Range	Supplier
DNA Marker	High Range DNA Ladder	10 kbp - 500 bp	Thermo Fisher Scientific Inc., USA
	Medium Range DNA Ladder	5 kbp - 500 bp	
	Low Range DNA Ladder	1.5 kbp – 50 bp	
Protein Marker	Unstained Protein Molecular Weight Marker	116 kDa – 14 kDa	Thermo Fisher Scientific Inc., USA

3.1.6. Commercial kits

Commercially available kits were used for plasmid extraction and DNA clean-up after gel extraction (Table 11).

Table 11: List of commercially available kits used.

Name	Supplier
peqGold Plasmid Miniprep Kit I	PEQLAB Biotechnologie GmbH, Germany
GeneJet Gel Extraction Kit	Thermo Fisher Scientific Inc., USA

3.1.7. Bacterial strains

Different *E. coli* strains were used for general plasmid transformations and cryo storage (DH5 α) or recombinant gene expression (BL21(DE3) and strain derivatives) (Table 12).

Table 12: Bacterial strains used.

Strain	Genotype	Supplier
DH5 α	F ⁻ <i>endA1 glnV44 thi-1 recA1 relA1</i> <i>gyrA96 deoR nupG purB20</i> ϕ 80 <i>dlacZ</i> Δ M15 Δ (<i>lacZYA-argF</i>)U169, <i>hsdR17(r_K⁻m_K⁺)</i> , λ ⁻	Invitrogen (Thermo Fisher Scientific Inc.), USA
BL21 (DE3)	F- <i>ompT hsdSB (rB-mB-)</i> <i>gal dcm</i> <i>rne131</i> (DE3)	Invitrogen (Thermo Fisher Scientific Inc.), USA
BL21 (DE3) Star	F- <i>ompT hsdSB (rB-mB-)</i> <i>gal dcm</i> <i>rne131</i> (DE3) pLysS (CamR)	Invitrogen (Thermo Fisher Scientific Inc.), USA

3.2. Molecular biology and biochemical Methods

3.2.1. Agarose-gel electrophoresis

Agarose gel electrophoresis is generally used to separate nucleic acids or their complexes with proteins by size. Larger nucleic acids or their complexes show a decreased electrophoretic mobility in comparison to smaller fragments or unbound nucleic acids.

Nucleic acids are visualized upon adding a stain, that typically intercalates into double stranded nucleic acids. The stain undergoes a conformational change after binding, which results in fluorescence emission after agitation with UV or blue light.

Depending on the fragment sizes 0.7%-2% (w/v) agarose was dissolved in 1x TAE buffer upon boiling the solution for two to three times. The agarose was allowed to cool down to approx. 50°C and the nucleic acid stain (SERVA DNA Stain G, SERVA Electrophoresis GmbH, Germany) was added (1:20000 dilution factor). The agarose was then poured evenly into a horizontal gel caster that was equipped with a suited comb to produce wells. After polymerization the comb was removed and the gel was covered with 1x TAE buffer. The samples were mixed with 5x DNA sample buffer and loaded into the wells of the agarose gel. A nucleic acid weight marker was loaded into a separate well to monitor the size of the separated fragments. A constant voltage of 90 V was applied and bands were visualized under a UV transilluminator or blue light scanner (Microtek International Inc., Taiwan).

3.2.2. DNA cleanup

DNA can be retrieved from the agarose gel for downstream use. The DNA band was excised from the gel with a scalpel and was extracted as described in the protocol of the peqGold Gel Extraction Kit (PEQLAB Biotechnologie GmbH, Germany). The DNA was eluted either in 15-30 µL bi-distilled water or the provided elution buffer.

3.2.3. Determination of nucleic acid concentration

The concentrations of nucleic acid solutions can be measured photometrically. The absorption maximum of nucleic acids is at 260 nm. An absorption of 1.0 at this wavelength corresponds to 50 ng/µL for double stranded DNA, and 40 ng/µL for RNA. For quantification the NanoDrop spectrophotometer was used. With this device, 1 µL of sample is sufficient for a measurement.

The concentration is derived from this modified Beer-Lambert equation:

$$c = \frac{A * \epsilon}{b}$$

with c being the sample concentration in $\text{ng}/\mu\text{L}$, A being the absorbance ϵ being the wavelength-dependent extinction coefficient in $\text{ng}\cdot\text{cm}/\mu\text{L}$ and b being the pathlength in cm .

To check the sample purity, the ratio between the absorption at 260 nm and 280 nm is determined. This value should be around 1.8 for pure DNA, and around 2.0 for pure RNA. Divergent values can indicate impurities, e.g. from proteins or sugars.

3.2.4. Preparation of chemically competent *E. coli* cells

To genetically modify *E. coli* strains, e.g. to transfer DNA plasmids with the genetic information of the protein to be recombinantly expressed, the cells were prepared to be chemically competent. One colony from a cultivation plate or some cells from a cryogenic stock were inoculated with 5 mL growth media (plus cognate antibiotics, if needed) over night at 37°C and 180 rpm. For the main culture, 100 mL growth media (plus cognate antibiotics, if needed) were inoculated with the preculture at an $\text{OD}_{600\text{nm}}$ of 0.1. The cells were incubated at 37°C and 180 rpm until the $\text{OD}_{600\text{nm}}$ reached 0.5. Afterwards, the culture was transferred to two 50 mL falcon tubes and put on ice and incubated for 15 min before being spun down at 4°C at max. rpm. The supernatant was discarded and the cell pellets were washed with 5 mL 100 mM ice-cold CaCl_2 solution. After another centrifugation step for 15 min at 4°C and max. rpm, the supernatant was discarded and the cells were resuspended in 1 mL ice-cold 100 mM CaCl_2 solution containing 10% glycerol. 50 μL aliquots were transferred to reaction tubes and flash frozen in liquid nitrogen and stored at -80°C.

3.2.5. Transformation of competent *E. coli* cells with pFurA

One aliquot of frozen chemically competent *E. coli* cells was thawed on ice, before 100 ng of plasmid DNA (pFurA) were pipetted into the reaction tube.

pFurA was kindly provided by Prof. Dr. Ralph Goethe from the Tierärztliche Hochschule Hannover, Institute of Microbiology. This plasmid is based on the pET28-B18R expression vector and the MAP *furA* gene was inserted downstream of the very strong T7 RNA polymerase promoter (p(T7)). The plasmid further contains a kanamycin resistance gene for mutant selection and the *lacI* repressor for induction of the gene expression with IPTG. IPTG is a molecular mimic of allolactose which is not

metabolized by *E. coli* and binds the *lacI* repressor upon which the recombinant gene expression is initiated.

Cells were briefly mixed with the DNA and incubated on ice for 30 min. Then the cells were heat shocked for 2.5 min at 42°C and transferred onto ice for 2 min. 500 µL LB was added and the cells were incubated at 37°C and 300 rpm for one hour. The cells were centrifuged for 30 sec at max. rpm and the supernatant was discarded by inverting the tube. The pellet was resuspended in the remaining LB medium and plated on LB agar plates, containing the antibiotic for which the resistance gene serves as selection marker for the transferred plasmid. Plates were incubated over-night at 37°C.

3.2.6. Preparation of bacterial plasmid DNA

5 mL LB media and suitable antibiotics for the resistance genes present on the plasmid were inoculated with one colony of the cells carrying the plasmid of choice or cells from a cryogenic culture overnight at 37°C and 180 rpm.

The cells were transferred successively to 2 mL reaction tubes and spun down for 1 min each. The supernatant was discarded and the reaction tube was filled up until all of the cell culture was used up. After the last centrifugation step, the cells were resuspended in resuspension buffer and spun down for 1 min and 12000 rpm. The supernatant was discarded carefully and the cells were resuspended in 500 µL lysis buffer and carefully inverted until the cell suspension became clear or for max. 4 minutes. The cell lysis was stopped by adding 500 µL neutralization buffer. Cells were then centrifuged for 5 minutes at 12000 rpm. The supernatant was transferred carefully to a DNA binding spin column and the column was spun down for 1 min at 12000 rpm. The flow through was discarded and the DNA binding membrane was twice washed with 500 µL washing buffer. Before elution, the membrane of the spin column was dried by centrifuging the empty column for 1 min at 12000 rpm. 50 µL elution buffer or ddH₂O were added and incubated with the membrane for 90 sec and the spin column was transferred to a fresh reaction tube. To elute the DNA, the spin column was centrifuged for 1.5 minutes at 10000 rpm. The eluted plasmid DNA was stored at -20°C.

3.2.7. DNA sequencing

To verify the nucleotide sequence of e.g. the gene of interest on an expression plasmid, the nucleotides were sequenced. Therefore, 5 µL of plasmid-DNA (approx. 100 ng) were

mixed with 5 μ L of suitable sequencing primer. The sequencing reaction and data analysis were carried out by Eurofins GATC, Germany.

3.2.8. Recombinant gene expression of *Mycobacterium avium* ssp. *paratuberculosis* (MAP) *furA*

To produce large amounts of protein as required for protein crystallization, the genes encoding the target proteins were recombinantly expressed in *E. coli* cells, that carry said gene on a DNA plasmid. A strong inducible promoter from the T7 RNA polymerase, p(T7) was located upstream of the gene to facilitate strong, controlled gene expression. The expression was induced upon IPTG addition, which is a non-combustible Lactose-analagon.

One colony of the plasmid carrying *E. coli* strain, was inoculated in 200 mL of LB medium with suitable antibiotics overnight at 37°C at 180 rpm. For the main culture, 25 mL of preculture was added to 1 L LB with the respective antibiotics. The cultures were incubated at 37°C and 180 rpm until the OD_{600nm} reached values between 0.5 and 0.8. Then 1 mM IPTG was added to each flask. 1 mL of culture was transferred to a reaction tube for SDS-PAGE analysis. After 1 h, 2 h, 3 h and 4 h of incubation, the OD_{600nm} was measured and 1 mL of culture was withdrawn and transferred to a reaction tube. The test samples were centrifuged for 1 min at max. rpm and the pellets were resuspended in 50 μ L 2x SDS-PAGE buffer before cooking them at 96°C for ten minutes. To validate the expression and protein production, approximately the same amount of cells were each applied to an SDS-PAGE.

After 4 h, the culture was transferred to a centrifuging bucket and centrifuged for 15-30 minutes at 4°C and 4000 rpm. The supernatant was discarded and the cell pellets were resuspended in the remaining LB medium. The resuspension was decanted into a 50 mL falcon tube and centrifuged for an additional 15-30 min at 4°C and 4000 rpm. The supernatant was then carefully removed and the pellets were stored at -20°C.

3.2.9. Preparation of cleared *E. coli* lysates

Cell pellets were thawed and resuspended in 15 mL of suitable lysis buffer and 100 μ M PMSF was added. The cells were sonicated in a water ice mixture for 10 seconds with 30 second break intervals on ice in between. After that, lysozyme, 25 U/ μ L SuperNuclease and MgCl₂ were added to an end-concentration of 2 mM and incubated

for 30 min at RT with slow shaking. The cell debris was separated from the soluble cell lysate by centrifuging for 30 min at 4°C and 17000 rpm. The cell lysate was filtered with a 0.2 µm syringe filter before purification.

3.2.10. Anion exchange chromatography

Anion exchange chromatography can be used to separate negatively charged proteins from positively charged proteins. The matrix consists of positively charged beads that bind the negatively charged biomolecules. The bound proteins can be eluted with a stepwise or continuously increasing salt gradient or with a pH gradient.

The column matrix was equilibrated with three column volumes of wash buffer before the cell lysate was applied. The column was then incubated for 30 min at 4°C on a horizontal shaker. The column was allowed to drain under gravity conditions and the matrix was washed three times with wash buffer. Other bound negatively charged proteins were eluted with one column volume of 300 mM NaCl containing wash buffer. The target protein was eluted in the same buffer, containing 500 mM NaCl. The rest of the proteins were eluted with 1 M NaCl before re-equilibration of the column with wash buffer.

To regenerate the column, the column was washed with 0.5 M NaOH solution and washed with water until the pH of the flow through was no longer basic. After that, the column was washed with one column volume of 70% Ethanol, followed by washing the matrix with water or with 20% EtOH for long-term storage.

3.2.11. Buffer exchange and sample desalting

3.2.11.1. Desalting with a spin filter

Depending on the sample, several purification steps were necessary to obtain a sample with the desired quality. Buffer exchange was sometimes needed to get rid of excess salt or additives. This was done quickly in a spin filter with a suitable molecular weight cutoff. The samples were spun down for 10 min at 4000 rpm each and resuspended in the exchange buffer so that the starting buffer was diluted by a factor of 50.

3.2.11.2. Dialysis

Dialysis was used to get rid of unwanted compounds through passive diffusion with the aid of a semi-permeable membrane with a suitable molecular weight (MW) cut-off for the target macromolecule.

The dialysis membrane was first soaked in distilled water for 30 min. After that, the membrane was briefly equilibrated with the exchange buffer before pipetting the sample into the membrane tubing. The exchange buffer had approx. 200 to 500 times the volume of the sample and was slowly stirred. The dialysis was carried out for 6 h to overnight at 4°C.

3.2.12. SDS polyacrylamide gel electrophoresis (SDS-PAGE)

An SDS-PAGE is used to separate proteins or nucleic acids by size. Its smaller pore size is the main difference to agarose gels and it is therefore more suitable for proteins <100 kDa and small nucleic acid fragments.

The main ingredient is acrylamide, which is polymerized by a reaction driven by TEMED and ammonium peroxide sulfate (APS). The addition of SDS (sodium dodecyl sulfate) ensures the denaturation of the proteins. SDS accumulates on the unfolded protein, with the sulfate groups of the SDS directed outwards. These are negatively charged and hence overlay the intrinsic charges of the proteins (Richter 2003).

The gel consists of a narrow pore separating gel, as well as a coarser stacking gel. The pH values of the two layers differ. In the stacking gel, the proteins are 'captured' between the glycerol and chloride anions. The stacking gel is acidic (pH 6.8) and the chloride anions flow faster than the glycine anions, causing the proteins to be focused between the anions. If the proteins enter the basic separating gel (pH 8.8), the charge of glycine increases, the proteins are no longer focused between the two anions and can be separated by size (Shi and Jackowski 1998). A list of the buffers for gel casting and electrophoresis is summarized in Table 13.

Protein samples were mixed with either 5x or 2x SDS-sample buffer before denaturing them at 96°C for 10 min. The samples were spun down briefly and 5 µL to 10 µL were loaded onto the gel. A protein marker was applied as well to estimate the molecular weights of the proteins. The gels were run in a vertical gel electrophoresis chamber and

1x electrode buffer was used. A constant current of 25 mA per gel was applied for approx. 1 h. After that, the gels were stained in a Coomassie staining solution with continuous shaking for 30 min to overnight. Further, the gel was de-stained by exchanging the Coomassie de-staining solution several times until the protein bands could be distinguished clearly from the background.

Table 13: Buffers and solutions used for SDS-PAGE gel casting.

Gel type	Component	Volume
Stacking gel (4%)	ddH ₂ O	9.2 mL
	30% acrylamide/bisacrylamide (37.5:1)	2.0 mL
	Stacking gel buffer	3.8 mL
	10% (w/v) SDS	150 µL
	TEMED	15 µL
	10% (w/v) APS	75 µL
Separating Gel (12%)	ddH ₂ O	10.2 mL
	30% acrylamide/bisacrylamide (37.5:1)	12.0 mL
	Stacking gel buffer	7.5 mL
	10% (w/v) SDS	300 µL
	TEMED	15 µL
	10% (w/v) APS	150 µL
Separating Gel (15%)	ddH ₂ O	7.2 mL
	30% acrylamide/bisacrylamide (37.5:1)	15.0 mL
	Stacking gel buffer	7.5 mL
	10% (w/v) SDS	300 µL
	TEMED	15 µL
	10% (w/v) APS	150 µL

3.2.13. Native PAGE

Native PAGE is used to analyze proteins and nucleic acids in their physiologically folded form. The proteins are not denatured and unfolded and separation is based on their mass and charge. Hence, oligomeric forms of a protein or complexes can be detected. Since the charge of the proteins are not masked, the stacking gel can be omitted. The main ingredient is acrylamide, which is polymerized by a reaction driven by TEMED and ammonium peroxide sulfate (APS). A list of the buffers for gel casting and electrophoresis can be found in Table 14.

Samples were mixed with 5x native PAGE sample buffer and then loaded onto the gel. The electrode buffer, as well as the electrophoresis chamber, were placed on ice. Electrophoresis was performed at 10 V/cm for approx. 2 h. After electrophoresis, the gel was incubated in 10% acetic acid for 15 min. The gel was rinsed three times with water and then incubated in a 0.5 $\mu\text{g}/\text{mL}$ ethidium bromide solution for approx. 15 min. After this, the gel was transilluminated with a UV source and the bands were visualized with a CCD camera. Alternatively, the gel was stained with Coomassie brilliant blue R-250 for 30 min, followed by de-staining for 60 min.

Table 14: Buffers and solutions used for Native-PAGE gel casting and electrophoresis.

Gel type	Component	Volume
Native Gel (15%)	ddH ₂ O	7.2 mL
	30% acrylamide/bisacrylamide (37.5:1)	15.0 mL
	Stacking gel buffer	7.5 mL
	TEMED	15 μL
	10% (w/v) APS	150 μL
1x Native PAGE electrode buffer	Glycine	192 mM
	Tris-HCl	25 mM

3.2.14. Protein quantification

The protein concentration can be estimated from the absorption at 280 nm, the wavelength at which aromatic amino acids, mainly tryptophan, have an absorption maximum. The protein sequence can be used to estimate the extinction coefficient. For MAP FurA, the extinction coefficient for a molecular weight of 31496 Da is 22920 cm⁻¹M⁻¹ (Gasteiger et al. 2005).

According to Beer's law, the concentration can be derived from the quotient of the absorption A and the product of the extinction coefficient ϵ and the path length b:

$$c = \frac{A}{\epsilon * b}$$

with c being the sample concentration in moles/liter, A is the absorbance ϵ is the wavelength-dependent extinction coefficient in liter/mol-cm and b is the pathlength in cm.

1-2 μ L of protein sample were used for one measurement with the NanoDrop photospectrometer.

3.2.15. Sample concentration

Protein solutions were concentrated by centrifugation of the solutions in a spin filter with a suitable molecular weight cutoff. The samples were spun down for 10 min at 4000 rpm each, until the desired protein concentration was reached. In between two centrifugation steps the sample was resuspended.

3.2.16. Size exclusion chromatography (SEC)

Matrices with different pore sizes can be used to separate macromolecules by size and shape. Small, globular particles penetrate the stationary phase of the matrix pores, whereas bigger, elongated particles travel faster and are eluted earlier. The ÄKTA purifier or the ÄKTA prime system were used for size exclusion chromatography.

The column of choice was first washed with one column volume of ddH₂O, followed by equilibration with one column volume of SEC buffer. The sample was concentrated to give a sample volume of 5 mL which was injected into to the column through the injection

valve. The flow rate was set to a constant value and the absorption of the eluate was monitored at 260 nm and 280 nm. Elution fractions with high absorption were collected and analyzed with SDS-PAGE.

3.2.17. Dynamic light scattering

With dynamic light scattering (DLS) the hydrodynamic radius (R_h) of particles in solution can be analyzed. When monochromatic light hits particles in solution it is scattered in all directions and interferes with the scattering of other particles. Because of Brownian motion, the position of the scatter origins vary all the time, and the scatter intensity fluctuates. The fluctuations over time give information about the velocity of the particles and the diffusion coefficient can be derived. With this knowledge, R_h can be derived according to the Stoke's-Einstein-equation (Kümmel 1989):

$$R_h = \frac{kT}{6\pi\eta D}$$

with k being the Boltzmann's-constant [J/K], T the temperature [K], η the viscosity of the solution [Ns/m²] and D the diffusion coefficient [m²/s].

From R_h the molecular weight of the particles can also be roughly estimated. Furthermore, the particle size distribution, the dispersity of a solution and information about the purity of a macromolecular sample solution can be evaluated.

DLS measurements were either performed applying the SpectroSize 300 (Xtal Concepts GmbH, Germany) using a cuvette, or the SpectroLight 600 (Xtal Concepts GmbH, Germany), for which different types of multiwell plates can be used. Prior to the measurements, samples were spun down for min. 10 min at max. velocity. For the SpectroSize300, 10 μ L sample was transferred to the cuvette. For standard sample analysis, 20 measurements for 20 seconds each were performed. For long term measurements, the SpectroLight 600 was utilized. 1 μ L of each sample was pipetted into a 48-well SWISSCI MRC plate (Hampton Research Inc., USA) along with 50 μ L of buffer into the respective well reservoir.

The plate was sealed and the position of the laser was adjusted for each sample. The instruments use a laser with 660 nm wavelength and the scattered light hits the detector at a 90° angle. The viscosity of the sample was either set to 1016 cP (pure water) or calculated using the Xtal Concepts software (respective buffer composition).

3.2.18. Circular dichroism (CD) spectroscopy

Macromolecules can be analyzed further with circular dichroism (CD) spectroscopy measurements. Because of the optical activity of biological macromolecules, circularly polarized light gets absorbed differently depending on the macromolecular composition. The difference in light absorption for different wavelengths can then be plotted in a so-called CD spectrum. This gives information about the secondary structure, or the folding state, of a protein. α -helices and β -sheets show certain absorption minima and maxima at distinct wavelengths and hence the relative content of these secondary structure elements can be estimated (Kelly, Jess, and Price 2005).

For sample preparation, the protein solution was aliquoted into 30 μ L aliquots (the protein concentration was 30 μ M). To study the protein in the reduced state, 0.5 mM TCEP was added and incubated for 30 min at RT. To study the influence of protein oxidation, 100 v/v eq. H_2O_2 was added and incubated for 2 min at RT. To check the CD-spectra under metal deprivation, the protein was treated with Chelex® 100 resin (Bio-Rad Laboratories, Inc., USA). All the buffers were also treated with Chelex®. After the measurement, $FeCl_3$ was added directly into the cuvette (end concentration of 20 μ M-60 μ M).

Measurements were performed using a J-815 CD-spectrometer (Jasco Inc., USA). The protein samples were centrifuged for 30 min at max. rpm at 4°C. Before each measurement, the protein buffer spectrum was measured for later background subtraction of the CD protein spectra. Analyses of the spectra were performed with the Spectra manager software provided by Jasco. Ten CD spectra were measured for each sample over a wavelength range of 260-190 nm in 0.1 nm intervals. The individual spectra were accumulated.

To further analyze the data, the measured ellipticity θ was converted into the mean residue ellipticity $[\theta]$ [$deg \cdot cm^2 \cdot dmol^{-1}$] with

$$[\theta] = \theta \frac{M}{10cln}$$

with θ being the measured ellipticity [mdeg], M the molar mass [g/mol], c the protein concentration [g/L], l the layer thickness of the cuvette [cm] and n the number of amino acids in a monomer.

3.2.19. Observation of protein oxidation with Fast Protein Liquid Chromatography (FPLC)

To check the time rate of protein oxidation and the dimer-monomer transition of MAP FurA, 20 μ M protein solution in 20 mM Bicine buffer (pH 8.5) with 150 mM NaCl was incubated with 2 mM H₂O₂ for different time points.

A Superose 12 10/300 GL column (GE Healthcare, USA) was first washed with 1 column volume (cv) distilled water followed by 1 cv FurA SEC buffer. 50 μ L of protein sample was applied onto the column for each run and chromatograms were recorded for each time point at 280 nm and 260 nm.

3.2.20. MAP FurA DNA binding site analysis with Electrophoretic Mobility Shift Assay (EMSA)

The electrophoretic mobility shift was used to study the binding of MAP FurA with different putative binding sites. A short 5'-fluorescently labeled DNA-oligo (LUEGO) was synthesized, as well as the upper and lower strand of the proposed binding regions. All oligos were purchased from metabion GmbH (Germany). The lower strand has the complement reversed sequence of the LUEGO oligo at the 3' end. A list of the oligos used is given in Table 15. The LUEGO approach was adapted from Jullien & Herman, 2011.

The DNA-oligos (*ahprC_str*, *ahprC_matr*, *furA_str*, *furA_matr*) were diluted to a concentration of 100 μ M each in either DEPC treated water (LUEGO) or in FurA SEC buffer. 1 μ M LUEGO was mixed with 1 μ M *ahprC_str* or *furA_str*, and 5 μ M *ahprC_matr* or *furA_matr*, respectively. For annealing, mixtures were denatured at 95°C for 2 min, then slowly cooled down to 4°C. dsDNA was then mixed with 2 μ M MAP FurA and incubated for 30 min at RT.

10 μ L aliquots were mixed with 5x native sample buffer and applied to a native PAGE gel. The electrophoresis chamber was placed on ice and the native PAGE buffer was stored at 4°C prior to electrophoresis. Electrophoresis was performed at 10 V/cm for approx. 2 h. After electrophoresis, the bands were visualized at a wavelength between 460 and 490 nm with a blue light-scanner (Microtek International Inc., Taiwan).

Table 15: DNA sequences used for EMSA. LUEGO binding sites are underlined.

Name	Sequence (5'-3')
LUEGO	Cy5-GTGCCCTGGTCTGG
<i>ahpC</i> _str	AGCTAATTTTGAGTTGATCCAGATTAAGTAGATCCAG
<i>ahpC</i> _matr	CTGGATCTACTTAATCTGGATCAACTCAAATTAGCT <u>CCAG</u> <u>ACCAGGGCAC</u>
<i>furA</i> _str	ATAAACTCTTGACTCGTTCCAAATAAGTGAGTCATTCTGGT G
<i>furA</i> _matr	CACCAGAATGACTCACTTATTTGGAACGAGTCAAGAGTTTA <u>TCCAGACCAGGGCAC</u>

3.2.21. MALDI mass spectrometry

With mass spectrometry the mass of atoms or molecules can be precisely measured. To gather mass and sequence information for proteins that have been separated by size with SDS PAGE, they need to be digested with Trypsin prior to analysis. Trypsin specifically cleaves proteins after the basic amino acids arginine and lysine through hydrolysis of the peptide bond at the C-terminus. The proteins are fragmented and the sizes of the fragments can be matched with the theoretical masses derived by the protein sequence.

For this, the bands containing the proteins of interest were cut with a sterile scalpel. The gel pieces were then cut into tiny pieces and transferred into a reaction tube with 100 μ L de-staining solution and vortexed for 10 min. The reaction tube was briefly spun down and the supernatant was discarded. After this, 100 μ L of ammonium hydrocarbonate solution was added and the gel pieces were rehydrated by vortexing the reaction tube for 10 min, followed by another de-staining step. These steps were repeated until the pieces were de-stained completely. The pieces were dried for 30 min in a SpeedVac. To fully reduce all cysteine residues, 30 μ L of reduction solution was added and incubated for 60 min at 56°C. The solution was discarded and the gel pieces were incubated with 30 μ L iodoacetamide solution in the dark at room temperature (RT) for 45 min. Through this procedure the cysteines are carboxymethylated and protected from oxidation. After

discarding the iodoacetamide, 100 μL of ammonium hydrogen carbonate solution was added and the reaction tube was vortexed for 10 min. The supernatant was discarded and the gel pieces were washed twice with the de-staining solution and vortexed for 5 min each. The pieces were dried in a SpeedVac and 20 μL of the Trypsin solution was added. Samples were incubated overnight at 37°C. The supernatant was transferred to a new reaction tube and 20 μL extraction solution was pipetted into the reaction tube containing the gel pieces, vortexed for 20 min and put in a sonication bath for 15 min. The solution was transferred into the new reaction tube and the last three steps were repeated three times before discarding the gel pieces. A list of all the buffers used for tryptic digestion is given in Table 16. The combined solution was concentrated to approx. 20 μL with a SpeedVac. Subsequently, the sample was desalted with ZipTipC18 Tips (Merck Millipore) according to the manufacturer's protocol. The samples were either stored at 20°C or directly handed over to the MS-unit of the chemistry department and measured by using a MALDI-TOF-TOF instrument.

Table 16: Solutions used for tryptic digestion.

Solution	Chemical	Concentration
Ammonium hydrogen carbonate solution	Ammonium hydrogen carbonate	25 mM
Destaining solution	Acetonitrile	50% (v/v)
	Ammonium hydrogen carbonate	25 mM
Extraction solution	Acetonitrile	50% (v/v)
	Formic acid	5% (v/v)
Trypsin solution	Ammonium hydrogen carbonate	25 mM
	Trypsin	12.5 ng/ μL
Reduction solution	Ammonium hydrogen carbonate	25 mM
	DTT	10 mM
Iodoacetamide solution	Ammonium hydrogen carbonate	25 mM
	Iodoacetamide	55 mM

3.2.22. Small angle X-ray scattering (SAXS)

Small angle X-ray scattering enables the study of particles, e.g. biological macromolecules, in solution with X-rays. With this technique, information about the size, mass and the overall shape, as well as the flexibility of macromolecules can be gathered. For a standard SAXS experiment, monodisperse macromolecule solutions are placed in a quartz capillary and are irradiated by a collimated, monochromatic X-ray beam. The X-rays are then scattered by the electrons in the macromolecules and the intensities are recorded by an integrating X-ray detector. To get the scattering profile of the macromolecule in solution, the scattering profile of the solvent alone is recorded as well and is subtracted from the scattering pattern of the macromolecule solution (Kikhney and Svergun 2015). From the radially integrated scattering profile the size and overall shape of macromolecules can be derived (Mertens and Svergun 2010; Jacques and Trewhella 2010).

To prepare the samples, the biological macromolecules were dialyzed overnight against a buffer of choice. The dialysis buffer was kept for the SAXS buffer subtraction measurements. Three different concentrations, for nucleic acids 1 mg/mL, 2 mg/mL and 3 mg/mL and for proteins 2 mg/mL, 5 mg/mL and 10 mg/mL were measured. SAXS measurements were performed at the P12 EMBL beamline at PETRA III. The samples were exposed for 0.45 s at a wavelength of 1.24 Å with a detector distance of 3 m.

The data was analyzed with programs from the ATSAS software suite (Franke et al. 2017). For initial data processing, PRIMUS (Konarev et al. 2003) and GNOM (Svergun 1992) were used. Firstly, all of the individual scattering profiles for one concentration were inspected individually for aggregation or radiation damage. After that, they were scaled to one another. If no differences between the profiles showed up, the curves were merged and averaged and the Guinier plots were calculated. The Guinier plot can be used to determine the radius of gyration (R_g) (Guinier 1939). From the scattering profile, the maximum dimension (D_{max}) of the macromolecule can be derived. *Ab initio* models were calculated using the DAMMIN program (Svergun 1999). Modelling of multisubunit complexes was done using SASREF (Petoukhov and Svergun 2005).

3.2.23. Thermal shift assay

To crystallize macromolecules, it is necessary that the molecules are pure, stable and soluble in solution, even at higher concentrations. The melting temperature T_m provides a good estimate for the stability of a protein. In a thermal shift assay, proteins are incubated with a fluorescent dye (e.g. SYPRO Orange). The samples are then heated slowly until they start to denature. The dye binds to hydrophobic residues of the protein that get exposed while unfolding. This results in an increase in the fluorescence emission. If the temperature is plotted against the fluorescence, a sigmoidal curve is derived, where the point of inflection corresponds to the melting temperature. In a Real-time PCR cycler, several buffers or additives can be tested at the same time.

The protein sample concentration was adjusted to 5 μ M with 20 mM Bicine buffer, pH 8.0 and mixed with SYPRO Orange (concentration 5000x), to a final dye concentration of 2x. Each sample was mixed with 10 μ L of different additives (Table 17). As negative control, the dye was mixed with the buffer. For fluorescence measurements, a Real-time PCR cycler was used (Mini8 Plus, Coyote Bioscience, USA). The samples were heated from 20°C to 90°C in 4°C increments and 20 s per cycle, then heated up to 95°C for 5 min.

For data analysis, the values of the negative control were subtracted from the measurements at each temperature. Then the temperature was plotted against the fluorescence and the data points after the fluorescence maximum was reached were deleted. The data were fitted to a Boltzmann Distribution Function:

$$Y = Bottom + (Top - Bottom) / (1 + e^{(T_m - \frac{X}{Slope})})$$

With Y= fluorescence emission in arbitrary units [AU]; X= temperature [°C], Bottom= baseline fluorescence at low temperatures [AU]; Top= maximal fluorescence at top of the truncated dataset [AU]; Slope= steepness of the curve; T_m = melting temperature of the protein [°C] (Huynh and Partch 2015).

Table 17: List of additives used for the thermal shift assay (taken from the RUBIC Additive Screen; Molecular Dimensions).

Additive	Concentration
MgCl ₂	312 μ M
CaCl ₂	312 μ M
MnCl ₂	312 μ M
NiCl ₂	312 μ M
FeCl ₃	312 μ M
ZnCl ₂	312 μ M
CoCl ₂	312 μ M
EDTA	1.56 mM
EGTA	1.56 mM

3.2.24. Solubility Screening

To improve protein solubility and stability for crystallization, a protein solubility screening was performed (Benvenuti and Mangani 2007). For this, 22 different buffers with a molarity of 100 mM each were used (Table 20). 2 μ L protein solution (2 mg/mL) were mixed with 2 μ L buffer and placed over a 500 μ L reservoir volume with the respective buffer in a Linbro crystallization Plate (hanging drop setup). The plate was incubated at RT and was screened under an optical microscope directly after set up, as well as after three and seven days to check for precipitate.

3.2.25. Complex formation

The lyophilized peptides were dissolved at RT at a concentration of 1 mM with 20 mM HEPES, pH 7.4, 100 mM NaCl (Peptide Buffer) and aliquots were flash frozen in liquid nitrogen and stored at -80°C. The Spiegelmers were obtained and produced by NOXXON Pharma AG. They were chemically synthesized using solid phase synthesis on controlled

pore glass support using ter-butyl-dimethylsilyl-protected phosphoramidites of L-nucleotides. The Spiegelmers were selected as described here (Helmling et al. 2004) and synthesized as described by Hoffmann et al. (2011). The Spiegelmers and their mirror image D-Aptamer were dissolved at 1 mM at 4°C in 20 mM HEPES, 100 mM NaCl, 5 mM KCl, 1 mM CaCl₂, 1 mM MgCl₂ (Binding Buffer). Aliquots were stored at -80°C. Prior to complex formation, the aptamers were thawed on ice and denatured at 94°C for 2 minutes and allowed to cool down to RT for approx. 5 min. The peptides were added equimolarly and the MgCl₂ concentration was adjusted to 10 mM. The complex was incubated over night at either 4°C or RT. The complex was filtered with a 0.2 µM spin filter and further stored at 4°C.

3.2.26. Complex formation evaluation with Electrophoretic Mobility Shift Assay (EMSA)

The electrophoretic mobility shift assay is routinely used to detect nucleic acid-protein interactions. Nucleic acid-protein complexes show a lower electrophoretic mobility in comparison to the nucleic acid component alone and can hence be detected.

Peptides and aptamers were diluted to a concentration of 30 µM in either peptide or binding buffer and mixed in ratios from 0.8:1:6. The final MgCl₂ concentration was adjusted to 10 mM and the mixtures were incubated for 30 min to 35 days at RT or 4°C. 2 µL aliquots were mixed with 5x native sample buffer at various time-points and applied to a native PAGE gel. The electrophoresis chamber was placed on ice and the native PAGE buffer was stored at 4°C prior to electrophoresis. Electrophoresis was performed at 10 V/cm for approx. 2 h. After electrophoresis, the gel was incubated in 10% acetic acid for 15 min. The gel was rinsed three times with water and then incubated in a 0.5 µg/mL Ethidium bromide solution for approx. 15 min. After this, the gel was transilluminated with a UV source and bands were visualized with a CCD camera. Alternatively, the gel was stained with Coomassie Brilliant Blue R-250 for 30 min, followed by de-staining for 60 min.

3.2.27. Screening for crystallization conditions

Before crystallization, the macromolecule solution was concentrated to ~10 mg/ml. The concentration was determined with the Pre-Crystallization Test (PCT, Hampton

Research, USA) according to the manufacturer's protocol. After that, the sample was centrifuged for 10 min at max. rpm and monodispersity was checked with DLS.

For initial crystallization trials, vapor-diffusion experiments were set up in MRC 96-well sitting drop crystallization plates (Molecular Dimensions, UK). Different high-throughput screens were tested (Table 18).

500 nL protein or complex solution was mixed with 500 nL precipitant solution, with 50 μ L precipitant solution in the respective reservoir. The plates were sealed and stored at either 4°C or 20°C. The plates were checked directly after setting them up with a light microscope, one and two days after, then every other day in the first week after that and then on a weekly basis.

Table 18: List of crystallization screens used.

Name of Screen	Supplier
AmSO ₄ -Suite	QIAGEN N.V., Netherlands
ComPAS-Suite	QIAGEN N.V., Netherlands
JSGC-plus	Molecular Dimensions Ltd., USA
MORPHEUS	Molecular Dimensions Ltd., USA
PACT premier	Molecular Dimensions Ltd., USA
Structure	Molecular Dimensions Ltd., USA
SturaFootprint&Macrosol	Molecular Dimensions Ltd., USA

3.2.28. Crystallization conditions optimization

Possible hits were further investigated with Second Order Nonlinear Imaging of Chiral Crystals (SONICC) or with a microscope that is equipped with a UV light source. Using SONICC, most salt crystals can be differentiated from protein crystals. The crystal is irradiated with a fs-laser impulse in the infrared spectrum. Chiral crystals can be detected by imaging the sample and detecting the frequency-doubled response, only occurring in chiral crystals. UV images are also recorded, as some salt crystals are non-centrosymmetric and can therefore give a false positive signal.

Crystal containing drops were also incubated with Izit Crystal Dye (Hampton Research, USA), a small molecule dye that is small enough to enter solvent channels of protein or nucleic acid crystals. It binds to negatively charged molecules, thereby coloring macromolecular crystals, but is too big to penetrate salt crystals. For this, a 1:10 dilution of Izit Crystal Dye and ddH₂O was prepared, and 0.5 μ L were pipetted directly onto the crystal containing drop. The drop was incubated for 30 min and was then inspected under a light microscope.

Positive crystal hits were subsequently optimized in Linbro plates, using a 1 mL reservoir volume, and different protein:precipitant solution ratios (1:1, 1:2 and 2:1). Different reservoir solutions were tested, with varying pH and precipitant concentrations. The protein concentration was also varied.

The salt and additive screening kit from Jena Bioscience (Germany) was also applied. In an MRC maxi 48 well plate, 500 nL of protein solution was mixed with 500 nL precipitant solution. 200 nL of the respective additive solution was added. Reservoir solution was 100 μ L each. The plates were sealed and stored at 20°C. The plates were checked directly after set-up with a light microscope, one and two days after, every other day in the first week and after that weekly.

3.2.29. *In situ* DLS

In situ DLS can be used to monitor particle properties during an experiment either for monitoring complex formation, stability and crystal formation over time. The SpectroLight 600 (Xtal Concepts GmbH, Germany) is compatible with various different standard multi well plate formats.

The wells of an MRC maxi plate were filled with either 2 μ L aptamer (1 mM in Binding Buffer with 10 mM MgCl₂) or 1 μ L aptamer (1 mM in Binding Buffer with 10 mM MgCl₂) and 1 μ L peptide (1 mM in Peptide Buffer with 10 mM MgCl₂). The reservoir contained the same respective buffer compositions. The peptide was added after approx. 1 hour to monitor complex formation.

To analyze nucleation, 2 μ L of precipitant solution were added to the drop after approx. 1 hour and the reservoir solution was exchanged with 50 μ L precipitant solution.

The drops were monitored with a light microscope in parallel to detect crystal formation.

3.2.30. Streak-Seeding

To prepare a seedstock, microcrystals were crushed with a crystal crusher tool (Hampton Research Corp., USA). 6 μ L of reservoir solution were transferred to the drop and the drop was transferred to a seed bead tube (Molecular Dimensions Ltd., USA). 10 μ L of the reservoir solution were pipetted to the remaining drop and the crystal crusher was washed in the drop. The 10 μ L were then also transferred to the tube and vortexed three times for 10 seconds each with a short break interval on ice in between. The seed stock was stored at -80°C .

Sitting or hanging drop experiments were set up by mixing a macromolecule solution 1:1 with precipitant solution. The drops were allowed to incubate overnight at 20°C or 4°C . The next day, the prepared seedstock was thawed on ice and streak seeding was applied using a horse hair that was briefly dipped in the seed stock solution. When needed, multiple rounds of seed stock preparation and streak seeding were applied until crystals suitable for diffraction experiments grew.

3.2.31. Fluorescent labeling of nucleic acids crystals

To verify that the crystals contain nucleic acids, SYBR Gold (ThermoFisher, Art.Nr. S11494) nucleic acid stain was diluted 1:5000 in 60 mM HEPES, pH 7.5, 100 mM NaCl, 30 mM MgCl_2 , 8% (w/v) PEG4000 and mixed 1:1 with the crystal containing drop. The dye was allowed to diffuse into the crystals protected from light for one hour. The crystal suspension was then transferred onto a cover slip and inspected with a fluorescence microscope. To gather information about the 3D size of the crystals, a Z-stack was generated, by recording pictures of the samples in increments at different focal planes using a focal drive.

3.2.32. Cryo protection and soaking procedure for derivative crystal production

X-ray diffraction patterns were recorded at cryogenic temperatures for standard X-ray crystallography, as radiation damage is significantly reduced at this temperature.

Crystals of biological macromolecules and the surrounding mother liquor contain a substantial amount of water that forms crystalline ice upon freezing in liquid nitrogen.

Therefore, a cryogenic solution that does not interfere with the crystal integrity, and freezes amorously, needs to be added before freezing (Shah et al. 2011).

Before data collection, crystals were transferred with a polymer loop to a cryogenic solution containing the precipitant solution and 10% Glycerol (v/v). The crystals were removed immediately and were either flash cooled in a cryo stream directly prior to data collection or stored in liquid nitrogen for later use.

For the generation of derivative crystals, single crystals were transferred into a separate drop containing mother liquor plus varying concentrations of a heavy atom soaking solution. The crystals were incubated with the soaking solutions for different time-periods, before being transferred to the cryogenic solution (Table 19). After a brief incubation time, crystals were either flash frozen directly prior to data collection in a cryo stream or stored in liquid nitrogen for later use.

Table 19: Overview of soaking solutions used for derivative production.

Solution	Concentration	Time			
NaBr	1 mM	5'	15'	2h	
	50 mM	5'	15'	2h	
	100 mM	dissolved			
	1 M	dissolved			
NaI	1 M	dissolved			
SmAcetat	50 mM	5'	15'	2h	
	10 mM	5'	15'	2h	
	1 mM	5'	15'	2h	
Selenourea	10 mM	10''			
	5 mM	10''			
	1 mM	10''	1'	10'	
CdBr ₂	50 mM	5'	15'	2h	
	10 mM	5'	15'	2h	
CdBr ₂	1 mM	5'	15'	2h	
Tb-X04	50 mM	30''	1'	2'	3' 5'

Solution	Concentration	Time		
K ₂ IrCl	10 mM	5'	15'	2h
	1 mM	5'	15'	2h
	0.1 mM	5'	15'	2h
K ₂ (HgI ₄)	1 - 10 mM	dissolved		
HgBr ₂	2 - 10 mM	30"	1'	2'
IrCl ₃	10 mM	dissolved		
	1 mM	dissolved		
	0.1 mM	5'	15'	2h
OsCl ₃	10 mM	dissolved		
	1 mM	dissolved		
	0.1 mM	5'	15'	2h
CdSO ₄	10 mM	5'		
CdI ₂	1 - 100 mM	dissolved		
[Co(NH ₃) ₆]Cl ₃	0.1-10 mM	30'-2 days		

3.2.33. Data collection

Diffraction data were collected either at beamlines P11 (DESY, PETRA III, Hamburg, Germany), P13 and P14 (EMBL, PETRA III, DESY, Hamburg, Germany) or I23 (Diamond Light Source, Didcot, United Kingdom).

All standard data collections were carried out at 100 K. Standard measurements for native data collection were carried out at 12 keV, with a rotation range of 190° and an oscillation angle of 0.1°. The exposure time was generally set to 40 ms and the X-ray transmission and beam size were adjusted depending on the diffraction power and size of the measured crystal.

Derivative data collection was conducted at P11 (DESY, PETRA III, Hamburg, Germany), where the wavelength of the X-rays can be tuned. Prior to data collection, a XANES spectrum of the derivative crystal was recorded, to check for the occurrence of the heavy atom soaking reagent and to determine the appropriate wavelengths for optimal data collection.

For data collection at lower X-ray energies (below 6 keV), a helium cone was installed at P13 to minimize the absorption of the X-rays at those wavelengths. Diffraction data were collected at 5 keV and 4 keV, with a rotation range of 720° and an oscillation angle of 0.1°. The diffraction patterns were checked for radiation damage and several datasets at different goniometer kappa positions were collected until the crystals showed severe radiation damage.

Because Ghrelin•NOX-B11 crystallization buffer contained CaCl₂, a XANES spectrum was recorded between 4 keV and 6 keV. Diffraction data sets were recorded at 3.07 Å, 3.074 Å and 2.48 Å to perform a MAD experiment around the calcium K-absorption edge.

At I23, data were collected in continuous sweeps with an oscillation angle of 0.1° and with an exposure time of 0.1 s. A curved in-vacuum Pilatus 12 M detector was used to minimize absorption, as mentioned above. The beam size was 200x170 µm. Samples were measured at a temperature below 43 K.

3.2.34. Data evaluation

3.2.34.1. Indexing

Data were processed with XDS (Kabsch et al. 2010; Kabsch, K., and G. 2010). The diffraction patterns were inspected manually to identify radiation damage, as well as statistics per batch was checked. For phasing Friedel's law was set to false and "STRICT-ABSORPTION-CORRECTION" was set to true. Data were cut at a resolution above where the overall R_{merge} rose above 10%, or I/σ dropped below 2.0.

3.2.34.2. Data reduction

Data reduction was performed using the AIMLESS pipeline (Evans and Murshudov 2013), as implemented in CCP4i (Winn et al. 2011). Each dataset was scaled on rotation with secondary beam correction.

3.2.34.3. Data analysis and multi crystal merging

If several datasets were merged to enhance the signal to noise ratio and the anomalous signal, they were analyzed and clustered with BLEND (Foadi et al. 2013) beforehand, which is part of the CCP4 software suite (Winn et al. 2011). Outlier datasets were rejected and datasets were merged into clusters.

3.2.35. Experimental Phasing

3.2.35.1. Substructure determination

For substructure determination different programs were used. The SHELX (Sheldrick 2008) pipeline was used as implemented in hk12map (Pape and Schneider 2004), applying direct methods and Patterson seeding for substructure determination with SHELXD (Sheldrick 2008). Different parameters were tested, the number of atoms making up the substructure (2, 10, 20, 40, 50, 60, 80 and 120), the number of trials (1000, 10000, 60000, 100000, 500000), the minimum distance between “heavy atoms” (3.5 Å, 4 Å, 4.5 Å, 5 Å), different E-values (1.2, 1.3, 1.5 and 1.8) and different high resolution cut-offs (2.29 Å – 6 Å, in 0.1 increments).

HySS (Hybrid Substructure Search) is part of the Phenix program package (McCoy et al. 2004; Grosse-Kunstleve, Adams 2003; Adams et al. 2010). HySS combines different search modes, such as direct-space and reciprocal Patterson interpretation, dual-space direct methods, Log likelihood Phaser completion, and the comparison of the solutions to find a consensus model. Search parameters, such as the high-resolution cutoff, are varied automatically according to the data or when initial trials fail.

PRASA employs phase retrieval methods based on a new adaptation of the charge-flipping algorithm and is implemented in the CRANK2 pipeline (Skubák 2018; Skubák and Pannu 2013; Potterton et al. 2018) in CCP4i and CCP4i2 (Winn et al. 2011) Here, different resolution cut-offs are tried automatically. The number of substructure atoms to be searched for was varied manually and were the same as described above.

3.2.35.2. Substructure refinement and Phasing

Different programs were employed for substructure refinement, electron density calculation, density modification and phase refinement.

As implemented in the hkl2map gui (Pape and Schneider 2004), SHELXE substructure refinement, phasing, density modification and hand-determination without model-building were used (Sheldrick 2008). If a native dataset with better resolution as the “derivative” datasets was available, phase extension up to the resolution limit of the native dataset was performed.

Substructures that were determined by HySS were used for refinement, LLG completion and electron density calculation by Phaser (Adams et al. 2010; McCoy et al. 2007). Density modification was performed afterwards for both hands with phenix_autobuild (Terwilliger et al. 2008).

Substructures determined by PRASA were improved as implemented in CRANK2 (Potterton et al. 2018). The right handedness was evaluated with Solomon (Abrahams and Leslie 1996) for density modification and Multicomb (Skubák, Waterreus, and Pannu 2010) for phase combination. Further rounds of density modification were performed for the chosen hand with Solomon (Abrahams and Leslie 1996). Refmac5 (Murshudov et al. 1997) was used for phase and structure refinement.

3.2.36. Molecular replacement

3.2.36.1. Search model generation by comparing experimental SAXS profiles and *in silico* generated 3D models

3D models of D-NOX-B11 were generated utilizing the MC-Fold|MC-Sym pipeline (Parisien and Major 2008). Secondary structure models were generated with MC-Fold, only entering the sequence, with the option ‘consider H-type pseudoknots’ turned on. The secondary structure with the lowest free energy value was chosen for 3D model generation applying MC-Sym. 1000 different 3D-models were generated, with the R_g that was obtained by SAXS measurements entered as a restraint. The models were then back calculated to theoretical SAXS scattering profiles and then compared with the experimental SAXS profile using CRY SOL (Svergun, Barberato, and Koch 1995), which is part of the ATSAS suite (Franke et al. 2017).

The z-coordinates of the model with the lowest χ^2 score were then reversed to generate the L-form of the model. The name of the bases was changed manually to 0A, 0G, 0C and 0U, which are the official PDB names for L-nucleobases.

The modified L-NOX-B11 model was used as the input search model to Phaser-MR (McCoy et al. 2007), implemented in the Phenix software suite (Adams et al. 2010). Molecular replacement searches were performed for one or two copies of the L-RNA-model in the asymmetric unit. Furthermore, a model only containing the phosphate-sugar-backbone was generated in PyMOL (Schrödinger, LLC 2015).

This modified model was then further used as the search model as described before.

3.2.36.2. Molecular replacement using secondary structural fragments according to Robertson and Scott (2008)

The secondary structure of NOX-B11 was predicted applying the Vienna RNA Websuite (Gruber et al. 2008). According to the prediction with the lowest minimum free energy, helical elements of 8 bp and 4 bp were created using coordinates from an RNA duplex in L-confirmation (1R3O; (Vallazza et al. 2004)) and applying the program PyMOL (Schrödinger, LLC 2015). Molecular replacement was performed with Phaser-MR (McCoy et al. 2007), a powerful software that is able to search for different structural fragments (called ensembles) simultaneously. One can also search for different components, in this case one component search for each ensemble. Each helical fragment was entered as an individual ensemble, with the structural identity set to 99%. The composition of the asymmetric unit was adjusted considering the molecular weights of the search fragments. Two components, containing one fragment each, were created as search fragment.

After molecular replacement the sigma-A-weighted 2Fo-Fc map was inspected and edited manually in Coot (Emsley and Lohkamp 2010). All nucleotides that showed only weak or broken up density at 1 σ -contour level or parts that showed steric clashes were deleted. The manually edited model was then refined with phenix.refine (Afonine et al. 2012). The refined model was entered in Phaser-MR as a new ensemble and a new molecular replacement search was performed with one component containing the refined model, and another component containing another 4 bp helical fragment. This was done sequentially, until the electron density could not be improved further. The resulting phase probability distributions from the last refined model were converted to Hendrickson-

3. Materials and Methods

Lattmann coefficients with HLTOFOM, which is part of the CCP4i software suite (Winn et al. 2011). The obtained phases were then combined with the experimental measured amplitudes using CAD (Winn et al. 2011). Phases were improved via density modification calculations, applying the program SOLOMON (Winn et al. 2011), using solvent-flipping mode.

4. Results

4.1. Structural and biochemical analysis of *Mycobacterium avium* ssp. *paratuberculosis* (MAP) Ferric Uptake Regulator A (FurA)

4.1.1. Expression of MAP FurA

For crystallization experiments, MAP FurA needs to be available in large amounts and of very high purity. The full-length DNA-sequence of MAP *furA* was subcloned without a tag in a pET28-B18R expression vector and was kindly provided by Prof. Dr. Ralph Goethe from the Tierärztliche Hochschule Hannover, Institute of Microbiology.

The protein was recombinantly expressed in *Escherichia coli* BL21 DE3 and different growth media were tested (Figure 5).

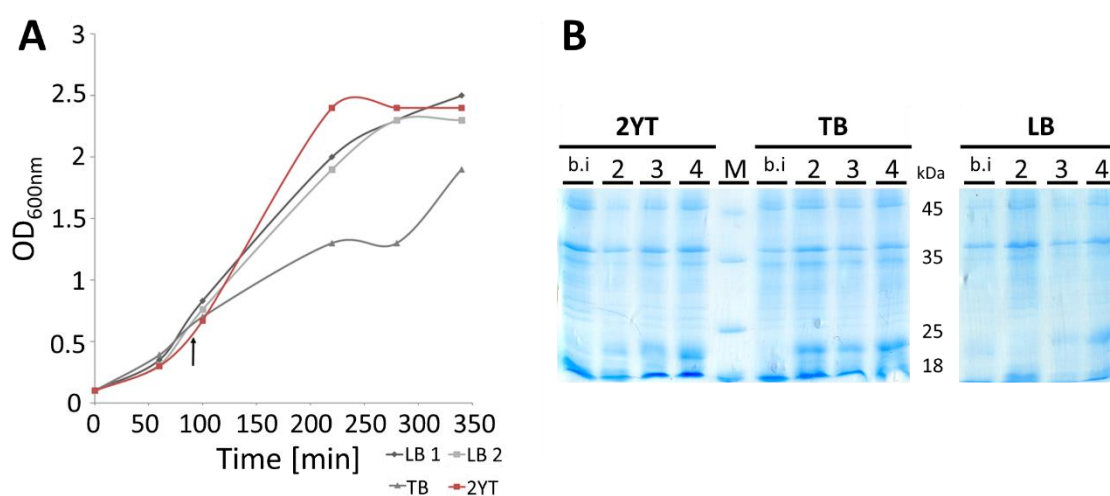


Figure 5: MAP FurA recombinantly expressed in *E. coli* BL21 DE3 cells. A: Growth curve of *E. coli* BL21 DE3 pMAP FurA-cultures in different growth media. The arrow marks the timepoint of 1 mM IPTG addition. B: SDS-PAGE of cell culture lysates pre- and post-IPTG induction. b.i.= before induction; numbers= hours after induction. M= protein molecular weight standard (Unstained Protein Molecular Weight Marker; Thermo Fisher Scientific)

Whereas the growth curves for LB and TB media were comparable, the growth curve with TB media was delayed, with lower optical density at 600 nm (OD_{600nm}) values after 1 mM IPTG addition at an OD_{600nm} of around 0.5. After incubation for 4 hours, the OD_{600nm} values of the LB-cultures and the 2YT cultures were comparable, with values

between 2.3 and 2.5, whereas the OD_{600nm} of the TB-culture was lower, indicating a higher expression and a resulting slower growth (Figure 5A). Expression profiles were analyzed with SDS-PAGE and MAP FurA was expressed in all growth cultures, with the highest expression levels in TB media, where elevated expression levels were already detected one hour after induction (Figure 5B). The theoretical molecular weight of one MAP FurA monomer is 15.8 kDa, and the electrophoretic mobility is higher at approx. 20 kDa.

4.1.2. Purification of MAP FurA

As MAP FurA is negatively charged at pH 8.0 with an estimated charge of -11.9, MAP FurA was purified with Anion Exchange chromatography. The elution fractions were analyzed on an SDS-PAGE (Figure 6A). MAP FurA was eluted at a concentration of 500 mM NaCl along with some high molecular weight impurities. Therefore, the protein was further purified with size exclusion chromatography (SEC). Aside from a small void peak, containing the high molecular weight impurities, two main peaks were observed from the elution profile (Figure 6C). The highest absorbance was observed at 67 mL, which corresponds to a molecular weight of approx. 32 kDa, therefore MAP FurA elutes mainly as dimer.

The second peak reached its absorbance maximum at an elution volume of 77 mL, which corresponds to a molecular weight of approx. 19 kDa. This suggests that MAP FurA is partly monomeric in solution, or that a second protein with this size is present after AEX. SDS-PAGE analysis of the elution fractions of the dimeric peak showed successful purification of the protein. This was also validated with native PAGE, depicting that only the dimeric form is present after size exclusion (Figure 6B).

Purified protein was concentrated to approx. 10 mg/mL and the particle distribution was analyzed using Dynamic Light Scattering (DLS) (Figure 7). The hydrodynamic radius was 2.8 nm \pm 0.1 nm. DLS measurements further confirmed that the particles in solution were monodisperse. However, the protein in solution was rather unstable and aggregation was observed after 2 days or at concentrations exceeding 10 mg/mL.

Hence, a solubility screening was performed as described in 3.2.25 (Table 20). In general, precipitation was observed in buffers with pH values below 7.0 and MAP FurA has a theoretical pI of 4.8. MAP FurA mixed with Bicine was the only approach where no precipitation was observed with and without reducing agents.

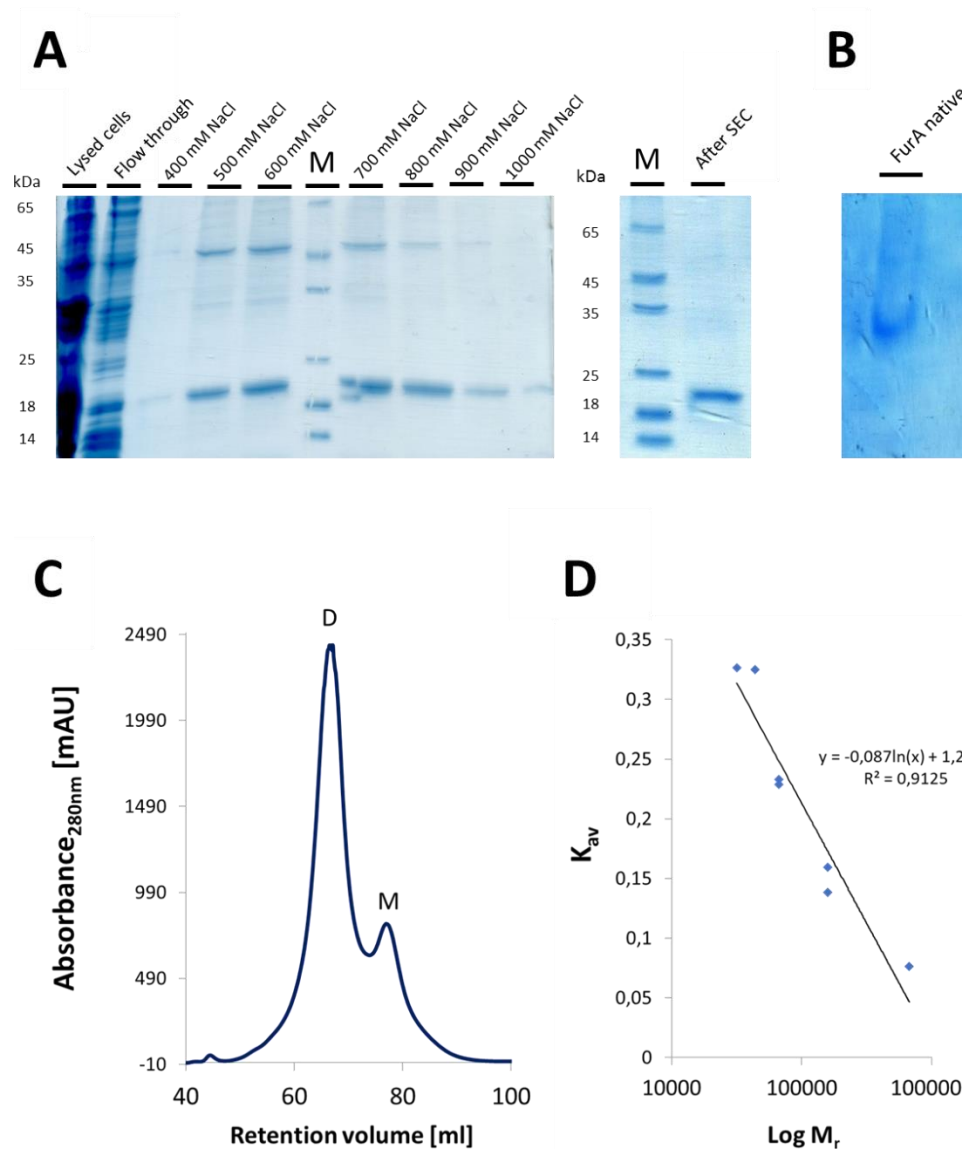


Figure 6: MAP FurA purification. A: Elution fractions from anion exchange chromatography and size exclusion chromatography. For the anion exchange, the protein was eluted with increasing amounts of NaCl in the elution buffer. The protein was eluted at 500 mM NaCl. The protein containing fractions were concentrated and subjected to size exclusion chromatography with a Superdex 75 column. After size exclusion the protein was pure, as shown on the SDS-PAGE. M= protein molecular weight standard (Unstained Protein Molecular Weight Marker; Thermo Fisher Scientific). B: Native PAGE of MAP FurA. The native PAGE revealed one single band, indicating that the protein was pure and showed no oligomeric forms. C: Elution profile of MAP FurA with the Superdex 75 column. A main peak corresponding to approx. 32 kDa was observed, as well as one smaller peak. The main peak corresponds to the dimeric form of MAP FurA, the second one most likely being the monomeric form. Dimeric MAP FurA was collected. D: Calibration curve of Superdex 75 column with the following protein standards: Thyroglobulin (670 kDa), Aldolase (158 kDa), g-Globulin (158 kDa), Albumin (67 kDa), BSA (67 kDa), Ovalbumin (44 kDa).

Table 20: Results from the MAP FurA solubility assay. + indicated precipitation. – indicates a clear drop after one week.

Buffer	pH	MAP FurA	MAP FurA + 0.5 mM TCEP
Ammonium acetate	7.3	+	+
Bicine	8.5	-	-
	9.0	-	-
Bis-Tris propane	6.5	+	+
HEPES	7.0	-	+
	7.5	-	+
	8.0	+	+
MES	5.8	+	+
	6.2	+	+
	6.5	+	+
Potassium/sodium phosphate	5.0	+	+
	6.0	+	+
	7.0	+	+
Sodium acetate	4.5	+	+
	5.0	+	+
Sodium citrate	4.7	+	+
	5.5	+	-
Tris	7.5	+	-
	8.0	+	-
	8.5	+	+

Hence, cell lysis and purification were performed again with 20 mM Bicine, 150 mM NaCl and 2 mM DTT supplemented in all purification steps. The addition of DTT reduced the amount of monomeric protein, as was observed in the size exclusion elution profile (Figure 18B). In addition, DLS measurements showed a highly monodisperse particle

distribution in comparison to the prior buffer composition (Figure 7). The protein was stable for approx. 14 days at 4°C and could be concentrated up to 40 mg/mL.

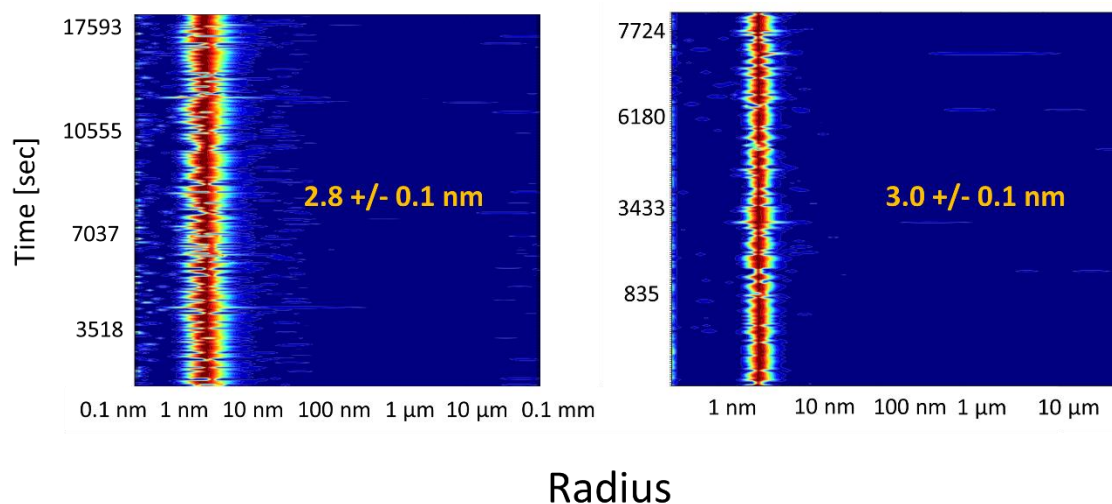


Figure 7: DLS measurements of MAP FurA. Left: Radius particle distribution over time for MAP FurA before buffer optimization. Right: Radius particle distribution over time for MAP FurA after buffer optimization.

4.1.3. Crystallization trials

After the purification was optimized, highly pure and stable MAP FurA protein was available for crystallization experiments. To find initial crystallization conditions, high throughput crystallization trials with commercial screens were performed. Two promising initial hits were further analyzed. The first precipitant, 0.2 M $\text{Ca}(\text{CH}_3\text{COO})_2$, 0.1 M HEPES, pH 7.5, 18% (w/v) PEG8000, yielded spherulite formation after two weeks (Figure 8A).

The spherulites fluoresced under UV light, indicating that they have intrinsic fluorescence from aromatic amino acids. The spherulites were further dyed with Izit dye (data not shown). Both results suggest the proteogenic character of the spherulites, so extensive optimization efforts were performed to succeed with crystallization. Unfortunately, all further trials only led to spherulite formation. The spherulites were tested at an X-ray source. Unfortunately, no diffraction could be observed in this case.

The second promising crystallization condition, 3.2 M AmSO_4 , 0.1 M Citric Acid, pH 5 (Figure 8B), yielded microcrystals overnight. To check whether the crystals were salt or protein, the crystallization droplet was analyzed with SONICC, as described in chapter 3.2.28. (Figure 8B). A positive signal was detected, indicating the presence of protein

crystals. Further optimization lead to crystals of approx. 5 μm in size. Izip dye was added to the crystallization drop, upon which the crystals turned blue, which is another indication of them being protein crystals (Figure 8C). Additional optimization efforts, as outlined in section 3.2.28, did not lead to larger crystals.

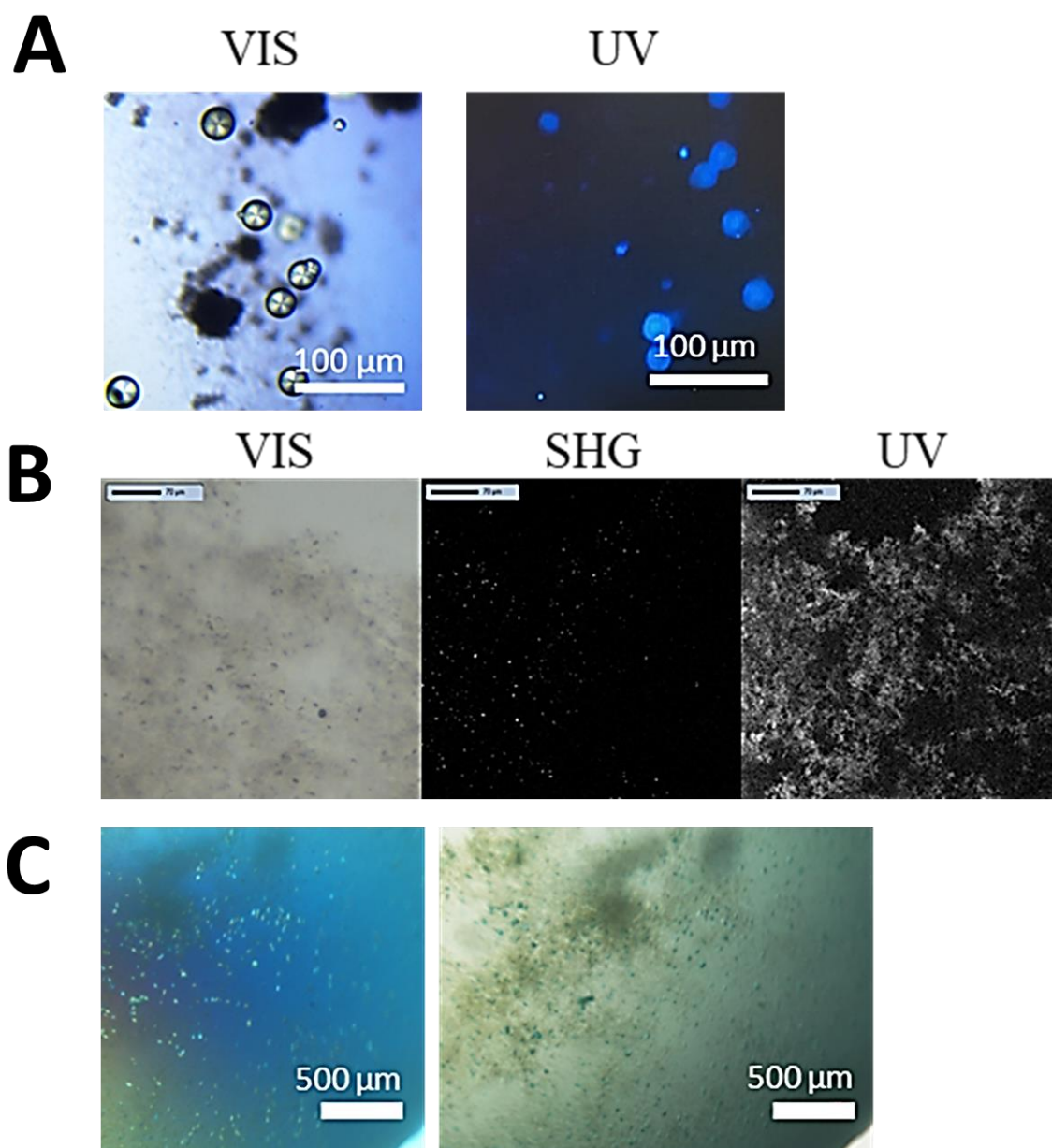


Figure 8: Crystallization trials for MAP FurA. A: Spherulite formation with 0.2 M $\text{Ca}(\text{CH}_3\text{COO})_2$, 0.1 M HEPES, pH 7.5, 18% (w/v) PEG8000 as the precipitant. Left: Light-microscopic image of the spherulites. Right: Spherulites illuminated with UV light. B: Microcrystal formation with 3.2 M AmSO_4 , 0.1 M Citric Acid, pH 5. Left: Light-microscope image of the microcrystals. Middle: Second harmonic generation image of the microcrystals. Right: UV image of the microcrystals. The precipitate is very radiant. Scale bars equal 70 μm . C: Microcrystals under the light microscope. Left: microcrystals under a polarization filter. Right: Microcrystals incubated with Izip dye. After incubation, the crystals were blue, indicating their proteogenic nature.

4.1.4. Bioinformatical information

Fur proteins are conserved throughout microorganisms. There is also structural information from several homologs available with sequence similarities ranging from 41% to 51%. PerR from *Bacillus subtilis* had the highest Bit-score (57.8 bits), a sequence identity of 27% and similarity of 48%. The Bit-score is a value indicating the sequence similarity \log_2 scaled and normalized against the raw alignment-score and is independent of the database size. The seven Fur family proteins with the highest Bit-scores were used for a structural alignment (Figure 9). Secondary structure information was used from PerR from *Bacillus subtilis* (PDB code: 2FE3).

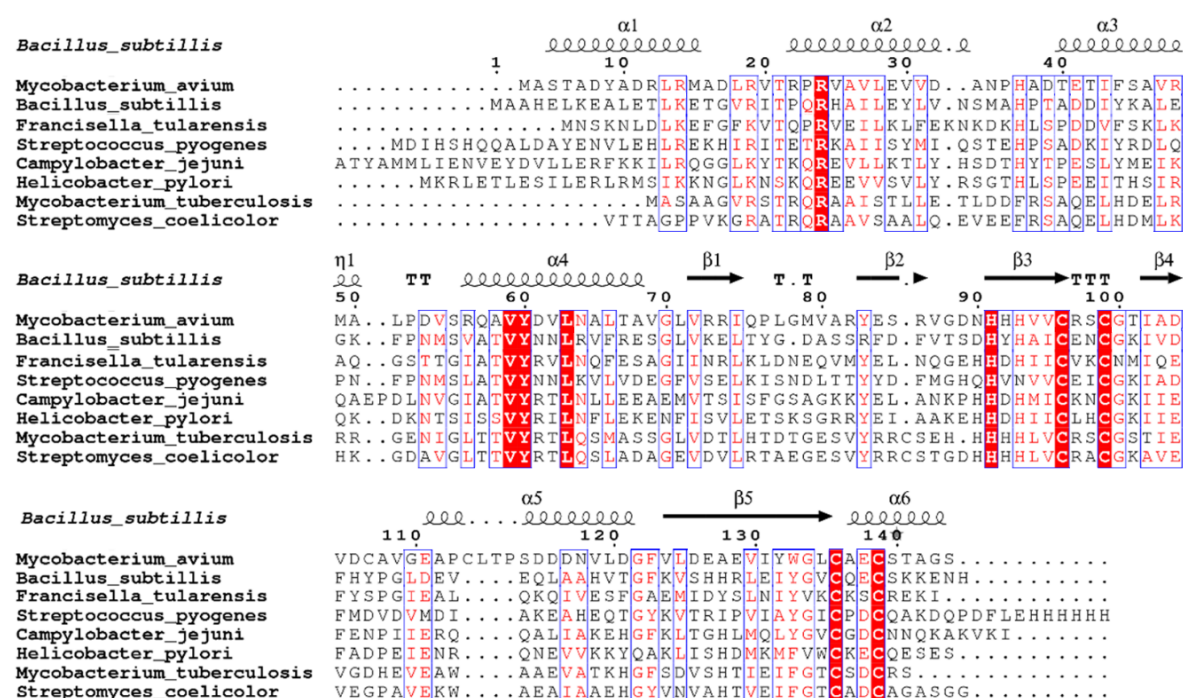


Figure 9: Multiple sequence alignment of MAP FurA amino acid sequence with its closest known homologues with structures deposited in the PDB. PerR from *Bacillus subtilis* is the phylogenetically closest known structural homologue and secondary structural information was taken from the respective pdb file (2FE3). Black spirals: α -helical secondary structure elements; black arrows: β -sheets. T: Turns. Red: conserved amino acids. Blue box with red letters: amino acid with similar physiochemical properties. The multiple sequence alignment was calculated with the ClustalOmega Web server (Chojnacki et al. 2017) and the graphic was created with the ESPript 3.0 server (Robert and Gouet 2014).

No structural information is known for FurA from any member of *mycobacteria*. Sequence comparison of MAP and PerR_{BS} shows, that the residues required for metal binding at PerR_{BS}'s second iron binding site (H37, H91, H93, D85 and D104) are all present in MAP FurA, except for D85 (serine in MAP FurA). The DNA-binding domain

at the N-terminus is also conserved, as well as the dimerization domain that is present at the C-terminus.

To predict an atomic model of MAP FurA, homology modeling was performed (Figure 10). Three different webservers, that apply different algorithms were used (I-Tasser (Zhang 2008), RaptorX (Peng and Xu 2011) and Phyre2 (Kelley et al. 2015)).

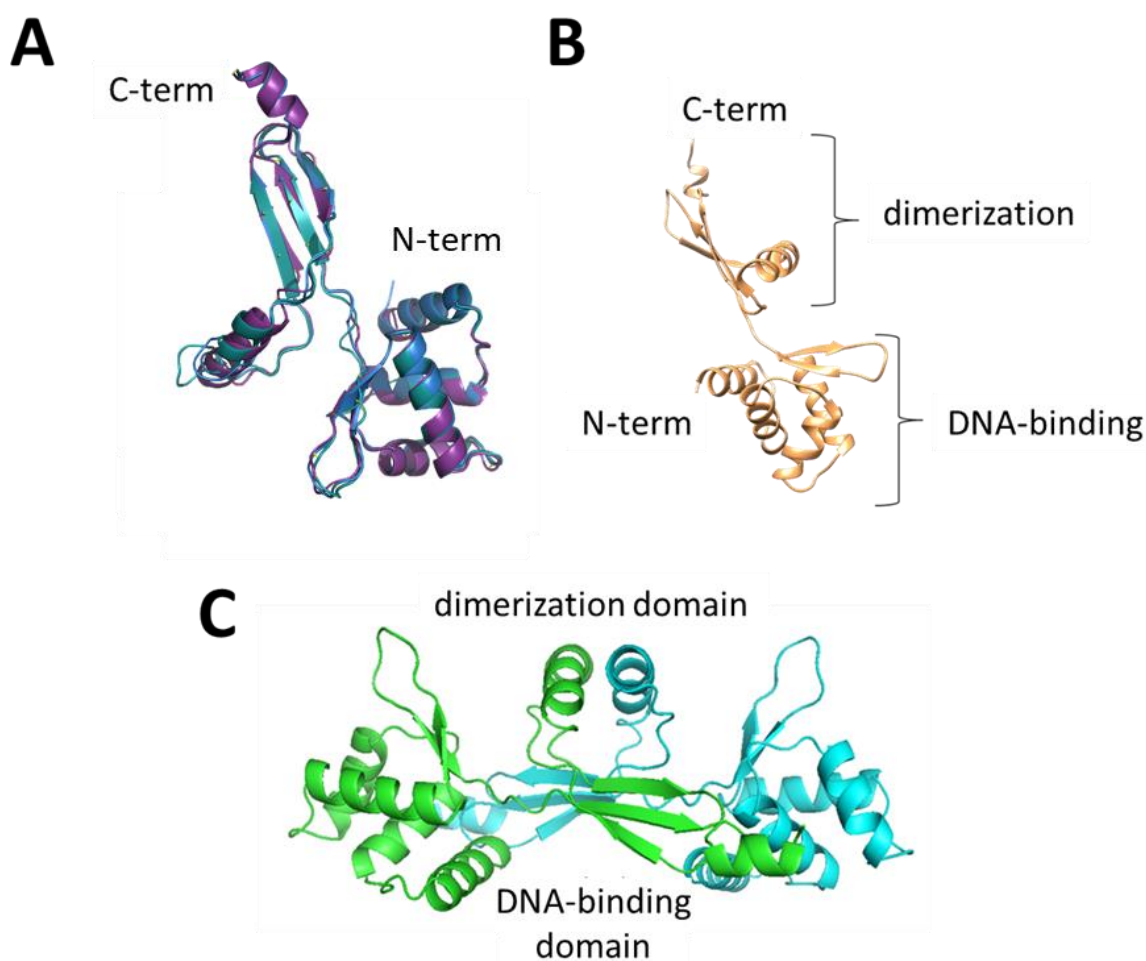


Figure 10: Homology modeling of MAP FurA. A: Comparison of MAP FurA homology models. The models were generated with I-TASSER (Zhang 2008) (purple), PHYRE2 (Kelley et al. 2015) (green) and RaptorX (Peng and Xu 2011) (blue). Alignment was performed with PyMOL and the image was also generated with the PyMOL molecular graphics package (The PyMOL Molecular Graphics System, Version 1.8 Schrödinger, LLC (Schrödinger, LLC 2015)). B: MAP FurA monomer homology model. The model was calculated with I-TASSER (Zhang 2008). The image was generated with UCSF Chimera (Pettersen et al. 2004) C: Putative MAP FurA dimer. The monomers were placed manually to generate the dimer. The image was generated with the PyMOL molecular graphics package (The PyMOL Molecular Graphics System, Version 1.8 Schrödinger, LLC (Schrödinger, LLC 2015)).

Alignment of the three homology models clearly shows the high similarity of the models, indicating a high homology of MAP FurA with the other Fur proteins. The secondary

structure prediction from Phyre2 suggests an alpha helical content of approx. 38%, a beta strand content of 21%, 32% turn and 9% disordered regions.

4.1.5. SAXS

As known for PerR_{BS}, the protein adapts different conformations as a result to oxidation and demetallation. For PerR_{BS}, an open conformation occurs if the protein is either oxidized or in its apo-form, which hinders DNA binding and gene regulation (Traoré et al. 2008, 2006). Based on this information, three different MAP FurA samples were prepared. The oxidized MAP FurA was purified without any reducing agents, the non-oxidized MAP FurA was purified with 1 mM TCEP, and the apo MAP FurA was treated with 10 mM EDTA prior to SAXS measurements.

SAXS measurements were performed at the EMBL beamline P12 (Germany). The data were analyzed with Primusqt from the ATSAS package (Franke et al. 2017). For oxidized MAP FurA, the resulting graph from the Guinier plot showed a linear progression and the calculated radius of gyration (R_g) was 2.64 nm +/- 0.07 nm. The distance distribution was calculated with GNOM (Svergun 1992) and was 9.2 nm with a Porod volume of 38.88 nm³ (Figure 11A).

For non-oxidized MAP FurA, the resulting graph from the Guinier plot showed a linear progression and the calculated radius of gyration (R_g) was 2.04 nm +/- 0.04 nm. The distance distribution was calculated with GNOM (Svergun 1992) and was 6.36 nm with a Porod volume of 23.05 nm³ (Figure 11B).

Apo-MAP FurA, that was incubated with 10 mM EDTA, had an R_g of 2.76 +/- 0.05 nm and the distance distribution function depicted a D_{max} of 9.5 nm and a Porod volume of 36.67 nm³ (Figure 11C).

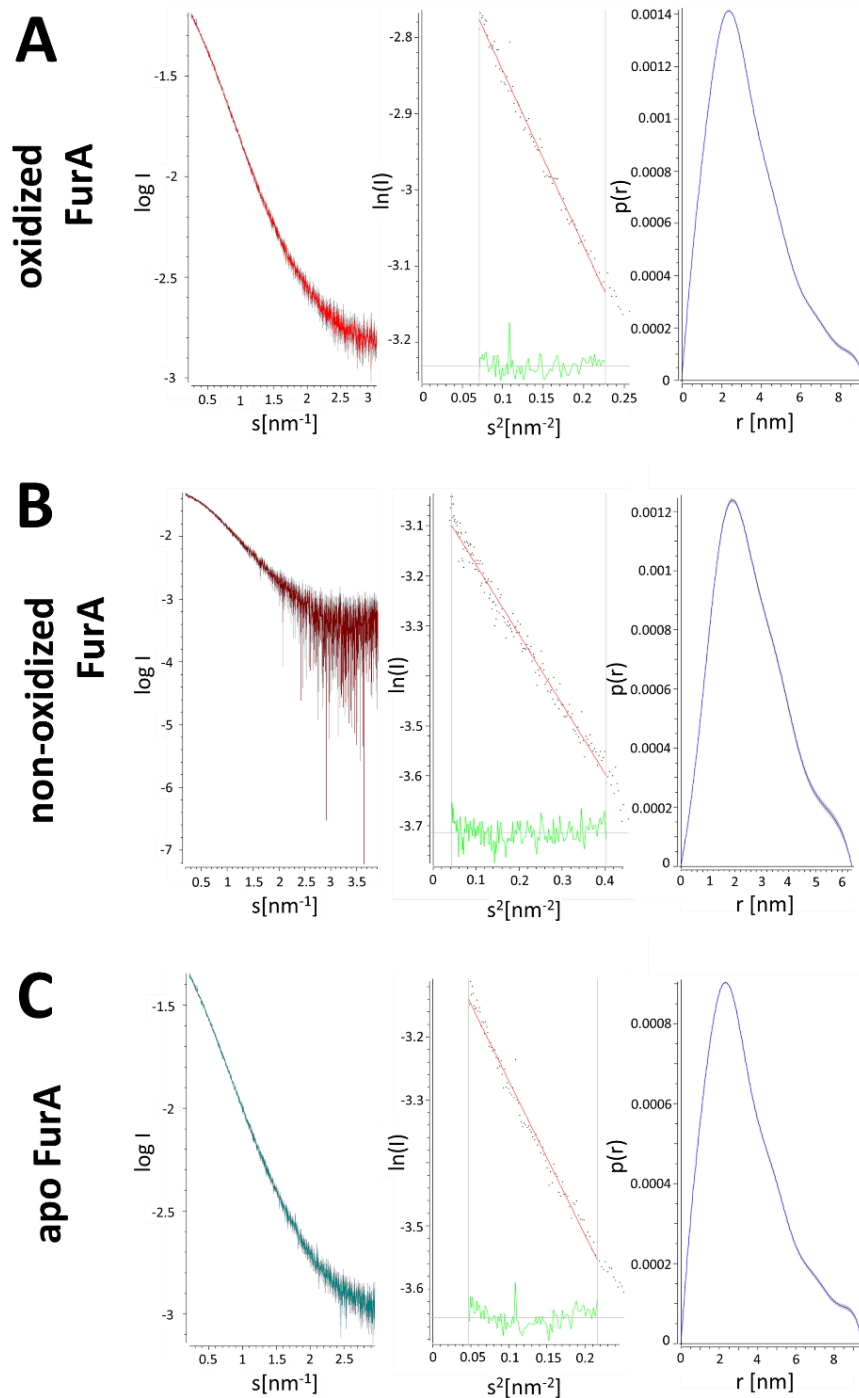


Figure 11: SAXS data analysis of MAP FurA. A: SAXS data analysis overview for oxidized MAP FurA. Left is the averaged and merged scattering curve. In the middle is the derived Guinier plot for small scattering angles. The R_g was 2.64 nm \pm 0.07 nm. On the right is the calculated distance distribution plot, with a D_{max} of approx. 9.2 nm. B: SAXS data analysis overview for non-oxidized FurA treated with 1 mM TCEP. Left is the averaged and merged scattering curve. In the middle is the derived Guinier plot for small scattering angles. The R_g was 2.04 nm \pm 0.04 nm. On the right is the calculated distance distribution plot, with a D_{max} of approx. 6.37 nm. C: SAXS data analysis overview for apo-FurA treated with 10 mM EDTA. Left is the averaged and merged scattering curve. In the middle is the derived Guinier plot for small scattering angles. The R_g was 2.76 nm \pm 0.05 nm. On the right is the calculated distance distribution plot, with a D_{max} of approx. 9.5 nm.

As is visible from the distance distribution functions, the overall shape of oxidized MAP FurA is more or less identical to the apo MAP FurA. The distance distribution function of the non-oxidized sample shows some differences and a smaller D_{\max} (6.36 nm). To get some insights into the low resolution structures and the overall shape of the samples, *ab initio* models were generated with DAMMIN (Svergun 1999) and are displayed in Figure 12.

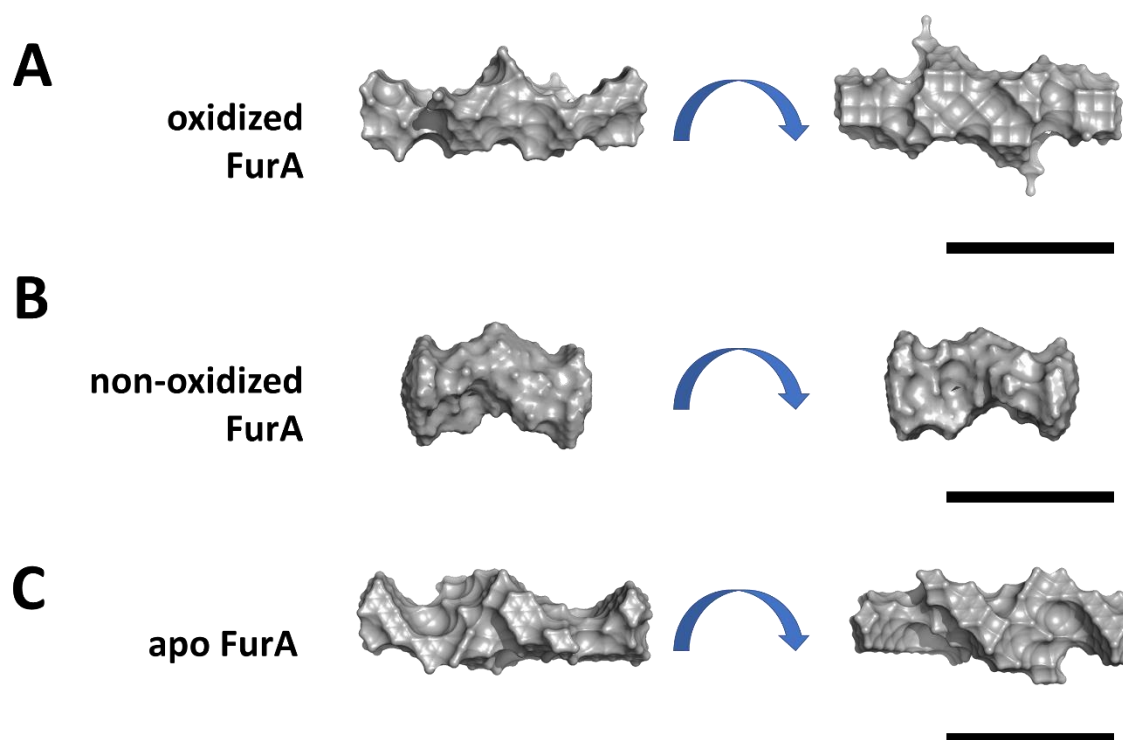


Figure 12: *Ab initio* models of MAP FurA calculated with DAMMIN (Dmitri I Svergun 1999). A: *Ab initio* model of untreated MAP FurA. B: *Ab initio* model of MAP FurA with 1 mM TCEP. C: *Ab initio* model of MAP FurA with 10 mM EDTA. Scale bar represents 5 nm. The images were generated with the PyMOL molecular graphics package (The PyMOL Molecular Graphics System, Version 1.8 Schrödinger, LLC (Schrödinger, LLC 2015)).

From the *ab initio* models, it is clearly evident, that MAP FurA is a homodimer in solution for all samples. The shape of the oxidized and the apo form of MAP FurA are very similar, depicting an open conformation. The non-oxidized MAP FurA on the other hand is more compact, showing a putative closed conformation.

Superposition of the non-oxidized *ab initio* model of the protein to the crystal structure of *Magnetospirillum gryphiswaldense* MSR-1 Fur- Mn^{2+} in complex with DNA was performed (Figure 13). Fur_{Mg} can recognize the DNA by base readout through direct contacts in the major groove and shape readout. This allows Fur to bind various DNA

substrates and hence the regulation of different genes. Interestingly, either one homodimer was bound to one promoter sequence, or two homodimers to another promoter sequence (Deng et al. 2015). The overall shape and position of the domains of the low-resolution model fits quite well onto *Magnetospirillum gryphiswaldense* MSR-1 Fur (Figure 13).

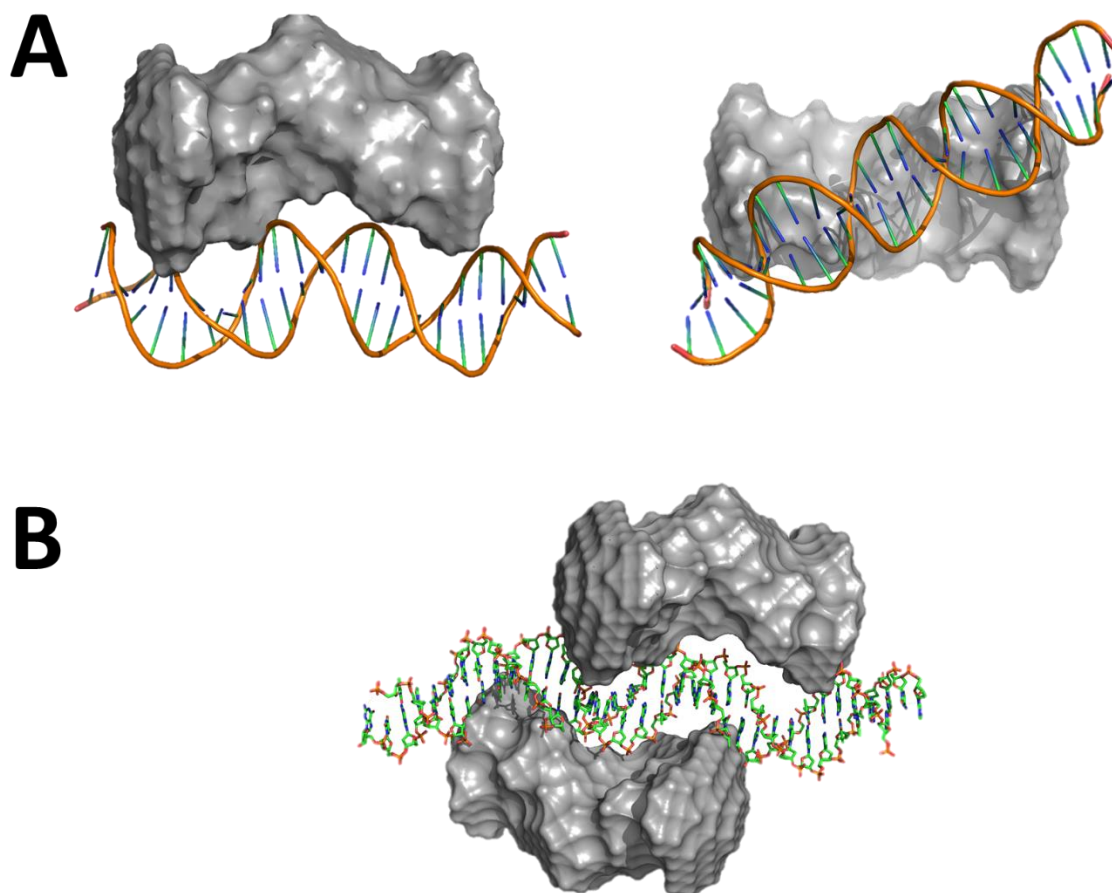


Figure 13: Putative DNA-binding of MAP FurA to DNA. A: One homodimer of MAP FurA is bound to DNA. B: Two homodimers of MAP FurA bound to DNA. The images were generated with the PyMOL molecular graphics package (The PyMOL Molecular Graphics System, Version 1.8 Schrödinger, LLC (Schrödinger, LLC 2015)).

4.1.6. Secondary structure information

To get more information about the conformational change upon oxidation of MAP FurA, CD measurements were performed. All samples were folded in solution and for

comparison the respective calculated secondary structure estimations derived of the experimental obtained data are summarized in Table 21.

Table 21: Secondary structure estimations of MAP FurA with different treatments derived from experimentally obtained circular dichroism data. Secondary structure predictions were calculated with the algorithm of Yang et al. (Yang, Wu, and Martinez 1986). The secondary structure information for apo-PerR from *Bacillus subtilis* was taken from its pdb file (2FE3).

	α -helix	β -sheet	turn	random	RMS
100 mM H ₂ O ₂	54.9	12.1	1.5	31.5	3.9
Chelex	35.8	26.5	0	37.7	4.3
60 μ M FeCl ₃	23.6	41.8	0	34.6	6.23
20 μ M FeCl ₃	10.6	46	0	43.3	5.3
TCEP	47.2	18.6	0	34.2	4.3
apo-PerR _{BS}	44	20	0	36	-

PerR from *Bacillus subtilis* has 44% α -helical and 20% β -sheet fractions in its apo- and oxidized form (Traoré et al. 2006). The non-oxidized, metal containing PerR_{BS}, has 35% α -helical and 15% β -sheet fractions (Jacquamet et al. 2009).

The non-oxidized MAP FurA (0.5 mM TCEP) sample showed 47.2% α -helical and 18.6% β -sheet fractions. Upon metal removal (Chelex) there is a slight conformational change with 35.8% α -helical and 26.5% β -sheet fractions. After adding different amounts of iron, the conformation changes significantly, with a large fraction of β -sheets (23.6% α -helical and 41.8% β -sheet). After adding hydrogen peroxide to the untreated sample, the calculated secondary structure prediction was 54.9% α -helical and 12.1% β -sheet.

The conformational changes can also be observed in the plotted CD-spectra of the respective samples (Figure 14).

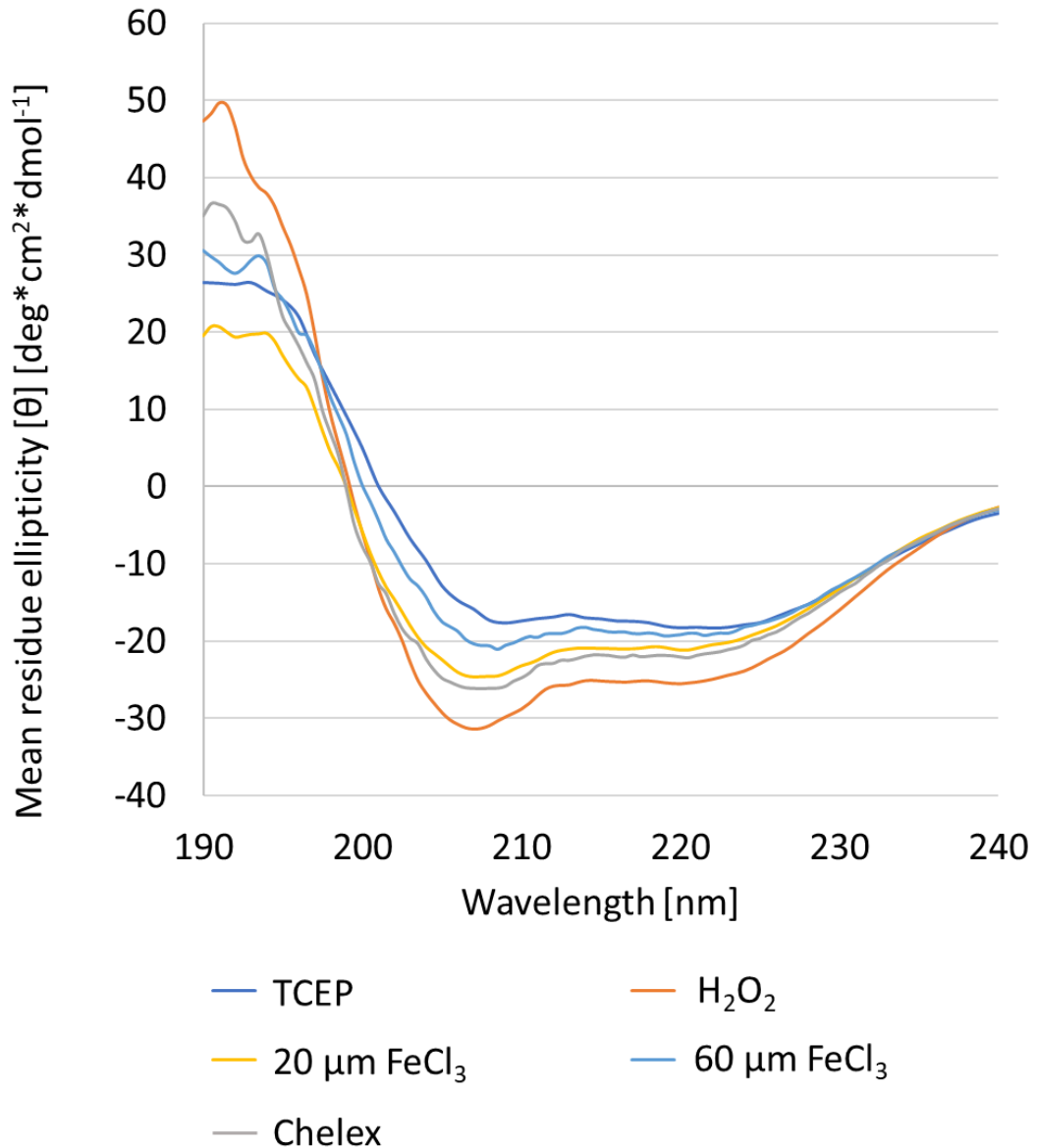


Figure 14: CD spectroscopic comparison of MAP FurA with different treatments. The mean residue ellipticity θ [$\text{deg} \cdot \text{cm}^2 \cdot \text{dmol}^{-1}$] is plotted against the wavelength. The shape of the different curves reveals a conformational change upon hydrogen peroxide treatment, metal deprivation with H_2O_2 and the addition of FeCl_3 .

4.1.7. Analysis of the MAP FurA dimer dissociation rate

For PerR_{BS} a complete dissociation of the dimer after incubation with high amounts of hydrogen peroxide was observed (Traoré et al. 2006).

To check the dissociation of MAP FurA under oxidative stress with progressing time, different FPLC runs were performed after H_2O_2 treatment (Figure 15). As is visible from the untreated sample, only one dimer peak was observed. At later time points and peroxide treatment, more peaks appeared, with increasing integrals with time.

Interestingly, not a single peak was observed, but three peaks, all with time-dependent AUC increases. The dimer peak was still the main peak after 6 h, indicating that either dissociation takes much longer, or that the dimerization state of MAP FurA is unaffected by peroxide treatment.

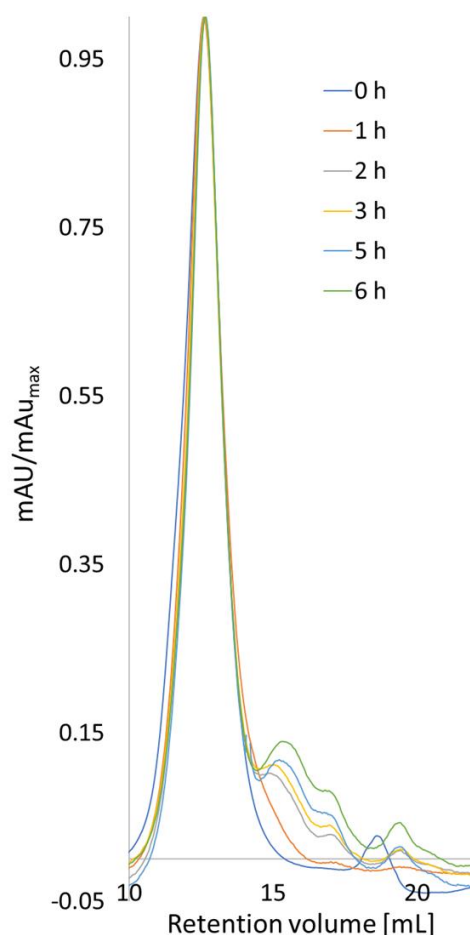


Figure 15: Influence of hydrogen peroxide on MAP FurA over time. MAP FurA was incubated with 100 eq. H_2O_2 . Equal amounts of sample were injected for each run and the absorption was recorded at 280 nm. All absorption values were normalized against the highest absorption value.

4.1.8. Influence of different metal ions and metal chelators on MAP FurA stability

To further gain some information about MAP FurA, a thermoflour assay was performed (Figure 16). With the results from the thermoflour assay, the melting temperature T_m of a protein can be calculated, which is an indicator for the protein's stability.

Here, untreated MAP FurA was incubated with different metals and chelating agents. The untreated sample had a melting temperature of 52.6°C . Upon metal addition, the melting temperature T_m of MAP FurA decreased, except for iron addition, were a small increase

4. Results

in T_m was observed (+2.24°C). EGTA led to aggregation of the protein. EDTA caused the biggest decrease of T_m with -21.29°C.

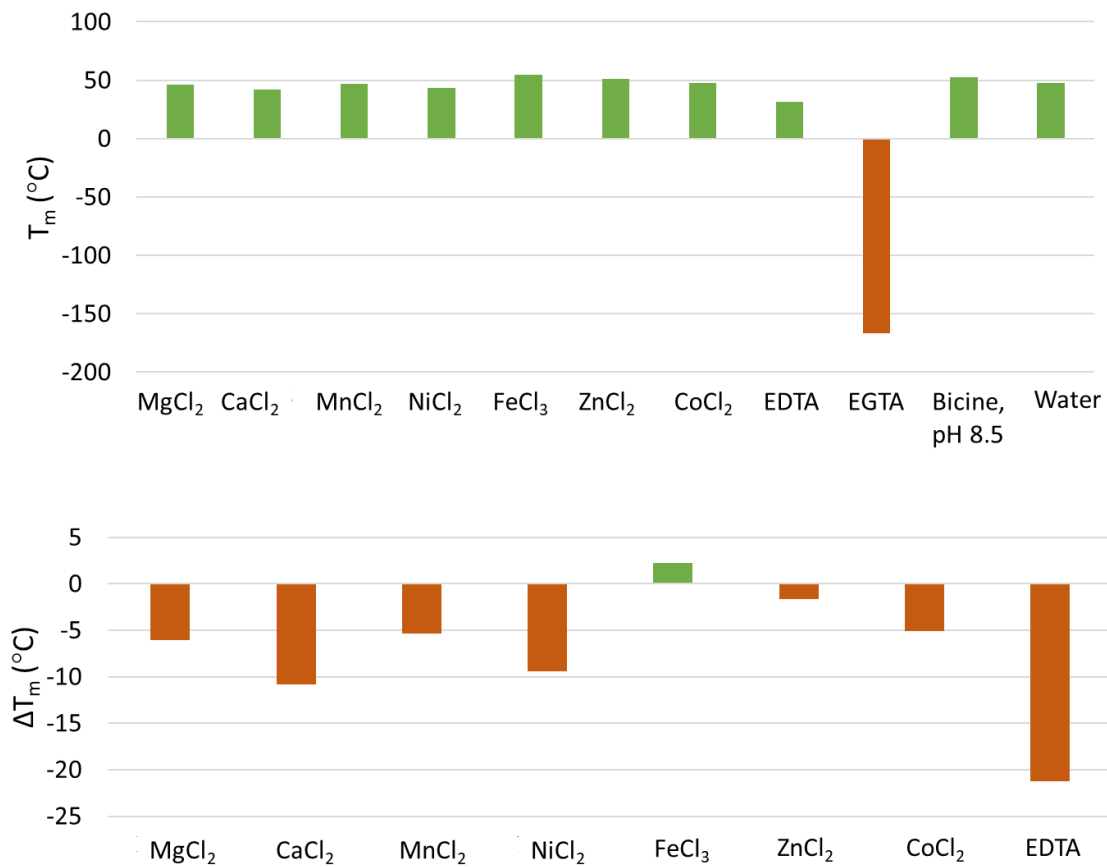


Figure 16: Melting temperatures T_m of MAP FurA upon incubation with different metals and metal chelators. Above: Absolute melting temperature T_m values in °C. Below: Differences in melting temperatures ΔT_m in comparison to MAP FurA in native buffer.

4.1.9. Metal binding analysis

Sequence analysis and 3D modelling of MAP FurA indicate that the three histidines (H89, H90, H91) and one aspartic acid residue (D101) that are necessary for metal binding in PerR_{BS} from *Bacillus subtilis*, are also present in MAP FurA (Traoré et al. 2006; Jacquamet et al. 2009). Since it is known for several Fur homologs that they are able to bind different metals with different affinities, the ability of metal deprived MAP FurA to bind different metals was evaluated (Figure 17).

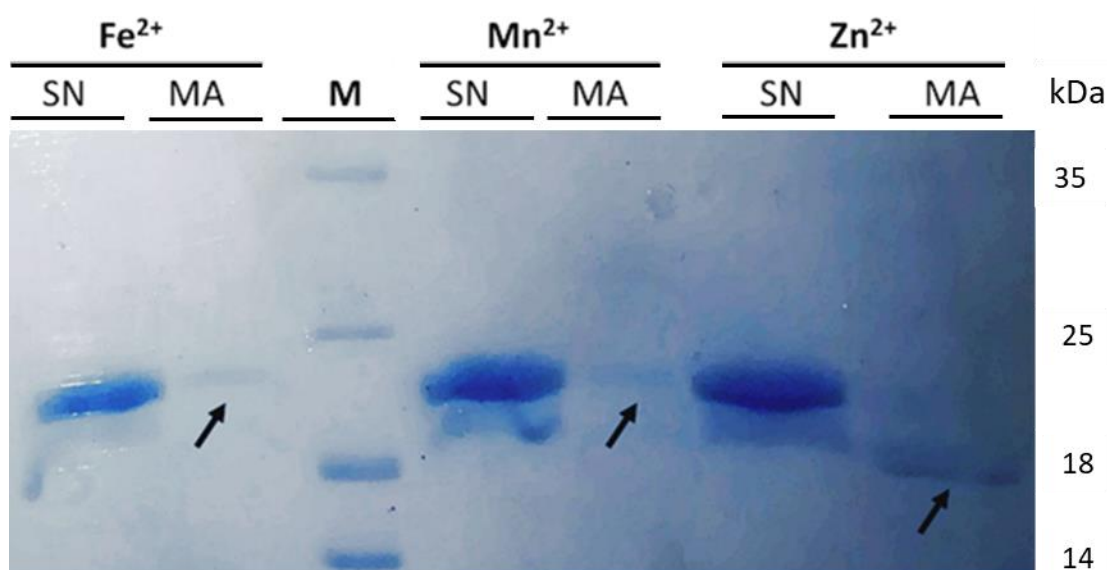


Figure 17: MAP FurA binding to different metals. Ni-NTA-Agarose matrix was stripped with EDTA and incubated with either FeCl₃, MnCl₂ or ZnCl₂. Purified MAP FurA was incubated with the matrices for 30 min respectively. The supernatant was collected and the matrices were washed several times with buffer. The supernatants and the matrices were applied to an SDS PAGE. MAP FurA and all buffers were Chelex100 treated. SN: Supernatant. MA: Matrix. M: M= protein molecular weight standard (Unstained Protein Molecular Weight Marker; Thermo Fisher Scientific).

MAP FurA was almost completely oxidized upon metal deprivation, which can be visualized by the dominant upper band in the supernatant lanes on the SDS-PAGE, as observed in PerR_{BS} (Lee and Helmann 2006). However, a small amount of unoxidized MAP FurA was also present in the sample (lower band). Interestingly, the oxidized form of MAP FurA is able to bind iron and manganese atoms, whereas the reduced form binds zinc ions.

4.1.10. Influence of reducing agents on MAP FurA

When purified MAP FurA samples are subjected to SDS PAGE analysis in the presence of reducing agents, a double band was routinely visible (Figure 18A). This effect was only occurring after samples were boiled (heated to above 98°C) and if the sample buffer contained SDS. With increasing amounts of DTT, the second band became more prominent and showed the lowest electrophoretic mobility, indicating that the protein is partially oxidized.

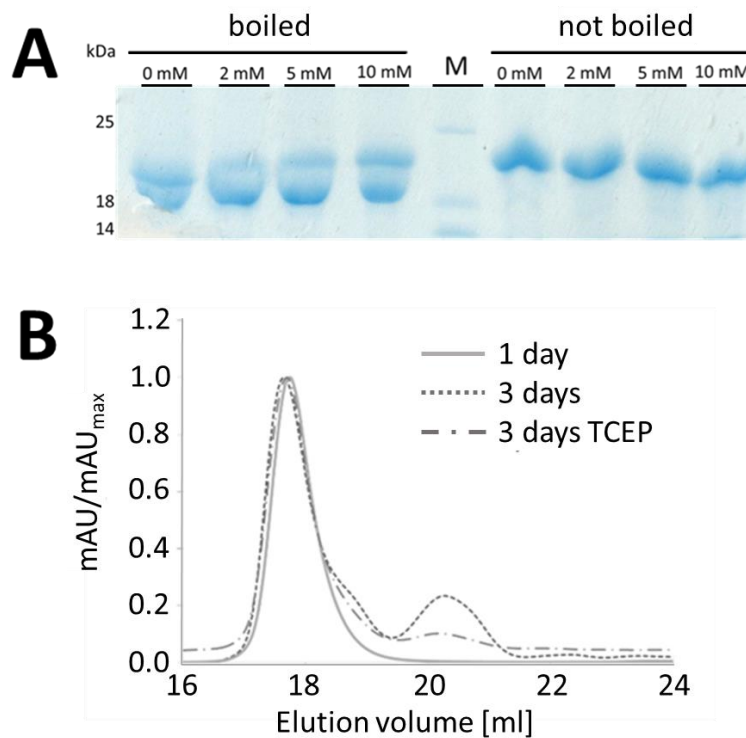


Figure 18: Influence of reducing agents on MAP FurA. A: SDS-PAGE of MAP FurA incubated with different amounts of DTT. Without DTT, a double band can be detected, with the upper band showing a lower electrophoretic mobility with increasing DTT concentrations. Unboiled samples only show one band. M= protein molecular weight standard (Unstained Protein Molecular Weight Marker; Thermo Fisher Scientific) B: Elution profile of purified MAP FurA at different time points. After purification, only one peak can be detected. After three days, a second peak appears. The second peak can be partially reversed upon incubation with 0.5 mM TCEP.

When MAP FurA was subjected to a Superose 6 increase size exclusion column after three days, a second peak appeared in the elution profile (Figure 18B). This peak could be partially reversed by the addition of 1 mM TCEP and an incubation of 30 min at RT.

4.2. Structural insights into the Ghrelin•NOX-B11 complex

4.2.1 Complex verification

The Spiegelmer NOX-B11 binds acyl ghrelin (octanoyl-ghrelin) with nanomolar affinity ($K_d = 35$ nm) *in vitro* and binding has been confirmed to be very effective *in vivo* as well (Helmling et al. 2004; Kobelt et al. 2006). Nonetheless, complex formation was monitored prior to crystallization, to ensure a stable complex formation with the chosen experimental set up. The samples were prepared as described in 3.2.26. 1 mM CaCl_2 , 1 mM MgCl_2 and 5 mM KCl were added, as it is known that divalent cations are necessary for complex formation (Helmling et al. 2004). When NOX-B11 and ghrelin were mixed equimolarly and incubated at RT for 2 hours complex formation could be detected via Native PAGE (Figure 19A). As ghrelin is positively charged, no migration band was visible in the ghrelin lane, whereas a migration band with lower electrophoretic mobility than NOX-B11 alone was detected in the complex approach. The gel was also dyed with Coomassie brilliant blue to verify that it is the complex and not differential RNA-folding products. There were also large amounts of free RNA detectable, indicating such effects. Therefore, NOX-B11 was denatured first, followed by a refolding step at RT. Furthermore, the MgCl_2 concentration was adjusted to 10 mM in the complex buffer. The incubation time was also increased to 16 h at 20°C. With these adjustments, complex formation could be detected via *in situ* DLS (Figure 19B). Upon ghrelin addition, a shift in the hydrodynamic radius (R_h) was observed, indicating a conformational change of the aptamer to a more compact conformation upon binding.

4.2.2. Complex stability

The enhanced stability of Spiegelmers *in vitro* and *in vivo* are a huge benefit for drug development and for application in molecular biology experiments in comparison to regular aptamers (Klußmann et al. 1996). RNases are abundant in the environment and handling of RNA in the laboratory can be quite challenging. The extraordinary stability of the Spiegelmer was observed with *in situ* DLS (Figure 20).

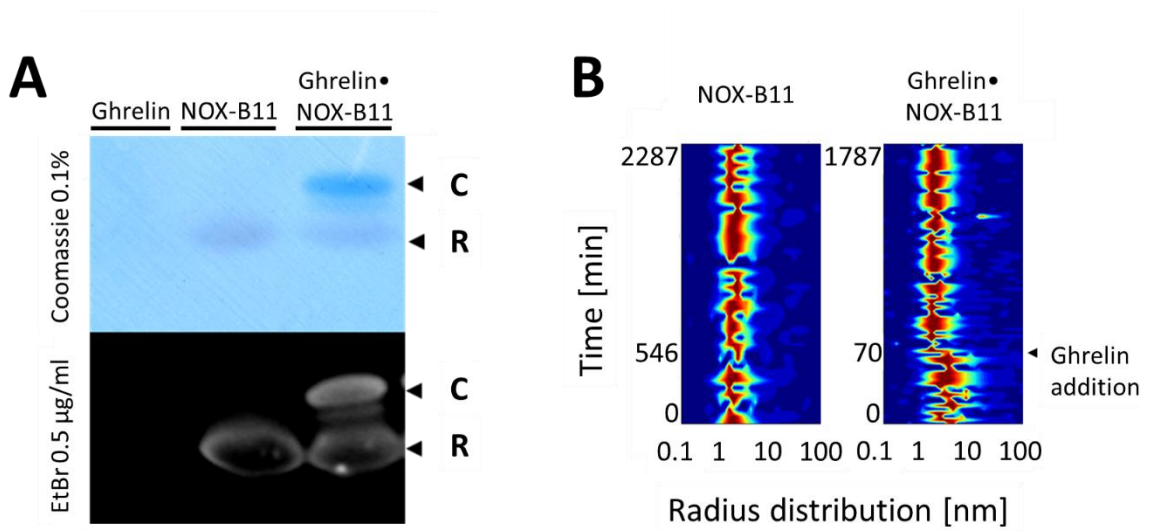


Figure 19: Ghrelin•NOX-B11 complex formation verification. A: Native PAGE. Ghrelin is positively charged, and therefore not present on the gel. NOX-B11(R) shows a higher electrophoretic mobility than the complex (C). B: *In situ* DLS measurements. Left: Particle distribution of NOX-B11. Right: Particle distribution of NOX-B11 before and after the addition of ghrelin. The hydrodynamic radius R_h of the complex decreased upon ghrelin addition. The complex showed a monodisperse particle distribution.

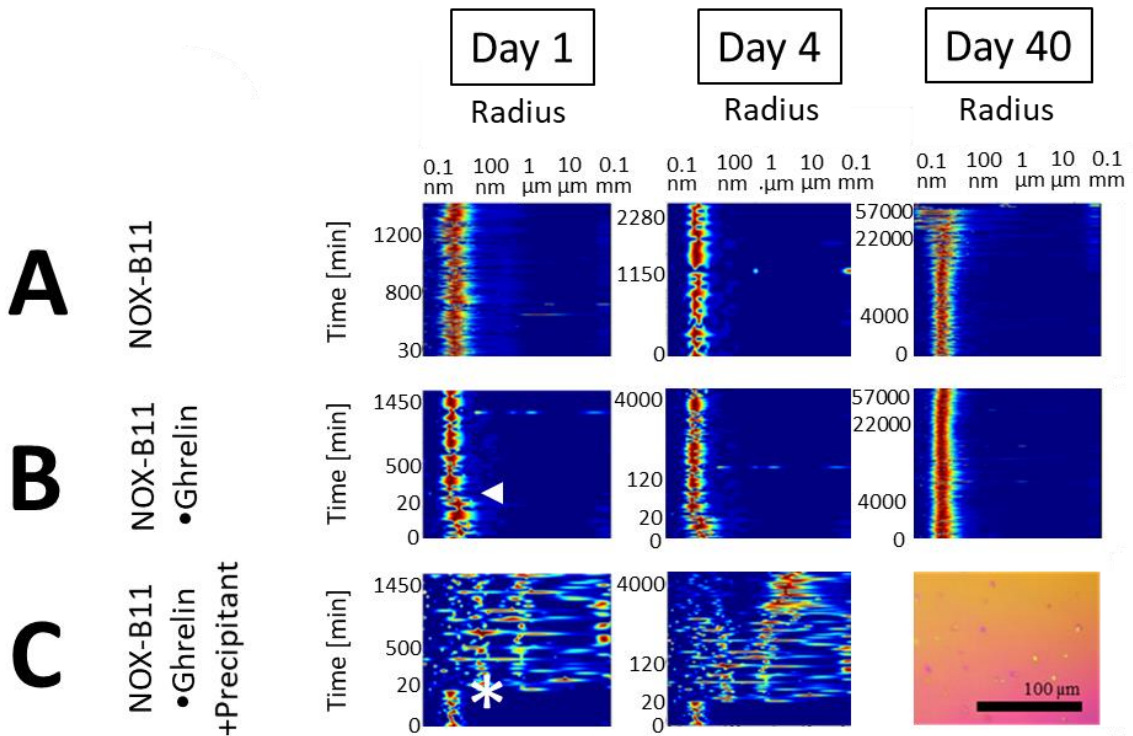


Figure 20: Long-term stability of Ghrelin•NOX-B11. Long-term DLS measurements showed a stable L-RNA and complex over a time-span of 40 days at RT (A, B). The arrow marks ghrelin addition. The nucleation of the complex was observed after precipitant addition (C). The asterisk marks the time point of precipitant addition. The complex peak disappeared instantly after precipitant addition, indicating nucleation events. Microcrystals were observed after 40 days.

NOX-B11 alone was stable for a time-span over 40 days, as well as the complex, showing a monodisperse particle distribution after 40 days. The long-term stability was further confirmed with native PAGE (data not shown). For this, aliquots from the same tube were withdrawn several times over a period of 35 days and complex formation was assessed.

4.2.3. SAXS

To further characterize the complex SAXS measurements were performed at the P12 EMBL beamline at the Deutsche Elektronen Synchrotron (DESY), Germany. The data were analyzed as outlined in 3.2.23. For NOX-B11, the resulting Guinier plot showed a linear progression and the calculated radius of gyration (R_g) was 2.56 nm +/- 0.2 nm. The distance distribution calculated with GNOM (Svergun 1992) has a D_{max} of 12.8 nm with a Porod volume of 30.9 nm³. The distance distribution function further indicates an elongated molecule (Figure 21A).

The molecular weight was calculated to be approx. 18 kDa. This molecular weight estimate indicates a monomeric form of the Spiegelmer in solution (MW_{theo} : 14 kDa (monomer)).

The complex has an R_g of 1.8 nm +/- 0.1 nm and the distance distribution function revealed a more compact molecule in comparison to the L-RNA alone, with a D_{max} of 6.2 nm and a Porod volume of 21.8 nm³ (Figure 21B). The molecular weight is approx. 16 kDa, implying a 1:1 stoichiometric relation with Ghrelin•NOX-B11 (MW_{theo} : 17.5 kDa).

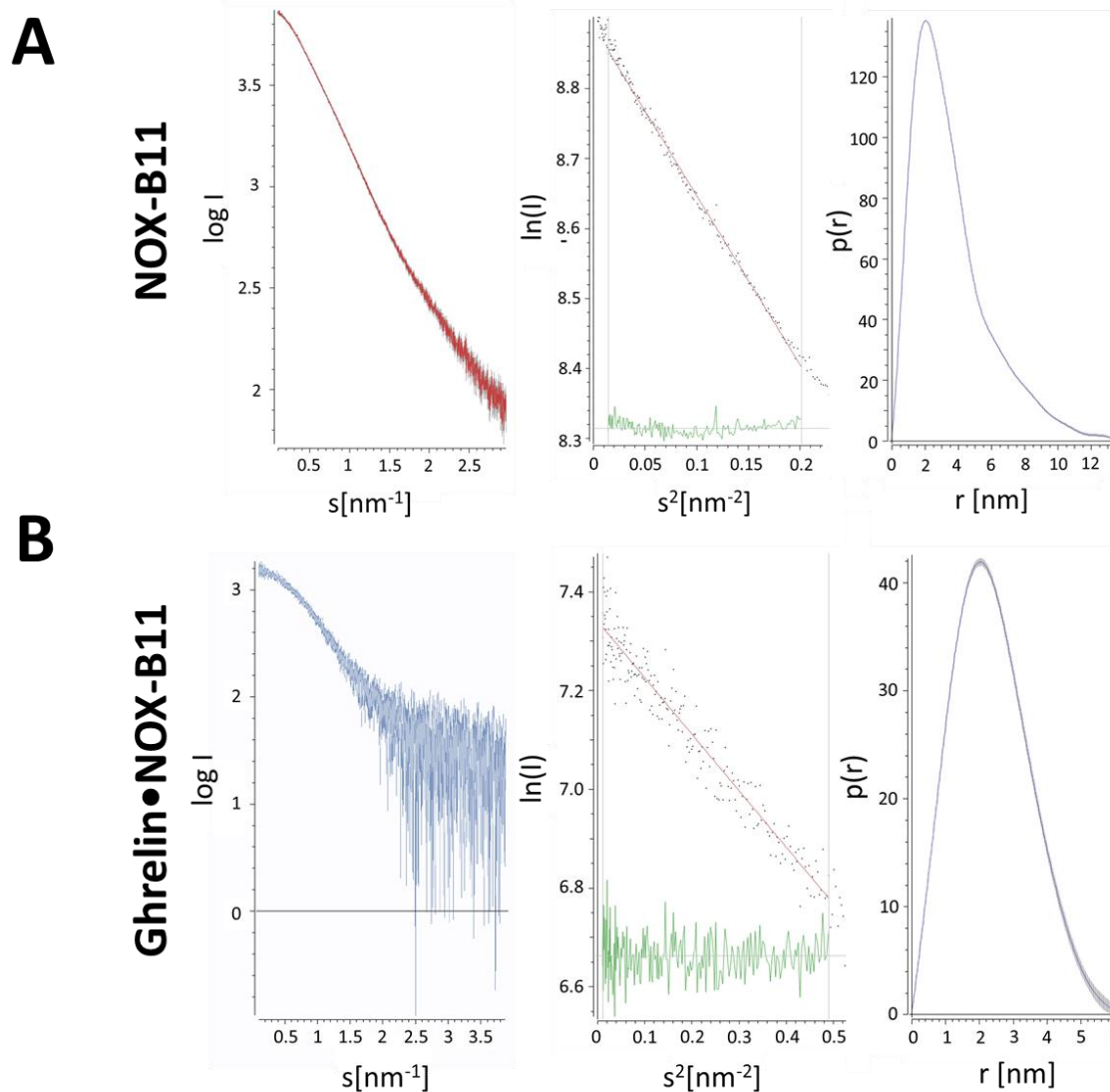


Figure 21: SAXS data analysis of NOX-B11 and Ghrelin•NOX-B11. A: SAXS data analysis overview of NOX-B11. Left: averaged and merged scattering curve. Middle: derived Guinier plot for small scattering angles. The calculated R_g is 2.56 nm \pm 0.2 nm. Right: distance distribution plot, with a D_{max} of approx. 12.81 nm. B: SAXS data analysis overview of Ghrelin•NOX-B11. Left: averaged and merged scattering curve. Middle: derived Guinier plot for small scattering angles. The calculated R_g is 1.78 nm \pm 0.1 nm. Right: calculated distance distribution plot, with a D_{max} of approx. 6.2 nm.

Ab initio models were calculated with DAMMIN (Svergun 1999) (Figure 22). NOX-B11 in solution is an elongated molecule with a compact head and a putative flexible tail and has a diameter of approx. 11 nm. NOX-B11•Ghrelin shows a more compact conformation with a smaller diameter of approx. 4.2 nm and length of approx. 5.8 nm.

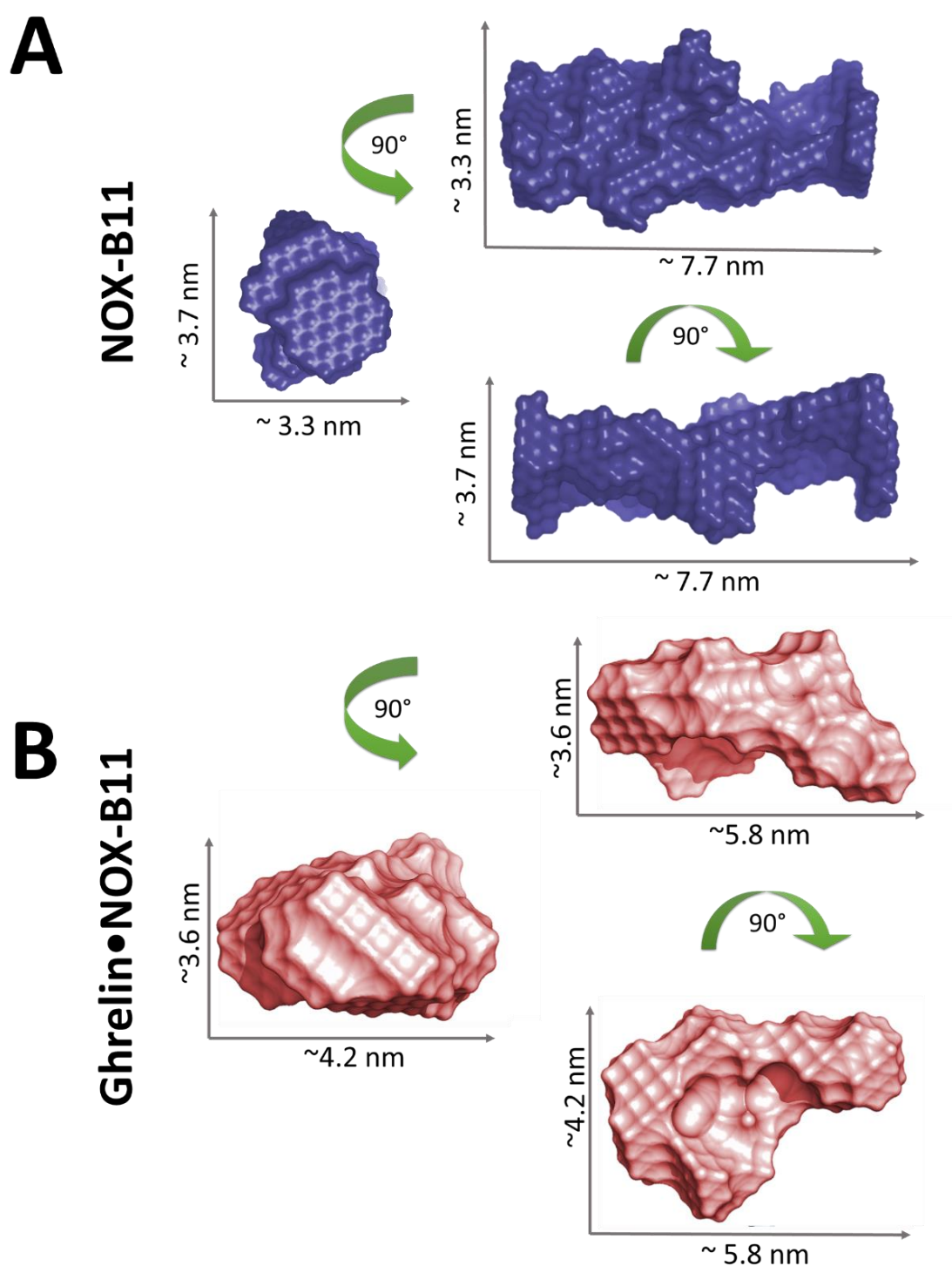


Figure 22: *Ab initio* models of NOX-B11 and Ghrelin•NOX-B11 calculated with DAMMIN. A: *Ab initio* model of NOX-B11. B: *Ab initio* model of Ghrelin•NOX-B11. The images were generated with the PyMOL molecular graphics package (The PyMOL Molecular Graphics System, Version 1.8 Schrödinger, LLC (Schrödinger, LLC 2015)).

Usually, RNA aptamers bind positively charged protein residues, as was also demonstrated in the other two published Spiegelmer complex structures (Oberthür et al.

2015; Yatime et al. 2015). In those crystal structures the Spiegelmers both bind positively charged surface sites, and only have very few apolar contacts (Oberthür et al. 2015; Yatime et al. 2015). Ghrelin is positively charged, as it contains seven positively charged residues and two negatively charged glutamine residues. It was shown that NOX-B11 rather binds ghrelin's fatty acid containing hydrophobic N-terminus and not its more flexible and hydrophilic C-terminus. This was demonstrated by the fact that the L-RNA was only able to bind the acylated form (Kobelt et al. 2006). To get some information about how ghrelin could interact with NOX-B11, SASREF (Petoukhov and Svergun 2005) quaternary modeling was performed. This program can model different subunits of a complex with known atomic coordinates against solution scattering data. Since no known atomic structures are available for both components, homology modeling for ghrelin was performed with I-Tasser (Zhang 2008), and for NOX-B11 the MC-Sym pipeline was used to generate a 3D model (Parisien and Major 2008) (Figure 23).

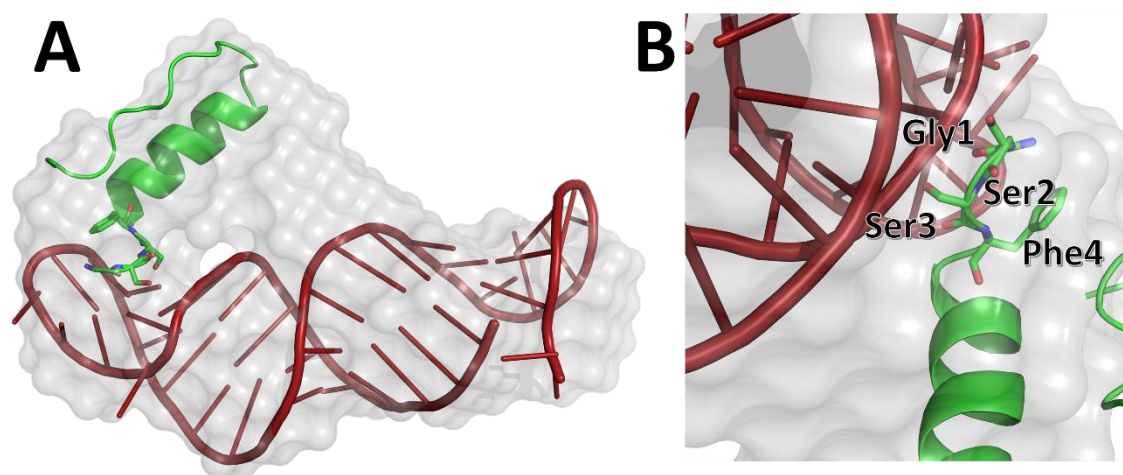


Figure 23: SASREF rigid body model of Ghrelin•NOX-B11 against solution scattering data. A: Overview of the proposed complex. B: Close-up of the four residues, that are essential for complex formation. The images were generated with the PyMOL molecular graphics package (The PyMOL Molecular Graphics System, Version 1.8 Schrödinger, LLC (Schrödinger, LLC 2015)).

The complex was modelled against the SAXS complex diffraction data with a χ^2 value of 1.4. The results from SASREF indicate that the alpha-helical part of ghrelin is pointing towards the L-RNA backbone. Furthermore, a direct contact of the N-terminal Gly1-Phe4 part is possible. These four residues are crucial for Spiegelmer binding (Kobelt et al. 2006).

4.2.4. Crystallization and data collection

After verifying the complex formation and stoichiometry, crystallization trials were set up as outlined in 3.2.28. Initial crystallization hits were observed after eight weeks in 100 mM HEPES, pH 7.5, 100 mM NaCl, 50 mM MgCl₂, 16% PEG4000. Microcrystals grew to a size of 5 μm x 5 μm x 1 μm (Figure 24A). The crystals were probed with X-ray radiation, giving an indication of being of macromolecular nature (Figure 24A). To further validate this and to monitor the crystallization, *in situ* DLS measurements were performed (Figure 20C). Upon precipitant addition the monodisperse particle distribution disappeared instantly, depicting rapid nuclei formation or a diffusion gradient at the point the measurement was being taken, caused by crystal growth. After 40 days, the drop was inspected under a light microscope and microcrystals were observed.

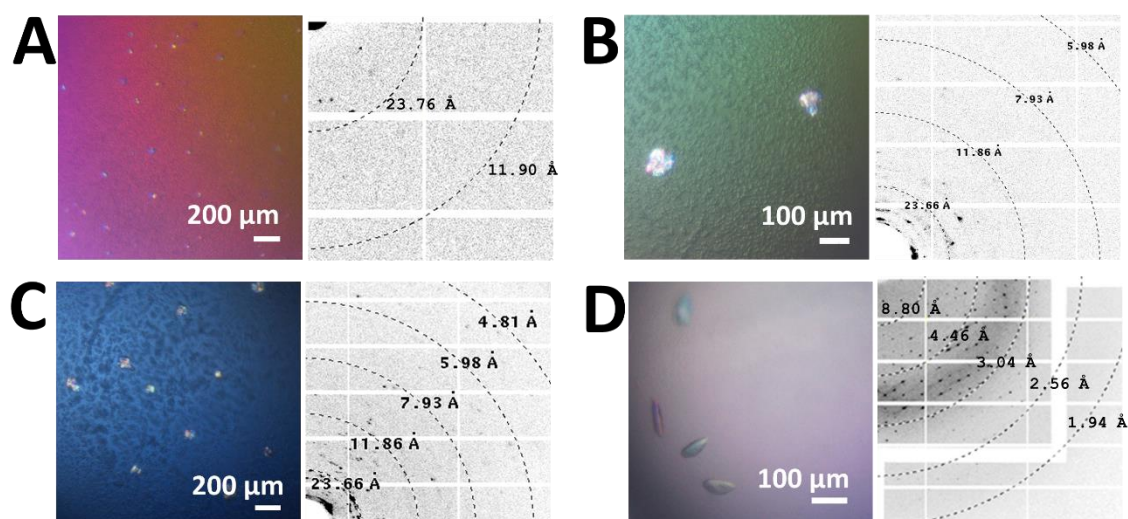


Figure 24: Improvement of Ghrelin•NOX-B11 crystal quality with several cycles of micro seeding. A: Initial crystals appeared after 8 weeks with a size of approx. 5 μm with poor diffraction. B: After the first cycle of streak seeding, bigger, but intergrown crystals appeared overnight and diffracted badly to about 12 Å. C: After the second cycle of streak seeding, slightly bigger crystals appeared overnight, but were still intergrown and diffracted up to ~ 5 Å. D: after a third cycle of streak seeding, single crystals that were approx. 50 μm x 30 μm x 10 μm grew and diffracted up to 2.65 Å.

Extensive optimization trials regarding temperature, precipitants and complex concentrations did not result in bigger crystals suitable for diffraction analysis. Therefore, streak seeding was applied, producing intergrown crystals with an approx. size of 50 μm x 50 μm x 5 μm, with slightly better diffraction to approx. 12 Å (Figure 24B). After two further cycles of streak seeding, crystals with dimensions of approx. 70 μm x 30 μm x 10 μm were obtained (Figure 24D).

4. Results

Figure 25 shows the SYBR Gold labeled crystals under a fluorescent microscope, confirming the presence of NOX-B11. The Z-stack recording of an individual crystal indicated dimensions of approx. $80\ \mu\text{m} \times 120\ \mu\text{m} \times 20\ \mu\text{m}$.

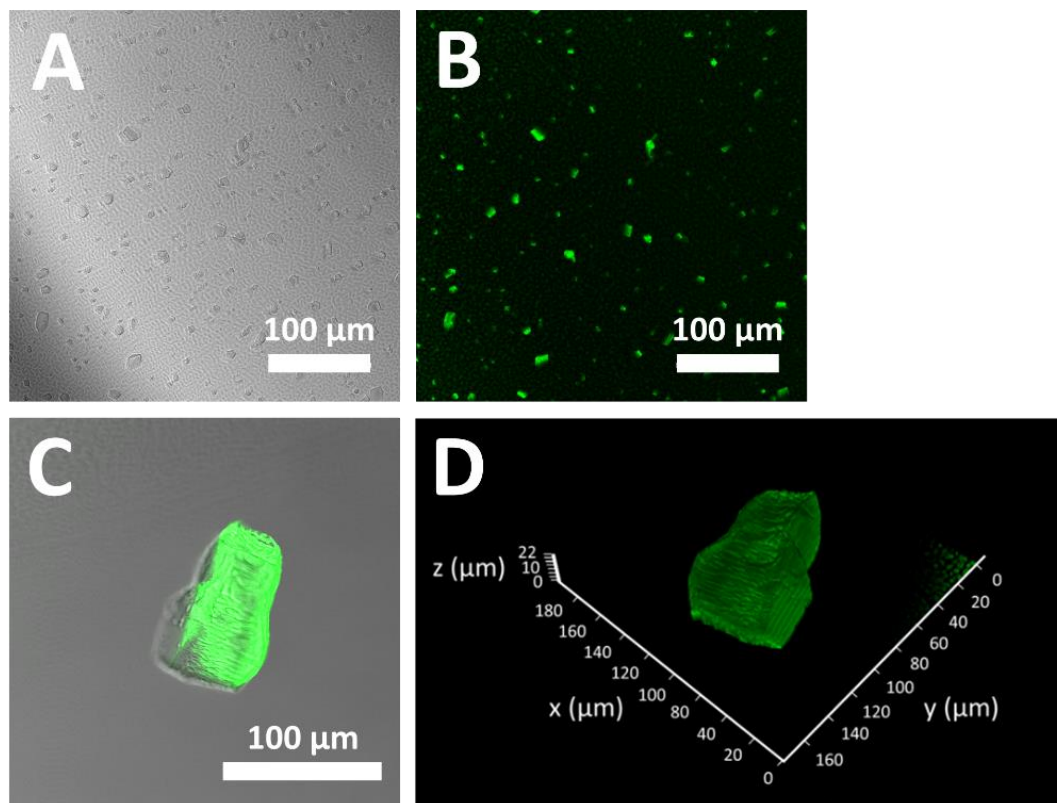


Figure 25: Evidence of NOX-B11 containing crystals. Fluorescent microscopy of a complex crystal treated with SYBR Gold. The observed fluorescence is an indicator for the presence of nucleic acids in the crystals. A: VIS image of the crystal containing drop. B: fluorescence image of the crystal containing drop. C: Overlay of a single crystal of Ghrelin•NOX-B11. D: Z-stack of one fluorescently labelled Ghrelin•NOX-B11 crystal.

These crystals were suitable for X-ray diffraction collection and diffracted up to $2.65\ \text{\AA}$. Data was recorded at the P13 EMBL beamline (DESY, Germany) and the data collection statistics is summarized in Table 22. The space group was determined to be C2 and the Matthews coefficient was calculated to be $2.75\ \text{\AA}^3\text{Da}^{-1}$, with a cell volume of $369752.5\ \text{\AA}^3$ and a solvent content of approx. 60%. For a protein/nucleic acid complex, the automatic molecular weight estimation was 33.7 kDa per asymmetric unit, which would correspond to two complexes per asymmetric unit ($MW_{\text{theo}}: 17.5\ \text{kDa}/1:1\ \text{complex}$).

Table 22: Summary of the data collection statistics for the Ghrelin•NOX-B11 native diffraction data. Values for the outer shells are given in parentheses.

X-ray source	P13, PETRA III
Wavelength (Å)	0.98
Temperature (K)	100 K
Detector	PILATUS 6M
Crystal-detector distance (mm)	419.8
Rotation range per image (°)	0.1
Total rotation range (°)	180
Exposure time per image (s)	0.04
Space group	C2
a, b, c (Å)	58.02, 86.65, 77.10
α, β, γ (°)	90, 107.48, 90
Mosaicity (°)	0.27
Resolution range (Å)	50-2.64 (2.80-2.64)
Total No. of reflections	33635 (2731)
No. of unique reflections	10875 (1328)
Completeness (%)	93.3% (70.8)
Redundancy	3.16 (2.06)
$\langle I/\sigma(I) \rangle$	20.7 (2.08)
CC(1/2)	99.9 (96.6)
Overall B factor from Wilson plot (Å ²)	56.14

4.2.5. *De novo* phase determination approaches

As there are no model coordinates available for neither ghrelin, nor NOX-B11, the crystal structure could not be solved using standard molecular replacement procedures. Therefore, several phase retrieval methods were applied. In the following chapters, native P-SAD and calcium Ca-MAD phase retrieval approaches, as well as Co-MAD and Co-SAD phase retrieval approaches with cobalt hexamine chloride-soaked crystals, are presented. These were the approaches with the most promising results for potential phase retrieval and structure solution. Furthermore, SIR, SIRAS, RIP and RIPAS phasing were also attempted during the course of this work, however with less promising results overall (data not shown).

4.2.5.1. Native P-SAD with intrinsic phosphates as anomalous scatterers

Dauter and Adamiak could prove the feasibility of using the intrinsic phosphates as anomalous scatterers for native P-SAD phasing (Dauter and Adamiak 2001). As a high signal/noise, high multiplicity and anomalous signal are crucial for the success of phasing, especially if the crystals diffract above 1.5 Å resolution, the diffraction data from multiple crystals were collected for data merging approaches at the long wavelengths at the P13 EMBL beamline (DESY, Germany).

25 data sets were collected at a wavelength of 2.48 Å (5 keV) with 7200 patterns per crystal with 0.1° rotation increments and an exposure time of 0.4 ms/increment. To minimize absorption effects, that increase at long wavelengths, the data collection took place under a helium atmosphere.

Diffraction quality of the crystals varied, 13 data sets were of sufficient quality and could be processed with XDS (Kabsch et al. 2010). The crystals diffracted to maximum resolutions ranging from 2.6 Å to 3.1 Å.

As noise could impede the low signal of the anomalous scattering, data from multiple crystals were analyzed and compared for multi crystal merging, which can counteract those effects. The datasets were compared regarding their unit cell constants (a , b , c , α , β , γ), cell volume and mosaicity, as shown in Figure 26 (A-D).

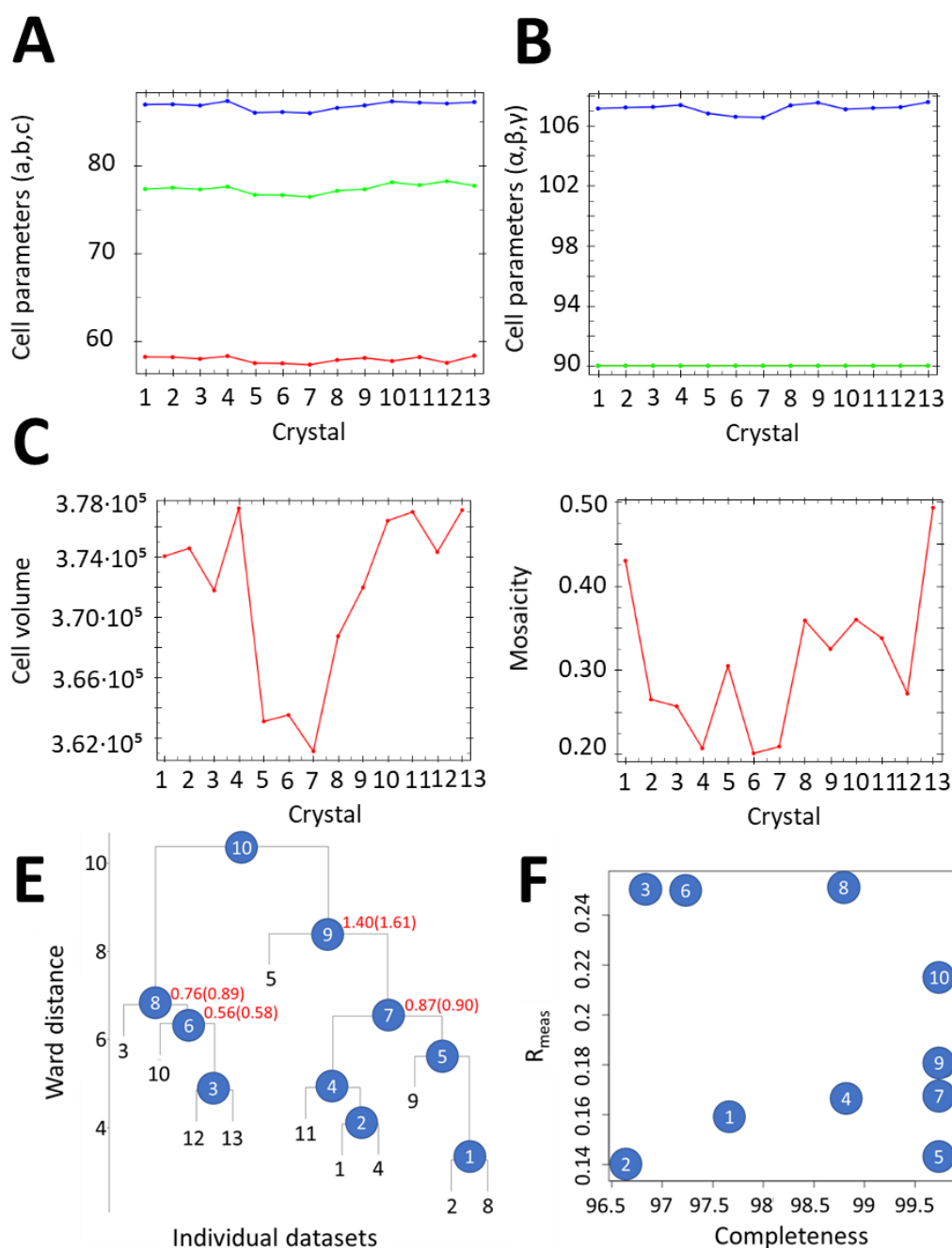


Figure 26: Multi-crystal analysis with BLEND (Foadi et al. 2013). A: Comparison of unit cell constants (a,b,c) of 13 data sets from different crystals. B: Comparison of the unit cell constants (α,β,γ) of 13 data sets from different crystals. C: Comparison of the cell volume of 13 data sets from different crystals. D: Comparison of the mosaicity of 13 data sets from different crystals. E: dendritic tree of 10 different clusters, after outlier rejection. The ward difference is given in red. Black numbers indicate the respective crystal number. White numbers in blue circle depict the cluster number of merged crystals. F: R_{meas} plotted against the completeness of the different merged crystal clusters. White number in blue circles depict a cluster as depicted in E. Graphs were generated with BLEND (Foadi et al. 2013).

Although, there are only minor differences regarding the unit cell constants, there were some higher discrepancies between the crystals regarding the cell volume and mosaicity. Crystals 5, 6 and 7 were the only crystals that showed some larger deviation in the unit cell constants, as well as for the cell volume. Crystals 6 and 7 were identified as outliers, and they were excluded from further merging, whereas crystal 5 was included. After outlier rejection, the datasets were compared again and a dendritic tree was generated (Figure 26E). There were two main clusters with sub-clusters, one with 4 crystals (cluster 8) and one with 6 crystals (cluster 9), respectively. The ten clusters that are depicted in Figure 26E were each merged and compared regarding completeness and R_{meas} (Figure 26F). Cluster 5, 7, 9 and 10 have the highest completeness (99.8%), whereas cluster 2 has the lowest completeness with 96.6%. The R_{meas} is lowest for cluster 2 and cluster 5, with 0.138 and 0.143, respectively. Cluster 3 and cluster 8 have the highest R_{meas} values, with 0.251 and 0.253, respectively. To compare the merged clusters a dataset with all 13 crystals merged was produced. To check the strength of the diffraction signals, the average Bijvoet differences $|\Delta F|$, normalized against $\sigma|\Delta F|$ ($\Delta F/\sigma(\Delta F)$), which can be used as an indicator for anomalous signal strength, and $I/\sigma(I)$ of each cluster were compared to the best single crystal dataset with the highest anomalous signal (crystal 1) (Figure 27).

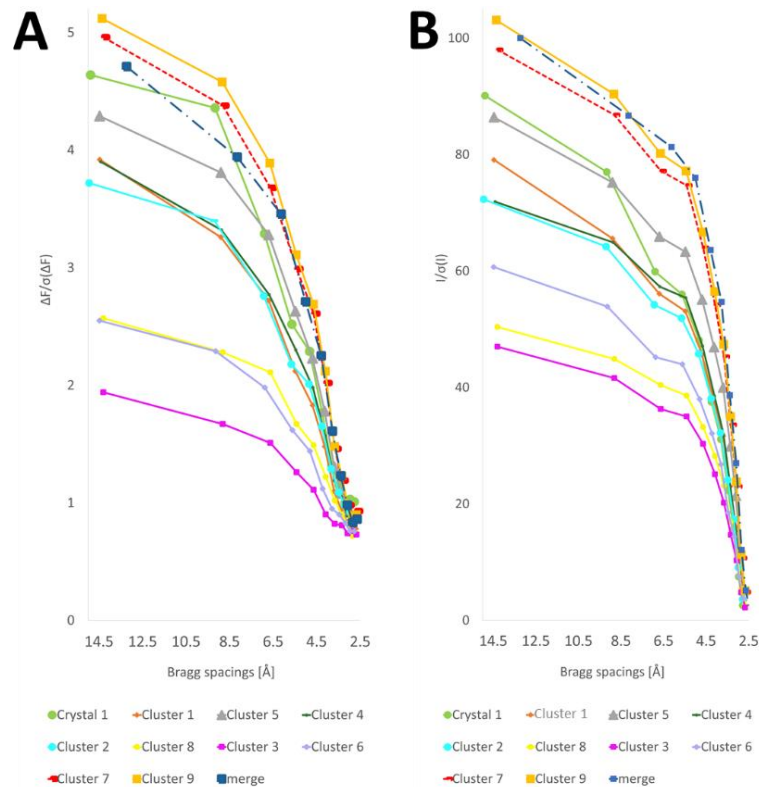


Figure 27: Comparison of diffraction strengths of the different merged crystal clusters. A: $\Delta F/\sigma(\Delta F)$ plotted against the resolution. B: $I/\sigma(I)$ plotted against the resolution.

The merging of cluster 7 and cluster 9 was beneficial for anomalous signal enhancement, as the $\Delta F/\sigma(\Delta F)$ of those clusters exceed the $\Delta F/\sigma(\Delta F)$ of crystal 1 as well as all crystals merged together. Furthermore, the $I/\sigma(I)$ levels were comparable to the $I/\sigma(I)$ levels of all crystals merged together. The $\Delta F/\sigma(\Delta F)$ and $I/\sigma(I)$ levels of the other clusters were worse, even if they contained the data from crystal 1. Table 23 gives an overview over the dataset statistics of all crystals merged together, cluster 9 and cluster 7.

Table 23: Comparison of the data statistics for all crystals merged together and cluster 7 and cluster 9, chosen after multi-crystal merging analysis with BLEND. Values for the outer shells are given in parentheses.

	Merged crystals	Cluster 7	Cluster 9
Number of crystals	15	6	7
Space group	C2	C2	C2
a, b, c (Å)	58.43, 87.21, 77.57	58.43, 87.21, 77.57	58.1, 86.81, 77.29
α, β, γ (°)	90, 107.16, 90	90, 107.162, 90	90, 107.18, 90
Resolution range (Å)	50-2.6 (3.0-2.6)	50-2.7(3.0-2.7)	50-2.7 (3.0-2.7)
Total No. of reflections	1651542 (526684)	753552 (187893)	866165 (214861)
No. of unique reflections	22503 (7851)	20100 (5450)	19812 (5338)
Completeness (%)	99.8% (99.8)	99.8% (99.8)	99.8% (99.8)
Redundancy	73.4 (67.1)	37.5 (34.5)	43.7 (40.3)
$\langle I/\sigma(I) \rangle$	24.19 (4.46)	24.73 (4.78)	25.83 (5.05)
R_{meas}	17.5 (115.5)	12.9 (88.4)	14.6 (87.8)
Sig_{ano}	1.58 (0.69)	1.64 (0.73)	1.66 (0.72)
CC(1/2)	99.9 (99.2)	99.8 (99.2)	99.8 (99.3)
Overall B factor from Wilson plot (Å ²)	66.4	63.1	52.5

4. Results

Furthermore, additional diffraction data were collected at the specially designated long wavelength beamline I23 at Diamond (United Kingdom). 15 crystals were screened and diffraction quality differed vastly. Diffraction data were collected and processed from several crystals, but the quality of two crystals were sufficient for downstream processing. Three datasets were collected from each crystal. The individual datasets were merged and the strength of the anomalous signal and the signal to noise was monitored (Figure 28).

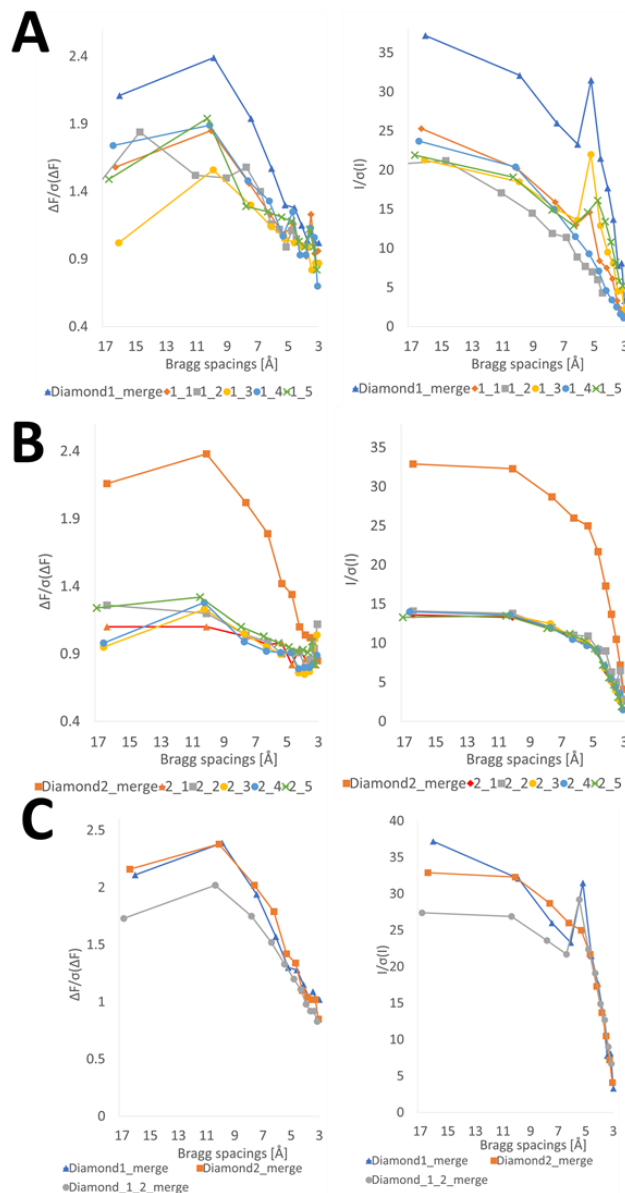


Figure 28: Comparison of diffraction strengths of the data collected at I23 at Diamond Light source. Left: $\Delta F/\sigma(\Delta F)$ plotted against resolution. Right: $I/\sigma(I)$ plotted against resolution. A: Data from crystal 1 (Diamond_1). B: Data from crystal 2 (Diamond_2). C: Data from merged crystals 1 and 2, and both crystals merged together (Diamond_1_2_merge).

The diffraction strength benefited significantly from multi dataset merging. In comparison, the merged datasets had similar $\Delta F/\sigma(\Delta F)$ values, as well as $I/\sigma(I)$. The

values were, however, lower compared to the data collected at P13. If both crystals were merged, the resulting dataset had lower $\Delta F/\sigma(\Delta F)$ values, as well as lower $I/\sigma(I)$ values (Figure 28C). The data statistics of the merged crystals are given in Table 24.

Table 24: Comparison of the data statistics of the diffraction data collected at I23 at the Diamond Light source. Values for the outer shells are given in parentheses.

	Diamond_1	Diamond_2
X-ray source	I23, Diamond Light Source	I23, Diamond Light Source
Wavelength (Å)	2.755	2.755
Temperature (K)	43 K	43 K
Detector	PILATUS 12M	PILATUS 12M
Crystal-detector distance (mm)	100	100
Rotation range per image (°)	0.1	0.1
Total rotation range (°)	360	360
Exposure time per image (s)	0.1	0.1
Space group	C2	C2
a, b, c (Å)	57.68 85.53 75.5	57.95 86.0 76.29
α, β, γ (°)	90.0 106.51 90.0	90.0 106.94 90.0
Mosaicity (°)	0.117	0.117
Resolution range (Å)	42.1-3.16 (3.2-3.16)	42.1 -3.16 (3.2-3.16)
Total No. of reflections	70322 (6468)	106690 (14545)
No. of unique reflections	11792 (929)	11868 (1613)
Completeness (%)	99.3 (99.2)	92.7 (78.3)
Redundancy	5.56 (6.96)	8.99 (9.01)
$\langle I/\sigma(I) \rangle$	7.28 (3.23)	9.7 (1.7)
R_{meas}	15.3 (35.3)	15.4 (89.7)
Sig_{ano}	1.23 (0.90)	1.21 (0.69)
CC(1/2)	99.6 (97.0)	99.7 (88.1)
Overall B factor from Wilson plot (Å ²)	57.6	62.5

4.2.5.2. Ca-MAD for substructure determination

Aside from the phosphorus atoms present in the nucleotides, other native substructure atoms can contribute to the anomalous scattering as well. Since the crystallization conditions contained calcium, and since it is known that calcium is essential for Ghrelin•NOX-B11 complex formation, Ca-MAD data were collected around the calcium K-absorption edge at 3.07 Å. An X-ray absorption near-edge structure spectroscopy (XANES) spectrum was recorded between 4010 eV and 4080 eV and a clear peak for calcium was detected (Figure 29).

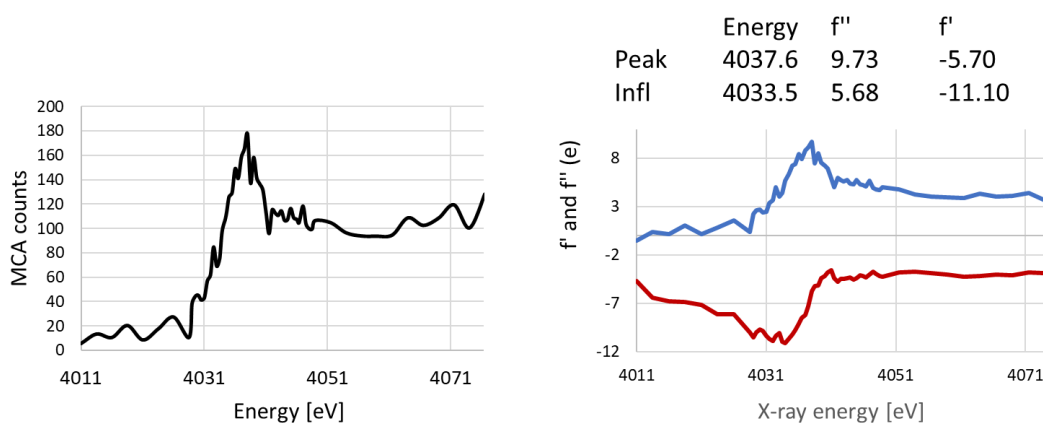


Figure 29: Fluorescence scan of a Ghrelin•NOX-B11 crystal around the calcium K-absorption edge region. Left: XANES spectrum between 4011 eV and 4080 eV. The theoretical K-absorption edge for calcium is 4038 eV. Right: the experimentally derived f'' values are plotted in blue, the f' values are plotted in red.

The peak was found to be at 4037.4 eV, which corresponds to the theoretical calcium K-absorption edge at 4038 eV. The inflection point was at 4033.5 eV. Since calcium was also present in the buffer, it can't be excluded, that the signal is produced by the buffer rather than the crystal. f' and f'' values were derived from the absorption spectra and three datasets from any one crystal were collected. The peak and the inflection datasets were recorded at the derived energies and the high energy remote dataset was recorded at 5000 eV. A resolution up to 3.1 Å was recorded for the peak and the inflection datasets, and up to 2.9 Å for the far energy remote dataset. The data statistics is summarized in Table 25.

Table 25: Summary of the data statistics for the Ghrelin•NOX-B11 calcium MAD data. Values for the outer shells are given in parentheses.

	Peak	Inflection	High energy remote
X-ray source	P13, PETRA III	P13, PETRA III	P13, PETRA III
Wavelength (Å)	3.07	3.074	2.48
Temperature (K)	100 K	100 K	100 K
Detector	PILATUS 6M	PILATUS 6M	PILATUS 6M
Crystal-detector distance (mm)	136.6	136.6	136.7
Rotation range per image (°)	0.1	0.1	0.1
Total rotation range (°)	720	720	720
Exposure time per image (s)	0.04	0.04	0.04
Space group	C2	C2	C2
a, b, c (Å)	57.77, 86.60, 77.07	57.85, 86.69, 77.16	58.24, 87.12, 77.76
α, β, γ (°)	90, 107.05, 90	90, 107.06, 90	90, 107.17, 90
Mosaicity (°)	0.28	0.29	0.34
Resolution range (Å)	73.7-3.1 (3.3-3.1)	73.8-3.1 (3.3-3.1)	74.3-2.9 (3.0-2.9)
Total No. of reflections	77448 (10361)	76821 (9222)	103079 (12377)
No. of unique reflections	12536 (1829)	12592 (1684)	16249(2281)
Completeness (%)	96.7 (86.8)	95.5 (79.9)	96.6 (84.8)
Redundancy	6.18 (5.7)	6.1 (5.5)	6.34 (5.4)
$\langle I/\sigma(I) \rangle$	10.45 (2.34)	10.72 (2.3)	14.79 (2.04)
R_{meas}	14.4 (46.4)	13.5 (44.5)	9.0 (65.3)
Sig_{ano}	1.68 (1.22)	1.52 (1.07)	1.30 (0.58)
$\text{CC}_{(1/2)}$	99.8 (98.4)	99.8 (98.5)	99.9 (97.5)
Overall B factor from Wilson plot (Å ²)	31.1	35.0	54.7

At approx. 4000 eV the K-absorption edge of phosphorous (2146 eV) is also closer than at 5000 eV. Therefore, the anomalous scattering contribution by the phosphorous atoms

is also stronger, and will contribute to the overall anomalous signal in the data as well. The $\Delta F/\sigma(\Delta F)$ values for the three datasets are plotted against the resolution in Figure 30.

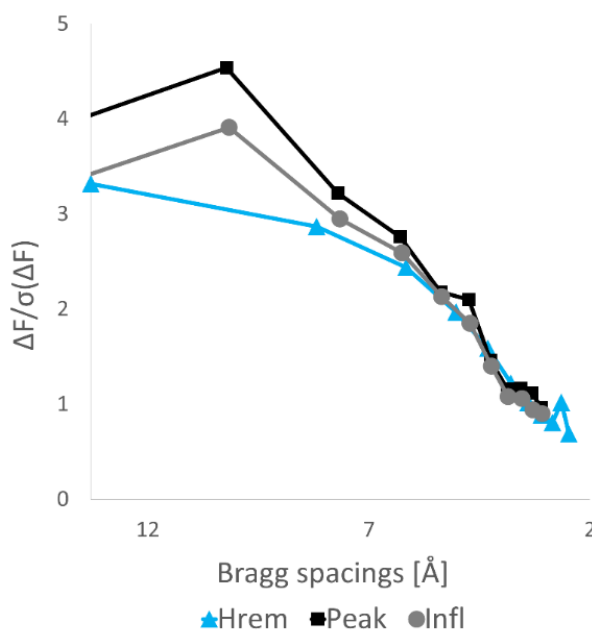


Figure 30: Comparison of the diffraction strength for the calcium MAD data. $\Delta F/\sigma(\Delta F)$ is plotted against the resolution.

As expected, the anomalous signal is highest for the peak data set, and lowest for the high energy remote diffraction data sets. There was no evidence of severe radiation damage in the high energy remote dataset, which was recorded last.

4.2.5.3. Derivative production for phase retrieval (Co-MAD/Co-SAD)

In addition to native SAD, heavy-atom derivatives for phase retrieval techniques, such as SIR/MIR, SAD/MAD, and their combination (MIRAS/SIRAS), are routinely produced. Problems can arise, if the intrinsic crystal order changes upon derivative interaction, and the crystal lattice is reordered or disordered. This can result in the loss of crystal quality or dissociation of the crystals. Therefore, different reagents at different concentrations and incubation times were tested (Table 19).

Sodium salts with negatively charged bromide and iodine atoms were ineffective, as the crystals dissolved instantly at higher concentrations. At lower concentrations the crystals did not diffract anymore. Mercury was also used for derivative production, as it is known to bind the O-4 position of uracil. The crystals soaked with $K_2(HgI_4)$ dissolved upon addition, $HgBr_2$ soaked crystals showed very weak diffraction.

Different cadmium salts were tested as well, as it has been reported that they can replace divalent magnesium or calcium cations (Dvir, Valera, and Choe 2010; Eriksen, Kadziola, and Larsen 2009). Similarly, to the cases above, the crystals either dissolved or the recorded diffraction data did not show any significant anomalous scattering contribution. This was also the case for selenourea, a salt that has been used for DNA phasing before (Luo 2016).

Lanthanide ions (e.g. Sm(III), Tb(III)) are known to form coordination bonds to the oxygen atoms of two adjacent phosphates. Therefore, two different iridium-salts, one samarium-salt and one terbium-salt were tested. Diffraction data from several crystals were recorded. Unfortunately, the crystals either did not diffract or diffracted badly, or the recorded diffraction data did not show any significant anomalous scattering contribution.

Hexamine cations have been used in the past to solve the phase problem of nucleic acid diffraction data as they can bind nucleic acid via direct contacts to the ammine groups of the hexamine cations. Therefore, $[\text{Co}(\text{NH}_3)_6]\text{Cl}_3$ was also used as a soaking agent at different concentrations and varying time spans. What was noteworthy is that the crystal surface did not change upon incubation with the salt, as was observed for the other soaking reagents. Furthermore, long incubation times were possible, without disturbing the crystal stability.

Derivative data were collected at P11 (DESY, Germany) and P13 (EMBL beamline at DESY, Germany). Prior to data collection fluorescence scans were performed. The native crystal that was also measured for comparison, and did not show a fluorescence peak, whereas the derivative crystal did show a peak at 7723 eV (Figure 31). The theoretical K-absorption edge for cobalt is 7709 eV. Interestingly, a second peak at approx. 7124.78 eV was detected (Figure 32). This would correspond approximately to the theoretical K-absorption edge for iron (7112 eV).

Six datasets from three different crystals were recorded at the experimentally derived K-absorption edge of cobalt at 7749 eV (1.6 Å), but will not be presented further. As anomalous signal was rather low for the respective crystals, the crystals were submerged to multi-crystal merging as described in 3.2.34.3. (data not shown).

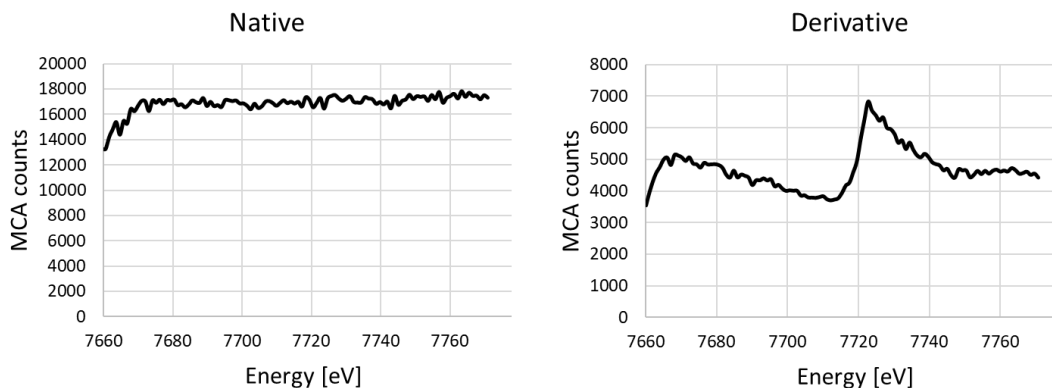


Figure 31: XANES spectrum between 7660 and 7770 eV for a native Ghrelin•NOX-B11 crystal and a derivative Ghrelin•NOX-B11 crystal soaked with 10 mM $[\text{Co}(\text{NH}_3)_6]\text{Cl}_3$. The theoretical K-absorption edge for cobalt is 7709 eV. Left: XANES spectra recorded from a native crystal. Right: XANES spectra of a Ghrelin•NOX-B11 crystal soaked with 10 mM $[\text{Co}(\text{NH}_3)_6]\text{Cl}_3$.

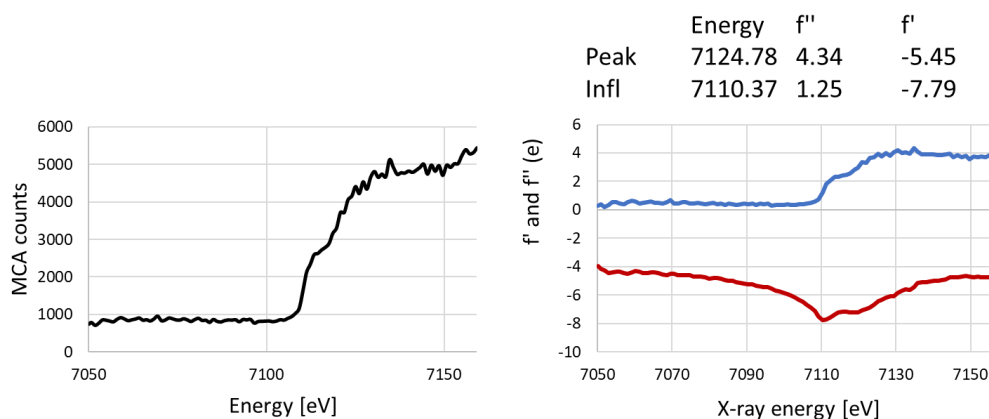


Figure 32: Absorption spectrum around the iron K-edge for a Ghrelin•NOX-B11 crystal soaked with 10 mM $[\text{Co}(\text{NH}_3)_6]\text{Cl}_3$. Left: XANES spectrum between 7050 eV and 7160 eV. The theoretical K-absorption edge for iron is 7112 eV. Right: the f'' values are plotted in blue, the f' values are plotted in red.

Furthermore, data were also collected at the experimentally derived K-absorption edge of iron at 7723 eV (1.7364 Å). Moreover, data were collected at the experimental derived inflection point of the iron K-edge at 7110.37 eV (1.743 Å) (Figure 32) and high remote at 7250 eV (1.71 Å) for a MAD experiment.

Data statistics for the three cobalt-MAD datasets are given in Table 26. The collected diffraction data at 7723 eV showed a higher anomalous signal and overall better statistics in comparison to the data collected at 7749 eV, and were thus used for phasing approaches. As from now, these following datasets are referred to as cobalt derivative data (Table 26).

Table 26: Summary of the Data statistics for the Ghrelin•NOX-B11 cobalt derivative MAD data around the experimentally derived K-absorption edge. Values for the outer shells are given in parentheses.

	Peak	Inflection	High energy remote
X-ray source	P11, PETRA III	P11, PETRA III	P11, PETRA III
Wavelength (Å)	1.736	1.743	1.71
Temperature (K)	100	100	100
Detector	Pilatus 6M fast	Pilatus 6M fast	Pilatus 6M fast
Crystal-detector distance (mm)	246	246	246
Rotation range per image (°)	0.1	0.1	0.1
Total rotation range (°)	360	360	360
Exposure time per image (s)	0.04	0.04	0.04
Space group	C2	C2	C2
a, b, c (Å)	57.90,86.31, 76.47	57.93,86.28, 76.53	57.93,86.21, 76.53
α, β, γ (°)	90, 106.39, 90	90, 106.26, 90	90, 106.16, 90
Mosaicity (°)	0.13	0.16	0.18
Resolution range (Å)	46.71-2.29	44.46-2.99	46.75-2.99
Total No. of reflections	69953	35896	35645
No. of unique reflections	15242	7243	7242
Completeness (%)	94.0 (64.9)	98.3 (94.7)	98.2 (94.6)
Redundancy	4.6 (3.4)	5.0 (4.9)	4.4 (4.7)
$\langle I/\sigma(I) \rangle$	16.3 (1.9)	19.7 (8.9)	14.3 (4.6)
R_{meas}	6.0 (69.3)	6.5 (16.8)	8.6 (32.2)
Sig_{ano}	1.138 (1.22)	1.136 (1.31)	1.18 (1.024)
$\text{CC}_{(1/2)}$	99.8 (75.6)	99.6 (99.1)	99.7 (97.6)
Overall B factor from Wilson plot (Å ²)	31.5	31.4	64.0

4.2.5.4. Substructure determination and phasing

The first step for *de novo* phase determination is the search for the location of the heavy atom (substructure) sites. The most common approaches are direct methods and Patterson methods. Parameters, that are important to test are resolution cut off, number of sites and number of trials for substructure determination. Phasing approaches were performed as described in 3.2.35.1. and 3.2.35.2.

SHELXD uses direct methods with Patterson seeding. For SAD phasing, the resolution where $\Delta F/\sigma(\Delta F)$ falls below 1.2 can be used as an approximate value for the resolution cut-off (Schneider and Sheldrick 2002). For native SAD, a rule of thumb is also to cut the data with $I/\sigma(I)$ lower than 30, but it is still advisable to test other resolution cut-offs as well. Therefore, the resolution cut-off was varied in 0.1 Å increments. Furthermore, the number of trials was varied, as it has been found before that, for large substructures, this parameter can be important. The number of sites need to be within approx. 20% of the real number of sites for successful substructure determination with SHELXD (Usón and Sheldrick 2018). In the native P-SAD case this was clear with 94 phosphorous per asymmetric unit. However, for derivative crystals precise knowledge of this number can be a bottleneck. Therefore, different numbers were tested. As an indicator for a correct substructure solution, a high CC_{all} and CC_{weak} are expected, with clustering of the unique solutions. An example for a single substructure solution is shown in (Figure 33).

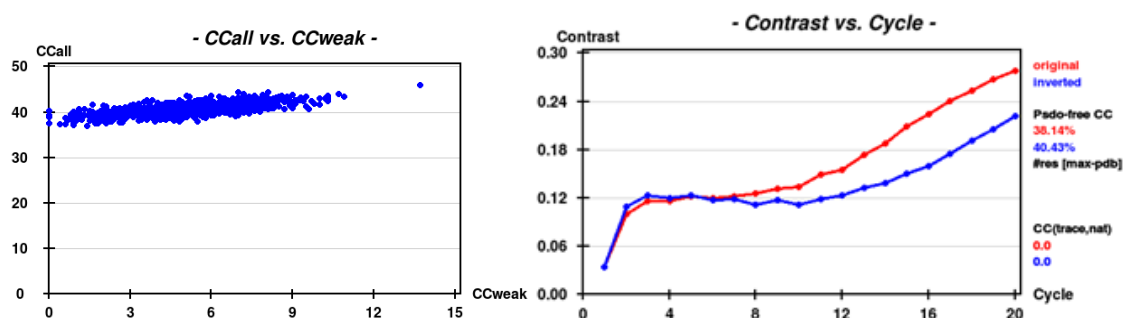


Figure 33: SHELXD/E example. Left: SHELXD for substructure determination of the P-SAD data. The data were cut to 3.28 Å, 10000 trials and the minimum distance between phosphate atoms was set to 3.5 Å. There was one solution that was not clustered with the other solutions and showed a higher CC_{weak} value (CFOM= 69.94, CC_{all} = 55.00, CC_{weak} = 14.94). Right: SHELXE during phasing coupled with density modification. Clear distinction between the original and the inverted hand was possible. The resulting electron densities were examined in coot, but none of the maps were interpretable. SHELXD/E was executed and plots were generated with the hkl2map gui (Pape and Schneider 2004).

As it is obvious, only one substructure solution dissociates from other solutions. This could indicate an incorrect solution, as usually a cluster of several correct solutions is expected when substructure solution converges. The CC_{all} was 55.00 and the CC_{weak} was 14.94. This substructure solution had 100 sites and SHELXE was used for phasing. For this the contrast is an indicator for successful phasing. As both the inverted and the original hand of the substructure atom coordinates were tested, a clear distinction between the hands should become evident after several cycles of density modification. As depicted in Figure 33, a small difference between the two maps was observed. The resulting electron densities however were similar and were not suitable for model building.

HySS (Hybrid Substructure Search) is part of the Phenix program package (Adams et al. 2010; McCoy et al. 2004; Grosse-Kunstleve, Adams 2003). HySS combines different search modes, such as direct-space and reciprocal Patterson interpretation, dual-space direct methods, Log likelihood Phaser completion, and compares the respective solutions to find a consensus model. Search parameters such as the high-resolution cutoff, are varied automatically according to the data or when initial trials fail. An indicator for a correct substructure is a CC above 0.3. The best solution found for this P-SAD data had a CC of 0.6 and found 29 putative phosphorous sites. The respective phasing with the substructure was performed using phaser EP. Some of the obtained electron density maps had some features that could potentially resemble an RNA helix (Figure 34A). Unfortunately, the map quality was not good enough for manual model building and standard automatic model building tools failed, possibly due to the unnatural L-nucleotides and associated constraints.

The calcium MAD data was analyzed as described in 3.2.35.1. Different number of sites were tested, as well as several resolution cut-offs. Unfortunately, no clear substructure could be determined.

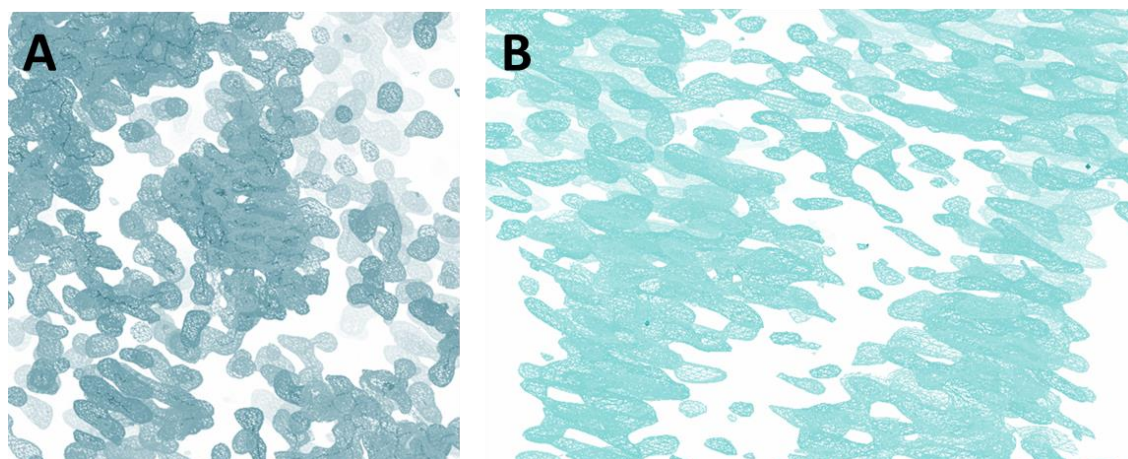


Figure 34: Example 2Fo-Fc electron density map contoured at 2.0 sigma. A: Native P-SAD example: A substructure solution was found with HySS, phasing was done with phaser EP, followed by density modification. B: Co-derivative MAD phasing example. Substructure solution and phasing was performed with PRASA and the programs implemented in the CRANK2 pipeline that is part of the CCP4i2 package.

For the cobalt derivative data, the same phasing efforts were performed as for the native P-SAD data. Furthermore, Co-MAD phasing was performed. Unfortunately, despite the electron density maps looking promising, they could again not be improved further (Figure 34B).

4.2.5.5. Racemic crystals for easier structure determination

Since standard experimental phase retrieval procedures were unsuccessful, the complex was crystallized with its mirror image complex (D-Ghrelin•D-NOX-B11). The idea behind this was to generate a racemic mixture of the complex. Evolution only favors the use of D-nucleotides and L-Amino acids. Furthermore, all biological macromolecules are chiral. Therefore, no centrosymmetric space groups are possible. For racemic crystal space groups the phase angle can either be 0° or 180° , which greatly facilitates phase determination (Matthews 2009). Wallach's rule was postulated in 1895, stating that "the densities of racemic crystals are higher and therefore are favored over the crystallization of the single enantiomers" (Wallach 1895). It was proposed, that the packing would be tighter and therefore the crystals show a higher stability and crystallization of racemic mixtures may be energetically favored. With the ability to synthesize D-proteins and L-nucleic acids, the idea occurred to transfer these findings to biological macromolecules. It has been shown for several peptides, small proteins and RNA, that indeed, centrosymmetric crystals were obtained. The crystals were also easier to obtain (Pentelute et al. 2008; Hung et al. 1999; Mandal et al. 2009; Zawadzke and Berg 1993). Furthermore,

the structure determination was facilitated, as one heavy atom replacement was enough (Zawadzke and Berg 1993) and direct methods are often possible, as the crystals tend to diffract to high resolution and the structure factors are either totally in phase or out of phase (Mandal et al. 2009).

Complexes of D-Ghrelin•D-NOX-B11 were set up identically to the Ghrelin•NOX-B11 trials and complex formation was verified with native PAGE (data not shown). High throughput crystallization trials with a 1:1 ratio racemic complex were performed. Several crystallization conditions yielded initial crystal growth. Some examples and crystallization conditions are depicted in Figure 35.

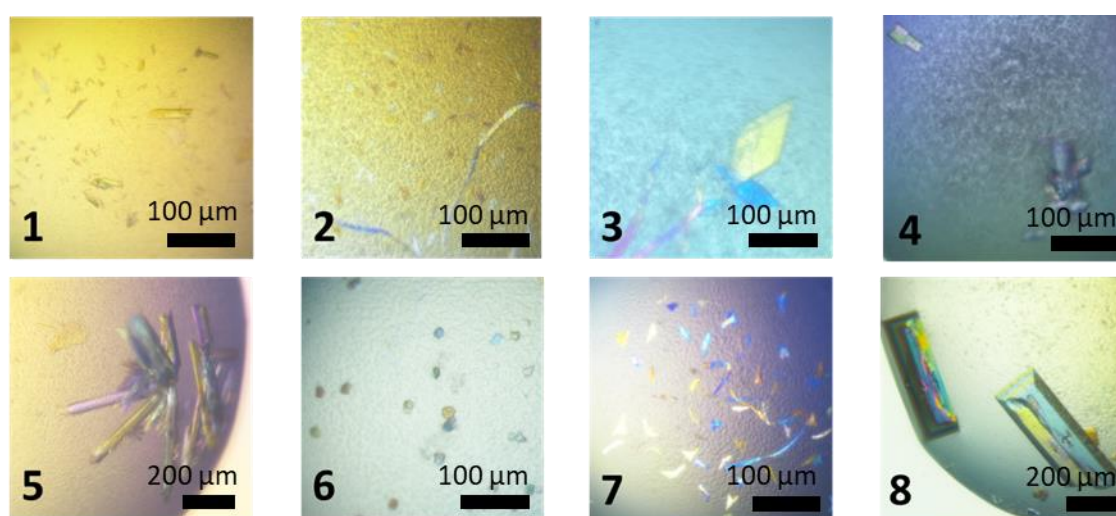


Figure 35: Crystallization approaches of Ghrelin•NOX-B11 D-Ghrelin•D-NOX-B11 racemate. 1: 0.01 M Magnesium chloride hexahydrate, 0.05 M MES monohydrate pH 5.6, 1.8 M Lithium sulfate monohydrate. 2: 0.2 M Potassium chloride, 0.01 M Magnesium chloride hexahydrate, 0.05 M MES monohydrate pH 5.6, 5% w/v Polyethylene glycol 8,000. 3: 0.005 M Magnesium sulfate heptahydrate, 0.05 M MES monohydrate pH 6.0, 5% w/v Polyethylene glycol 4,000. 4: 0.1 M Potassium chloride, 0.01 M Magnesium chloride hexahydrate, 0.05 M TRIS hydrochloride pH 8.5, 30% v/v Polyethylene glycol 400. 5: 0.2 M Calcium chloride dihydrate, 0.05 M HEPES sodium pH 7.5, 28% v/v Polyethylene glycol 400, 0.002 M Spermine. 6: 0.01 M Magnesium chloride hexahydrate, 0.05 M MES monohydrate pH 5.6, 1.8 M Lithium sulfate monohydrate. 7: 0.2 M Potassium chloride, 0.01 M Magnesium chloride hexahydrate, 0.05 M MES monohydrate pH 5.6, 5% w/v Polyethylene glycol 8,000. 8: 0.015 M Magnesium acetate tetrahydrate, 0.05 M MES pH 6.0, 1.7 M Ammonium sulfate.

Several crystals were tested for diffraction at the P13 EMBL beamline at DESY (Germany). Some crystals diffracted, although the diffraction was not sufficient for data collection. An example diffraction pattern of a crystal that grew with 0.005 M Magnesium sulfate heptahydrate, 0.05 M MES monohydrate pH 6.0, 5% w/v Polyethylene glycol 4,000 as precipitant is depicted in Figure 36.

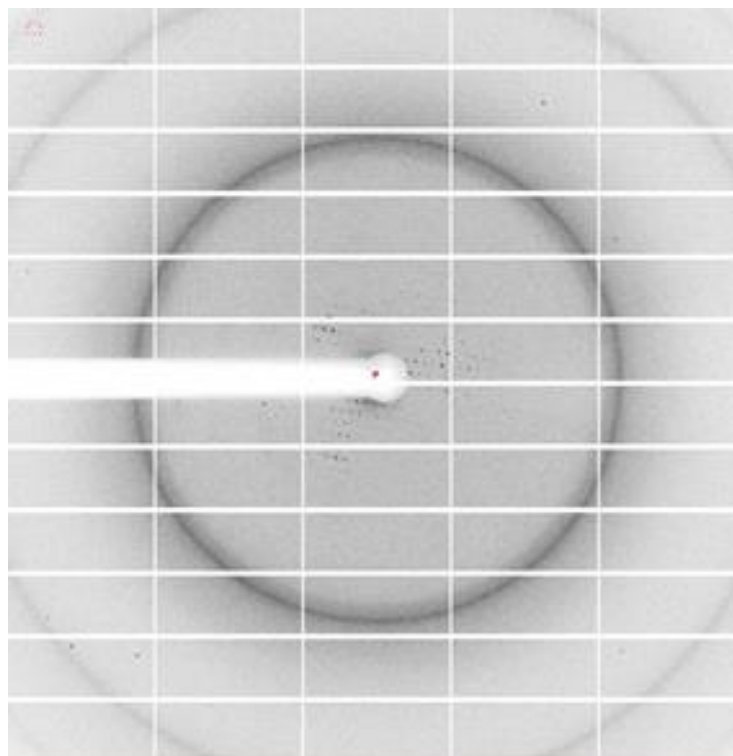


Figure 36: Diffraction image of a Ghrelin•NOX-B11 D-Ghrelin•D-NOX-B11 racemate crystal.

Two diffraction patterns were used for space group determination with iMosflm (Battye et al. 2011). The most probable space group was determined to be P3 with unit cell dimensions of 85.2, 85.2, 313.7 and 90°, 90° and 120°. The crystals were optimized as described before but it was not possible to obtain crystals with sufficient quality to collect a full dataset.

4.2.6. Molecular replacement phase retrieval approaches

4.2.6.1. Molecular replacement with the use of helical L-RNA fragments

For nucleic acid structures the building blocks are simpler compared to proteins, with only four possible nucleobases instead of 20 amino acids. Therefore, the sequence is less important than the overall fold (Marcia et al., 2013). With today's powerful phase refinement programs various secondary structure fragments can be used as search models simultaneously, e.g. several domains, nucleic acid helices, hairpins etc. Furthermore, structural elements of nucleic acids are typically closely related to idealized structural motifs (A-form Watson-Crick-helices, stable tetraloops, etc. (Antao et al., 1992)). It has been possible to solve the 142-nucleotide L1 ligase heterodimer with only RNA structural

fragments and iterative molecular replacement cycles (Robertson & Scott, 2007). This method was used several times and has shown to be useful for structure determination, if derivative production is not successful and no homologous structures are available (Robertson & Scott, 2008; Robertson et al., 2010; Zhang et al., 2013). It was shown that it is possible to solve unknown RNA and RNA-protein complex crystal structures, even if no information about the ternary structure, nor the sequence are known. The sequence itself is not important for the overall fold of the RNA, as it consists of only four, rather similar building blocks, in comparison to the structurally more diverse amino acid residues. Furthermore, secondary structure predictions for RNAs are pretty decent, and therefore the length of helices can be predicted with high confidence.

The secondary structure of NOX-B11 was predicted with the Vienna RNA Websuite (Figure 37) (Gruber et al. 2008). According to the prediction, NOX-B11 contains a stem with 8 base pairs, a larger bulge and another short stem with 4 base pairs, followed by a small loop. The minimum free energy was calculated to be -8.73 kcal/mol. L-helical fragments of different sizes (4 bp, 8 bp) were obtained from the crystal structure of an L-RNA helix (1R3O) (Vallazza et al. 2004).

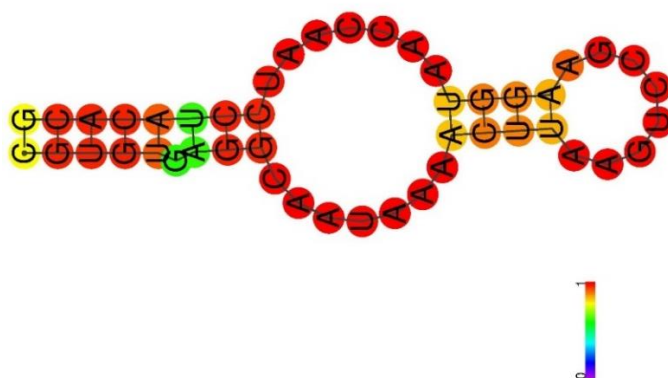


Figure 37: Secondary structure prediction of NOX-B11 created with the Vienna RNA Websuite (Gruber et al. 2008).

The cobalt derivative peak dataset was used as the experimental data for this case, as it has the best overall statistics and highest resolution. The initial molecular replacement search with one 4 bp and one 8 bp helical fragment had a TFZ of 4.5. The TFZ describes the Z-score of a translation function, with the Z-score being the number of deviations exceeding the mean value. A value above seven most likely indicates a correct solution. Figure 38 displays the electron density map that was obtained after the first MR and refinement cycle.

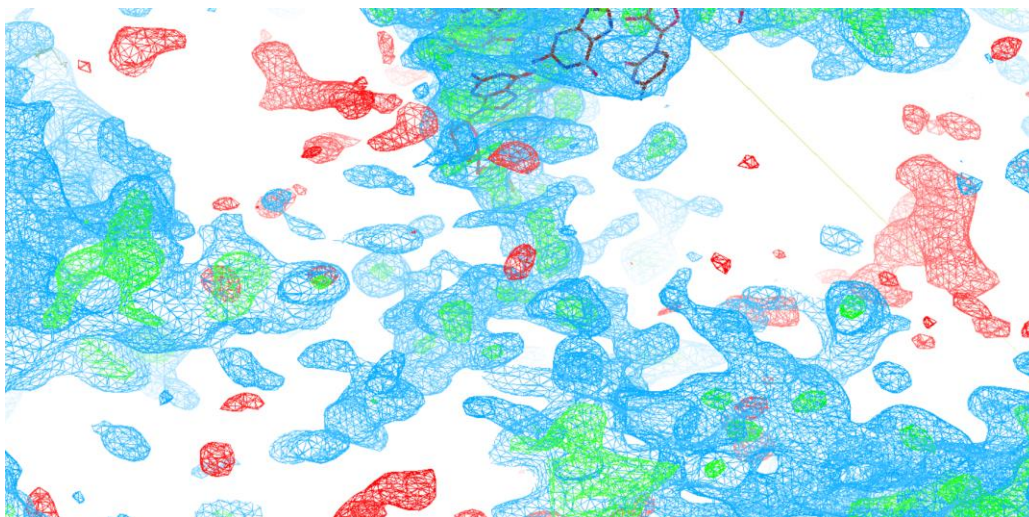


Figure 38: 2mFo-DFc electron density map contoured at 1σ with the mFo-DFc difference density map contoured at 3σ after one cycle of molecular replacement with helical fragments. The 2mFo-DFc electron density maps is depicted in blue. The mFo-DFc difference density map is depicted in green and red. The electron density was visualized with COOT (Emsley and Lohkamp 2010).

In addition to the electron density around the placed nucleotides, additional density became visible that indicated some success. Thus, several cycles of MR were performed (as described in chapter 3.2.36.1.) and the obtain electron density maps are shown in Figure 39.

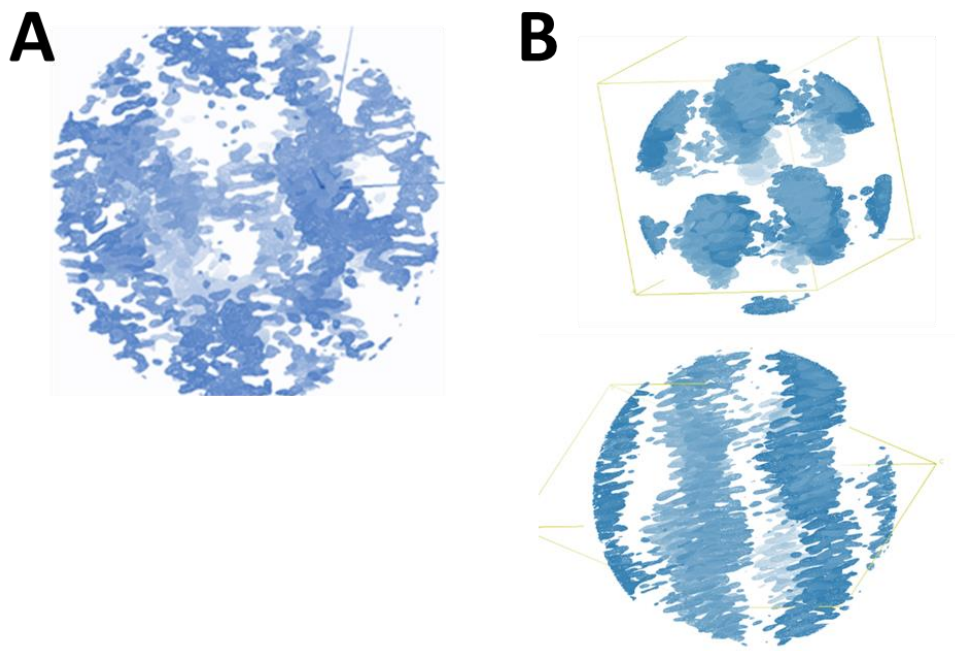


Figure 39: 2Fo-Fc electron density maps obtained with the molecular replacement approach using helical L-RNA-fragments as the search model (Robertson and Scott 2008). A: Final 2Fo-Fc electron density map after five cycles of molecular replacement and manual editing in Coot (Emsley and Lohkamp 2010). B: “Pseudo-MIR” 2Fo-2Fc electron density map using the rough phase estimates from the molecular replacement solution as quasi experimentally derived phases. The electron density maps are contoured at 2σ and were visualized in Coot (Emsley and Lohkamp 2010)

The electron density map that was calculated with the “pseudo-MIR” derived phases looked different from the biased MR map, but the quality was not sufficient for manual model building. The electron density map had some continuous helical features, which is common for nucleic acid crystal formation, but the quality was too low to identify sole nucleotides or a continuous phosphate backbone for manual model building.

4.2.6.2. Molecular replacement with generated 3D models

Since no atomic coordinates for NOX-B11 are known, the generation of a theoretical 3D model, that is as close to the actual structure as possible, for molecular replacement would maximize the probability of successfully estimating the real phases. The available software programs are, however, all implement natural D-nucleotides, which makes the generation of a large pool of L-nucleotide models cumbersome, as the coordinates would have to be mirrored one by one for each model, as well as modifying the natural restraints. Hence, SAXS data were measured for the D-RNA, under the assumption, that the overall fold of the D-RNA would be the same, as has been shown before with CD measurements (Szabat et al. 2016). The SAXS data also revealed a similar R_g and D_{max} (data not shown).

The secondary structure of NOX-B11 was predicted with the MC-Sym pipeline (Parisien and Major 2008). 1000 different 3D models were generated using the R_g that was derived from the SAXS data as a restraint. In Figure 40, the superposition of 100 different 3D models is shown, demonstrating the structural variations of the different structures.

The atomic coordinates of the models were then compared with the experimental SAXS data. Figure 40 shows the χ^2 -values of the models in comparison to the experimental data. The smallest χ^2 -value was 2.6 and the highest was 42.3.

The coordinates of the best model were converted to generate the mirrored version and this was used as the search model for molecular replacement with Phaser (McCoy et al. 2007). Since no MR solution could be found, the nucleobases were removed and only the phosphate-ribose backbone was used as the search model. The electron density map was inspected and some positive electron density was visible next to the ribose of some bases (Figure 41).

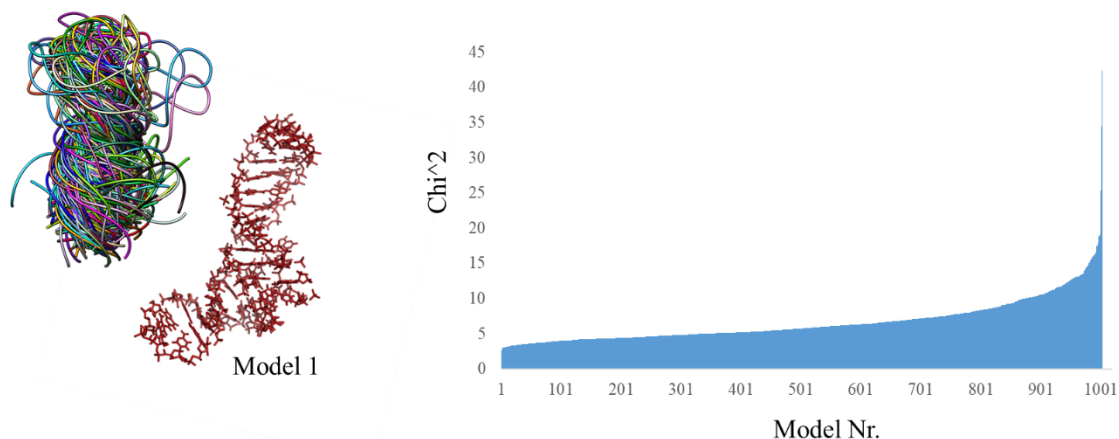


Figure 40: Comparison of the generated 3D models with the experimental SAXS data. Left: superposition of 100 different 3D models generated with the MC-Sym pipeline (Parisien and Major 2008) and from model 1 alone, which represents the model, that had the best fit against the experimental SAXS data. The image was created using UCSF Chimera (Pettersen et al. 2004). Right: The fit of the 3D models with the experimental data was calculated with CRY SOL (Svergun, Barberato, and Koch 1995) and the resulting χ^2 values were ordered by size.

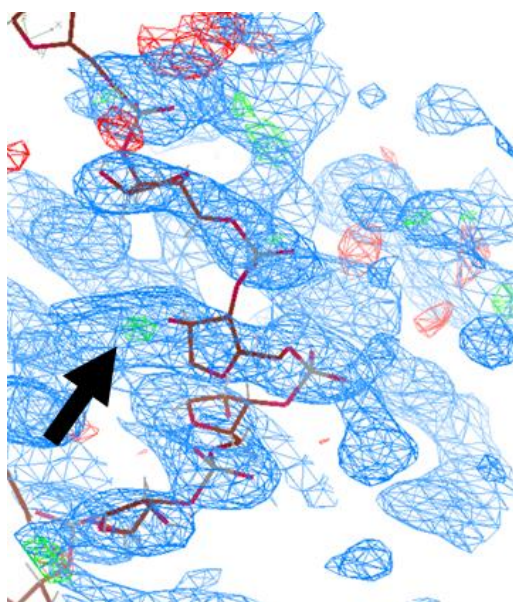


Figure 41: 2mFo-DFc electron density map and mFo-DFc difference density map, calculated from the molecular replacement solution using the backbone of model 1. The electron density is calculated applying Coot (Emsley and Lohkamp 2010). The 2mFo-DFc electron density map is depicted in blue and contoured at 1σ . The mFo-DFc difference density map is contoured at 3σ and depicted in green (positive) and red (negative).

The nucleobases were manually added consecutively, with refinement cycles in between. Unfortunately, the electron density did not improve and the R values did not decrease, therefore a structure solution was not possible.

5. Discussion

5.1. Structural and biochemical analysis of MAP FurA

Even though, Fur-like proteins are common in every microbial kingdom, their functions vary vastly from the first discovered iron dependent gene repression. This also includes the activation of gene expression, oxidative stress regulation and virulence, and gene regulation independent from metal binding (Butcher et al. 2012; Carpenter et al. 2013; Carpenter, Whitmire, and Merrell 2009). MAP FurA is a putative metal-dependent repressor, that regulates the peroxide-inducible expression of oxidative stress genes and virulence associated genes. Here, the structural assembly of MAP FurA under metalized, metal deprived and oxidation conditions were studied, to get further insights into the mode of action of MAP FurA in *Mycobacterium avium* ssp. *paratuberculosis*.

In terms of this investigations, the purification of large, pure amounts of MAP FurA was established. The full-length MAP FurA was used without a tag, making purification effective, since no tag splicing step needed to be performed.

With the aid of low-resolution structures, that were obtained via SAXS diffraction analysis the open and closed conformations of MAP FurA were observed, similar to PerR_{BS} (Traoré et al. 2006, 2008) (Figure 12). The open conformation occurs if MAP FurA is either oxidized or is treated with chelating agents. This suggests that, upon oxidative stress the bound metals get displaced from the active form of the protein, resulting in dissociation of MAP FurA from the DNA. This would also suggest, that apo-MAP FurA is unable to bind to the DNA. A putative model of specific gene regulation is shown in Figure 42. However, RNA deep sequencing analysis revealed that MAP FurA is involved in the regulation of virulence associated genes. qRT-PCR results indicated, that expression of the virulence associated genes *0847* and *0047c* is neither induced by metal deprivation of MAP, nor by oxidative stress (Eckelt et al. 2015), negating the SAXS results. This suggests that MAP FurA is either regulating gene expression via direct DNA sequence binding in its apo-form, or this might also indicate an indirect regulation. The promoter region of *0047c* does not contain a conserved fur box binding region, whereas for *0874*, a conserved binding region was found (Eckelt et al. 2015). It has also been shown for other Fur homologs, that they are able to bind DNA in their apo-forms (Butcher

et al. 2012; Ernst et al. 2005; Palyada, Threadgill, and Stintzi 2004). This needs to be addressed in further studies, either by Electrophoretic Mobility Shift Assay (EMSA) experiments or other interaction studies. It is also possible, that in the obtained apo-SAXS structure the structural zinc is also missing, hence inducing a conformational change of MAP FurA and a possible fourth MAP FurA conformation, that is still able to bind the DNA.

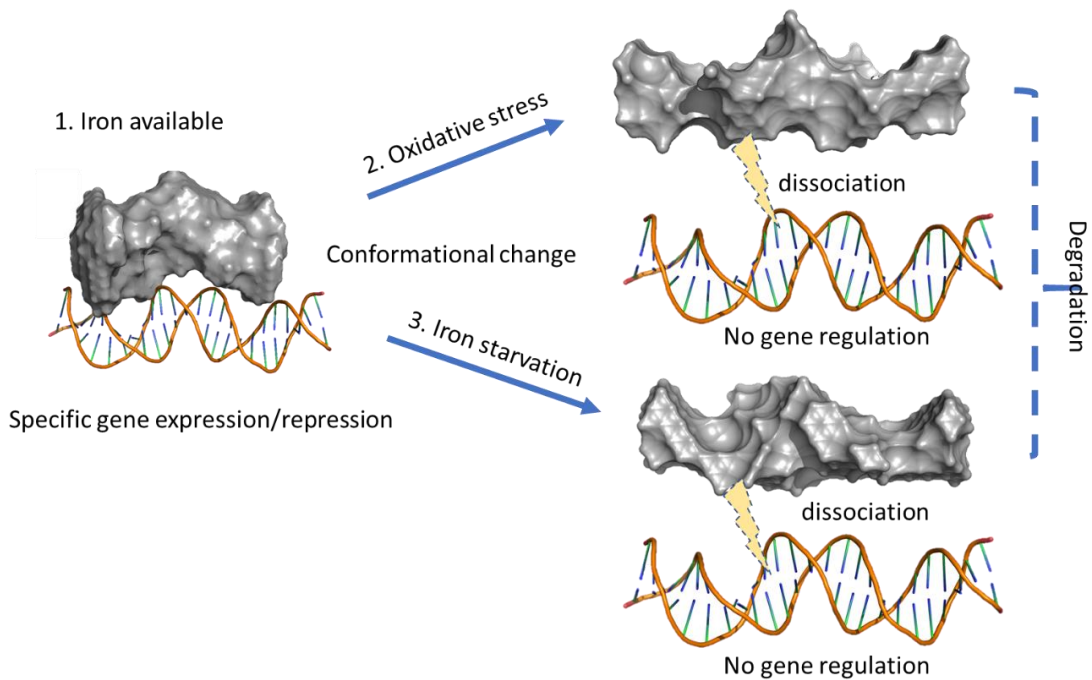


Figure 42: Putative gene regulation of MAP FurA under different stress conditions, as indicated by the obtained SAXS results. If enough iron is available, MAP FurA is either inducing or repressing gene expression of specific genes via binding to specific DNA binding motifs. Upon oxidative stress, a conformational change into the oxidized open form takes place, leading to dissociation of the protein from the DNA. Upon iron starvation, the metal ion gets misplaced from the protein, inducing a conformational change into the open apo-form of MAP FurA. This results in the dissociation of the protein from the DNA and gene regulation is hindered. The open forms could then be degraded by a protease until iron is available again or peroxide levels decreased again. Dashed lines indicate putative processes, that were not studied yet. The images were generated with the PyMOL molecular graphics package (The PyMOL Molecular Graphics System, Version 1.8 Schrödinger, LLC (Schrödinger, LLC 2015)).

MAP FurA adopts the open conformation when the protein is in its non-oxidized form. This indicates, that upon oxidative stress, MAP FurA undergoes a conformational change leading to dissociation from the DNA, enabling the stop of the gene regulation and hence adaptation to environmental changes.

The overall shape similarity of MAP FurA to *Magnetospirillum gryphiswaldense* MSR-1 Fur-Mn²⁺ could indicate a similar regulation mechanism for MAP FurA (as described in chapter 4.1.5). In further studies, the complex formation of MAP FurA to different promoter sequences should be analyzed to study the binding mechanism of MAP FurA DNA binding with regards to the availability of metals or under oxidative stress. Information from native MS, SAXS or with FPLC experiments could elucidate, if positive and negative regulation may be facilitated by the binding of one or two homodimers of MAP FurA to the cognate promoter sequence. Till now, it has not been possible to detect any DNA binding of MAP FurA with EMSA. This is exacerbated by the fact, that no conclusive consensus sequence for MAP FurA binding could be found by sequence analysis (Eckelt 2014).

CD measurements revealed significant conformational changes of MAP FurA after treatment with different reagents (see chapter 4.1.6.). Firstly, the untreated sample had large amounts of α -helices (~47%) and ~18.6% β -sheets. A drastic decrease of the α -helical portion was observed upon iron addition. For the redox sensing Fur homologs, a shift towards lower α -helical protein portion was detected as well (PDB entries: 4raz, 3f8n (Deng et al. 2015; Jacquamet et al. 2009)). However, there was no change observed in the β -sheet content of the proteins. This might indicate a major conformational change for MAP FurA, that differs from PerR_{BS} and *Magnetospirillum gryphiswaldense* MSR-1 Fur-Mn²⁺. After H₂O₂ treatment a further conformational change was observed. This validates the proteins sensitivity towards oxidative stress on a structural level. This further conformational change could lead to the dissociation of the MAP FurA dimer from the DNA, if significantly high amounts of H₂O₂ are threatening the cell.

It was further shown, that upon peroxide stress a dissociation of PerR_{BS} dimer is induced (Traoré *et al.*, 2006). This is not the case for MAP FurA, as there is no rapid dimer dissociation after treatment with H₂O₂ (see chapter 4.1.7.). Even after 6 h, where PerR_{BS} was completely monomeric, only a small fraction of the whole MAP FurA protein was monomeric, whereas most of the protein was dimeric. Moreover, several other peaks were detected, indicating proteolytic processes. It seems, that some regulatory mechanisms between PerR_{BS} and MAP FurA differ, despite their homology and more information about those processes could elucidate the mode of action of MAP FurA in response to host-induced defense mechanisms.

Several Fur homologs are able to bind different metals with different affinities to further broaden the regulation abilities. Therefore, the influence of different metals on MAP FurA were examined (see chapter 4.1.8). Thermofluor analysis revealed, that the protein does not show severe differences relating to the melting temperature T_m . Only the addition of iron increased the T_m slightly, which corresponds to the proposed binding of iron to MAP FurA for it to be in its active state and is maybe needed for the stabilization of the dimer. EDTA addition decreased the stability of MAP FurA. This could be related to the fact, that in PerR_{BS}, the demetallized apo-PerR_{BS} gets degraded by the LonA protease and is hence useless (Ahn and Baker 2016). Binding studies of MAP FurA to zinc, iron and manganese cations revealed that MAP FurA is able to bind all three metals, as revealed by SDS-PAGE (see chapter 4.1.9). This further suggests that MAP FurA not only uses iron as a cofactor, but is also able to bind manganese ions as well. In *Bacillus subtilis*, the addition of manganese to the growth media led to a repression of the PerR_{BS} mediated gene regulation to oxidative stress, whereas the addition of iron caused the normal expression profile that occurs, if oxidative stress is present (Fuangthong et al. 2002). Therefore, under physiological cytosolic conditions, manganese binds to the protein and genes are differentially regulated. If oxidative stress occurs, iron levels rise, iron binds to PerR_{BS} and gene expression is altered. The results for MAP FurA indicate, that the regulation might be similar in MAP. It was shown, to my knowledge for the first time, that a mycobacterial Fur protein is able to bind manganese. So far it could only be shown for FurA from *Mycobacterium tuberculosis* that it can bind zinc and iron (Lucarelli 2006). Interestingly, the unoxidized portion of MAP FurA was able to bind to zinc ions. This might indicate, that the essential structural zinc ions, like they are present in PerR_{BS}, are not bound to MAP FurA when treated with metal chelators. An apo-form lacking any metal ion has previously been reported (Deng et al. 2015). It must be noted, that Fur proteins routinely show two bands when resolved via SDS PAGE (Lee and Helmann 2006). It was shown for PerR_{BS}, that the lower migrating band contains the structural important zinc ion, whereas the higher migrating band does not. This effect was enhanced if the protein was pretreated with EDTA or high levels of H₂O₂ (Lee and Helmann 2006). To further investigate the structural changes more thoroughly, data at atomic resolution would be beneficial. Crystallization trials led to some promising conditions, nonetheless obtaining crystals suitable for X-ray diffraction analysis failed (see chapter 4.1.3).

Interestingly, the condition that produced microcrystals (Figure 8C) was only slightly modified from the crystallization of the MAP FurA homolog from *Magnetospirillum gryphiswaldense* (Liu, Chen, and Wu 2012). Unfortunately, optimization of crystals failed so far. Further optimization of the protein quality, e.g. the addition of additives or a further purification step could be beneficial. Furthermore, the oxidation status of the protein could be a problem. Most of the homologs are metal uptake regulators and not redox sensing proteins and hence the crystallized version is oxidized, which does not seem problematic for crystallization success in those cases. Citric acid is a metal chelator, resulting in the formation of apo-FurA or a mixture of oxidized and unoxidized protein. The purification under anaerobic conditions could be tried to circumvent the mixture of protein species over time. Furthermore, the slow transition from MAP FurA dimer to monomer upon metal deprivation could lead to inhomogeneities, hindering high quality crystal formation.

5.2. Structural insights into Spiegelmer-Peptide complexes

5.2.1. Ghrelin•NOX-B11 characterization and crystallization

Ghrelin is often described as one of the key players in the regulation of energy metabolism and food uptake. Moreover, the peptide is associated with many physiological functions, such as aging, memory, motivation and several other important functions, rendering it to be an important and an interesting target for studies (Asakawa et al. 2001; Masuda et al. 2000; Szentirmai et al. 2006; Tolle et al. 2002; Weikel et al. 2003; Cai et al. 2013; Druce et al. 2005; Jerlhag et al. 2006, 2007; Overduin et al. 2012; Skibicka et al. 2012). An aptamer inhibiting ghrelin binding its receptor could be used in therapeutic applications, e.g. by downregulating circulating acyl-ghrelin levels in insatiable patients with Prader-Willi-syndrome. Furthermore, this aptamer could be used for basic biochemical research.

In this study it was shown, that the 47 bp Spiegelmer shows an exceptional stability in an RNase abundant environment (see chapter 4.2.2.). The L-RNA nucleotides are not susceptible to any degradation machinery for a long time before being degraded. NOX-B11 and the Ghrelin•NOX-B11 complex were stable at room temperature, which was revealed by a monodisperse particle distribution during *in situ* DLS measurements, that were ongoing for 40 days.

Furthermore, the *in situ* DLS measurements revealed a conformational change of the L-RNA, since a decrease of the R_h was detected right after ghrelin addition (see chapter 4.2.2.). This was also verified with SAXS analysis (see chapter 4.2.3.). Here, the low-resolution *ab initio* model of NOX-B11 shows an elongated molecule, whereas the complex had a more compact shape. It is likely, that the RNA refolds upon ghrelin binding. There are only a few aptamer structures available alone or in complex with their binding partners. It has been demonstrated that aptamers may change their conformation upon complex formation, but several features also remain (Reiter et al., 2008; Davlieva et al., 2014). In other studies, the structure does not change significantly (Jaeger et al., 1998; Padlan et al., 2014) but some loss in flexibility was observed (Padlan et al., 2014). This could also apply for the Ghrelin•NOX-B11 complex, as neither ghrelin, nor NOX-B11 could be crystallized individually.

Crystallization of the complex was successful after cumbersome screening and optimization efforts were performed. Over 200 different reagents were tested, but only one condition produced microcrystals (see chapter 4.2.4.). This might indicate, that albeit being stable in the complex buffer for an extended time period, the introduction of other chemicals, such as high salt concentrations, heavy atoms and additives such as spermine, is critical for the complex integrity. The crystallization condition for the complex is almost identical to the complex buffer composition, apart from the addition of PEG4000. With multiple cycles of iterative seed stock preparation and streak seeding, crystals that were suitable for X-ray analysis could be produced.

The results indicate that Spiegelmers are interesting molecules with extraordinary stability which classifies them to be the appropriate molecules for different applications, e.g. to study interactions, enhancing the stability of proteins, or restrain the flexibility of proteins. As they are synthesized chemically, modifications can be made according to the intended application.

5.2.2. Ghrelin•NOX-B11 phasing approaches

Extensive experimental approaches were performed in order to solve the phase problem, as there is no structural information available about NOX-B11 and ghrelin. The first approach was to use the inherent phosphorous atoms of NOX-B11 as anomalous scatterers (see chapter 4.2.5.1.). This native P-SAD approach holds several advantages,

but also has some pitfalls. The biggest bottlenecks are the relatively low anomalous signal, resolution of the data, noise, crystal size, low symmetry space groups, multiplicity and the number of substructure atoms. All of these detrimental criteria were unfortunately fulfilled in the presented approach.

In this study it was shown, that multi-crystal merging for Ghrelin•NOX-B11 crystals measured at P13 (EMBL, DESY, Germany) led to an overall increase in the $I/\sigma(I)$, multiplicity, resolution and anomalous signal strength ($\Delta F/\sigma(\Delta F)$) in comparison to single crystal data. It is noteworthy, that the $\Delta F/\sigma(\Delta F)$ in cluster 9 and 7 is higher than $\Delta F/\sigma(\Delta F)$ from all crystals merged together, demonstrating the importance of multi-crystal analysis prior to merging (see chapter 4.2.5.1.). The $\Delta F/\sigma(\Delta F)$ in cluster 9 was 1.657 overall and 0.9 in the highest resolution shell and CC_{ano} was 60. The critical limit of $\Delta F/\sigma(\Delta F)$ is 0.7, where values below can't be deciphered from noise.

To further enhance the f'' values for phosphorous, data were collected at the I23 beamline at Diamond, United Kingdom, at 4.5 keV (see chapter 4.2.5.1.). As described earlier, resolution limits of the crystals varied vastly and unfortunately crystals diffracted only up to 3.2 Å. Surprisingly, albeit measurements taking place at longer wavelengths, the $\Delta F/\sigma(\Delta F)$ was lower in both of the Diamond datasets with values of 1.21 and 1.23 respectively (Table 24), in comparison to the best single crystal from P13 with a value of 1.64. This could be due to the absorption effects that are occurring at such long wavelengths. A further increase in absorption effects could arise from excess cryo solution present around the crystals, and the solvents that are present inside the macromolecule crystal. This could explain why the anomalous signal was lower in the data collected at I23. This might also indicate that it is important to find the balance between enhancing the anomalous signal at shorter wavelengths, closer to the phosphorous K-edge, and the related increase in absorption effects that can negatively affect the data quality.

Despite the good data statistics and the high anomalous signal from the intrinsic anomalous scatterers, structure solution failed unfortunately. As stated before, reasons for this could be the low symmetry space-group, the rather large substructure, with 94 phosphorous atoms, and the medium resolution. Highly redundant data are harder to obtain, when the symmetry is low as in space group C2, as well as the determination of the substructure is more complex in low symmetry space groups. A high number of

substructure atoms is also detrimental, as the substructure atoms are determined with direct methods or Patterson methods. As more atoms needed to be searched for, more variables come into play and the determination gets more complex. The Cas9-RNA-DNA complex, which was solved with native SAD, is comparable to Ghrelin•NOX-B11 in terms of the crystal space group and the number of atoms in the substructure (phosphorous and sulfur atoms), which is 144 in this case (Olieric et al. 2016). Here, the structure was solved with a multiplicity of 156.7, which is higher than the multiplicity of the merged Ghrelin•NOX-B11 P-SAD dataset, which has a multiplicity of 73.4. Cluster 9 has a lower multiplicity with 43.7. The $\Delta F/\sigma(\Delta F)$ and CC_{ano} values otherwise were lower with 1.466 and 44 in comparison to 1.657 and 60, respectively. The $I/\sigma(I)$ values are comparable with 30.38 for Cas9-RNA-DNA versus 25.83 for Ghrelin•NOX-B11. A comparison between the data statistics from Cas9-RNA-DNA and Ghrelin•NOX-B11 is given in Table 27. Therefore, simply collecting more data to increase the redundancy of the Ghrelin•NOX-B11 data could potentially have led to a structure solution. This was however not possible due to the limited amount of NOX-B11 that was available for this study and lack of beamtime at designated long-wavelength beamlines.

In the case of Cas9-RNA-DNA, the substructure was determined with SHELXD and only 65 out of the 144 sites were searched for. The CC_{all} and CC_{weak} values were very low with approx. 25 and 12, respectively. Substructure refinement and completion was used to find the other sites that were then used for phasing. In this case, a clear hand separation during density modification indicated a correct solution. Furthermore, chain-tracing was applied to refine the phases. It is noteworthy, that the structure had already been solved before and the substructure sites were therefore checked for their correctness. This was unfortunately not possible for Ghrelin•NOX-B11, where no part of the structure is known.

Table 27: Data statistic comparison of datasets collected in this study and example dataset Cas9-RNA-DNA.

	Cas9-RNA-DNA (Olieric et al. 2016)	Cobalt_data	P13_merge P-SAD (Cluster9)	Best P-SAD	Best native	Diamond
Crystals	3	1	9	1	1	2
Resolution	50-2.2	44.5-2.3	40-2.7	40-2.8	50-2.65	40-3.2
Space Group	C2	C2	C2	C2	C2	C2
No. of reflections	16157127	69953	866165	110331	34327	180681
No. of unique reflections	205825	15242	19812	16029	10876	13511
Multiplicity	156.7	4.6	43.7	6.9	3.16	13.37
Completeness	99.3 (95.8)	94.0 (64.9)	100.0 (99.7)	90.6 (78.0)	93.3 (70.8)	99.9 (99.6)
$I/\sigma(I)$	30.38 (1.88)	16.3 (1.9)	25.83 (5.09)	18.49 (1.79)	20.7 (2.08)	7.49 (2.76)
R_{meas} (%)	14.1 (135.0)	6.0 (69.3)	14.6 (87.5)	8.2 (88.4)	3.9 (38.7)	15.7 (50.7)
$R_{p.i.m}$ (%)	1.1 (24.1)	3.6 (22.3)	2.2 (24.2)	2.6 (26.2)	2.6 (14.7)	3.9 (24.1)
$CC_{1/2}$	100 (62.1)	99.8 (75.6)	99.8 (99.3)	99.9 (95.6)	99.9 (96.6)	99.5 (99.7)
$\Delta F/\sigma(\Delta F)$	1.477	1.138	1.657	1.645	0.681	1.213
CC_{ano} (%)	44	35	60	59	-15	37

Another example where native S-SAD phasing was feasible, is for the TorT-TorSs protein complex (Liu, Zhang, and Hendrickson 2011). This complex also crystallizes in the crystal space group C2 and the high-resolution limit was comparable to Ghrelin•NOX-B11 diffraction data with 2.8 Å. Data were collected from 13 crystals, resulting in a multiplicity of 211.3, a $\Delta F/\sigma(\Delta F)$ of 1.35 and a CC_{ano} of 52. In this example, the multiplicity is also the only value that is higher as in the merged data from P13. The substructure was substantially smaller comprising only 31 substructure sulfur atoms. In this case, model building was also applied to refine the phases and to validate the phasing success. Again, more data could have improved the multiplicity in the Ghrelin•NOX-B11 case, but was not possible to collect due to the limited availability of NOX-B11. Furthermore, as mentioned previously, the lower number of substructure atoms substantially aided substructure solution compared to Ghrelin•NOX-B11.

Native P-SAD was only successful twice to date for nucleic acid structures with phosphorous being the sole anomalous scatterer (Dauter and Adamiak 2001; Raiber et al. 2015). The substructures were significantly smaller with 12 and 11 phosphorous atoms per molecule respectively. Moreover, the Z-DNA data had an exceptional high-resolution limit of 0.6 Å (Dauter and Adamiak 2001). For larger nucleic acid molecules and for diffraction data at intermediate to low resolution limits, P-SAD phasing is apparently much more difficult.

It was proposed that problems that arise with phosphate phasing are linked to the relative thermal motion of the phosphorous atoms compared to the other atoms (Harp et al. 2016). This effect is not present in the sulfur atoms of proteins, where the B-factor of S-atoms is in general lower than the other non-hydrogen atoms, which is why they are useful for native S-SAD phasing (Shen et al. 2003; Harp et al. 2016). As the B-factor increases with lower resolution limits, the success of P-SAD phasing might be, besides the multiplicity, tightly linked to the resolution limits as well (Harp et al. 2016).

For multiple cases of native S-/P-SAD, a clear hand separation was only possible after several cycles of model building (Olieric et al. 2016). It is therefore difficult to depict whether the bottleneck for successful structure solution for Ghrelin•NOX-B11 was the substructure determination or the phase retrieval itself.

It is also not clear, if more data would aid structure solution, by mitigating systematic errors in the data, as the multiplicity seems to be more important than other data statistics. Furthermore, the generation of crystals with higher resolution would be beneficial.

The second approach was to measure diffraction data close to the calcium K-absorption edge (3.07 Å, 4038.57 eV) (see chapter 4.2.5.2.). Surface plasmon resonance (SPR) measurements have shown, that calcium is needed for complex formation and calcium was hence included in the complex buffer (Helmling et al. 2004). Therefore, bound calcium atoms are likely, as has been reported for the two other Spiegelmer structures as well (Yatime et al. 2015; Oberthür et al. 2015). The data statistics indicate some potential absorption effects, as the R_{meas} was higher in both the peak dataset (14.4) and the inflection dataset (13.5), with data cut to a resolution of 3 Å, in comparison to the far remote data set (9.0), which was recorded at 2.48 Å with data cut at 2.9 Å. Interestingly, the overall B-factor derived from Wilson statistics was smaller in the peak and inflection data, with values of 31.1 Å² and 35.0 Å², respectively, in comparison to the far remote dataset with 54.7 Å². This could be explained by the higher energy the data were recorded. The anomalous signal from the peak data was 1.68, which exceeds the value of the merged P-SAD data with 1.657. However, both the Ca-MAD and Ca-SAD structure solution attempts failed. Since the search number of anomalous scattering atoms is important for substructure determination, the presence of various types of anomalous scattering atoms could be problematic.

The data collected at the calcium K-edge showed that data collection at the edge is possible, with some absorption effects, with an increase in the anomalous signal. On the one hand, the collection of more data at this wavelength from multiple crystals could enhance the anomalous signal further and would aid in structure solution. On the other hand, the high resolution is limited to 3.1 Å due to the experimental set-up constraints at the P13 beamline (EMBL, DESY, Germany). Low scattering angles are especially important, as the anomalous signal is the lowest due to minimal absorption.

The third phasing approach attempted in this work was the conventional derivative production approach with heavy atom soaking solutions (see chapter 4.2.5.3.). Numerous different soaking solutions were tested in order to generate a derivative crystal, that did not dissolve upon heavy atom addition and still yielded good diffraction. Both classical solutions and chemicals, especially those routinely used for DNA/RNA-soaking, were

tested. It was evident, that the complex itself is very delicate towards the introduction of ions, as the crystals were really fragile and often dissolved instantly upon heavy atom addition. The macromolecule interacts with the heavy atoms and is dependent on a set of parameters, such as the charge of the atom, the ligands that coordinate the metal, residues and backbone atoms of the protein that are free for interaction, and reactions with the crystallization cocktail. The binding affinity of the heavy atom must be higher towards the macromolecule instead of towards the buffer components in the crystallization drop, or any of the ligands used to purify the heavy atom ions. Since ghrelin is a small peptide, whose surface is most likely covered by NOX-B11 to a large degree, it is possible that ghrelin's side chains and residues are not accessible, and that if a heavy atom interacts with ghrelin, this destabilizes the complex. Furthermore, the negatively charged phosphate backbone of NOX-B11 is detrimental for derivatization, as anions are repelled. The only solution tested that produced derivative crystals was cobalt hexamine chloride. Hexamine cations have been used for phasing RNA structures several times before (Batey, Gilbert, and Montange 2004; Cate et al. 1996; Cochrane, Lipchock, and Strobel 2007; Toor et al. 2008; Pfingsten, Costantino, and Kieft 2006; Peselis and Serganov 2012; Smith et al. 2009; Garst et al. 2008; Kazantsev et al. 2005; Costantino et al. 2008).

It has been reported, that G-U wobble pairs are a potential binding site for cations, e.g. hexamine cations (Masquida and Westhof 2000; Varani and McClain 2000; Cate and Doudna 1996; Colmenarejo and Tinoco 1999; Montange and Batey 2006; Stefan et al. 2006). In NOX-B11, one G-U wobble base pair is likely to be present with regards to secondary structure predictions. The C5a•NOX-D20 complex, was phased with Os(NH₃)₆ molecules, as other extensive phasing efforts were unsuccessful (Yatime et al. 2015).

In the work presented here, the Ghrelin•NOX-B11 crystals were soaked with Co(NH₃)₆ over-night and then back-soaked prior to cryo protection and data collection. Fluorescence screens were performed to identify cobalt in the crystals. An X-ray absorption edge was detected at the expected energy (1.6 Å) for the cobalt K-absorption edge, which was not visible in native, unsoaked, crystals (Figure 31).

Since the anomalous signal was rather low, it can't be excluded completely, that cobalt was not covalently linked to the L-RNA, but was present in trace amounts in the solvent surrounding the crystal. This could occur either if the backsoaking time was not long enough, since the cryo condition did contain glycerol, hence being viscous. Further the

cobalt could have bound at different positions to the L-RNA, and not consistently across molecules, as required for successful substructure solution. Surprisingly, a second absorption edge was discovered at the X-ray energy corresponding to the iron K-absorption edge, although no iron was present in the buffer, nor in the crystallization cocktail (Figure 32). It would be possible, that traces of iron were present in one of the synthesized compounds, plastic or glassware or in one of the used buffer components. If iron would be present in the crystal structure this would also be an explanation why derivatization was difficult, as the introduction of other ions could impede structural integrity of the complex.

Furthermore, the derivatized crystals collected close to the experimentally derived absorption edge diffracted to a higher resolution (2.3 Å), than the native crystals (around 2.5 - 3.1 Å). It has been shown before, that the resolution improved after hexamine cations addition (Clemons et al. 2001). The anomalous signal was quite low, significantly lower than for the native P-SAD data, with an overall anomalous signal up to 1.138. A comparison of the data statistics is given in Table 27. Unfortunately, Co-SAD and Co-MAD phasing was unsuccessful for the cobalt derivatized crystals, most probably because of a combination of low anomalous signal and the uncertainty in the number of substructure sites. As stated above, it is not clear if substructure solution failed or phasing, as no model building could be applied to enhance the electron density maps.

For Ghrelin•NOX-B11 main-chain tracing was not possible, as the main part of the structure consists of L-RNA nucleotides. To date, only two other Spiegelmer-protein complexes were published (Oberthür et al. 2015; Yatime et al. 2015). In those cases, the initial electron density maps were sufficient for model building after density modification. Model building was also facilitated as the atomic coordinates of both of the proteins in the complexes were known and the resolution limits of the crystals were higher. For NOX-D20:MC5a, the resolution limit of the native data was 1.8 Å (Yatime et al. 2015), for CCL2•NOX-E36 the resolution limit was 2.05 Å (Oberthür et al. 2015).

The fourth approach attempted for phase retrieval was to crystalize a racemate of Ghrelin•NOX-B11 with the enantiomeric D-Ghrelin•D-NOX-B11 complex (see chapter 4.2.5.5.). Racemic protein crystallography has been shown to facilitate crystal growth, phase determination and enhance diffraction quality (Pentelute *et al.*, 2008; Hung *et al.*, 1999; Mandal *et al.*, 2009; Zawadzke & Berg, 1993;). As proposed, in comparison to

crystallization of the L-complex, the racemic complexes crystallized in several conditions. On the other hand, the obtained crystals did not diffract to higher resolution. Due to lack of material, no extensive optimization efforts could be performed. The space group of one crystal (Figure 36) could be determined and was P3, which is a non-centrosymmetric space group. To date, all eight racemic protein crystal structures crystallized in centrosymmetric space groups. Therefore, it is possible, that the D-/L- complexes did not crystallize in a centrosymmetric space group. On the other hand, for Ghrelin•NOX-B11 alone only one crystallization condition producing crystals was identified.

Racemic crystallization was, to my knowledge hitherto not yet performed for nucleic acid-protein complexes. It could be possible, that the racemic mixtures cannot arrange a centrosymmetric lattice, as the respective enantiomers are more likely to rearrange them and dissociation of the complex might occur. This could be further addressed with native PAGE, however that was not possible during this study, as only few crystals were available.

The fifth approach was to use two different molecular replacement (MR) methods for obtaining rough phase estimates, that could then be used for structure solution. The first MR approach was adapted from Robertson & Scott (2008) and is based on the observation, that helical fragments, that are placed individually in an iterative manner into the calculated electron density, provide phase estimates that are sufficient to solve the structure (see chapter 4.2.6.1.).

Whereas the first molecular replacement calculations did show electron density around the placed fragments, and also some additional density next to them, hinting at some success (Figure 38). Further attempts of MR did not enhance the map quality. This could be due to the small size of the RNA, where the number of helical fragments constitutes only half of the molecule. The success of this method is based on approx. 70% of the asymmetric unit to be filled, until the density improves (Robertson and Scott 2008).

Based on this, 1000 different 3D RNA models of the complete molecule were generated, in order to find a suitable search model for MR search and to get information about the probable structure of L-NOX-B11 (see chapter 4.2.6.2.). As stated before, secondary structure prediction is rather reliable, but ternary structure modelling calls for more information about the shape, folding, base pairing and so forth. Information about the

overall shape of RNA molecules can be obtained from SAXS experiments and can be used to reduce the number of possible dimensionalities for 3D modelling (Jacques and Trehwella 2010; Russell et al. 2002).

More secondary structure information would have been advantageous for secondary structure predictions. Unfortunately, the small length of the RNA is most probably too short, so standard methods for secondary structure determination, such as selective 2'-hydroxyl acylation analyzed by primer extension (SHAPE) can't be applied.

Furthermore, SAXS data of unbound NOX-B11 and Ghrelin•NOX-B11 could reveal a conformational change of the RNA upon ligand binding. This could also be a reason, why the search model was not sufficient for molecular replacement. In future studies, extensive modeling approaches with both ghrelin and NOX-B11 could be performed. This would imply the need of computational power and some additional information about the structure of both ghrelin and the RNA, as well as the interaction of both molecules. NMR-studies could also be performed to elucidate the atomic structure of the complex in solution. This could not be performed in this study, since material in the milligram range would be required and manufacturing costs are extremely high for a 47 bp L-RNA, as well as for an octanoylated peptide and the time this study would consume was not available during this thesis.

In conclusion, in this study, several different well established, as well as not yet very established approaches for phase retrieval were applied extensively. Phase retrieval was unfortunately unsuccessful for all approaches, depicting the difficulties that can arise during the crystallization of RNA and peptide complexes, when no structural information about the different entities is known. Native P-SAD was hampered by the limited diffraction resolution and the large substructure.

Further problems encountered as the instability of the complex after soaking procedures, and the small anomalous signal of the only derivative that could be produced.

Furthermore, automated model building could not be applied, as the RNA consists of unnatural building blocks, that are not yet included in standardly available model building software.

Chemical modification of ghrelin and NOX-B11 for derivative production was also not possible. Ghrelin is a short flexible peptide, and the only known structural feature is the octanoylation at Ser3 and an α -helix at the N-terminus. Therefore, modification at the N-terminus could impede helix formation and complex formation, since the N-terminus is involved in NOX-B11 binding. The C-terminus was determined to be flexible, so modification of it is not be feasible. Furthermore, there are no methionine, nor cysteine residues in the sequence of ghrelin that could be modified to Seleno-methionine or Seleno-cysteine for Se-SAD. As a last possibility for structure solution, several L-RNAs with Seleno-modified or bromilated L-RNA bases could potentially be produced. Since none of the nucleobases are available commercially, they would have to be produced first, followed by production of the 47 bp L-RNA. Both are non-standard procedures and were not possible to be applied during this study.

6. Conclusion and Outlook

6.1. Biochemical analysis of MAP FurA

For the first time the open and closed conformations of *Mycobacterium avium* ssp. *paratuberculosis* (MAP) FurA could be resolved with the help of low resolution structures. The data provides insights into the response of MAP to initial host-defence mechanisms, namely metal sequestration and oxidative stress induction. It was shown with different biochemical assays, that MAP FurA is sensitive to treatment with hydrogen peroxide and metal chelation, further depicting MAP FurA's function similar to *Bacillus subtilis* redox sensing protein PerR. In comparison to other MAP FurA homologues, no consensus DNA binding sequence was found in the genome of MAP (Eckelt et al. 2015). It was also not possible to detect direct DNA binding with the proposed binding sequences (data not shown). A pool of randomized DNA sequences could be used to check if MAP FurA is able to bind DNA.

In the course of this thesis the purification of MAP FurA was optimized, allowing the production of large amounts of pure protein that can be used for further studies to analyse the structure and mode of action of MAP FurA. Crystallization of MAP FurA was not successful during this thesis, even though two promising conditions were found. In future work the crystallization of MAP FurA under the three different conditions (oxidized, non-oxidized and apo-MAP FurA) could lead to successful crystallization trials. For this, the purification needs to be further optimized, to guarantee a homogenous sample. Furthermore, samples could be directly frozen after purification to circumvent a dimer monomer transition.

Getting structural information about MAP FurA in its different conformations would help to further understand the mode of action in MAP FurA in comparison to its homologs. Furthermore, MAP FurA could be an interesting drug target, as it is involved in oxidative stress regulation and virulence. Hence, atomic resolution structures could support in structure-based drug discovery investigation.

6.2. Ghrelin•NOX11 phasing and structure solution

In this study, first structural information about Ghrelin•NOX-B11 was obtained. Ghrelin is a unique peptide, with high physiological importance, and structural information is scarce. It was shown that the complex is exceptionally stable at RT over a long time-period. DLS measurements and SAXS measurements revealed a conformational change of the L-RNA upon ghrelin binding. Furthermore, the complex was needed for crystallization, as complex formation decreased flexibility of the L-aptamer and the peptide.

It was possible to obtain crystals of sufficient quality for diffraction data collection. All available phase retrieval methods were applied, such as conventional SAD/MAD/SIR/SIRAS approaches with heavy atom derivatives and more novel approaches as native P-SAD phasing and calcium MAD, racemic crystallization, molecular replacement with helical fragments and generation of a molecular replacement model, with the aid of experimental SAXS data.

Since the amount of material available for this project was limited and the production of derivatives was difficult, native SAD was performed. For this, the designated beamlines P13 (EMBL, DESY, Germany) and I23 (Diamond Light Source, United Kingdom) were used. At P13, several crystals were measured and a merged dataset with high anomalous signal was obtained. Phasing was not successful, despite extensive efforts regarding programs and variation of parameters. In comparison to other successful native SAD approaches, the multiplicity was lower, which is why it seems that this might be the limiting factor. Multiple data collections are time-consuming and beam time at synchrotrons is limited. Because of this, low dose datasets could be collected. If new material becomes available and the beamline is accessible, additional datasets could be collected with the same experimental set-up to increase the multiplicity.

To optimize the anomalous signal and to get the scattering at low angles and to collect data at even lower energies, data were collected at Diamond Light Source, the most advanced beamline regarding instrumentation and equipment for long wavelength experiments in Europe at the moment. Despite the specialized set-up, structure solution failed, most probable due limited diffraction of the crystals and due to absorption effects that hamper the recording of accurate reflections.

Since the flux at such wavelengths is rather low, data may be recorded at more brilliant light sources, such as X-ray free electron lasers (XFEL), where sulfur and chlorine phasing was already successfully applied (Barends 2014, Nakane *et al.*, 2015). With the diffraction before destruction approach, radiation damage can be more or less excluded, leading to accurate data collection. Furthermore, the high-resolution limits at XFELs could be increased in comparison to the lower flux at state-of-the-art long wavelength beamlines. In comparison to synchrotron beamlines, where beam-time can be accessed more regular, XFEL beamtime is limited. Micro crystals of sufficient quality must be produced and rather large amounts of sample are needed, explaining further, why it was not possible to test this approach during the course of this thesis.

The limitation of the L-RNA material was hindering further optimization of the Ghrelin•NOX-B11 crystals, which would be beneficial for structure solution. It would be advantageous to obtain crystals diffracting to higher resolution and higher symmetry, to enhance the accuracy of measured reflections and to obtain higher multiplicity with less datasets from multiple crystals. Random matrix seeding with the obtained seedstock (as described in 3.2.31) was performed and some crystallization drops showed microcrystals (data not shown). Due to sample limitation and lack of time it was not possible to further optimize those conditions during the course of this study. If more material becomes available, further optimization can be performed.

Unfortunately, all of the applied experimental phase retrieval methods did not lead to a clear solution of the structure, highlighting the difficulties of structure determination for non-natural macromolecules at intermediate resolution. Also, structure solution was impaired by the non-existence of L-nucleotides in the conventional structure solution software. As those software packages are evolving and more and more ligands are implemented it might be possible in the future to perform automatic model building for L-RNA molecules.

References

- Abrahams, J. P., and A. G. W. Leslie. 1996. "Methods Used in the Structure Determination of Bovine Mitochondrial F1 ATPase." *Acta Crystallographica Section D Biological Crystallography* 52 (1). International Union of Crystallography: 30–42. doi:10.1107/S0907444995008754.
- Adams, Paul D, Pavel V Afonine, Gábor Bunkóczi, Vincent B Chen, Ian W Davis, Nathaniel Echols, Jeffrey J Headd, et al. 2010. "PHENIX: A Comprehensive Python-Based System for Macromolecular Structure Solution." *Acta Crystallographica Section D* 66 (2): 213–21. doi:10.1107/S0907444909052925.
- Afonine, Pavel V, Ralf W Grosse-Kunstleve, Nathaniel Echols, Jeffrey J Headd, Nigel W Moriarty, Marat Mustyakimov, Thomas C Terwilliger, Alexandre Urzhumtsev, Peter H Zwart, and Paul D Adams. 2012. "Towards Automated Crystallographic Structure Refinement with *Phenix.Refine*." *Acta Crystallographica Section D* 68 (4): 352–67. doi:10.1107/S0907444912001308.
- Agranoff, Daniel, and Sanjeev Krishna. 2004. "Metal Ion Transport and Regulation in *Mycobacterium Tuberculosis*." *Frontiers in Bioscience : A Journal and Virtual Library* 9 (September): 2996–3006. <http://www.ncbi.nlm.nih.gov/pubmed/15353332>.
- Ahn, Bo-Eun, and Tania A Baker. 2016. "Oxidization without Substrate Unfolding Triggers Proteolysis of the Peroxide-Sensor, PerR." *Proceedings of the National Academy of Sciences of the United States of America* 113 (1). National Academy of Sciences: E23-31. doi:10.1073/pnas.1522687112.
- Ahn, Bo-Eun, Joonseok Cha, Eun-Jin Lee, Ah-Reum Han, Charles J Thompson, and Jung-Hye Roe. 2006. "Nur, a Nickel-Responsive Regulator of the Fur Family, Regulates Superoxide Dismutases and Nickel Transport in *Streptomyces Coelicolor*." *Molecular Microbiology* 59 (6). England: 1848–58. doi:10.1111/j.1365-2958.2006.05065.x.
- Allard, Kimberly A, V K Viswanathan, and Nicholas P Cianciotto. 2006. "*LbtA* and *LbtB* Are Required for Production of the *Legionella Pneumophila* Siderophore Legiobactin." *Journal of Bacteriology* 188 (4): 1351 LP-1363. doi:10.1128/JB.188.4.1351-1363.2006.
- Althaus, Ellen Wang, Caryn E Outten, Katherine E Olson, Hua Cao, and Thomas V O'Halloran. 1999. "The Ferric Uptake Regulation (Fur) Repressor Is a Zinc Metalloprotein." *Biochemistry* 38 (20). American Chemical Society: 6559–69. doi:10.1021/bi982788s.
- Andresen, Michael C., and Diana L. Kunze. 1994. "Nucleus Tractus Solitarius—Gateway to Neural Circulatory Control." *Annual Review of Physiology* 56 (1): 93–116. doi:10.1146/annurev.ph.56.030194.000521.
- Andrews, Simon C, Andrea K Robinson, and Francisco Rodríguez-Quiñones. 2003. "Bacterial Iron Homeostasis." *FEMS Microbiology Reviews* 27 (2): 215–37. doi:https://doi.org/10.1016/S0168-6445(03)00055-X.

- Asakawa, Akihiro, Akio Inui, Toshihiro Kaga, Hideki Yuzuriha, Toshiaki Nagata, Naohiko Ueno, Susumu Makino, et al. 2001. "Ghrelin Is an Appetite-Stimulatory Signal from Stomach with Structural Resemblance to Motilin." *Gastroenterology* 120 (2): 337–45. doi:10.1053/gast.2001.22158.
- Ashley, Gary W. 1992. "Modeling, Synthesis, and Hybridization Properties of (L)-Ribonucleic Acid." *Journal of the American Chemical Society* 114 (25). American Chemical Society: 9731–36. doi:10.1021/ja00051a001.
- Atalayer, Deniz, Charlisa Gibson, Alexandra Konopacka, and Allan Geliebter. 2013. "Ghrelin and Eating Disorders." *Progress in Neuro-Psychopharmacology & Biological Psychiatry* 40 (January): 70–82. doi:10.1016/j.pnpbp.2012.08.011.
- Aurelius, O., K. El Omari, R. Duman, A. Wagner, and V. Mykhaylyk. 2016. "Long-Wavelength Macromolecular Crystallography – First Successful Native SAD Experiment Close to the Sulfur Edge." *Nuclear Instruments and Methods in Physics Research Section B: Beam Interactions with Materials and Atoms* 411. Diamond Light Source: 12–16. doi:10.1016/j.nimb.2016.12.005.
- Bagg, Anne, and J B Neilands. 1987. "Ferric Uptake Regulation Protein Acts as a Repressor, Employing Iron(II) as a Cofactor to Bind the Operator of an Iron Transport Operon in *Escherichia Coli*." *Biochemistry* 26 (17). American Chemical Society: 5471–77. doi:10.1021/bi00391a039.
- Baichoo, Noel, Tao Wang, Rick Ye, and John D Helmann. 2002. "Global Analysis of the *Bacillus Subtilis* Fur Regulon and the Iron Starvation Stimulon." *Molecular Microbiology* 45 (6). John Wiley & Sons, Ltd (10.1111): 1613–29. doi:10.1046/j.1365-2958.2002.03113.x.
- Baldanzi, Gianluca, Nicoletta Filigheddu, Santina Cutrupi, Filomena Catapano, Sara Bonissoni, Alberto Fubini, Daniela Malan, et al. 2002. "Ghrelin and Des-Acyl Ghrelin Inhibit Cell Death in Cardiomyocytes and Endothelial Cells through ERK1/2 and PI 3-Kinase/AKT." *The Journal of Cell Biology* 159 (6): 1029–37. doi:10.1083/jcb.200207165.
- Batey, Robert T., Sunny D. Gilbert, and Rebecca K. Montange. 2004. "Structure of a Natural Guanine-Responsive Riboswitch Complexed with the Metabolite Hypoxanthine." *Nature* 432 (7015): 411–15. doi:10.1038/nature03037.
- Battye, T Geoff G, Luke Kontogiannis, Owen Johnson, Harold R Powell, and Andrew G W Leslie. 2011. "IMOSFLM: A New Graphical Interface for Diffraction-Image Processing with MOSFLM." *Acta Crystallographica. Section D, Biological Crystallography* 67 (Pt 4). International Union of Crystallography: 271–81. doi:10.1107/S0907444910048675.
- Bednarek, M A, S D Feighner, S S Pong, K K McKee, D L Hreniuk, M V Silva, V A Warren, A D Howard, L H Van Der Ploeg, and J V Heck. 2000. "Structure-Function Studies on the New Growth Hormone-Releasing Peptide, Ghrelin: Minimal Sequence of Ghrelin Necessary for Activation of Growth Hormone Secretagogue Receptor 1a." *Journal of Medicinal Chemistry* 43 (23): 4370–76. <http://www.ncbi.nlm.nih.gov/pubmed/11087562>.
- Beevers, Andrew J, and Andreas Kukol. 2006. "Conformational Flexibility of the Peptide Hormone Ghrelin in Solution and Lipid Membrane Bound: A Molecular

- Dynamics Study.” *Journal of Biomolecular Structure & Dynamics* 23 (4): 357–64. doi:10.1080/07391102.2006.10531231.
- Bender, Brian Joseph, Gerrit Vortmeier, Stefan Ernicke, Mathias Bosse, Anette Kaiser, Sylvia Els-Heindl, Ulrike Krug, Annette Beck-Sickinger, Jens Meiler, and Daniel Huster. 2019. “Structural Model of Ghrelin Bound to Its G Protein-Coupled Receptor.” *Structure (London, England : 1993)* 27 (3): 537–544.e4. doi:10.1016/j.str.2018.12.004.
- Benvenuti, Manuela, and Stefano Mangani. 2007. “Crystallization of Soluble Proteins in Vapor Diffusion for X-Ray Crystallography.” *Nature Protocols* 2 (June). Nature Publishing Group: 1633. <https://doi.org/10.1038/nprot.2007.198>.
- Biesecker, G, L Dihel, K Enney, RA Bendele - Immunopharmacology, and undefined 1999. 2019. “Derivation of RNA Aptamer Inhibitors of Human Complement C5.” *Elsevier*. Accessed March 9. <https://www.sciencedirect.com/science/article/pii/S016231099900020X>.
- Blanch, Ewan W, Ludmilla A Morozova-Roche, Duncan A.E Cochran, Andrew J Doig, Lutz Hecht, and Laurence D Barron. 2000. “Is Polyproline II Helix the Killer Conformation? A Raman Optical Activity Study of the Amyloidogenic Prefibrillar Intermediate of Human Lysozyme 1 1Edited by A. R. Fersht.” *Journal of Molecular Biology* 301 (2): 553–63. doi:10.1006/jmbi.2000.3981.
- Blencowe, Dayle K, and Andrew P Morby. 2003. “Zn(II) Metabolism in Prokaryotes.” *FEMS Microbiology Reviews* 27 (2–3): 291–311. doi:10.1016/S0168-6445(03)00041-X.
- Botello-Morte, L, A González, M T Bes, M L Peleato, and M F Fillat. 2013. “Chapter Four - Functional Genomics of Metalloregulators in Cyanobacteria.” In *Genomics of Cyanobacteria*, edited by Franck Chauvat and Corinne B T - Advances in Botanical Research Cassier-Chauvat, 65:107–56. Academic Press. doi:<https://doi.org/10.1016/B978-0-12-394313-2.00004-4>.
- Bouchard, P.R., R.M. Hutabarat, and K.M. Thompson. 2010. “Discovery and Development of Therapeutic Aptamers.” *Annual Review of Pharmacology and Toxicology* 50 (1): 237–57. doi:10.1146/annurev.pharmtox.010909.105547.
- Bowers, C Y, F Momany, G A Reynolds, D Chang, A Hong, and K Chang. 1980. “Structure-Activity Relationships of a Synthetic Pentapeptide That Specifically Releases Growth Hormone *in Vitro*.” *Endocrinology* 106 (3): 663–67. doi:10.1210/endo-106-3-663.
- Braun, V. 2001. “Iron Uptake Mechanisms and Their Regulation in Pathogenic Bacteria.” *International Journal of Medical Microbiology : IJMM* 291 (2): 67–79. doi:10.1078/1438-4221-00103.
- Briggs, Dana I., and Zane B. Andrews. 2011. “Metabolic Status Regulates Ghrelin Function on Energy Homeostasis.” *Neuroendocrinology* 93 (1): 48–57. doi:10.1159/000322589.
- Bsat, Nada, Andrew Herbig, Lilliam Casillas-Martinez, Peter Setlow, and John D Helmann. 1998. “*Bacillus Subtilis* Contains Multiple Fur Homologues: Identification of the Iron Uptake (Fur) and Peroxide Regulon (PerR) Repressors.”

- Molecular Microbiology* 29 (1). John Wiley & Sons, Ltd (10.1111): 189–98.
doi:10.1046/j.1365-2958.1998.00921.x.
- Butcher, James, Sabina Sarvan, Joseph S Brunzelle, Jean-François Couture, and Alain Stintzi. 2012. “Structure and Regulon of *Campylobacter Jejuni* Ferric Uptake Regulator Fur Define Apo-Fur Regulation.” *Proceedings of the National Academy of Sciences* 109 (25): 10047 LP-10052. doi:10.1073/pnas.1118321109.
- Cai, Huan, Wei na Cong, Caitlin M. Daimon, Rui Wang, Matthias H. Tschöp, Jean Sévigny, Bronwen Martin, and Stuart Maudsley. 2013. “Altered Lipid and Salt Taste Responsivity in Ghrelin and GOAT Null Mice.” *PLoS ONE* 8 (10). doi:10.1371/journal.pone.0076553.
- Callahan, Holly S, David E Cummings, Margaret S Pepe, Patricia A Breen, Colleen C Matthys, and David S Weigle. 2004. “Postprandial Suppression of Plasma Ghrelin Level Is Proportional to Ingested Caloric Load but Does Not Predict Intermeal Interval in Humans.” *The Journal of Clinical Endocrinology and Metabolism* 89 (3): 1319–24. doi:10.1210/jc.2003-031267.
- Canneva, Fabio, Manuela Branzoni, Giovanna Riccardi, Roberta Provvedi, and Anna Milano. 2005. “Rv2358 and FurB: Two Transcriptional Regulators from *Mycobacterium Tuberculosis* Which Respond to Zinc.” *Journal of Bacteriology* 187 (16). American Society for Microbiology: 5837–40. doi:10.1128/JB.187.16.5837-5840.2005.
- Carpenter, Beth M, Jeremy J Gilbreath, Oscar Q Pich, Ann M McKelvey, Ernest L Maynard, Zhao-Zhang Li, and D Scott Merrell. 2013. “Identification and Characterization of Novel *Helicobacter Pylori* Apo-Fur-Regulated Target Genes.” *Journal of Bacteriology* 195 (24): 5526 LP-5539. doi:10.1128/JB.01026-13.
- Carpenter, Beth M, Jeannette M Whitmire, and D Scott Merrell. 2009. “This Is Not Your Mother’s Repressor: The Complex Role of Fur in Pathogenesis.” *Infection and Immunity* 77 (7). American Society for Microbiology Journals: 2590–2601. doi:10.1128/IAI.00116-09.
- Carter, C W, and C W Carter. 1979. “Protein Crystallization Using Incomplete Factorial Experiments.” *The Journal of Biological Chemistry* 254 (23): 12219–23. <http://www.ncbi.nlm.nih.gov/pubmed/500706>.
- Cate, J H, A R Gooding, E Podell, K Zhou, B L Golden, C E Kundrot, T R Cech, and J A Doudna. 1996. “Crystal Structure of a Group I Ribozyme Domain: Principles of RNA Packing.” *Science (New York, N.Y.)* 273 (5282). United States: 1678–85.
- Cate, Jamie H, and Jennifer A Doudna. 1996. “Metal-Binding Sites in the Major Groove of a Large Ribozyme Domain.” *Structure* 4 (10). Elsevier: 1221–29. doi:10.1016/S0969-2126(96)00129-3.
- Chamberlin, William, Thomas J Borody, and Jordana Campbell. 2011. “Primary Treatment of Crohn’s Disease: Combined Antibiotics Taking Center Stage.” *Expert Review of Clinical Immunology* 7 (6): 751–60. doi:10.1586/eci.11.43.
- Chen, L, L Keramati, and J D Helmann. 1995. “Coordinate Regulation of *Bacillus Subtilis* Peroxide Stress Genes by Hydrogen Peroxide and Metal Ions.” *Proceedings of the National Academy of Sciences of the United States of America*

- 92 (18): 8190–94. <https://www.ncbi.nlm.nih.gov/pubmed/7667267>.
- Chen, L Q, J P Rose, E Breslow, D Yang, W R Chang, W F Furey, M Sax, and B C Wang. 1991. “Crystal Structure of a Bovine Neurophysin II Dipeptide Complex at 2.8 Å Determined from the Single-Wavelength Anomalous Scattering Signal of an Incorporated Iodine Atom.” *Proceedings of the National Academy of Sciences of the United States of America* 88 (10). National Academy of Sciences: 4240–44. doi:10.1073/PNAS.88.10.4240.
- Chen, Lei, and John D Helmann. 1995. “*Bacillus Subtilis* MrgA Is a Dps(PexB) Homologue: Evidence for Metalloregulation of an Oxidative-Stress Gene.” *Molecular Microbiology* 18 (2). John Wiley & Sons, Ltd (10.1111): 295–300. doi:10.1111/j.1365-2958.1995.mmi_18020295.x.
- Chiancone, Emilia, and Pierpaolo Ceci. 2010. “The Multifaceted Capacity of Dps Proteins to Combat Bacterial Stress Conditions: Detoxification of Iron and Hydrogen Peroxide and DNA Binding.” *Biochimica et Biophysica Acta (BBA) - General Subjects* 1800 (8): 798–805. doi:<https://doi.org/10.1016/j.bbagen.2010.01.013>.
- Choi, Daniel Y, Maria Carolina Ortube, Colin A Mccannel, David Sarraf, Jean-Pierre Hubschman, Tara A Mccannel, and Michael B Gorin. 2011. “Sustained Elevated Intraocular Pressures after Intravitreal Injection of Bevacizumab, Ranibizumab, and Pegaptanib.” *Retina* 31 (6): 1028–35. doi:10.1097/IAE.0b013e318217ffde.
- Chojnacki, Szymon, Andrew Cowley, Joon Lee, Anna Foix, and Rodrigo Lopez. 2017. “Programmatic Access to Bioinformatics Tools from EMBL-EBI Update: 2017.” *Nucleic Acids Research* 45 (W1): W550–53. doi:10.1093/nar/gkx273.
- Chuang, Jen-Chieh, Mario Perello, Ichiro Sakata, Sherri Osborne-Lawrence, Joseph M. Savitt, Michael Lutter, and Jeffrey M. Zigman. 2011. “Ghrelin Mediates Stress-Induced Food-Reward Behavior in Mice.” *Journal of Clinical Investigation* 121 (7): 2684–92. doi:10.1172/JCI57660.
- Clarke, C J. 1997. “The Pathology and Pathogenesis of Paratuberculosis in Ruminants and Other Species.” *Journal of Comparative Pathology* 116 (3): 217–61. <http://www.ncbi.nlm.nih.gov/pubmed/9147244>.
- Clemons, William M., Ditlev E. Brodersen, John P. McCutcheon, Joanna L.C. May, Andrew P. Carter, Robert J. Morgan-Warren, Brian T. Wimberly, and V. Ramakrishnan. 2001. “Crystal Structure of the 30 S Ribosomal Subunit from *Thermus Thermophilus*: Purification, Crystallization and Structure Determination.” *Journal of Molecular Biology* 310 (4): 827–43. doi:10.1006/jmbi.2001.4778.
- Cochrane, Jesse C., Sarah V. Lipchock, and Scott A. Strobel. 2007. “Structural Investigation of the GlmS Ribozyme Bound to Its Catalytic Cofactor.” *Chemistry & Biology* 14 (1): 97–105. doi:10.1016/j.chembiol.2006.12.005.
- Cocito, C, P Gilot, M Coene, M de Kesel, P Poupart, and P Vannuffel. 1994. “Paratuberculosis.” *Clinical Microbiology Reviews* 7 (3): 328–45. <http://www.ncbi.nlm.nih.gov/pubmed/7923053>.
- Colmenarejo, Gonzalo, and Ignacio Tinoco. 1999. “Structure and Thermodynamics of Metal Binding in the P5 Helix of a Group I Intron Ribozyme 1 Edited by P. E.

- Wright.” *Journal of Molecular Biology* 290 (1): 119–35.
doi:10.1006/jmbi.1999.2867.
- Cossu, Davide, Eleonora Cocco, Daniela Paccagnini, Speranza Masala, Niyaz Ahmed, Jessica Frau, Maria Giovanna Marrosu, and Leonardo A. Sechi. 2011. “Association of *Mycobacterium Avium* Subsp. *Paratuberculosis* with Multiple Sclerosis in Sardinian Patients.” Edited by Delia Goletti. *PLoS ONE* 6 (4): e18482.
doi:10.1371/journal.pone.0018482.
- Costantino, David A, Jennifer S Pflingsten, Robert P Rambo, and Jeffrey S Kieft. 2008. “TRNA-MRNA Mimicry Drives Translation Initiation from a Viral IRES.” *Nature Structural & Molecular Biology* 15 (1). NIH Public Access: 57–64.
doi:10.1038/nsmb1351.
- Cummings, David E., Karine Clement, Jonathan Q. Purnell, Christian Vaisse, Karen E. Foster, R. Scott Frayo, Michael W. Schwartz, Arnaud Basdevant, and David S. Weigle. 2002. “Elevated Plasma Ghrelin Levels in Prader–Willi Syndrome.” *Nature Medicine* 8 (7): 643–44. doi:10.1038/nm0702-643.
- D’Autréaux, Benoît, Ludovic Pecqueur, Anne Gonzalez de Peredo, Rutger E M Diederix, Christelle Caux-Thang, Lyes Tabet, Beate Bersch, Eric Forest, and Isabelle Michaud-Soret. 2007. “Reversible Redox- and Zinc-Dependent Dimerization of the *Escherichia Coli* Fur Protein.” *Biochemistry* 46 (5). American Chemical Society: 1329–42. doi:10.1021/bi061636r.
- Date, Yukari, Masamitsu Nakazato, Suzuko Hashiguchi, Katsuya Dezaki, Muhtashan S Mondal, Hiroshi Hosoda, Masayasu Kojima, et al. 2002. “Ghrelin Is Present in Pancreatic Alpha-Cells of Humans and Rats and Stimulates Insulin Secretion.” *Diabetes* 51 (1): 124–29. <http://www.ncbi.nlm.nih.gov/pubmed/11756331>.
- Dauter, Z, and D A Adamiak. 2001. “Anomalous Signal of Phosphorus Used for Phasing DNA Oligomer: Importance of Data Redundancy.” *Acta Crystallographica. Section D, Biological Crystallography* 57 (Pt 7). United States: 990–95.
- Dauter, Z, and M Dauter. 1999. “Anomalous Signal of Solvent Bromides Used for Phasing of Lysozyme.” *Journal of Molecular Biology* 289 (1). England: 93–101.
doi:10.1006/jmbi.1999.2744.
- Davenport, A. P., Tom I Bonner, Steven M Foord, Anthony J Harmar, Richard R Neubig, Jean-Philippe Pin, Michael Spedding, Masayasu Kojima, and Keniji Kangawa. 2005. “International Union of Pharmacology. LVI. Ghrelin Receptor Nomenclature, Distribution, and Function.” *Pharmacological Reviews* 57 (4): 541–46. doi:10.1124/pr.57.4.1.
- Davis, William C, J Todd Kuenstner, and Shoor Vir Singh. 2017. “Resolution of Crohn’s (Johne’s) Disease with Antibiotics: What Are the next Steps?” *Expert Review of Gastroenterology & Hepatology* 11 (5): 393–96.
doi:10.1080/17474124.2017.1300529.
- DelParigi, Angelo, Matthias Tschöp, Mark L. Heiman, Arline D. Salbe, Barbora Vozarova, Susan M. Sell, Joy C. Bunt, and P. Antonio Tataranni. 2002. “High Circulating Ghrelin: A Potential Cause for Hyperphagia and Obesity in Prader–Willi Syndrome.” *The Journal of Clinical Endocrinology & Metabolism* 87 (12):

- 5461–64. doi:10.1210/jc.2002-020871.
- Deng, Zengqin, Qing Wang, Zhao Liu, Manfeng Zhang, Ana Carolina Dantas Machado, Tsu Pei Chiu, Chong Feng, et al. 2015. “Mechanistic Insights into Metal Ion Activation and Operator Recognition by the Ferric Uptake Regulator.” *Nature Communications* 6 (May). doi:10.1038/ncomms8642.
- Dian, Cyril, Sylvia Vitale, Gordon A Leonard, Christelle Bahlawane, Caroline Fauquant, Damien Leduc, Cécile Muller, Hilde de Reuse, Isabelle Michaud-Soret, and Laurent Terradot. 2011. “The Structure of the *Helicobacter Pylori* Ferric Uptake Regulator Fur Reveals Three Functional Metal Binding Sites.” *Molecular Microbiology* 79 (5). John Wiley & Sons, Ltd (10.1111): 1260–75. doi:10.1111/j.1365-2958.2010.07517.x.
- Diaz-Mireles, E, M Wexler, G Sawers, D Bellini, J D Todd, and A W B Johnston. 2004. “The Fur-like Protein Mur of *Rhizobium Leguminosarum* Is a Mn²⁺-Responsive Transcriptional Regulator.” *Microbiology (Reading, England)* 150 (Pt 5). England: 1447–56. doi:10.1099/mic.0.26961-0.
- Dickson, Suzanne L., and Simon M. Luckman. 1997. “Induction of C- Fos Messenger Ribonucleic Acid in Neuropeptide Y and Growth Hormone (GH)-Releasing Factor Neurons in the Rat Arcuate Nucleus Following Systemic Injection of the GH Secretagogue, GH-Releasing Peptide-6¹.” *Endocrinology* 138 (2): 771–77. doi:10.1210/endo.138.2.4907.
- Doudna, J A, C Grosshans, A Gooding, and C E Kundrot. 1993. “Crystallization of Ribozymes and Small RNA Motifs by a Sparse Matrix Approach.” *Proceedings of the National Academy of Sciences* 90 (16): 7829 LP-7833. doi:10.1073/pnas.90.16.7829.
- Druce, M R, A M Wren, A J Park, J E Milton, M Patterson, G Frost, M A Ghatei, C Small, and S R Bloom. 2005. “Ghrelin Increases Food Intake in Obese as Well as Lean Subjects.” *International Journal of Obesity* 29 (9). Nature Publishing Group: 1130–36. doi:10.1038/sj.ijo.0803001.
- Dvir, Hay, Elvira Valera, and Senyon Choe. 2010. “Structure of the MthK RCK in Complex with Cadmium.” *Journal of Structural Biology* 171 (2): 231–37. doi:10.1016/j.jsb.2010.03.020.
- Eckelt, Elke. 2014. “FurA and FurB - the Impact of Two Transcriptional Metalloregulators on *Mycobacterium Avium* Ssp. *Paratuberculosis* Stress Response and Metal Homeostasis.” University of Veterinary Medicine Hannover.
- Eckelt, Elke, Thorsten Meißner, Jochen Meens, Kristin Laarmann, Andreas Nerlich, Michael Jarek, Siegfried Weiss, Gerald-F Gerlach, and Ralph Goethe. 2015. “FurA Contributes to the Oxidative Stress Response Regulation of *Mycobacterium Avium* Ssp. *Paratuberculosis*.” *Frontiers in Microbiology* 6 (February). Frontiers Media S.A.: 16. doi:10.3389/fmicb.2015.00016.
- Eker, Fatma, Kai Griebenow, and Reinhard Schweitzer-Stenner. 2004. “Aβ1-28 Fragment of the Amyloid Peptide Predominantly Adopts a Polyproline II Conformation in an Acidic Solution†.” American Chemical Society. doi:10.1021/BI049542+.

- Ellington, Andrew D., and Jack W. Szostak. 1990. "In Vitro Selection of RNA Molecules That Bind Specific Ligands." *Nature* 346 (6287). Nature Publishing Group: 818–22. doi:10.1038/346818a0.
- Eltholth, M M, V R Marsh, S Van Winden, and F J Guitian. 2009. "Contamination of Food Products with *Mycobacterium Avium Paratuberculosis*: A Systematic Review." *Journal of Applied Microbiology* 107 (4): 1061–71. doi:10.1111/j.1365-2672.2009.04286.x.
- Emsley, P, and B Lohkamp. 2010. "Research Papers Features and Development of Coot Research Papers." *International Union of Crystallography*, 486–501. doi:10.1107/S0907444910007493.
- Eriksen, Tine A., Anders Kadziola, and Sine Larsen. 2009. "Binding of Cations in *Bacillus Subtilis* Phosphoribosyldiphosphate Synthetase and Their Role in Catalysis." *Protein Science* 11 (2): 271–79. doi:10.1110/ps.28502.
- Ernst, F. D., Stefan Bereswill, Barbara Waidner, Jeroen Stoof, Ulrike Mäder, Johannes G Kusters, Ernst J Kuipers, Manfred Kist, Arnoud H M van Vliet, and Georg Homuth. 2005. "Transcriptional Profiling of *Helicobacter Pylori* Fur- and Iron-Regulated Gene Expression." *Microbiology* 151 (2): 533–46. doi:10.1099/mic.0.27404-0.
- Escolar, Lucía, José Pérez-Martín, and Víctor de Lorenzo. 1998. "Binding of the Fur (Ferric Uptake Regulator) Repressor of *Escherichia Coli* to Arrays of the GATAAT Sequence." *Journal of Molecular Biology* 283 (3): 537–47. doi:https://doi.org/10.1006/jmbi.1998.2119.
- Eulberg, Dirk, Werner Purschke, Hans-Joachim Anders, Norma Selve, and Sven Klussmann. 2008. "Chapter 9. Spiegelmer NOX-E36 for Renal Diseases." In , 200–225. doi:10.1039/9781847558275-00200.
- Evans, Philip R, and Garib N Murshudov. 2013. "How Good Are My Data and What Is the Resolution?" *Acta Crystallographica. Section D, Biological Crystallography* 69 (Pt 7). International Union of Crystallography: 1204–14. doi:10.1107/S0907444913000061.
- Fang, Ferric C. 2004. "Antimicrobial Reactive Oxygen and Nitrogen Species: Concepts and Controversies." *Nature Reviews Microbiology* 2 (October). Nature Publishing Group: 820. https://doi.org/10.1038/nrmicro1004.
- Faulkner, Melinda J, and John D Helmann. 2011. "Peroxide Stress Elicits Adaptive Changes in Bacterial Metal Ion Homeostasis." *Antioxidants & Redox Signaling* 15 (1). Mary Ann Liebert, Inc.: 175–89. doi:10.1089/ars.2010.3682.
- Faulkner, Melinda J, Zhen Ma, Mayuree Fuangthong, and John D Helmann. 2012. "Derepression of the *Bacillus Subtilis* PerR Peroxide Stress Response Leads to Iron Deficiency." *Journal of Bacteriology* 194 (5). American Society for Microbiology: 1226–35. doi:10.1128/JB.06566-11.
- FDA, FDA. 2004. "Approves New Drug Treatment for Age-Related Macular Degeneration." https://scholar.google.com/scholar?q=%22FDA. (2004) FDA approves new drug treatment for age-related macular degeneration%22.
- Ferre-D'Amare, A. R., and J. A. Doudna. 1996. "Use of Cis- and Trans-Ribozymes to

- Remove 5' and 3' Heterogeneities From Milligrams of In Vitro Transcribed RNA." *Nucleic Acids Research* 24 (5). Oxford University Press: 977–78. doi:10.1093/nar/24.5.977.
- Ferré-D'Amaré, Adrian R, and Jennifer A Doudna. 2000. "Methods to Crystallize RNA." *Current Protocols in Nucleic Acid Chemistry* 1 (1). John Wiley & Sons, Ltd: 7.6.1-7.6.13. doi:10.1002/0471142700.nc0706s00.
- Filigheddu, Nicoletta, Viola F. Gnocchi, Marco Coscia, Miriam Cappelli, Paolo E. Porporato, Riccardo Taulli, Sara Traini, et al. 2007. "Ghrelin and Des-Acyl Ghrelin Promote Differentiation and Fusion of C2C12 Skeletal Muscle Cells." Edited by Carl-Henrik Heldin. *Molecular Biology of the Cell* 18 (3): 986–94. doi:10.1091/mbc.e06-05-0402.
- Fillat, María F. 2014. "The FUR (Ferric Uptake Regulator) Superfamily: Diversity and Versatility of Key Transcriptional Regulators." *Archives of Biochemistry and Biophysics* 546: 41–52. doi:https://doi.org/10.1016/j.abb.2014.01.029.
- Foadi, James, Pierre Aller, Yilmaz Alguel, Alex Cameron, Danny Axford, Robin L. Owen, Wes Armour, David G. Waterman, So Iwata, and Gwyndaf Evans. 2013. "Clustering Procedures for the Optimal Selection of Data Sets from Multiple Crystals in Macromolecular Crystallography." *Acta Crystallographica Section D Biological Crystallography* 69 (8): 1617–32. doi:10.1107/S0907444913012274.
- Franke, D, M V Petoukhov, P V Konarev, A Panjkovich, A Tuukkanen, H D T Mertens, A G Kikhney, et al. 2017. "ATSAS 2.8: A Comprehensive Data Analysis Suite for Small-Angle Scattering from Macromolecular Solutions." *J. Appl. Cryst* 50: 1212–25. doi:10.1107/S1600576717007786.
- Fuangthong, Mayuree, and John D Helmann. 2003. "Recognition of DNA by Three Ferric Uptake Regulator (Fur) Homologs in *Bacillus Subtilis*." *Journal of Bacteriology* 185 (21): 6348 LP-6357. doi:10.1128/JB.185.21.6348-6357.2003.
- Fuangthong, Mayuree, Andrew F Herbig, Nada Bsat, and John D Helmann. 2002. "Regulation of the *Bacillus Subtilis* Fur and PerR Genes by PerR: Not All Members of the PerR Regulon Are Peroxide Inducible." *Journal of Bacteriology* 184 (12). American Society for Microbiology: 3276–86. doi:10.1128/JB.184.12.3276-3286.2002.
- Gaballa, Ahmed, Haike Antelmann, Claudio Aguilar, Sukhjit K Khakh, Kyung-Bok Song, Gregory T Smaldone, and John D Helmann. 2008. "The *Bacillus Subtilis* Iron-Sparing Response Is Mediated by a Fur-Regulated Small RNA and Three Small, Basic Proteins." *Proceedings of the National Academy of Sciences of the United States of America* 105 (33). National Academy of Sciences: 11927–32. doi:10.1073/pnas.0711752105.
- Garst, Andrew D., Annie Héroux, Robert P. Rambo, and Robert T. Batey. 2008. "Crystal Structure of the Lysine Riboswitch Regulatory MRNA Element." *Journal of Biological Chemistry* 283 (33): 22347–51. doi:10.1074/jbc.C800120200.
- Gasteiger, Elisabeth, Christine Hoogland, Alexandre Gattiker, Séverine Duvaud, Marc R Wilkins, Ron D Appel, and Amos Bairoch. 2005. "Protein Analysis Tools on the ExPASy Server." *The Proteomics Protocols Handbook Protein Identification and Analysis Tools on the ExPASy Server*, 571–607. doi:10.1385/1592598900.

- Geliebter, Allan, Marci E Gluck, and Sami A Hashim. 2005. "Plasma Ghrelin Concentrations Are Lower in Binge-Eating Disorder." *The Journal of Nutrition* 135 (5): 1326–30. doi:10.1093/jn/135.5.1326.
- Gnanapavan, Sharmilee, Blerina Kola, Stephen A. Bustin, Damian G. Morris, Patrick McGee, Peter Fairclough, Satya Bhattacharya, Robert Carpenter, Ashley B. Grossman, and Márta Korbonits. 2002. "The Tissue Distribution of the mRNA of Ghrelin and Subtypes of Its Receptor, GHS-R, in Humans." *The Journal of Clinical Endocrinology & Metabolism* 87 (6): 2988–2988. doi:10.1210/jcem.87.6.8739.
- Greig, A, K Stevenson, D Henderson, V Perez, V Hughes, I Pavlik, M E Hines, I McKendrick, and J M Sharp. 1999. "Epidemiological Study of Paratuberculosis in Wild Rabbits in Scotland." *Journal of Clinical Microbiology* 37 (6): 1746–51. <http://www.ncbi.nlm.nih.gov/pubmed/10325318>.
- Grifantini, Renata, Shite Sebastian, Elisabetta Frigimelica, Monia Draghi, Erika Bartolini, Alessandro Muzzi, Rino Rappuoli, Guido Grandi, and Caroline Attardo Genco. 2003. "Identification of Iron-Activated and -Repressed Fur-Dependent Genes by Transcriptome Analysis of *Neisseria Meningitidis* Group B." *Proceedings of the National Academy of Sciences* 100 (16): 9542 LP-9547. doi:10.1073/pnas.1033001100.
- Groebe, Duncan R, Gary W Witherell, John F Milligan, and Olke C Uhlenbeck. 1987. "Oligoribonucleotide Synthesis Using T7 RNA Polymerase and Synthetic DNA Templates." *Nucleic Acids Research* 15 (21): 8783–98. doi:10.1093/nar/15.21.8783.
- Grosse-Kunstleve, R. W., P. D. Adams, and IUCr. 2003. "Substructure Search Procedures for Macromolecular Structures." *Acta Crystallographica Section D Biological Crystallography* 59 (11). International Union of Crystallography: 1966–73. doi:10.1107/S0907444903018043.
- Gruber, A. R., R. Lorenz, S. H. Bernhart, R. Neubock, and I. L. Hofacker. 2008. "The Vienna RNA Website." *Nucleic Acids Research* 36 (Web Server): W70–74. doi:10.1093/nar/gkn188.
- Guan, Guohua, Azul Pinochet-Barros, Ahmed Gaballa, Sarju J Patel, José M Argüello, and John D Helmann. 2015. "PfeT, a P1B4 -Type ATPase, Effluxes Ferrous Iron and Protects *Bacillus Subtilis* against Iron Intoxication." *Molecular Microbiology* 98 (4): 787–803. doi:10.1111/mmi.13158.
- Guan, X M, H Yu, O C Palyha, K K McKee, S D Feighner, D J Sirinathsinghji, R G Smith, L H Van der Ploeg, and A D Howard. 1997. "Distribution of mRNA Encoding the Growth Hormone Secretagogue Receptor in Brain and Peripheral Tissues." *Brain Research. Molecular Brain Research* 48 (1): 23–29. <http://www.ncbi.nlm.nih.gov/pubmed/9379845>.
- Guinier, André. 1939. "La Diffraction Des Rayons X Aux Très Petits Angles : Application à l'étude de Phénomènes Ultramicroscopiques." *Ann. Phys.* 11 (12): 161–237. doi:10.1051/anphys/193911120161.
- Guo, F, Y Wang, J Liu, S C Mok, F Xue, and W Zhang. 2016. "CXCL12/CXCR4: A Symbiotic Bridge Linking Cancer Cells and Their Stromal Neighbors in

- Oncogenic Communication Networks.” *Oncogene* 35 (7): 816–26.
doi:10.1038/onc.2015.139.
- Guo, Ke-Tai, Richard Schäfer, Angela Paul, Annika Gerber, Gerhard Ziemer, and Hans P. Wendel. 2006. “A New Technique for the Isolation and Surface Immobilization of Mesenchymal Stem Cells from Whole Bone Marrow Using High-Specific DNA Aptamers.” *Stem Cells* 24 (10). John Wiley & Sons, Ltd: 2220–31.
doi:10.1634/stemcells.2006-0015.
- Guss, J M, E A Merritt, R P Phizackerley, B Hedman, M Murata, K O Hodgson, and H C Freeman. 1988. “Phase Determination by Multiple-Wavelength x-Ray Diffraction: Crystal Structure of a Basic ‘Blue’ Copper Protein from Cucumbers.” *Science (New York, N.Y.)* 241 (4867). United States: 806–11.
- Gutierrez, Jesus A, Patricia J Solenberg, Douglas R Perkins, Jill A Willency, Michael D Knierman, Zhaoyan Jin, Derrick R Witcher, Shuang Luo, Jude E Onyia, and John E Hale. 2008. “Ghrelin Octanoylation Mediated by an Orphan Lipid Transferase.” *Proceedings of the National Academy of Sciences of the United States of America* 105 (17). National Academy of Sciences: 6320–25. doi:10.1073/pnas.0800708105.
- Hantke, Klaus. 1981. “Regulation of Ferric Iron Transport in *Escherichia Coli* K12: Isolation of a Constitutive Mutant.” *Molecular & General Genetics : MGG* 182 (2). Germany: 288–92.
- . 2001. “Iron and Metal Regulation in Bacteria.” *Current Opinion in Microbiology* 4 (2): 172–77. doi:https://doi.org/10.1016/S1369-5274(00)00184-3.
- Harp, Joel, Pradeep Pallan, Martin Egli, Joel M. Harp, Pradeep S. Pallan, and Martin Egli. 2016. “Phosphorus SAD Phasing for Nucleic Acid Structures: Limitations and Potential.” *Crystals* 6 (10). Multidisciplinary Digital Publishing Institute: 125. doi:10.3390/cryst6100125.
- Helmann, John D, Ming Fang Winston Wu, Ahmed Gaballa, Phil A Kobel, Maud M Morshedi, Paul Fawcett, and Chris Paddon. 2003. “The Global Transcriptional Response of *Bacillus Subtilis* to Peroxide Stress Is Coordinated by Three Transcription Factors.” *Journal of Bacteriology* 185 (1). American Society for Microbiology: 243–53. doi:10.1128/JB.185.1.243-253.2003.
- Helmling, Steffen, Christian Maasch, Dirk Eulberg, Klaus Buchner, Werner Schröder, Christian Lange, Stefan Vonhoff, et al. 2004. “Inhibition of Ghrelin Action *in Vitro* and *in Vivo* by an RNA-Spiegelmer.” *Proceedings of the National Academy of Sciences of the United States of America* 101 (36). National Academy of Sciences: 13174–79. doi:10.1073/pnas.0404175101.
- Hendrickson, W A, J R Horton, and D M LeMaster. 1990. “Selenomethionyl Proteins Produced for Analysis by Multiwavelength Anomalous Diffraction (MAD): A Vehicle for Direct Determination of Three-Dimensional Structure.” *The EMBO Journal* 9 (5). England: 1665–72.
- Hendrickson, W A, A Pahler, J L Smith, Y Satow, E A Merritt, and R P Phizackerley. 1989. “Crystal Structure of Core Streptavidin Determined from Multiwavelength Anomalous Diffraction of Synchrotron Radiation.” *Proceedings of the National Academy of Sciences of the United States of America* 86 (7). United States: 2190–94.

- Hendrickson, W A, J L Smith, R P Phizackerley, and E A Merritt. 1988. "Crystallographic Structure Analysis of Lamprey Hemoglobin from Anomalous Dispersion of Synchrotron Radiation." *Proteins* 4 (2). United States: 77–88. doi:10.1002/prot.340040202.
- Hendrickson, Wayne A. 1985. "Analysis of Protein Structure from Diffraction Measurement at Multiple Wavelengths." *Transactions of the American Crystallographic Association* 21.
- Hendrickson, Wayne A, and Martha M Teeter. 1981. "Structure of the Hydrophobic Protein Crambin Determined Directly from the Anomalous Scattering of Sulphur." *Nature* 290 (5802). England: 107–13. doi:10.1038/290107a0.
- Heppner, Kristy M., Nilika Chaudhary, Timo D. Müller, Henriette Kirchner, Kirk M. Habegger, Nickki Ottaway, David L. Smiley, et al. 2012. "Acylation Type Determines Ghrelin's Effects on Energy Homeostasis in Rodents." *Endocrinology* 153 (10): 4687–95. doi:10.1210/en.2012-1194.
- Hicks, Joshua M., and Victor L. Hsu. 2004. "The Extended Left-Handed Helix: A Simple Nucleic Acid-Binding Motif." *Proteins: Structure, Function, and Bioinformatics* 55 (2). Wiley Subscription Services, Inc., A Wiley Company: 330–38. doi:10.1002/prot.10630.
- Higgins, Susie C., Maria Gueorguiev, and Márta Korbonits. 2007. "Ghrelin, the Peripheral Hunger Hormone." *Annals of Medicine* 39 (2): 116–36. doi:10.1080/07853890601149179.
- Hoellenriegel, J., D. Zboralski, C. Maasch, N. Y. Rosin, W. G. Wierda, M. J. Keating, A. Kruschinski, and J. A. Burger. 2014. "The Spiegelmer NOX-A12, a Novel CXCL12 Inhibitor, Interferes with Chronic Lymphocytic Leukemia Cell Motility and Causes Chemosensitization." *Blood* 123 (7): 1032–39. doi:10.1182/blood-2013-03-493924.
- Hoffmann, Stefanie, Johannes Hoos, Sven Klussmann, and Stefan Vonhoff. 2011. "RNA Aptamers and Spiegelmers: Synthesis, Purification, and Post-Synthetic PEG Conjugation." In *Current Protocols in Nucleic Acid Chemistry*, Chapter 4:4.46.1-4.46.30. Hoboken, NJ, USA: John Wiley & Sons, Inc. doi:10.1002/0471142700.nc0446s46.
- Hofmann, HP, S Limmer, V Hornung, M Sprinzl - Rna, and undefined 1997. 2019. "Ni²⁺-Binding RNA Motifs with an Asymmetric Purine-Rich Internal Loop and a GA Base Pair." *Rnajournal.Cshlp.Org*. Accessed March 9. <http://rnajournal.cshlp.org/content/3/11/1289.short>.
- Hung, Li-Wei, Masanori Kohmura, Yasuo Ariyoshi, and Sung-Hou Kim. 1999. "Structural Differences in d and l -Monellin in the Crystals of Racemic Mixture 1 Edited by D. C. Rees." *Journal of Molecular Biology* 285 (1): 311–21. doi:10.1006/jmbi.1998.2308.
- Huynh, Kathy, and Carrie L Partch. 2015. "Analysis of Protein Stability and Ligand Interactions by Thermal Shift Assay." *Current Protocols in Protein Science* 79: 28.9.1-14. doi:10.1002/0471140864.ps2809s79.
- Imlay, James A. 2013. *Theoxidative Stress : Lessons from a Model Bacterium*. *Nature*

- Reviews Microbiology*. Vol. 11. doi:10.1038/nrmicro3032.The.
- Inui, Akio, Akihiro Asakawa, Cyril Y. Bowers, Giovanni Mantovani, Alessandro Laviano, Michael M. Meguid, and Mineko Fujimiya. 2004. "Ghrelin, Appetite, and Gastric Motility: The Emerging Role of the Stomach as an Endocrine Organ." *The FASEB Journal* 18 (3): 439–56. doi:10.1096/fj.03-0641rev.
- Jacquamet, L, D A K Traoré, J.-L. Ferrer, O Proux, D Testemale, J.-L. Hazemann, E Nazarenko, et al. 2009. "Structural Characterization of the Active Form of PerR: Insights into the Metal-Induced Activation of PerR and Fur Proteins for DNA Binding." *Molecular Microbiology* 73 (1). John Wiley & Sons, Ltd (10.1111): 20–31. doi:10.1111/j.1365-2958.2009.06753.x.
- Jacques, David A, and Jill Trehwella. 2010. "Small-Angle Scattering for Structural Biology—Expanding the Frontier While Avoiding the Pitfalls." *Protein Science* 19 (4): 642–57. doi:10.1002/pro.351.
- Jancarik, J, and S.-H. Kim. 1991. "Sparse Matrix Sampling: A Screening Method for Crystallization of Proteins." *Journal of Applied Crystallography* 24 (4): 409–11. doi:10.1107/S0021889891004430.
- Jerlhag, Elisabet, Emil Egecioglu, Suzanne L. Dickson, Malin Andersson, Lennart Svensson, and Jörgen A. Engel. 2006. "Ghrelin Stimulates Locomotor Activity and Accumbal Dopamine-Overflow via Central Cholinergic Systems in Mice: Implications for Its Involvement in Brain Reward." *Addiction Biology* 11 (1). Blackwell Publishing Ltd: 45–54. doi:10.1111/j.1369-1600.2006.00002.x.
- Jerlhag, Elisabet, Emil Egecioglu, Suzanne L. Dickson, Annika Douhan, Lennart Svensson, and Jörgen A. Engel. 2007. "Ghrelin Administration into Tegmental Areas Stimulates Locomotor Activity and Increases Extracellular Concentration of Dopamine in the Nucleus Accumbens." *Addiction Biology* 12 (1). Blackwell Publishing Ltd: 6–16. doi:10.1111/j.1369-1600.2006.00041.x.
- Johne, HA, and L Frothingham. 1895. "Ein Eigentümlicher Fall von Tuberkulose Beim Rind." *Deutsche Zeitung Für Thiermedizin Und Vergl. Path* 21: 438–54.
- Jullien, Nicolas, and Jean-Paul Herman. 2011. "LUEGO: A Cost and Time Saving Gel Shift Procedure." *BioTechniques* 51 (4). Future Science: 267–69. doi:10.2144/000113751.
- Jurica, Melissa S, Lawrence J Licklider, Steven P Gygi, Nikolaus Grigorieff, and Melissa J Moore. 2002. "Purification and Characterization of Native Spliceosomes Suitable for Three-Dimensional Structural Analysis." *RNA* 8 (4). Cambridge University Press: 426–39. doi:DOI: 10.1017/S1355838202021088.
- Kabsch, Wolfgang, Wilson K., and Ravelli R. B. G. 2010. "XDS." *Acta Crystallographica Section D Biological Crystallography* 66 (2). International Union of Crystallography: 125–32. doi:10.1107/S0907444909047337.
- Kabsch, Wolfgang, Bolotovskiy R., Rossmann M. G., and Minor W. 2010. "Integration, Scaling, Space-Group Assignment and Post-Refinement." *Acta Crystallographica Section D Biological Crystallography* 66 (2). International Union of Crystallography: 133–44. doi:10.1107/S0907444909047374.
- Kahn, R, R Fourme, R Bosshard, M Chiadmi, J L Risler, O Dideberg, and J P Wery.

1985. "Crystal Structure Study of Opsanus Tau Parvalbumin by Multiwavelength Anomalous Diffraction." *FEBS Letters* 179 (1). England: 133–37.
- Kamiji, Mayra M, and Akio Inui. 2008. "The Role of Ghrelin and Ghrelin Analogues in Wasting Disease." *Current Opinion in Clinical Nutrition and Metabolic Care* 11 (4): 443–51. doi:10.1097/MCO.0b013e328303dee4.
- Karle, J, and H Hauptman. 1950. "The Phases and Magnitudes of the Structure Factors." *Acta Crystallographica* 3 (3): 181–87. doi:10.1107/S0365110X50000446.
- . 1956. "A Theory of Phase Determination for the Four Types of Non-Centrosymmetric Space Groups $1P222$, $2P22$, $3P_12$, $3P_22$." *Acta Crystallographica* 9 (8): 635–51. doi:10.1107/S0365110X56001741.
- Kazantsev, Alexei V., Angelika A. Krivenko, Daniel J. Harrington, Stephen R. Holbrook, Paul D. Adams, and Norman R. Pace. 2005. "Crystal Structure of a Bacterial Ribonuclease P RNA." *Proceedings of the National Academy of Sciences of the United States of America* 102 (38). National Academy of Sciences: 13392. doi:10.1073/PNAS.0506662102.
- Keefe, Anthony D., Supriya Pai, and Andrew Ellington. 2010. "Aptamers as Therapeutics." *Nature Reviews Drug Discovery* 9 (7). Nature Publishing Group: 537–50. doi:10.1038/nrd3141.
- Kelley, Lawrence A, Stefans Mezulis, Christopher M Yates, Mark N Wass, and Michael J E Sternberg. 2015. "The Pyre2 Web Portal for Protein Modeling, Prediction and Analysis." *Nature Protocols* 10 (6): 845–58. doi:10.1038/nprot.2015.053.
- Kelly, Sharon M, Thomas J Jess, and Nicholas C Price. 2005. "How to Study Proteins by Circular Dichroism." *Biochimica et Biophysica Acta* 1751 (2): 119–39. doi:10.1016/j.bbapap.2005.06.005.
- Kikhney, Alexey G, and Dmitri I Svergun. 2015. "A Practical Guide to Small Angle X-Ray Scattering (SAXS) of Flexible and Intrinsically Disordered Proteins." *FEBS Letters* 589 (19). Federation of European Biochemical Societies: 2570–77. doi:10.1016/j.febslet.2015.08.027.
- Kim, In Hwang, Yancheng Wen, Jee-Soo Son, Kyu-Ho Lee, and Kun-Soo Kim. 2013. "The Fur-Iron Complex Modulates Expression of the Quorum-Sensing Master Regulator, SmcR, To Control Expression of Virulence Factors in *Vibrio Vulnificus*." Edited by A Camilli. *Infection and Immunity* 81 (8): 2888 LP-2898. doi:10.1128/IAI.00375-13.
- Kirchner, Henriette, Jesus A Gutierrez, Patricia J Solenberg, Paul T Pfluger, Traci A Czyzyk, Jill A Willency, Annette Schürmann, et al. 2009. "GOAT Links Dietary Lipids with the Endocrine Control of Energy Balance." *Nature Medicine* 15 (7): 741–45. doi:10.1038/nm.1997.
- Klußmann, Sven, Alexis Nolte, Rolf Bald, Volker A. Erdmann, and Jens P. Fürste. 1996. "Mirror-Image RNA That Binds D-Adenosine." *Nature Biotechnology* 14 (9): 1112–15. doi:10.1038/nbt0996-1112.
- Kobelt, P, S Helmling, A Stengel, B Wlotzka, V Andresen, B F Klapp, B Wiedenmann, S Klussmann, and H Mönnikes. 2006. "Anti-Ghrelin Spiegelmer NOX-B11

- Inhibits Neurostimulatory and Orexigenic Effects of Peripheral Ghrelin in Rats.” *Gut* 55 (6): 788–92. doi:10.1136/gut.2004.061010.
- Kojima, M, H Hosoda, Y Date, M Nakazato, H Matsuo, and K Kangawa. 1999. “Ghrelin Is a Growth-Hormone-Releasing Acylated Peptide from Stomach.” *Nature* 402 (6762): 656–60. doi:10.1038/45230.
- Kojima, Masayasu, and Kenji Kangawa. 2005. “Ghrelin: Structure and Function.” *Physiological Reviews* 85 (2): 495–522. doi:10.1152/physrev.00012.2004.
- Konarev, Petr V, Vladimir V Volkov, Anna V Sokolova, Michel H J Koch, and Dmitri I Svergun. 2003. “PRIMUS: A Windows PC-Based System for Small-Angle Scattering Data Analysis.” *Journal of Applied Crystallography* 36 (5): 1277–82. doi:10.1107/S0021889803012779.
- Koutouratsas, Tilemachos, Theodora Kalli, Georgios Karamanolis, and Maria Gazouli. 2019. “Contribution of Ghrelin to Functional Gastrointestinal Disorders’ Pathogenesis.” *World Journal of Gastroenterology* 25 (5). Baishideng Publishing Group Inc.: 539–51. doi:10.3748/wjg.v25.i5.539.
- Kuehnel, M P, R Goethe, A Habermann, E Mueller, M Rohde, G Griffiths, and P Valentin-Weigand. 2001. “Characterization of the Intracellular Survival of *Mycobacterium Avium* Ssp. *Paratuberculosis*: Phagosomal PH and Fusogenicity in J774 Macrophages Compared with Other Mycobacteria.” *Cellular Microbiology* 3 (8): 551–66. <http://www.ncbi.nlm.nih.gov/pubmed/11488816>.
- Kümmel, R. 1989. “P. W. Atkins: Physikalische Chemie. Weinheim, VCH Verlagsgesellschaft, 1987, 890 S., 542 Abb., 74 Tab., DM 98,-, ISBN 3-527-25913-9.” *Acta Hydrochimica et Hydrobiologica* 17 (2). John Wiley & Sons, Ltd: 227. doi:10.1002/ahch.19890170216.
- Kuwahara, Masayasu, and Naoki Sugimoto. 2010. “Molecular Evolution of Functional Nucleic Acids with Chemical Modifications.” *Molecules* 15 (8): 5423–44. doi:10.3390/molecules15085423.
- Lee, Jin-Won, and John D Helmann. 2006. “The PerR Transcription Factor Senses H₂O₂ by Metal-Catalysed Histidine Oxidation.” *Nature* 440 (March). Nature Publishing Group: 363. <https://doi.org/10.1038/nature04537>.
- Lee, Jin Won, and John D. Helmann. 2006. “Biochemical Characterization of the Structural Zn₂₊ Site in the *Bacillus Subtilis* Peroxide Sensor PerR.” *Journal of Biological Chemistry* 281 (33): 23567–78. doi:10.1074/jbc.M603968200.
- Lim, Chung Thong, Blerina Kola, Ashley Grossman, and Márta Korbonits. 2011. “The Expression of Ghrelin O-Acyltransferase (GOAT) in Human Tissues.” *Endocrine Journal* 58 (8): 707–10. <http://www.ncbi.nlm.nih.gov/pubmed/21646729>.
- Liu, Qun, Qinglian Liu, and Wayne A Hendrickson. 2013. “Robust Structural Analysis of Native Biological Macromolecules from Multi-Crystal Anomalous Diffraction Data.” *Acta Crystallographica Section D* 69 (7): 1314–32. doi:10.1107/S0907444913001479.
- Liu, Qun, Zhen Zhang, and Wayne A Hendrickson. 2011. “Multi-Crystal Anomalous Diffraction for Low-Resolution Macromolecular Phasing.” *Acta Crystallographica. Section D, Biological Crystallography* 67 (Pt 1). United States:

- 45–59. doi:10.1107/S0907444910046573.
- Liu, Zhao, Zhongzhou Chen, and Wei Wu. 2012. “Crystallization and Preliminary X-Ray Studies of Ferric Uptake Regulator from *Magnetospirillum Gryphiswaldense*.” *Acta Crystallographica. Section F, Structural Biology and Crystallization Communications* 68 (Pt 8). International Union of Crystallography: 902–5. doi:10.1107/S1744309112024311.
- Losinger, Willard C. 2005. “Economic Impact of Reduced Milk Production Associated with Johne’s Disease on Dairy Operations in the USA.” *Journal of Dairy Research* 72 (4). Cambridge University Press: 425–32. doi:DOI: 10.1017/S0022029905001007.
- Louvel, H el ene, Tamotsu Kanai, Haruyuki Atomi, and John N Reeve. 2009. “The Fur Iron Regulator-like Protein Is Cryptic in the Hyperthermophilic Archaeon *Thermococcus Kodakaraensis*.” *FEMS Microbiology Letters* 295 (1): 117–28. doi:10.1111/j.1574-6968.2009.01594.x.
- Lucarelli, Debora. 2006. “Structural Studies on Ferric Uptake Regulator Proteins from *Mycobacterium Tuberculosis*.”
- Lucarelli, Debora, Santina Russo, Elspeth Garman, Anna Milano, Wolfram Meyer-klaucke, and Ehmke Pohl. 2007. “Crystal Structure and Function of the Zinc Uptake Regulator FurB from *Mycobacterium Tuberculosis*” 282 (13): 9914–22. doi:10.1074/jbc.M609974200.
- Lucarelli, Debora, Michael L Vasil, Wolfram Meyer-Klaucke, and Ehmke Pohl. 2008. “The Metal-Dependent Regulators FurA and FurB from *Mycobacterium Tuberculosis*.” *International Journal of Molecular Sciences* 9 (8). Molecular Diversity Preservation International (MDPI): 1548–60. doi:10.3390/ijms9081548.
- Luo, Zhipu. 2016. “Selenourea: A Convenient Phasing Vehicle for Macromolecular X-Ray Crystal Structures.” *Scientific Reports* 6 (1). Nature Publishing Group: 37123. doi:10.1038/srep37123.
- Lutter, Michael, Ichiro Sakata, Sherri Osborne-Lawrence, Sherry A Rovinsky, Jason G Anderson, Saendy Jung, Shari Birnbaum, et al. 2008. “The Orexigenic Hormone Ghrelin Defends against Depressive Symptoms of Chronic Stress.” *Nature Neuroscience* 11 (7): 752–53. doi:10.1038/nn.2139.
- Ma, Kan, Lou-sing Kan, and Kuan Wang. 2001. “Polyproline II Helix Is a Key Structural Motif of the Elastic PEVK Segment of Titin.” *Biochemistry* 40 (12): 3427–38. doi:10.1021/bi0022792.
- Ma, Zhen, Scott E Gabriel, and John D Helmann. 2011. “Sequential Binding and Sensing of Zn(II) by *Bacillus Subtilis* Zur.” *Nucleic Acids Research* 39 (21): 9130–38. doi:10.1093/nar/gkr625.
- Maasch, C., K. Buchner, D. Eulberg, S. Vonhoff, and S. Klussmann. 2008. “Physicochemical Stability of NOX-E36, a 40mer L-RNA (Spiegelmer) for Therapeutic Applications.” *Nucleic Acids Symposium Series* 52 (1): 61–62. doi:10.1093/nass/nrn031.
- Maciag, Anna, Elisa Dainese, G Marcela Rodriguez, Anna Milano, Roberta Provvedi, Maria R Pasca, Issar Smith, Giorgio Pal u, Giovanna Riccardi, and Riccardo

- Manganelli. 2007. "Global Analysis of the *Mycobacterium Tuberculosis* Zur (FurB) Regulon." *Journal of Bacteriology* 189 (3). American Society for Microbiology: 730–40. doi:10.1128/JB.01190-06.
- Mandal, Kalyaneswar, Brad L. Pentelute, Valentina Tereshko, Vilasak Thammavongsa, Olaf Schneewind, Anthony A. Kossiakoff, and Stephen B H Kent. 2009. "Racemic Crystallography of Synthetic Protein Enantiomers Used to Determine the X-Ray Structure of Plectasin by Direct Methods." *Protein Science* 18 (6): 1146–54. doi:10.1002/pro.127.
- Martín-Pastor, Manuel, Antonia De Capua, Carlos J.P. Álvarez, M. Dolores Díaz-Hernández, Jesús Jiménez-Barbero, Felipe F. Casanueva, and Yolanda Pazos. 2010. "Interaction between Ghrelin and the Ghrelin Receptor (GHS-R1a), a NMR Study Using Living Cells." *Bioorganic & Medicinal Chemistry* 18 (4): 1583–90. doi:10.1016/j.bmc.2010.01.004.
- Masquida, B, and E Westhof. 2000. "On the Wobble GoU and Related Pairs." *RNA (New York, N.Y.)* 6 (1): 9–15. <http://www.ncbi.nlm.nih.gov/pubmed/10668794>.
- Massé, Eric, and Susan Gottesman. 2002. "A Small RNA Regulates the Expression of Genes Involved in Iron Metabolism in *Escherichia Coli*." *Proceedings of the National Academy of Sciences* 99 (7): 4620 LP-4625. doi:10.1073/pnas.032066599.
- Master, S S, B Springer, P Sander, E C Boettger, V Deretic, and G S Timmins. 2002. "Oxidative Stress Response Genes in *Mycobacterium Tuberculosis*: Role of *AhpC* in Resistance to Peroxynitrite and Stage-Specific Survival in Macrophages." *Microbiology (Reading, England)* 148 (Pt 10). England: 3139–44. doi:10.1099/00221287-148-10-3139.
- Masuda, Yutaka, Tsuguhiko Tanaka, Norio Inomata, Norio Ohnuma, Shoji Tanaka, Zen Itoh, Hiroshi Hosoda, Masayasu Kojima, and Kenji Kangawa. 2000. "Ghrelin Stimulates Gastric Acid Secretion and Motility in Rats." *Biochemical and Biophysical Research Communications* 276 (3): 905–8. doi:10.1006/bbrc.2000.3568.
- Matthews, Brian W. 2009. "Racemic Crystallography - Easy Crystals and Easy Structures: What's Not to Like?" *Protein Science* 18 (6): 1135–38. doi:10.1002/pro.125.
- McCoy, Airlie J., Laurent C. Storoni, Randy J. Read, and IUCr. 2004. "Simple Algorithm for a Maximum-Likelihood SAD Function." *Acta Crystallographica Section D Biological Crystallography* 60 (7). International Union of Crystallography: 1220–28. doi:10.1107/S0907444904009990.
- McCoy, Airlie J, Ralf W Grosse-Kunstleve, Paul D Adams, Martyn D Winn, Laurent C Storoni, and Randy J Read. 2007. "Phaser Crystallographic Software." *Journal of Applied Crystallography* 40 (4): 658–74. doi:10.1107/S0021889807021206.
- McPherson, Alexander. 1991. "A Brief History of Protein Crystal Growth." *Journal of Crystal Growth* 110 (1): 1–10. doi:[https://doi.org/10.1016/0022-0248\(91\)90859-4](https://doi.org/10.1016/0022-0248(91)90859-4).
- Mertens, Haydyn D T, and Dmitri I Svergun. 2010. "Structural Characterization of Proteins and Complexes Using Small-Angle X-Ray Solution Scattering." *Journal*

- of Structural Biology* 172 (1): 128–41.
doi:<https://doi.org/10.1016/j.jsb.2010.06.012>.
- Montange, Rebecca K., and Robert T. Batey. 2006. “Structure of the S-Adenosylmethionine Riboswitch Regulatory mRNA Element.” *Nature* 441 (7097): 1172–75. doi:10.1038/nature04819.
- Morton, GJ, and MW Schwartz. 2001. “The NPY/AgRP Neuron and Energy Homeostasis.” *International Journal of Obesity* 25 (S5): S56–62. doi:10.1038/sj.ijo.0801915.
- Müller, T. D., R. Nogueiras, M. L. Andermann, Z. B. Andrews, S. D. Anker, J. Argente, R. L. Batterham, et al. 2015. “Ghrelin.” *Molecular Metabolism* 4 (6): 437–60. doi:10.1016/j.molmet.2015.03.005.
- Müller, Timo D., Diego Perez-Tilve, Jenny Tong, Paul T. Pfluger, and Matthias H. Tschöp. 2010. “Ghrelin and Its Potential in the Treatment of Eating/Wasting Disorders and Cachexia.” *Journal of Cachexia, Sarcopenia and Muscle* 1 (2): 159–67. doi:10.1007/s13539-010-0012-4.
- Murshudov, G. N., A. A. Vagin, E. J. Dodson, and IUCr. 1997. “Refinement of Macromolecular Structures by the Maximum-Likelihood Method.” *Acta Crystallographica Section D Biological Crystallography* 53 (3). International Union of Crystallography: 240–55. doi:10.1107/S09074444996012255.
- Nakane, Takanori, Changyong Song, Mamoru Suzuki, Eriko Nango, Jun Kobayashi, Tetsuya Masuda, Shigeyuki Inoue, et al. 2015. “Native Sulfur/Chlorine SAD Phasing for Serial Femtosecond Crystallography.” *Acta Crystallographica Section D Biological Crystallography* 71 (12): 2519–25. doi:10.1107/S139900471501857X.
- Naser, Saleh A, Saisathya Thanigachalam, C Thomas Dow, and Michael T Collins. 2013. “Exploring the Role of *Mycobacterium Avium* Subspecies *Paratuberculosis* in the Pathogenesis of Type 1 Diabetes Mellitus: A Pilot Study.” *Gut Pathogens* 5 (1): 14. doi:10.1186/1757-4749-5-14.
- Nelson, N. 1999. “Metal Ion Transporters and Homeostasis.” *The EMBO Journal* 18 (16): 4361–71. doi:10.1093/emboj/18.16.4361.
- Nishi, Yoshihiro, Hiroshi Hiejima, Hiroshi Hosoda, Hiroyuki Kaiya, Kenji Mori, Yoshihiko Fukue, Toshihiko Yanase, Hajime Nawata, Kenji Kangawa, and Masayasu Kojima. 2005. “Ingested Medium-Chain Fatty Acids Are Directly Utilized for the Acyl Modification of Ghrelin.” *Endocrinology* 146 (5): 2255–64. doi:10.1210/en.2004-0695.
- Oberthür, Dominik, John Achenbach, Azat Gabdulkhakov, Klaus Buchner, Christian Maasch, Sven Falke, Dirk Rehders, Sven Klussmann, and Christian Betzel. 2015. “Crystal Structure of a Mirror-Image L-RNA Aptamer (Spiegelmer) in Complex with the Natural L-Protein Target CCL2.” *Nature Communications* 6: 6923. doi:10.1038/ncomms7923.
- Ochsner, U A, A I Vasil, and M L Vasil. 1995. “Role of the Ferric Uptake Regulator of *Pseudomonas Aeruginosa* in the Regulation of Siderophores and Exotoxin A Expression: Purification and Activity on Iron-Regulated Promoters.” *Journal of*

- Bacteriology* 177 (24): 7194 LP-7201. doi:10.1128/jb.177.24.7194-7201.1995.
- Okumura, Hiroyuki, Noritoshi Nagaya, Mitsunobu Enomoto, Eiichiroh Nakagawa, Hideo Oya, and Kenji Kangawa. 2002. "Vasodilatory Effect of Ghrelin, an Endogenous Peptide from the Stomach." *Journal of Cardiovascular Pharmacology* 39 (6): 779–83. <http://www.ncbi.nlm.nih.gov/pubmed/12021570>.
- Olieric, Vincent, Tobias Weinert, Aaron D. Finke, Carolin Anders, Dianfan Li, Natacha Olieric, Camelia N. Borca, et al. 2016. "Data-Collection Strategy for Challenging Native SAD Phasing." *Acta Crystallographica Section D Structural Biology* 72 (3): 421–29. doi:10.1107/s2059798315024110.
- Ollinger, Juliane, Kyung-Bok Song, Haike Antelmann, Michael Hecker, and John D Helmann. 2006. "Role of the *Fur* Regulon in Iron Transport in *Bacillus Subtilis*." *Journal of Bacteriology* 188 (10). American Society for Microbiology: 3664–73. doi:10.1128/JB.188.10.3664-3673.2006.
- Overduin, Joost, Dianne P. Figlewicz, Jennifer Bennett-Jay, Sepideh Kittleson, and David E. Cummings. 2012. "Ghrelin Increases the Motivation to Eat, but Does Not Alter Food Palatability." *American Journal of Physiology - Regulatory, Integrative and Comparative Physiology* 303 (3). <http://ajpregu.physiology.org/content/303/3/R259.long>.
- Paccagnini, Daniela, Lee Sieswerda, Valentina Rosu, Speranza Masala, Adolfo Pacifico, Maria Gazouli, John Ikonomopoulos, Niyaz Ahmed, Stefania Zanetti, and Leonardo A Sechi. 2009. "Linking Chronic Infection and Autoimmune Diseases: *Mycobacterium Avium* Subspecies *Paratuberculosis*, SLC11A1 Polymorphisms and Type-1 Diabetes Mellitus." Edited by Stefan Bereswill. *PloS One* 4 (9): e7109. doi:10.1371/journal.pone.0007109.
- Palyada, K., D. Threadgill, and A. Stintzi. 2004. "Iron Acquisition and Regulation in *Campylobacter Jejuni*." *Journal of Bacteriology* 186 (14): 4714–29. doi:10.1128/JB.186.14.4714-4729.2004.
- Pape, Thomas, and Thomas R. Schneider. 2004. "*HKL2MAP* : A Graphical User Interface for Macromolecular Phasing with *SHELX* Programs." *Journal of Applied Crystallography* 37 (5). International Union of Crystallography (IUCr): 843–44. doi:10.1107/S0021889804018047.
- Parisien, Marc, and François Major. 2008. "The MC-Fold and MC-Sym Pipeline Infers RNA Structure from Sequence Data." *Nature* 452 (March). Nature Publishing Group: 51. <https://doi.org/10.1038/nature06684>.
- Patzer, S I, and Klaus Hantke. 1998. "The ZnuABC High-Affinity Zinc Uptake System and Its Regulator Zur in *Escherichia Coli*." *Molecular Microbiology* 28 (6). England: 1199–1210.
- Peng, Jian, and Jinbo Xu. 2011. "RaptorX: Exploiting Structure Information for Protein Alignment by Statistical Inference." *Proteins* 79 Suppl 10 (Suppl 10). NIH Public Access: 161–71. doi:10.1002/prot.23175.
- Pentelute, Brad L., Zachary P. Gates, Valentina Tereshko, Jennifer L. Dashnau, Jane M. Vanderkooi, Anthony A. Kossiakoff, and Stephen B. H. Kent. 2008. "X-Ray Structure of Snow Flea Antifreeze Protein Determined by Racemic Crystallization

- of Synthetic Protein Enantiomers.” *Journal of the American Chemical Society* 130 (30): 9695–9701. doi:10.1021/ja8013538.
- Peselis, Alla, and Alexander Serganov. 2012. “Structural Insights into Ligand Binding and Gene Expression Control by an Adenosylcobalamin Riboswitch.” *Nature Structural & Molecular Biology* 19 (11): 1182–84. doi:10.1038/nsmb.2405.
- Petoukhov, Maxim V, and Dmitri I Svergun. 2005. “Global Rigid Body Modeling of Macromolecular Complexes against Small-Angle Scattering Data.” *Biophysical Journal* 89 (2). The Biophysical Society: 1237–50. doi:10.1529/biophysj.105.064154.
- Pettersen, Eric F., Thomas D. Goddard, Conrad C. Huang, Gregory S. Couch, Daniel M. Greenblatt, Elaine C. Meng, and Thomas E. Ferrin. 2004. “UCSF Chimera?A Visualization System for Exploratory Research and Analysis.” *Journal of Computational Chemistry* 25 (13): 1605–12. doi:10.1002/jcc.20084.
- Pfingsten, J. S., D. A. Costantino, and J. S. Kieft. 2006. “Structural Basis for Ribosome Recruitment and Manipulation by a Viral IRES RNA.” *Science* 314 (5804): 1450–54. doi:10.1126/science.1133281.
- Phillips, James C, David H Templeton, Lieselotte K Templeton, and Keith O Hodgson. 1978. “LIII-Edge Anomalous X-Ray Scattering by Cesium Measured with Synchrotron Radiation.” *Science* 201 (4352). American Association for the Advancement of Science: 257–59. doi:10.1126/science.201.4352.257.
- Pinochet-Barros, Azul, and John D Helmann. 2017. “Redox Sensing by Fe²⁺ in Bacterial Fur Family Metalloregulators.” *Antioxidants & Redox Signaling* 29 (18). Mary Ann Liebert, Inc., publishers: 1858–71. doi:10.1089/ars.2017.7359.
- Potterton, Liz, Jon Agirre, Charles Ballard, Kevin Cowtan, Eleanor Dodson, Phil R. Evans, Huw T. Jenkins, et al. 2018. “CCP 4 i 2: The New Graphical User Interface to the CCP 4 Program Suite.” *Acta Crystallographica Section D Structural Biology* 74 (2). International Union of Crystallography: 68–84. doi:10.1107/S2059798317016035.
- Pym, Alexander S, Pilar Domenech, Nadine Honoré, Jian Song, Vojo Deretic, and Stewart T Cole. 2001. “Regulation of *Catalase-peroxidase (KatG)* Expression, Isoniazid Sensitivity and Virulence by *FurA* of *Mycobacterium Tuberculosis*.” *Molecular Microbiology* 40 (4). John Wiley & Sons, Ltd (10.1111): 879–89. doi:10.1046/j.1365-2958.2001.02427.x.
- Raiber, Eun-Ang, Pierre Murat, Dimitri Y Chirgadze, Dario Beraldi, Ben F Luisi, and Shankar Balasubramanian. 2015. “5-Formylcytosine Alters the Structure of the DNA Double Helix.” *Nature Structural & Molecular Biology* 22 (1): 44–49. doi:10.1038/nsmb.2936.
- Reed, Jacquelyn A, Stephen C Benoit, Paul T Pfluger, Matthias H Tschöp, David A D’Alessio, and Randy J Seeley. 2008. “Mice with Chronically Increased Circulating Ghrelin Develop Age-Related Glucose Intolerance.” *American Journal of Physiology. Endocrinology and Metabolism* 294 (4): E752-60. doi:10.1152/ajpendo.00463.2007.
- Ricco, Riccardo De, Daniela Valensin, Elena Gaggelli, and Gianni Valensin. 2013.

- “Conformation Propensities of Des-Acyl-Ghrelin as Probed by CD and NMR.” *Peptides* 43 (May): 62–67. doi:10.1016/j.peptides.2013.02.021.
- Richter, Gerhard. 2003. *Praktische Biochemie*. Stuttgart [u.a.]: Thieme.
- Rizzo, Manfredi, Ali A Rizvi, Emina Sudar, Sanja Soskic, Milan Obradovic, Giuseppe Montalto, Mohamed Boutjdir, Dimitri P Mikhailidis, and Esma R Isenovic. 2013. “A Review of the Cardiovascular and Anti-Atherogenic Effects of Ghrelin.” *Current Pharmaceutical Design* 19 (27): 4953–63. <http://www.ncbi.nlm.nih.gov/pubmed/23278489>.
- Robert, Xavier, and Patrice Gouet. 2014. “Deciphering Key Features in Protein Structures with the New ENDscript Server.” *Nucleic Acids Research* 42 (W1). Narnia: W320–24. doi:10.1093/nar/gku316.
- Robertson, Debra L., and Gerald F. Joyce. 1990. “Selection *in Vitro* of an RNA Enzyme That Specifically Cleaves Single-Stranded DNA.” *Nature* 344 (6265): 467–68. doi:10.1038/344467a0.
- Robertson, Michael P, and William G Scott. 2008. “A General Method for Phasing Novel Complex RNA Crystal Structures without Heavy-Atom Derivatives.” *Acta Crystallographica. Section D, Biological Crystallography* D64 (Pt 7). International Union of Crystallography: 738–44. doi:10.1107/S0907444908011578.
- Rose, John P., Bi-Cheng Wang, and Manfred S. Weiss. 2015. “Native SAD Is Maturing.” *IUCrJ* 2 (4). International Union of Crystallography: 431–40. doi:10.1107/S2052252515008337.
- Rosenbaum, G, K C Holmes, and J Witz. 1971. “Synchrotron Radiation as a Source for X-Ray Diffraction.” *Nature* 230 (5294): 434–37. doi:10.1038/230434a0.
- Rossmann, Michael G. 1990. “The Molecular Replacement Method.” *Acta Crystallographica. Section A, Foundations of Crystallography* 46 (Pt 2): 73–82.
- Russell, R., X. Zhuang, H. P. Babcock, I. S. Millett, S. Doniach, S. Chu, and D. Herschlag. 2002. “Exploring the Folding Landscape of a Structured RNA.” *Proceedings of the National Academy of Sciences* 99 (1): 155–60. doi:10.1073/pnas.221593598.
- Sakata, Ichiro, Jing Yang, Charlotte E. Lee, Sherri Osborne-Lawrence, Sherry A. Rovinsky, Joel K. Elmquist, and Jeffrey M. Zigman. 2009. “Colocalization of Ghrelin O -Acyltransferase and Ghrelin in Gastric Mucosal Cells.” *American Journal of Physiology-Endocrinology and Metabolism* 297 (1): E134–41. doi:10.1152/ajpendo.90859.2008.
- Sala, Claudia, Francesca Forti, Elisabetta Di Florio, Fabio Canneva, Anna Milano, Giovanna Riccardi, and Daniela Ghisotti. 2003. “*Mycobacterium Tuberculosis* FurA Autoregulates Its Own Expression.” *Journal of Bacteriology* 185 (18). American Society for Microbiology: 5357–62. doi:10.1128/JB.185.18.5357-5362.2003.
- Salem, Mohamed, Carsten Heydel, Amr El-Sayed, Samia A Ahmed, Michael Zschöck, and George Baljer. 2013. “*Mycobacterium Avium* Subspecies *Paratuberculosis*: An Insidious Problem for the Ruminant Industry.” *Tropical Animal Health and Production* 45 (2): 351–66. doi:10.1007/s11250-012-0274-2.

- Salgado, M, M Alfaro, F Salazar, E Troncoso, R M Mitchell, L Ramirez, A Naguil, P Zamorano, and M T Collins. 2013. "Effect of Soil Slope on the Appearance of *Mycobacterium Avium* Subsp. *Paratuberculosis* in Water Running off Grassland Soil after Application of Contaminated Slurry." *Applied and Environmental Microbiology* 79 (12): 3544–52. doi:10.1128/AEM.00610-13.
- Sanger, Gareth J., John Broad, Brid Callaghan, and John B. Furness. 2016. "Ghrelin and Motilin Control Systems in GI Physiology and Therapeutics." In *Handbook of Experimental Pharmacology*, 239:379–416. doi:10.1007/164_2016_104.
- Sanger, Gareth J., and John B. Furness. 2016. "Ghrelin and Motilin Receptors as Drug Targets for Gastrointestinal Disorders." *Nature Reviews Gastroenterology & Hepatology* 13 (1): 38–48. doi:10.1038/nrgastro.2015.163.
- Sato, T., Y. Nakamura, Y. Shiimura, H. Ohgusu, K. Kangawa, and M. Kojima. 2012. "Structure, Regulation and Function of Ghrelin." *Journal of Biochemistry* 151 (2): 119–28. doi:10.1093/jb/mvr134.
- Sayed, S. G., H. Hägele, O. P. Kulkarni, K. Endlich, S. Segerer, D. Eulberg, S. Klusmann, and H.-J. Anders. 2009. "Podocytes Produce Homeostatic Chemokine Stromal Cell-Derived Factor-1/CXCL12, Which Contributes to Glomerulosclerosis, Podocyte Loss and Albuminuria in a Mouse Model of Type 2 Diabetes." *Diabetologia* 52 (11): 2445–54. doi:10.1007/s00125-009-1493-6.
- Schneider, Thomas R, and George M Sheldrick. 2002. "Substructure Solution with SHELXD." *Acta Crystallographica. Section D, Biological Crystallography* 58 (Pt 10 Pt 2): 1772–79. <http://www.ncbi.nlm.nih.gov/pubmed/12351820>.
- Schöneich, Christian. 2000. "Mechanisms of Metal-Catalyzed Oxidation of Histidine to 2-Oxo-Histidine in Peptides and Proteins." *Journal of Pharmaceutical and Biomedical Analysis* 21 (6): 1093–97. doi:[https://doi.org/10.1016/S0731-7085\(99\)00182-X](https://doi.org/10.1016/S0731-7085(99)00182-X).
- Schrödinger, LLC. 2015. "The {PyMOL} Molecular Graphics System, Version~1.8."
- Schürer, Heike, Jens Schuster, Kathrin Lang, and Mario Mörl. 2002. "A Universal Method to Produce *in Vitro* Transcripts with Homogeneous 3' Ends." *Nucleic Acids Research* 30 (12): e56–e56. doi:10.1093/nar/gnf055.
- Scott, William G, John T Finch, Richard Grenfell, Jan Fogg, Terry Smith, Michael J Gait, and Aaron Klug. 1995. "Rapid Crystallization of Chemically Synthesized Hammerhead RNAs Using a Double Screening Procedure." *Journal of Molecular Biology* 250 (3): 327–32. doi:<https://doi.org/10.1006/jmbi.1995.0380>.
- Seaver, L C, and J A Imlay. 2001. "Alkyl Hydroperoxide Reductase Is the Primary Scavenger of Endogenous Hydrogen Peroxide in *Escherichia Coli*." *Journal of Bacteriology* 183 (24). American Society for Microbiology: 7173–81. doi:10.1128/JB.183.24.7173-7181.2001.
- Sebastian, Shite, Sarika Agarwal, John R Murphy, and Caroline Attardo Genco. 2002. "The Gonococcal Fur Regulon: Identification of Additional Genes Involved in Major Catabolic, Recombination, and Secretory Pathways." *Journal of Bacteriology* 184 (14): 3965 LP-3974. doi:10.1128/JB.184.14.3965-3974.2002.
- Secott, T E, T L Lin, and C C Wu. 2004. "*Mycobacterium Avium* Subsp.

- Paratuberculosis* Fibronectin Attachment Protein Facilitates M-Cell Targeting and Invasion through a Fibronectin Bridge with Host Integrins.” *Infection and Immunity* 72 (7): 3724–32. doi:10.1128/IAI.72.7.3724-3732.2004.
- Sethu, Ramakrishnan, Eric Gouré, Luca Signor, Christelle Caux-Thang, Martin Clémancey, Victor Duarte, and Jean-Marc Latour. 2016. “Reaction of PerR with Molecular Oxygen May Assist H₂O₂ Sensing in Anaerobes.” *ACS Chemical Biology* 11 (5). American Chemical Society: 1438–44. doi:10.1021/acscchembio.5b01054.
- Sevilla, Emma, Beatriz Martin-Luna, Laura Vela, M Teresa Bes, Maria F Fillat, and M Luisa Peleato. 2008. “Iron Availability Affects *McyD* Expression and Microcystin-LR Synthesis in *Microcystis Aeruginosa* PCC7806.” *Environmental Microbiology* 10 (10). John Wiley & Sons, Ltd (10.1111): 2476–83. doi:10.1111/j.1462-2920.2008.01663.x.
- Shah, Binal N, Unmesh Chinte, Stephen J Tomanicek, B Leif Hanson, and Constance A Schall. 2011. “Flash Cooling Protein Crystals: Estimate of Cryoprotectant Concentration Using Thermal Properties.” *Crystal Growth & Design* 11 (5). American Chemical Society: 1493–1501. doi:10.1021/cg1013939.
- Sheldrick, George M. 2008. “A Short History of SHELX.” *Acta Crystallographica Section A Foundations of Crystallography* 64 (1): 112–22. doi:10.1107/S0108767307043930.
- Shen, Qun, Jun Wang, Steven E. Ealick, and IUCr. 2003. “Anomalous Difference Signal in Protein Crystals.” *Acta Crystallographica Section A Foundations of Crystallography* 59 (4). International Union of Crystallography: 371–73. doi:10.1107/S0108767303009115.
- Sherman, D R, K Mdluli, M J Hickey, C E 3rd Barry, and C K Stover. 1999. “AhpC, Oxidative Stress and Drug Resistance in *Mycobacterium Tuberculosis*.” *BioFactors (Oxford, England)* 10 (2–3). Netherlands: 211–17.
- Shi, Q, and G. Jackowski. 1998. “One-Dimensional Polyacrylamide Gel Electrophoresis.” In *Gel Electrophoresis of Proteins: A Practical Approach*, edited by B D Hames, 3rd editio, 1–52. New York: IRL Press/Oxford University Press.
- Shiia, Tomomi, Masamitsu Nakazato, Masanari Mizuta, Yukari Date, Muhtashan S. Mondal, Muneki Tanaka, Shin-Ichi Nozoe, Hiroshi Hosoda, Kenji Kangawa, and Shigeru Matsukura. 2002. “Plasma Ghrelin Levels in Lean and Obese Humans and the Effect of Glucose on Ghrelin Secretion.” *The Journal of Clinical Endocrinology & Metabolism* 87 (1): 240–44. doi:10.1210/jcem.87.1.8129.
- Shin, Jung-Ho, Hoi Jong Jung, Young Jun An, Yoo-Bok Cho, Sun-Shin Cha, and Jung-Hye Roe. 2011. “Graded Expression of Zinc-Responsive Genes through Two Regulatory Zinc-Binding Sites in *Zur*.” *Proceedings of the National Academy of Sciences* 108 (12): 5045 LP-5050. doi:10.1073/pnas.1017744108.
- Shu, Yi, Fengmei Pi, Ashwani Sharma, Mehdi Rajabi, Farzin Haque, Dan Shu, Markos Leggas, B. Mark Evers, and Peixuan Guo. 2014. “Stable RNA Nanoparticles as Potential New Generation Drugs for Cancer Therapy.” *Advanced Drug Delivery Reviews* 66 (February): 74–89. doi:10.1016/j.addr.2013.11.006.

- Silva Elipe, Maria Victoria, Maria A. Bednarek, and Ying-Duo Gao. 2001. "1H NMR Structural Analysis of Human Ghrelin and Its Six Truncated Analogs." *Biopolymers* 59 (7). John Wiley & Sons, Inc.: 489–501. doi:10.1002/1097-0282(200112)59:7<489::AID-BIP1054>3.0.CO;2-S.
- Sisto, Margherita, Liana Cucci, Massimo D'Amore, Thomas C Dow, Vincenzo Mitolo, and Sabrina Lisi. 2010. "Proposing a Relationship between *Mycobacterium Avium* Subspecies *Paratuberculosis* Infection and Hashimoto's Thyroiditis." *Scandinavian Journal of Infectious Diseases* 42 (10): 787–90. doi:10.3109/00365541003762306.
- Skibicka, Karolina P, Caroline Hansson, Emil Egecioglu, and Suzanne L Dickson. 2012. "Role of Ghrelin in Food Reward: Impact of Ghrelin on Sucrose Self-Administration and Mesolimbic Dopamine and Acetylcholine Receptor Gene Expression." *Addiction Biology* 17 (1). Wiley-Blackwell: 95–107. doi:10.1111/j.1369-1600.2010.00294.x.
- Skubák, Pavol. 2018. "Substructure Determination Using Phase-Retrieval Techniques." *Acta Crystallographica Section D Structural Biology* 74 (2). International Union of Crystallography: 117–24. doi:10.1107/S2059798317014462.
- Skubák, Pavol, and Navraj S. Pannu. 2013. "Automatic Protein Structure Solution from Weak X-Ray Data." *Nature Communications* 4 (1). Nature Publishing Group: 2777. doi:10.1038/ncomms3777.
- Skubák, Pavol, Willem-Jan Waterreus, and Navraj S. Pannu. 2010. "Multivariate Phase Combination Improves Automated Crystallographic Model Building." *Acta Crystallographica Section D Biological Crystallography* 66 (7): 783–88. doi:10.1107/s0907444910014642.
- Smaldone, Gregory T, Haike Antelmann, Ahmed Gaballa, and John D Helmann. 2012. "The FsrA SRNA and FbpB Protein Mediate the Iron-Dependent Induction of the *Bacillus Subtilis* LutABC Iron-Sulfur-Containing Oxidases." *Journal of Bacteriology* 194 (10). American Society for Microbiology: 2586–93. doi:10.1128/JB.05567-11.
- Smith, Kathryn D, Sarah V Lipchock, Tyler D Ames, Jimin Wang, Ronald R Breaker, and Scott A Strobel. 2009. "Structural Basis of Ligand Binding by a C-Di-GMP Riboswitch." *Nature Structural & Molecular Biology* 16 (12). NIH Public Access: 1218–23. doi:10.1038/nsmb.1702.
- Spencer, Sarah J, Lu Xu, Melanie A Clarke, Moyra Lemus, Alex Reichenbach, Bram Geenen, Tamás Kozicz, and Zane B Andrews. 2012. "Ghrelin Regulates the Hypothalamic-Pituitary-Adrenal Axis and Restricts Anxiety after Acute Stress." *Biological Psychiatry* 72 (6): 457–65. doi:10.1016/j.biopsych.2012.03.010.
- Staes, Edith, Pierre-Antoine Absil, Laurence Lins, Robert Bresseur, Magali Deleu, Nathalie Lecouturier, Virginie Fievez, et al. 2010. "Acylated and Unacylated Ghrelin Binding to Membranes and to Ghrelin Receptor: Towards a Better Understanding of the Underlying Mechanisms." *Biochimica et Biophysica Acta* 1798 (11): 2102–13. doi:10.1016/j.bbamem.2010.07.002.
- Stefan, Liliana R, Rui Zhang, Aaron G Levitan, Donna K Hendrix, Steven E Brenner, and Stephen R Holbrook. 2006. "MeRNA: A Database of Metal Ion Binding Sites

- in RNA Structures.” *Nucleic Acids Research* 34 (Database issue). Oxford University Press: D131-4. doi:10.1093/nar/gkj058.
- Steffensmeier, Andrew C.G., Antoine E. Azar, Jeffrey J. Fuller, Barbara A. Muller, and Stephen R. Russell. 2007. “Vitreous Injections of Pegaptanib Sodium Triggering Allergic Reactions.” *American Journal of Ophthalmology* 143 (3): 512–13. doi:10.1016/j.ajo.2006.10.007.
- Svergun, D, C Barberato, and M H J Koch. 1995. “CRY SOL - a Program to Evaluate X-Ray Solution Scattering of Biological Macromolecules from Atomic Coordinates.” *Journal of Applied Crystallography* 28 (6): 768–73. doi:10.1107/S0021889895007047.
- Svergun, D I. 1992. “Determination of the Regularization Parameter in Indirect-Transform Methods Using Perceptual Criteria.” *Journal of Applied Crystallography* 25 (4): 495–503. doi:10.1107/S0021889892001663.
- Svergun, Dmitri I. 1999. “Restoring Low Resolution Structure of Biological Macromolecules from Solution Scattering Using Simulated Annealing.” *Biophysical Journal* 76 (6): 2879–86. doi:10.1016/S0006-3495(99)77443-6.
- Sweeney, Raymond W. 2011. “Pathogenesis of Paratuberculosis.” *Veterinary Clinics of North America: Food Animal Practice* 27 (3): 537–46. doi:10.1016/j.cvfa.2011.07.001.
- Szabat, Marta, Dorota Gudanis, Weronika Kotkowiak, Zofia Gdaniec, Ryszard Kierzek, and Anna Pasternak. 2016. “Thermodynamic Features of Structural Motifs Formed by β -L-RNA.” Edited by Heidar-Ali Tajmir-Riahi. *PLOS ONE* 11 (2). Public Library of Science: e0149478. doi:10.1371/journal.pone.0149478.
- Szentirmai, E., I. Hajdu, F. Obal, and James M. Krueger. 2006. “Ghrelin-Induced Sleep Responses in Ad Libitum Fed and Food-Restricted Rats.” *Brain Research* 1088 (1): 131–40. doi:10.1016/j.brainres.2006.02.072.
- Tack, J, I Depoortere, R Bisschops, C Delporte, B Coulie, A Meulemans, J Janssens, and T Peeters. 2006. “Influence of Ghrelin on Interdigestive Gastrointestinal Motility in Humans.” *Gut* 55 (3): 327–33. doi:10.1136/gut.2004.060426.
- Terwilliger, Thomas C., Ralf W. Grosse-Kunstleve, Pavel V. Afonine, Nigel W. Moriarty, Peter H. Zwart, Li-Wei Hung, Randy J. Read, Paul D. Adams, and IUCr. 2008. “Iterative Model Building, Structure Refinement and Density Modification with the PHENIX AutoBuild Wizard.” *Acta Crystallographica Section D Biological Crystallography* 64 (1). International Union of Crystallography: 61–69. doi:10.1107/S090744490705024X.
- Teubner, Brett J W, and Timothy J Bartness. 2013. “Anti-Ghrelin Spiegelmer Inhibits Exogenous Ghrelin-Induced Increases in Food Intake, Hoarding, and Neural Activation, but Not Food Deprivation-Induced Increases.” *American Journal of Physiology. Regulatory, Integrative and Comparative Physiology* 305 (4). American Physiological Society: R323-33. doi:10.1152/ajpregu.00097.2013.
- Thompson, Dorothea K, Alexander S Beliaev, Carol S Giometti, Sandra L Tollaksen, Tripti Khare, Douglas P Lies, Kenneth H Nealson, et al. 2002. “Transcriptional and Proteomic Analysis of a Ferric Uptake Regulator (Fur) Mutant of *Shewanella*

- Oneidensis*: Possible Involvement of Fur in Energy Metabolism, Transcriptional Regulation, and Oxidative Stress.” *Applied and Environmental Microbiology* 68 (2): 881 LP-892. doi:10.1128/AEM.68.2.881-892.2002.
- Tolle, Virginie, Marie Helene Bassant, Philippe Zizzari, Frederique Poindessous-Jazat, Catherine Tomasetto, Jacques Epelbaum, and Marie Therese Bluet-Pajot. 2002. “Ultradian Rhythmicity of Ghrelin Secretion in Relation with Gh, Feeding Behavior, and Sleep-Wake Patterns in Rats.” *Endocrinology* 143 (4): 1353–61. doi:10.1210/en.143.4.1353.
- Tong, Jenny, Erica Mannea, Pascaline Aimé, Paul T Pfluger, Chun-Xia Yi, Tamara R Castaneda, Harold W Davis, et al. 2011. “Ghrelin Enhances Olfactory Sensitivity and Exploratory Sniffing in Rodents and Humans.” *The Journal of Neuroscience : The Official Journal of the Society for Neuroscience* 31 (15). NIH Public Access: 5841–46. doi:10.1523/JNEUROSCI.5680-10.2011.
- Toor, Navtej, Kevin S Keating, Sean D Taylor, and Anna Marie Pyle. 2008. “Crystal Structure of a Self-Spliced Group II Intron.” *Science (New York, N.Y.)* 320 (5872). NIH Public Access: 77–82. doi:10.1126/science.1153803.
- Torsello, Antonio, Corrado Ghe’, Elena Bresciani, Filomena Catapano, Ezio Ghigo, Romano Deghenghi, Vittorio Locatelli, and Giampiero Muccioli. 2002. “Short Ghrelin Peptides Neither Displace Ghrelin Binding *In Vitro* Nor Stimulate GH Release *In Vivo*.” *Endocrinology* 143 (5): 1968–1968. doi:10.1210/endo.143.5.8894.
- Traoré, Daouda A K, Abdelnasser El Ghazouani, Sougandi Ilango, Jérôme Dupuy, Lilian Jacquamet, Jean-Luc Ferrer, Christelle Caux-Thang, Victor Duarte, and Jean-Marc Latour. 2006. “Crystal Structure of the Apo-PerR-Zn Protein from *Bacillus Subtilis*.” *Molecular Microbiology* 61 (5). John Wiley & Sons, Ltd (10.1111): 1211–19. doi:10.1111/j.1365-2958.2006.05313.x.
- Traoré, Daouda A K, Abdelnasser El Ghazouani, Lilian Jacquamet, Franck Borel, Jean-Luc Ferrer, David Lascoux, Jean-Luc Ravanat, et al. 2008. “Structural and Functional Characterization of 2-Oxo-Histidine in Oxidized PerR Protein.” *Nature Chemical Biology* 5 (December). Nature Publishing Group: 53. <https://doi.org/10.1038/nchembio.133>.
- Trivedi, Abhishek, Nisha Singh, Shabir Ahmed Bhat, Pawan Gupta, and Ashwani Kumar. 2012. “Redox Biology of Tuberculosis Pathogenesis.” *Advances in Microbial Physiology* 60: 263–324. doi:10.1016/B978-0-12-398264-3.00004-8.
- Tschöp, Matthias, Christian Weyer, P. Antonio Tataranni, Viswanath Devanarayan, Eric Ravussin, and Mark L. Heiman. 2001. “Circulating Ghrelin Levels Are Decreased in Human Obesity.” *Diabetes* 50 (4). <http://diabetes.diabetesjournals.org/content/50/4/707.long>.
- Tuerk, C, and L Gold. 1990. “Systematic Evolution of Ligands by Exponential Enrichment: RNA Ligands to Bacteriophage T4 DNA Polymerase.” *Science (New York, N.Y.)* 249 (4968): 505–10. <http://www.ncbi.nlm.nih.gov/pubmed/2200121>.
- Turner, D H, N Sugimoto, and S M Freier. 1988. “RNA Structure Prediction.” *Annual Review of Biophysics and Biophysical Chemistry* 17 (1). Annual Reviews: 167–92. doi:10.1146/annurev.bb.17.060188.001123.

- Twort, FW, and GLY Ingram. 1912. "A Method for Isolating and Cultivating the *Mycobacterium Enterididis Chronicae Pseudotuberculosis Johne* and Some Experiments on the Preparation of a Diagnostic Vaccine for Pseudotuberculous Enteritis of Bovines." *Proceedings of the Royal Society* 84: 517–43.
- Usón, Isabel, and George M Sheldrick. 2018. "An Introduction to Experimental Phasing of Macromolecules Illustrated by *SHELX*; New Autotracing Features." *Acta Crystallographica Section D* 74 (2): 106–16. doi:10.1107/S2059798317015121.
- Valentin-Weigand, P, and R Goethe. 1999. "Pathogenesis of *Mycobacterium Avium* Subspecies *Paratuberculosis* Infections in Ruminants: Still More Questions than Answers." *Microbes and Infection* 1 (13): 1121–27. <http://www.ncbi.nlm.nih.gov/pubmed/10572316>.
- Valentin-Weigand, P, and K M Moriarty. 1992. "*Mycobacterium Paratuberculosis* Binds Fibronectin." *Research in Microbiology* 143 (1): 75–79. <http://www.ncbi.nlm.nih.gov/pubmed/1641514>.
- Vallazza, M, M Perbandt, S Klussmann, W Rypniewski, H M Einspahr, V A Erdmann, and Ch. Betzel. 2004. "First Look at RNA in L-Configuration." *Acta Crystallographica Section D* 60 (1): 1–7. doi:10.1107/S0907444903027690.
- Varani, Gabriele, and William H McClain. 2000. "The G·U Wobble Base Pair." *EMBO Reports* 1 (1): 18–23. doi:10.1093/embo-reports/kvd001.
- Vater, Axel, and Sven Klussmann. 2015. "Turning Mirror-Image Oligonucleotides into Drugs: The Evolution of Spiegelmer® Therapeutics." *Drug Discovery Today* 20 (1). Elsevier Ltd: 147–55. doi:10.1016/j.drudis.2014.09.004.
- Veldhuis, Johannes D., and Cyril Y. Bowers. 2010. "Integrating GHS into the Ghrelin System." *International Journal of Peptides* 2010: 1–40. doi:10.1155/2010/879503.
- Ventura, Marco, Carlos Canchaya, Andreas Tauch, Govind Chandra, Gerald F Fitzgerald, Keith F Chater, and Douwe van Sinderen. 2007. "Genomics of Actinobacteria: Tracing the Evolutionary History of an Ancient Phylum." *Microbiology and Molecular Biology Reviews : MMBR* 71 (3). American Society for Microbiology (ASM): 495–548. doi:10.1128/MMBR.00005-07.
- Vortmeier, Gerrit, Stephanie H. DeLuca, Sylvia Els-Heindl, Constance Chollet, Holger A. Scheidt, Annette G. Beck-Sickingler, Jens Meiler, and Daniel Huster. 2015. "Integrating Solid-State NMR and Computational Modeling to Investigate the Structure and Dynamics of Membrane-Associated Ghrelin." Edited by Patrick van der Wel. *PLOS ONE* 10 (3): e0122444. doi:10.1371/journal.pone.0122444.
- Walker, Scott C, Johanna M Avis, and Graeme L Conn. 2003. "General Plasmids for Producing RNA *in Vitro* Transcripts with Homogeneous Ends." *Nucleic Acids Research* 31 (15): e82–e82. doi:10.1093/nar/gng082.
- Wallach, O. 1895. "Zur Kenntniss Der Terpene Und Der Ätherischen Oele." *Justus Liebig's Annalen Der Chemie* 286 (1). John Wiley & Sons, Ltd: 90–118. doi:10.1002/jlac.18952860105.
- Wang, Bi-Cheng B T - Methods in Enzymology. 1985. "Resolution of Phase Ambiguity in Macromolecular Crystallography." In *Diffraction Methods for Biological Macromolecules Part B*, 115:90–112. Academic Press.

- doi:[https://doi.org/10.1016/0076-6879\(85\)15009-3](https://doi.org/10.1016/0076-6879(85)15009-3).
- Weigoldt, Mathias, Jochen Meens, Franz-Christoph Bange, Andreas Pich, Gerald F Gerlach, and Ralph Goethe. 2013. "Metabolic Adaptation of *Mycobacterium Avium* Subsp. *Paratuberculosis* to the Gut Environment." *Microbiology (Reading, England)* 159 (Pt 2): 380–91. doi:10.1099/mic.0.062737-0.
- Weigoldt, Mathias, Jochen Meens, Klaus Doll, Isabel Fritsch, Petra Möbius, Ralph Goethe, and Gerald F Gerlach. 2011. "Differential Proteome Analysis of *Mycobacterium Avium* Subsp. *Paratuberculosis* Grown *in Vitro* and Isolated from Cases of Clinical Johne's Disease." *Microbiology (Reading, England)* 157 (Pt 2): 557–65. doi:10.1099/mic.0.044859-0.
- Weikel, J C, A Wichniak, M Ising, H Brunner, E Friess, K Held, S Mathias, D A Schmid, M Uhr, and A Steiger. 2003. "Ghrelin Promotes Slow-Wave Sleep in Humans." *American Journal of Physiology. Endocrinology and Metabolism* 284 (2): E407-15. doi:10.1152/ajpendo.00184.2002.
- Whittington, R J, D J Begg, K de Silva, A C Purdie, N K Dhand, and K M Plain. 2017. "Case Definition Terminology for Paratuberculosis (Johne's Disease)." *BMC Veterinary Research* 13 (1). BioMed Central: 328. doi:10.1186/s12917-017-1254-6.
- Willesen, M G, P Kristensen, and J Rømer. 1999. "Co-Localization of Growth Hormone Secretagogue Receptor and NPY mRNA in the Arcuate Nucleus of the Rat." *Neuroendocrinology* 70 (5): 306–16. doi:10.1159/000054491.
- Winn, Martyn D., Charles C. Ballard, Kevin D. Cowtan, Eleanor J. Dodson, Paul Emsley, Phil R. Evans, Ronan M. Keegan, et al. 2011. "Overview of the CCP 4 Suite and Current Developments." *Acta Crystallographica Section D Biological Crystallography* 67 (4). International Union of Crystallography: 235–42. doi:10.1107/S0907444910045749.
- Wortley, Katherine E, Juan-Pablo del Rincon, Jane D Murray, Karen Garcia, Keiji Iida, Michael O Thorner, and Mark W Sleeman. 2005. "Absence of Ghrelin Protects against Early-Onset Obesity." *The Journal of Clinical Investigation* 115 (12): 3573–78. doi:10.1172/JCI26003.
- Wren, A. M., L. J. Seal, M. A. Cohen, A. E. Brynes, G. S. Frost, K. G. Murphy, W. S. Dhillo, M. A. Ghatei, and S. R. Bloom. 2001. "Ghrelin Enhances Appetite and Increases Food Intake in Humans." *The Journal of Clinical Endocrinology & Metabolism* 86 (12). Oxford University Press: 5992–5992. doi:10.1210/jcem.86.12.8111.
- Yang, J., T.-J. Zhao, J. L. Goldstein, and M. S. Brown. 2008. "Inhibition of Ghrelin O-Acyltransferase (GOAT) by Octanoylated Pentapeptides." *Proceedings of the National Academy of Sciences* 105 (31): 10750–55. doi:10.1073/pnas.0805353105.
- Yang, J T, C S Wu, and H M Martinez. 1986. "Calculation of Protein Conformation from Circular Dichroism." *Methods in Enzymology* 130: 208–69. <http://www.ncbi.nlm.nih.gov/pubmed/3773734>.
- Yang, Jing, Michael S. Brown, Guosheng Liang, Nick V. Grishin, and Joseph L. Goldstein. 2008. "Identification of the Acyltransferase That Octanoylates Ghrelin,

- an Appetite-Stimulating Peptide Hormone.” *Cell* 132 (3): 387–96. doi:10.1016/j.cell.2008.01.017.
- Yatime, Laure, Christian Maasch, Kai Hoehlig, Sven Klussmann, Gregers R Andersen, and Axel Vater. 2015. “Structural Basis for the Targeting of Complement Anaphylatoxin C5a Using a Mixed L-RNA/L-DNA Aptamer.” *Nature Communications* 6. Nature Publishing Group: 6481. doi:10.1038/ncomms7481.
- Yin, Yue, Yin Li, and Weizhen Zhang. 2014. “The Growth Hormone Secretagogue Receptor: Its Intracellular Signaling and Regulation.” *International Journal of Molecular Sciences* 15 (3): 4837–55. doi:10.3390/ijms15034837.
- Zahrt, Thomas C, Jian Song, Jessica Siple, and Vojo Deretic. 2001. “Mycobacterial FurA Is a Negative Regulator of Catalase–peroxidase Gene *KatG*.” *Molecular Microbiology* 39 (5). John Wiley & Sons, Ltd (10.1111): 1174–85. doi:10.1111/j.1365-2958.2001.02321.x.
- Zawadzke, Laura E., and Jeremy M. Berg. 1993. “The Structure of a Centrosymmetric Protein Crystal.” *Proteins: Structure, Function, and Genetics* 16 (3). John Wiley & Sons, Ltd: 301–5. doi:10.1002/prot.340160308.
- Zhang, Yang. 2008. “I-TASSER Server for Protein 3D Structure Prediction.” *BMC Bioinformatics* 9 (1). BioMed Central: 40. doi:10.1186/1471-2105-9-40.
- Zhao, T.-J., G. Liang, R. L. Li, X. Xie, M. W. Sleeman, A. J. Murphy, D. M. Valenzuela, G. D. Yancopoulos, J. L. Goldstein, and M. S. Brown. 2010. “Ghrelin O-Acyltransferase (GOAT) Is Essential for Growth Hormone-Mediated Survival of Calorie-Restricted Mice.” *Proceedings of the National Academy of Sciences* 107 (16): 7467–72. doi:10.1073/pnas.1002271107.
- Zheleznova, Ekaterina E, Jorge H Crosa, and Richard G Brennan. 2000. “Characterization of the DNA- and Metal-Binding Properties of *Vibrio Anguillarum* Fur Reveals Conservation of a Structural Zn²⁺ Ion.” *Journal of Bacteriology* 182 (21): 6264 LP-6267. doi:10.1128/JB.182.21.6264-6267.2000.
- Zhou, Jiehua, and John Rossi. 2017. “Aptamers as Targeted Therapeutics: Current Potential and Challenges.” *Nature Reviews. Drug Discovery* 16 (3). NIH Public Access: 181–202. doi:10.1038/nrd.2016.199.
- Zhu, Yixuan, Sunil Kumar, Angeli L Menon, Robert A Scott, and Michael W W Adams. 2013. “Regulation of Iron Metabolism by *Pyrococcus Furiosus*.” *Journal of Bacteriology* 195 (10): 2400 LP-2407. doi:10.1128/JB.02280-12.

Appendix

A1. Chemicals and Hazards

A1.1. Chemicals

Compound	CAS-No.	GHS hazard	Hazard statements	Precautionary Statements
Acetic acid	64-19-7	GHS02, GHS05	H226, H314	P280, P305+351+338, P310
Acrylamide 37%	79-06-1	GHS06, GHS08	H301, H312, H315, H317, H319, H332, H340, H350, H316f, H372	P201, P280, P301+310, P305+351+338, P308+313
Agarose	9012-36-6	-	-	-
(NH ₄) ₂ SO ₄	7283-20-2	-	-	-
Ampicillin	69-52-3	GHS08	H334, H317	P280, P261, P302+352, P342+311
APS	7727-54-0	GHS03, GHS07, GHS08	H272, H302, H315, H317, H319, H334, H335	P280, P305+351+338, P302+352, P304+341, P342+311
Bromphenol blue	115-39-9	-	-	-
CaCl ₂	10043-52-4	GHS07	H319	P305+351+338
Ca(CH ₃ COO) ₂	114460-21-8	-	-	-
Citric acid	77-92-9	GHS05	H318	P305+351+338, P311
Coomassie Brilliant Blue R250	6104-59-2	-	-	-
DTT	577517	GHS07	H302, H315, H319, H335	P302,352, P305+351+338
EDTA	60-00-4	GHS07	H319	P305+351+338

Appendix

Ethanol	64-17-5	GHS02	H225, H319	P210, P240, P305+351+338, P403+233
Ethidiumbromid	1239-45-8	GHS06, GHS08	H302, H330, H341	P260, P281, P284, P310
Glycerol	56-81-5	-	-	-
Guanidinhydrochlorid	50-01-1	GHS07	H302, H315, H319	P305+351+388, P302+352
Hepes	7365-45-9	-	-	-
Hydrochloric acid >25%	7647-01-0	GHS05, GHS07	H314, H335	P261, P280, P310, P305+351+338
Isopropanol	67-63-0	GHS02, GHS07	H225, H319, H336	P210, P233, P305+351+338
KCl	7447-40-7	-	-	-
MgCl ₂	7786-30-03	-	-	-
NaBr	7647-15-6	-	-	-
NaH ₂ PO ₄	10049-21-5	-	-	-
NaOH	1310-73-2	GHS05	H314	P280, P310, P305+351+338
Na ₃ citrate	6132-04-3	-	-	-
Paraffin	8002-74-2	-	-	-
PEG4000	25322-68-3	-	-	-
PEG8000	25322-68-3	-	-	-
PMSF	329-98-6	GHS05, GHS06	H301, H314	P280, P305+351+338, P310
SDS	151-21-3	GHS02, GHS06	H228, H302, H311, H315, H319, H335	P210, P261, P280, P301+312+330, P305+351+338+310, P370+P378
TEMED	110-18-9	GHS02, GHS05, GHS07	H225, H302, H314, H332	P261, P280, P305+351+338
Tris	1185-53-1	GHS07	H315, H319, H335	P261, P305+351+338
Glycine	56-40-6	-	-	-
Tryptone	91079-40-2	-	-	-

Yeast Extract	8013-01-2	-	-	-
Casein	9000-71-9	-	-	-
K ₂ HPO ₄	16788-57-1	-	-	-
KH ₂ PO ₄	7778-77-0	-	-	-
Kanamycin	8063-07-8	GHS08	H360	P201, P308+313
Chloramphenicol	56-75-7	GHS08	H351	P280
Tetracyclin	60-54-8	GHS07	H302	-
Isopropyl-β-D-thiogalactopyranosid (IPTG)	367-93-1	-	-	-
Xylene cyanol	2650-17-1	GHS07	H315, H319, H335	P261, P305+351+338
Bicine	150-25-4	GHS07	H315, H319, H336	P321
Ammonium Acetate	631-61-8	-	-	-
Bis-Tris	6976-37-0	GHS07	H315, H319, H335	P261, P305+351+338
MES	4432-31-9	GHS07	H315, H319, H336	P261, P305+351+339
Sodium Acetate	6131-90-4	-	-	-
Sodium Citrate	68-04-2	-	-	-
[Co(NH ₃) ₆]Cl ₃	10534-89-1	GHS07	H315, H319, H336	P261, P264, P271, P280, P302+352, P304+340, P305+351+338, P312, P321, P332+313, P337+313, P362, P403+233, P405, P501
CdBr ₂	13464-92-1	GHS07, GHS09	H302, H312, H332, H410	P220, P273, P280, P501
CdI ₂	7790-80-9	GHS06, GHS08, GHS09	H301+331, H351, H373, H410	P260, P280, P301+330+331+310, P304+340+311, P403+233
CdSO ₄	13477-20-8	GHS06, GHS08, GHS09	H301, H330, H340, H350, H360FD, H372, H410	P201, P260, P273, P284, P301+310+330, P304+340+310

Appendix

CH ₄ N ₂ Se	630-10-4	GHS06, GHS08, GHS09	H301, H331, H373, H410	P261, P273, P301+310, P311, P501
FeCl ₃	10025-77-1	GHS05, GHS07	H290, H302, H315, H318	P280, P305+351+338
HgBr ₂	7789-47-1	GHS06, GHS08, GHS09	H300, H310, H330, H373, H410	P269, P280, P301+310+330, P302+352, P310, P304+340+310, P403+233
IrCl ₃	14996-61-3	GHS07	H319	P305+351+338
K ₂ (HgI ₄)	7783-33-7	GHS06, GHS08, GHS09	H300, H310, H330, H373, H410	P260, P301+310, P320, P361, P405, P501
MnCl ₂	13446-34-9	GHS06, GHS09	H301, H411	P273, P309+310
NaI	7681-82-5	GHS09	H400	P273
NiSO ₄	10101-97-0	GHS07, GHS08, GHS09	H302, H332, H315, H317, H334, H341, H350i, H360D, H372, H410	P201, P273, P280, P302+352, P304+340, P308+313
OsCl ₃	14996-60-2	GHS05, GHS06	H301+311+331, H314	P260, P280, P303+361+352, P304+340+310, P305+351+338, P310
Sm(CH ₃ CO ₂) ₃	100587-91-5	-	-	-
ZnCl ₂	7646-85-7	GHS05, GHS07, GHS09	H302, H314, H410	P273, P280, P301+330+331, P305+351+338, P308+310
Ammonium hydrogen carbonate	1066-33-7	GHS07	H302	P301+312, P330
Acetonitrile	75-05-8	GHS02, GHS07	H225, H332, H302, H312, H319	P210, P240, P302+352, P305+351+338, P403+233
Formic Acid	64-18-6	GHS02, GHS05, GHS06	H226, H302, H314, H331, EUH:071	P210, P280, P303+361+353, P304+340+310, P305+351+338, P403+233

Iodoacetamide	144-48-9	GHS06, GHS08	H301, H317, H334, H413	P261, P280, P301+310, P341+311
CoCl ₂	7791-13-1	GHS07, GHS08, GHS09	H350i, H360F, H302, H317, H334, H341, H410	P201, P273, P280, P302+352, P304+340, P342+311
EGTA	67-42-5	-	-	-
TCEP	5961-85-3	GHS05	H314	P280, P305+351+338, P310

A1.2. Crystallization Screens

Crystallization Screen	Supplier	GHS hazard	Hazard statements	Precautionary Statements
AmSO ₄ -Suite	Qiagen	GHS02, GHS06, GHS08, GHS09	H225, H301, H330, H350, H340, H360FD, H371, H411	P101, P201, P273, P280, P309+311
ComPAS-Suite	Qiagen	GHS02, GHS06, GHS07, GHS08, GHS09	H225, H301, H302, H315, H319, H331, H332, H335, H340, H350, H360FD, H373, H411	P101, P201, P270, P273, P280, P305+351+338, P309+311, P313
JSGC-plus	Molecular Dimensions	GHS02, GHS05, GHS06, GHS07, GHS08, GHS09	H225, H301, H312, H315, H318, H331, H335, H350, H411	P101, P201, P270, P273, P280, P305+351+338, P309+311, P313
MORPHEUS	Molecular Dimensions	GHS02, GHS06, GHS07, GHS08, GHS09	H225, H301, H302, H315, H319, H331, H332, H335, H340, H350, H360FD, 361d, H373, H411	P101, P201, P270, P273, P280, P305+351+338, P309+311, P313
PACT premier	Molecular Dimensions	GHS06	H301, H331, H412	P101, P270, P273, P280, P309+311

A1.3. GHS and Risk Symbols

Structure	Molecular Dimensions	GHS02, GHS06, GHS07, GHS08, GHS09	H225, H301, H302, H315, H319, H331, H332, H335, H340, H350, H360FD, 361d, H373, H411	P101, P201, P270, P273, P280, P305+351+338, P309+311, P313
SturaFootprint & MacroSol	Molecular Dimensions	GHS02, GHS06, GHS07, GHS08, GHS09	H225, H301, H302, H315, H319, H331, H332, H335, H340, H350, H360FD, H373, H411	P101, P201, P270, P273, P280, P305+351+338, P309+311, P313
GeneJET Gel Extraction Kit	Thermo Fisher Scientific	GHS07	H302, H412	P264, P270, P273, P301+312, P330, P501
peqGold Plasmid Miniprep Kit I	PEQLAB Biotechnologie	GHS02, GHS05, GHS07	H225, H290, H302, H315, H318, H319, H336	P243, P280, P301+330+331, P302+352, P304+340, P305+351+338, P308+310, P308+311, P403+235, P210,

A1.3. GHS and Risk Symbols



Figure 43: GHS Pictograms. Summary of all GHS pictograms along with the respective nomenclature.

A1.4. Hazard Statements

H225	Highly flammable liquid and vapour.
H226	Flammable liquid and vapour.
H228	Flammable solid.
H272	May intensify fire; oxidiser.
H280	Contains gas under pressure; may explode if heated.
H290	May be corrosive to metals.
H300	Fatal if swallowed.
H301	Toxic if swallowed.
H302	Harmful if swallowed.
H302+H332	Harmful if swallowed or if inhaled.
H304	May be fatal if swallowed and enters airways.
H310	Fatal in contact with skin.
H311	Toxic in contact with skin.
H312	Harmful in contact with skin.
H314	Causes severe skin burns and eye damage.
H315	Causes skin irritation.
H317	May cause an allergic skin reaction.
H318	Harmful if swallowed or if inhaled.
H319	Causes serious eye irritation.
H330	Fatal if inhaled.
H331	Toxic if inhaled.
H332	Harmful if inhaled.
H334	May cause allergy or asthma symptoms or breathing difficulties if inhaled.
H335	May cause respiratory irritation.
H336	May cause drowsiness or dizziness.
H340	May cause genetic defects.
H341	Suspected of causing genetic defects.
H350	May cause cancer.
H360fd	May damage fertility or the unborn child.
H361f	Suspected of damaging fertility.
H370	Causes damage to organs.
H372	Causes damage to organs through prolonged or repeated exposure.
H373	May cause damage to organs through prolonged or repeated exposure.
H400	Very toxic to aquatic life.
H410	Very toxic to aquatic life with long lasting effects.
H411	Toxic to aquatic life with long lasting effects.
H412	Harmful to aquatic life with long lasting effects.
EUH066	Repeated exposure may cause skin dryness or cracking.

A1.5. Precautionary Statements

- P101 If medical advice is needed, have product container or label at hand.
- P201 Obtain special instructions before use.
- P210 Keep away from heat, hot surfaces, sparks, open flames and other ignition sources. No smoking.
- P220 Keep away from clothing and other combustible materials.
- P233 Keep container tightly closed.
- P240 Ground and bond container and receiving equipment.
- P260 Do not breathe dust/fume/gas/mist/vapors/spray.
- P261 Avoid breathing dust/fume/gas/mist/vapours/spray.
- P264 Wash thoroughly after handling.
- P270 Do not eat, drink or smoke when using this product.
- P273 Avoid release to the environment.
- P280 Wear protective gloves/protective clothing/eye protection/face protection.
- P301+310 IF SWALLOWED: Immediately call a POISON CENTRE or doctor/physician.
- P301+312 IF SWALLOWED: Call a POISON CENTRE or doctor if you feel unwell.
- P301+312 IF SWALLOWED: Call a POISON CENTRE or doctor/physician if you
+330 feel unwell. Rinse mouth.
- P301+330 IF SWALLOWED: Rinse mouth. Do NOT induce vomiting.
+331
- P302+352 IF ON SKIN: Wash with plenty of soap and water.
- P303+361 IF ON SKIN (or hair): Remove/Take off immediately all contaminated
+353 clothing. Rinse skin with water or shower.
- P304+340 IF INHALED: Remove person to fresh air and keep comfortable for
breathing.
- P304+340 IF INHALED: Remove person to fresh air and keep comfortable for
+310 breathing. Immediately call a POISON CENTRE or doctor/physician.
- P305+351 IF IN EYES: Rinse cautiously with water for several minutes. Remove
+338 contact lenses, if present and easy to do. Continue rinsing.
- P305+351 IF IN EYES: Rinse cautiously with water for several minutes. Remove
+338+310 contact lenses, if present and easy to do. Continue rinsing. Immediately
call a POISON CENTRE or doctor/physician.
- P308+310 IF exposed or concerned: Immediately call a POISON CENTRE or doctor.
- P308+313 IF exposed or concerned: Get medical advice/attention.
- P309+311 IF exposed or you feel unwell: Call a POISON CENTRE or doctor/
physician.
- P310 Immediately call a POISON CENTRE or doctor.
- P321 Specific treatment (see respective MSDS).
- P330 Rinse mouth.
- P331 Do NOT induce vomiting.
- P342+311 If experiencing respiratory symptoms: Call a POISON CENTRE or doctor.
- P370+378 In case of fire: Use dry sand, dry extinguishing powder or alcoholresistant
foam for extinction.
- P391 Collect spillage.
- P403 Store in a well-ventilated place.

- P403+233 Store in a well-ventilated place. Keep container tightly closed.
- P403+235 Store in a well-ventilated place. Keep cool.
- P405 Store locked up.
- P501 Dispose of contents / container in accordance with local / regional / national / international regulations.

A2. List of Figures

Figure 1: Putative regulatory mechanisms of FurA in MAP (Eckelt <i>et al.</i> , 2015).....	14
Figure 2: Experimental absorption spectra for a calcium containing macromolecular crystal around the theoretical K-absorption edge of calcium.	25
Figure 3 Structure factor relationship for the anomalous scattering contribution and Harker diagram for single wavelength anomalous diffraction.....	26
Figure 4: Properties of long wavelength experiments.....	28
Figure 5: MAP FurA recombinantly expressed in <i>E. coli</i> BL21 DE3 cells.	72
Figure 6: MAP FurA purification.	73
Figure 7: DLS measurements of MAP FurA.	75
Figure 8: Crystallization trials for MAP FurA.....	76
Figure 9: Multiple sequence alignment of MAP FurA amino acid sequence with its closest known homologues with structures deposited in the PDB.....	77
Figure 10: Homology modeling of MAP FurA.....	78
Figure 11: SAXS data analysis of MAP-FurA.....	80
Figure 12: <i>Ab initio</i> models of MAP FurA calculated with DAMMIN (Svergun, 1999).	81
Figure 13: Putative DNA-binding of MAP FurA to DNA.....	82
Figure 14: CD spectroscopic comparison of MAP FurA with different treatments.....	84
Figure 15: Influence of hydrogen peroxide on MAP FurA over time.	85
Figure 16: Melting temperatures T_m of MAP FurA upon incubation with different metals and metal chelators.	86
Figure 17: MAP FurA binding to different metals.....	87
Figure 18: Influence of reducing agents on MAP FurA.....	88
Figure 19: Ghrelin•NOX-B11 complex formation verification.	90
Figure 20: Long-term stability of Ghrelin•NOX-B11.....	91
Figure 21: SAXS data analysis of NOX-B11 and Ghrelin•NOX-B11.....	92
Figure 22: <i>Ab initio</i> models of NOX-B11 and Ghrelin•NOX-B11 calculated with DAMMIN..	93
Figure 23: SASREF rigid body model of Ghrelin•NOX-B11 against solution scattering data. .	94
Figure 24: Improvement of Ghrelin•NOX-B11 crystal quality with several rounds of micro seeding.	95
Figure 25: Evidence of NOX-B11 containing crystals.	96
Figure 26: Multi-crystal analysis with BLEND.	99
Figure 27: Comparison of diffraction strengths of the different merged crystal clusters.	101
Figure 28: Comparison of diffraction strengths of the data collected at I23 at Diamond Light source.	102

Figure 29: Fluorescence scan of a Ghrelin•NOX-B11 crystal around the calcium K-absorption edge region.	104
Figure 30: Comparison of the diffraction strength for the calcium MAD data.	106
Figure 31: XANES spectrum between 7660 and 7770 eV for a native Ghrelin•NOX-B11 crystal and a derivative Ghrelin•NOX-B11 crystal soaked with 10 mM [Co(NH ₃) ₆]Cl ₃	108
Figure 32: Absorption spectrum around the iron K-edge for a Ghrelin•NOX-B11 crystal soaked with 10 mM [Co(NH ₃) ₆]Cl ₃	108
Figure 33: SHELXD/E example.	110
Figure 34: Example 2Fo-Fc electron density map contoured at 2.0 sigma.	112
Figure 35: Crystallization approaches of Ghrelin•NOX-B11 D-Ghrelin•D-NOX-B11 racemate	113
Figure 36: Diffraction image of a Ghrelin•NOX-B11 D-Ghrelin•D-NOX-B11 racemate crystal.	114
Figure 37: Secondary structure prediction of NOX-B11 created with the Vienna RNA Websuite (Gruber <i>et al.</i> , 2008).	115
Figure 38: 2mFo-DFc electron density map contoured at 1 σ with the mFo-DFc difference density map contoured at 3 σ after one round of molecular replacement with helical fragments.	116
Figure 39: 2Fo-Fc electron density maps obtained with the molecular replacement approach using helical L-RNA-fragments as the search model (Robertson & Scott, 2008).	116
Figure 40: Comparison of the generated 3D models with the experimental SAXS data.	118
Figure 41: 2mFo-DFc electron density map and <i>mFo-DFc</i> difference density map cut-out of the calculated from the molecular replacement solution using the backbone of model.	118
Figure 42: Putative gene regulation of MAP FurA under different stress conditions as indicated by the obtained SAXS results.	120

A3. List of Tables

Table 1: Consumables used in this work.....	30
Table 2: List of equipment used in this work.....	31
Table 3: Growth media for bacterial cultures.	34
Table 4: Antibiotics used for <i>E. coli</i> mutant strain selection.	35
Table 5: Generally used buffers and solutions.....	36
Table 6: Buffers used for Ghrelin•NOX-B11 complex formation and purification.....	38
Table 7: Lysis and purification buffers for cell lysis and FurA purification.....	38
Table 8: Buffers used for solubility screening (Benvenuti & Mangani, 2007).	39
Table 9: Stock solutions for buffer preparation or soaking to generate derivative crystals.	40
Table 10: Molecular-weight size markers and their size ranges.	41
Table 11: List of commercially available kits used in this work.....	42
Table 12: Bacterial strains used in this work.	42
Table 13: Buffers and solutions used for SDS-PAGE gel casting.	49
Table 14: Buffers and solutions used for Native-PAGE gel casting and electrophoresis.....	50
Table 15: DNA sequences used for EMSA. LUEGO binding sites are underlined.	55
Table 16: Solutions used for tryptic digestion.	56
Table 17: List of additives used in thermal shift assay (taken from the RUBIC Additive Screen; Molecular Dimensions).....	59
Table 18: List of crystallization screens used in this work.	61
Table 19: Overview of soaking solutions used for derivative production.	64
Table 20: Results from the MAP FurA solubility assay.	74
Table 21: Secondary structure predictions of MAP FurA with different treatments..	83
Table 22: Summary of the Data collection statistics for the Ghrelin•NOX-B11 native diffraction data.	97
Table 23: Comparison of the data statistics for all crystals merged together and cluster 7 and cluster 9, chosen after multi-crystal merging analysis with BLEND.....	101
Table 24: Comparison of the data statistics of the diffraction data collected at I23 at Diamond Light source.....	103
Table 25: Summary of the data statistics for the Ghrelin•NOX-B11 calcium MAD data.	105
Table 26: Summary of the Data statistics for the Ghrelin•NOX-B11 cobalt derivative MAD data around the experimentally derived K-absorption edge.	109
Table 27: Data statistic comparison of datasets collected in this study and example dataset Cas9-RNA-DNA.	127

Acknowledgements

Ich möchte mich herzlich bei meinem Doktorvater Prof. Betzel für die Bereitstellung meines Themas, die Betreuung und die Begutachtung meiner Arbeit bedanken. Darüber hinaus möchte ich mich für die Möglichkeit der Teilnahme an der Dienstreise in die USA und den Workshop in Nové Hradý bedanken. Des Weiteren danke ich Markus Perbandt für seine Unterstützung und Ideen als mein Zweitbetreuer.

Weiterer Dank gilt Prof. Torda für die Übernahme des Zweitgutachtens meiner Dissertation. Außerdem danke ich meinen Disputationsgutachtern Prof. Holl und Dr. Hackl.

Vielen Dank an die nette Zusammenarbeit mit der NOXXON AG, insbesondere an Dr. Sven Klußmann und Dr. Dirk Eulberg für die Durchsicht und Kommentare zu meinem Manuskript. Des Weiteren danke ich Dr. John Achenbach, der mir insbesondere am Anfang meiner Doktorarbeit mir mit viel Hilfe und Wissen zur Seite stand.

Außerdem danke ich dem Arbeitskreis rund um Prof. Ralph Goethe der Tierärztlichen Hochschule Hannover für die Bereitstellung des MAP FurA Vektors.

Ein großes Dankeschön geht an das Team von P11 und besonders an Dr. Olga Lorbeer. Vielen Dank fürs Mutmachen und für die hilfreichen Tipps und Ideen.

Vielen lieben Dank auch an Guillaume Pompidour und dem Team von P13. Vielen Dank für die Strahlzeit, Hilfestellung, und Geduld! Vielen lieben Dank auch an Thomas Schneider für deine Zeit und sehr hilfreichen Anregungen und Tipps.

Danke an Jan Knop vom Institut für molekulare Pflanzenphysiologie für die Aufnahmen mit dem Fluoreszenzmikroskop!

Vielen lieben Dank auch an das Team der I23 Beamline der Diamond Light Source, besonders an Dr. Ramona Duman und Dr. Armin Wagner! Vielen lieben Dank, für das Ermöglichen der Messungen und für die folgenden Diskussionen und Anregungen.

Darüber hinaus danke ich Dr. Dominik Oberthür, Dr. Azat G. Gabdoulkhakov und Prof. Winfried Hinrichs. Vielen lieben Dank für eure Zeit, Anregungen und Hilfe!

Ich danke meiner Arbeitsgruppe für die vielen Erlebnisse und Erfahrungen, die ich hier machen durfte und danke an all die Menschen, die ich kennen lernen durfte. Mein

Acknowledgements

allergrößter Dank geht an Sabine. Ich danke dir dafür, dass du am Anfang meiner Promotion so geduldig und lieb warst, mir so viel beigebracht hast und für deine Unterstützung privat und beruflich während meiner Promotion und während des Schreibprozesses. Danke auch für die viele Zeit, die du in das Korrekturlesen meiner Arbeit investiert hast! Außerdem danke ich Tessie und Svetlana, danke, dass ihr von Anfang an meine tausend Fragen beantwortet habt. Danke, dass ihr mich so unterstützt habt und natürlich danke für den ganzen Spaß, den wir zusammen hatten! Danke an Dana, Aline und an Aileen, danke dass ihr mir den Laboralltag versüßt habt und besonders danke ich Dana und Aileen für eure Unterstützung und Zeit seit Beginn dieses Jahrs.

Eidesstattliche Versicherung

Hiermit versichere ich an Eides statt, die vorliegende Dissertation selbst verfasst und keine anderen als die angegebenen Hilfsmittel benutzt zu haben. Die eingereichte schriftliche Fassung entspricht der auf dem elektronischen Speichermedium. Ich versichere, dass diese Dissertation nicht in einem früheren Promotionsverfahren eingereicht wurde.

Hamburg, 10.07.2019

Christina Schmidt